PHYSICAL VOLCANOLOGY, EMPLACEMENT HISTORY AND INFERRED VISCOSITY OF TWO RHYOLITES.

A thesis

submitted in fulfilment

of the requirements

of

Doctor of Philosophy in Earth Sciences

at the

University of Waikato

by

RICHARD JOHN STEVENSON

University of Waikato

1989.

ABSTRACT

Rhyolite lavas have not been observed to erupt in New Zealand. No detailed measurement of the physical volcanological properties of lavas has been undertaken to date. However, the detailed measurement of fabric parameters from lava flow unit profiles, provides an insight into emplacement history, rheological behaviour, and ultimately volcanic hazards of rhyolite lavas.

Two constrasting Cenozoic rhyolites were studied: Ben Lomond flow - a calc-alkaline rhyolite flow 3.5 km length of 110 ka age; and a pantelleritic flow sequence of Quaternary age from Mayor Island.

The general stratigraphy of a rhyolite flow comprises: finely vesicular pumice; upper obsidian layer; central crystalline rhyolite; lower obsidian layer; and a basal breccia. Fabric measurements include density, proportions of primary and secondary voids, void and autoclast aspect ratios, and microlite length. Porosity data provide information on the distribution of volatiles in an emplacing lava, and spherulites on post-emplacement volatile migration.

Primary voids are suppressed below 10 m depth. The largest spherulites most commonly occur above the central rhyolite core, suggesting late flow migration of volatiles from a crystallising flow centre. Supportive evidence is: vesiculation of explosion breccia at c.30 m depth; a coincident peak in water content; and subtle trace element variations. Microlites of uniform length formed prior to emplacement. Subsurface evidence (microlite shape) supports an increasing undercooling, and degassing of an originally hydrous magma, collapsing from an inflated foam before emplacing as a viscous flow. Effervescence occurred within the carapace during flow. Isobaric crystallisation within the flow centre, triggered explosion breccia formation just before and after the flow front stopped advancing. Sixteen years elapsed as the flow centre cooled below the glass transition temperature. Late-flow migration of soluble trace elements is consistent with subtle variations in Na_2O, Cl, H_2O and the development of secondary fabrics. Groundwater metasomatism is manifest in pumiceous fabrics. Viscosity, calculated from major element chemistry, temperature, and water content, is 10^7 poise for the magma (chamber); 10^{12} poise (conduit); and 10^{11} poise for the central flow.

Three peralkaline flows from Mayor Island were studied: Panui flow (a lava pond within a tuff ring); Pre-8 ka flow; and the 8 ka flow sheet. No explosion breccia and no significant spherulitisation or lithophysae occur. Carapace sections show ramp structures, anticlines compressed into spines, and synclinal troughs. In contrast to Ben Lomond, more bubbles occur in the upper obsidian layer. A high flow temperature ($\sim$950°C), variations in microlite length throughout the flow profiles and viscous deformation of powdered and block samples (furnace experiments) point to a fluidal rheology. The main differences between pantelleritic and calc-alkaline emplacement models is a spatter-fed emplacement mode, microlite growth and high temperature isobaric crystallisation during flow. Significant variations in Na_2O, La, Ce and Cl support high temperature migration of volatiles associated with the crystallisation of rhyolite. Sodic fluids were more concentrated in Cl and F in fluid lavas containing 2 - 10 times less water than Ben Lomond.

Estimated viscosity of Mayor Island lavas is between 10^7 - 10^8 poise. Temperature has a significant contribution to the fluidity of the lava allowing a spatter-fed emplacement and rehomogenisation of the spatter as a distally tapering flow sheet.

Void aspect ratio and porosity are parameters that best approximate the theoretical viscosity profile, whereas mean microlite length approximates the temperature curve only for the Mayor Island lavas.

The calc-alkaline emplacement model was tested on two poorly exposed rhyolitic centres: Pauanui (Miocene age); and the Okataina Volcanic Centre flows (19 ka - 5.5 ka age).

Ben Lomond and Mayor Island flows are compared with overseas rhyolites. The range of morphology of rhyolite landforms is primarily dependent on effusive volume and effusion rate. No significant difference occurs in the viscosity of domes, coulees and flows of similar eruptive chemistry and temperature, from the same volcanic centre.

ACKNOWLEDGEMENTS

Many people have contributed to the completion of this project and have sustained my personal well-being over the last three and a half years. Firstly, I would like to acknowledge my supervisors: Dr Peter Hodder and Dr Roger Briggs. Peter had faith in me and my initially risky project, providing encouragement and a high standard of advice. Roger Briggs is commended for his careful editing and valuable comment on aspects of chemistry, and for the final chapters. Other members of staff from the Department of Earth Sciences, University of Waikato, are also thanked, particularly Dr R. Albrook (DTA analysis). The secretaries and technicians are acknowledged for their help. Special thanks go to Stephen Stokes and Penny Cooke for their SEM photography of my pumices and the university draughting and photography teams for their fine work. This project would have been more difficult to complete without the UGC Scholarship and fieldwork assistance from the Broad Memorial Fund, awarded to me.

Drs. Bruce Houghton and Ted Lloyd (NZGS, Rotorua) were most helpful on matters concerning Mayor Island and Ben Lomond respectively, and Dr Steve Weaver (University of Canterbury) is thanked for his rapid analyses of chlorine. Dr Henry Westrich (Sandia Laboratories, Albuquerque, USA) kindly provided me with some Karl Fischer analyses for water. Ken Palmer (analytical facility, Victoria University of Wellington) is thanked for his tireless XRF analyses.

The IAVCEI Financial Aid Committee and the Royal Society of New Zealand supported my attendance at the IAVCEI 1989 Congress in Santa Fe, New Mexico in June-July 1989. Many thanks go to Dr Jon Fink (Arizona State University) who initially inspired me in studies of rhyolite flows and Curtis Manley (Stanford University) for his friendly discussion on aspects of thermal modelling. Dr Roy Bailey (USGS Menlo Park) organised a memorable field trip to the Long Valley Caldera giving me . . . access to the Inyo Domes.

Access to field areas would have been difficult without the local knowledge and permission of the owner of the Ben Lomond Station. The friendly co-operation of Goldie (Mayor Island Trust Board) and the Mayor Island staff of the Tauranga Big Game Fishing Club was much appreciated.

The support of my friends deserves a special mention and ideally should be placed near the top of the acknowledgements. Special mention goes to: Mark Tippet; Thomas Clemm, Carsten Harms and Brigette Bauer; Heather Middleton; and my Tauranga friends - Martin and Chris Penfold. Mark's insights into hypothesis testing, his proofreading, and receptive ear were much appreciated, and together with Sharleen, sustained me with good humour and warm companionship. Thomas Clemm is thanked for his crisp black and white photography and structural geology expertise during our visit to Mayor Island in Easter 1989. Many thanks to Tony Fenton for his user-friendly computing help and my "colleagues" - Alan Moyle, Shane McMahon, Fiona Bowling and Tony Sadler for their company.

Finally, my family deserves a medal for their help with typing, editing, computor access, and their kind support and encouragement. After about ten versions on six separate computer packages, this thesis is finally completed.

TABLE OF CONTENTS

CHAPTER 1.

INTRODUCTION AND OBJECTIVES.

1.1. Introduction.

Rhyolite lavas have not been observed to erupt in New Zealand during historical times. The most recent extrusion of rhyolitic lavas was at Tarawera, Okataina Volcanic Centre, c. 700 yrs B.P.(Nairn, 1986). In the western hemisphere, eruptions of silicic lavas have been rare, namely:

a. Novarupta (1912), a rhyolite dome described in Eichelberger and Hildreth, (1986);
b. Trident rhyodacite (1953), Friedman et al. (1963);
c. Santiaguito - dacite flows and pyroclastic deposits from an andesitic volcano (Rose, 1987);
d. Mt. St. Helens dacite dome (Swanson et al. 1987).

Their small volumes, restricted distribution and remote locations have relegated them to relative obscurity in the geologic literature. In addition, studies on rhyolites are largely from a petrogenetic perspective. However, through detailed studies of active systems such as Santiaguito and Mt. St. Helens, together with the discoveries from the Valles and Long Valley drilling projects that have penetrated flow interiors and feeder dikes of fresh Holocene lavas, rheological models relating morphology or form to their emplacement history may be developed.

Exposures of fabrics and flow structures in the field provide frozen examples of the original subliquidus rheology of ancient lavas. Quantitative studies of fabric variations may provide a guide to original emplacement properties such as lava viscosity.

1.2. Stratigraphy, Physical Properties and Emplacement History of Rhyolite Lava Flows: Previous Work.

The problem of inferring emplacement conditions from extinct rhyolite lavas has been addressed by relatively few workers. Christiansen and Lipman (1966) studied the Tertiary Comb Peak rhyolite flows, describing petrography, stratigraphy, chemistry and structure from dissected outcrops. Cole (1966, 1970) deduced the emplacement of the Tarawera domes from qualitative observations and derived a simple structural model based on dome cross sections exposed by the 1886 rift. Loney (1968) mapped the flow structures of the Southern Coulee, Mono Craters, where flow surface structures were correlated with flow front and drillhole sections. Fink (1978) originally aimed to investigate the mechanics of formation of obsidian flow folds at Little Glass Mountain, Northern California, but was constrained by the lack of rheological knowledge on rhyolites. Therefore he mapped the surface structures of the outer surface or carapace of the well exposed Holocene flow. The arrangement of the flow fabric units indicated deformation of the original flow stratigraphy. Fink was able to model gravity instability, surface folding and fracture of obsidian flows, developing an emplacement model (Fink 1980a, 1980b) that made inferences from semi-quantitative data on the rheology of the Little Glass Mountain lavas (Fink, 1983) from structural geologic evidence (Fink, 1984). Only flow front and carapace sections were available for study. The Inyo Domes Drilling Project provided both quantitative

and qualitative information on the development of textures in an obsidian flow and the importance of volatile content in controlling the original properties of pumice and obsidian (Fink and Manley, 1987). Bonnichsen and Kauffman (1987) examined the physical volcanology of large-scale silicic flows, previously identified as welded tuffs or rheoignimbrites, and generated a well constrained emplacement history for the rhyolite lavas of the Snake River Plain, SW Idaho.

1.3. The Inyo Drilling Project; the Legacy of Multidisciplinary Studies for Modern Silicic Systems.

The development of well constrained degassing models of rhyolite magmas was only possible from acquiring subsurface samples. Eichelberger & Westrich (1981) measured the total volatile content of flow obsidian and tephra glasses. Taylor et al. (1983) found a significant difference in the hydrogen isotopic signature of airfall tephra and flow obsidian. Eichelberger et al. (1986) and Westrich et al. (1988) concluded that hydrous rhyolite magmas degassed from 4% volatiles (chamber) to 0.2% (surface) and that the magma was emplaced as a collapsed foam. This model is supported by hydrofracturing of dike wall rock (Heiken et al. 1985) suggesting that most of the dissolved volatile content was lost at less than 1 km depth.

Other Drilling Project studies provided valuable data on geothermometry (Vogel et al. 1985), microlite morphology which provides implications for the thermal history of the magma (Swanson et al. 1985a,b), and differences in crystallinity between the dome and intrusion as a function of cooling in the system (Kasameyer et al. 1985). Measurements of water contents of Inyo dome and dike (Westrich and Eichelberger, 1985; Westrich et al. 1985), enabled the development of a degassing model. In addition, textural studies by Fink et al. (1985) using backscatter scanning electron microscopy, largely supports the contention of O'Neil and Taylor (1985) that some degassing of obsidian magma occurred during and after emplacement. Additional detailed studies include the thermometry of rhyolitic obsidians based on water speciation (Pickett and Stolper, 1984). More recent studies on the chemical variations of the Obsidian Dome (Sampson and Cameron, 1987; Vogel et al. 1987) have been integrated with mineralogical, stratigraphic and structural data showing that two magma types were stratified within the feeder dike prior to eruption (Sampson, 1987).

1.4. Towards the Development of a Research Project.

Major questions needing to be addressed from sections 1.2 and 1.3 above are:

a. What controls do the volatiles in the system have on ultimate emplacement properties?
b. What is the relative importance or contribution of the chemical composition, temperature, and volatile content to the viscosity of rhyolite lavas?
c. What causes the differences between the flow behaviour of lavas emplacing as domes and flows?

An initial approach was to look at the controls on viscosity of rhyolite lavas so that from the resultant viscosity value, the form of the lava could be predicted. As no rhyolite lava flows have been accurately observed, unlike basalt flows (Lipman and Banks, 1987; Moore, 1987), the rheological properties of rhyolite as the basis of the developing research project was impractical.

Hence the only successful way to elucidate the properties and viscosity of rhyolite lavas was to infer the viscosity from the resultant form, in light of detailed profiling of fabric textural parameters, structural studies and chemical data. Detailed systematic profiling of the physical properties of rhyolite lava flows has been done by only a few workers, namely Fink (1983) and Manley and Fink (1987), and has not been done in New Zealand before. The application of such studies and techniques can ultimately give a greater understanding of the eruptive behaviour of silicic volcanic centres for future volcanic hazard surveys.

1.5. Research Objectives.

The broad aim of this research project is to advance knowledge of the physical volcanology of rhyolite lava flows in order to constrain, as accurately as possible, the emplacement history and viscosity of two contrasting rhyolitic lava types. This study will contribute to the North American dominated literature and initiate studies of this type on New Zealand examples to complement the physical volcanology of pyroclastic deposits.

By quantifying fabric parameters down sections that bisect extinct rhyolite lava flows, an insight can be gained into the physical properties of the original lava and ultimately their emplacement histories.

This approach is applied to two New Zealand examples where no lava flow profiling has been attempted. Ultimately with subsurface inferences from the testing and adoption of degassing models of Westrich et al. (1988), and the application and testing of pre-existing methods of calculating viscosity (e.g. Shaw, 1972; Hulme, 1974), the behaviour and controls on the rheology of the emplacing lavas can be addressed. Two contrasting Cenozoic New Zealand rhyolitic lavas from the North Island were studied: (1) a calc-alkaline rhyolitic obsidian flow from Ben Lomond Station, Taupo Volcanic Centre; and (2), a pantelleritic sequence of flows from Mayor Island, Tuhua Volcanic Centre.

However, in contrast to the best examples from North America (e.g. the Inyo domes), lavas from both New Zealand localities were poorly exposed (Fig. 1.1). Pre-requisites include fresh glasses, un-weathered exposures that bisect the flow stratigraphy and sufficient areal exposure including some carapace outcrop.

In order to address the questions stated in section 1.4 above, the specific objectives of this research project were:

1. to chronicle the stratigraphic history of the poorly studied Ben Lomond region, Taupo Volcanic Centre, and to present new chemical data for lavas in the region;
2. to apply methods from the physical volcanological studies of pyroclastic deposits to rhyolite lavas;
3. to produce profiles of the textural characteristics of rhyolite lavas;
4. from qualitative and quantitative studies of lava flow sections, to establish the respective emplacement histories of the Ben Lomond and Mayor Island flows;
5. to test the degassing models of Eichelberger et al. (1986) and Westrich et al. (1988) from petrographic data at Ben Lomond;

6. to test the viscosity models and methods of Shaw (1972), Hulme (1974), McBirney and Murase (1985) and others, and apply them to Ben Lomond and Mayor Island to provide a semi-quantitative viscosity profile throughout the flows;

Fig. 1.1. Two rhyolite lava flows: the well preserved surface of the Glass Creek Flow, Inyo Domes, northern California, that erupted 550 years ago (above) and the relatively poorly preserved Ben Lomond Flow that emplaced about 100,000 years ago. Both photographs include flow front and vent (summit) areas.

7. to identify and attempt to assign relative importance to the major controls on the viscosities of the lavas through analysis of resultant form;
8. to find parameters that can act as useful approximations to flow viscosity;
9. to identify the constraints that the inferred rheology has on the eruption modes of both Ben Lomond and Mayor Island magmas;
10. to test and apply the derived emplacement model for Ben Lomond to two poorly exposed lavas - Pauanui (Miocene age) and Quaternary Okataina Volcanic Centre lavas.

Ideas to consider include the following:

1. the textures observed in outcrop reflect both the volatile content and the emplacement behaviour of the lava;
2. long axes of primary voids reflect the stress directions in the lava during cooling, the rheology of the surrounding fluid and the vapour pressure of the voids;
3. the zonation of secondary textures is in response to the migration of volatiles after emplacement;
4. the aspect ratio of autoclasts within the flow is a function of flow shear between and within units and local changes in flow velocity;
5. the change of flattening ratio (of primary voids) with depth serves as an approximate guide to intraflow viscosity variations;
6. the major element chemistry of obsidian, adjusted to anhydrous conditions, represents the chemistry of the original lavas and may be used in calculations of viscosity via the method of Shaw (1972);
7. the form of the temperature profile during emplacement is constrained by textural variations at the top and base of flows including basal tuffs;
8. emplacement temperature is approximately equivalent to the chamber temperature during the crystallisation of phenocrysts, or for aphyric lavas near that of the liquidus within the chamber, owing to low rates of thermal conduction during magma ascent.

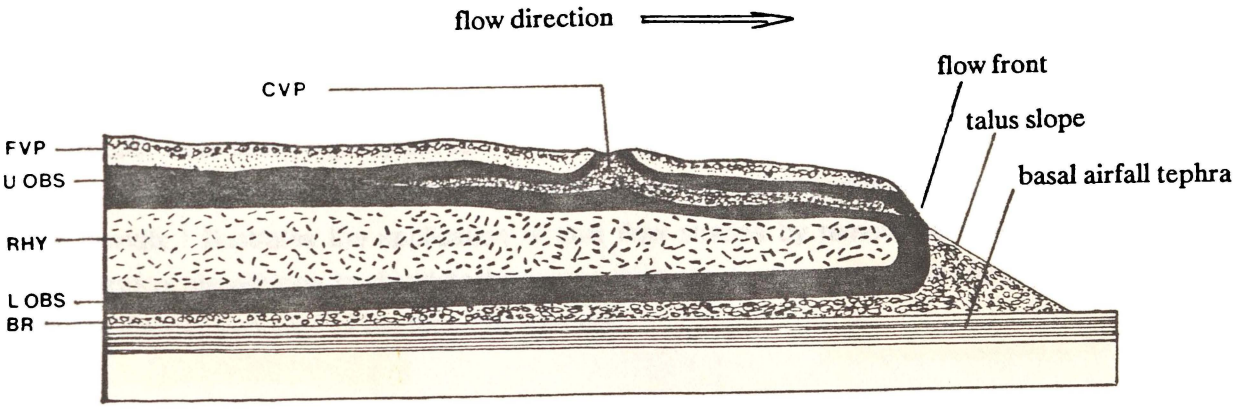

Fig. 1.2. The stratigraphy of fabric units in a rhyolite lava flow (adapted from Fink and Manley, 1987 and Cas and Wright, 1987). FVP = finely vesicular pumice, OBS = obsidian (U = upper and L = lower layers), CVP = coarsely vesicular pumice, RHY = lithoidal rhyolite, and BR = basal breccia.

1.6. Definition of a Flow Stratigraphy.

The intraflow layering or stratigraphy of fabric units is in response to the emplacement stratification of volatiles, and post-flow variations in crystallisation. Thus, the following sequence is formed from flow top to base: finely vesicular pumice; upper obsidian layer; rhyolite; basal obsidian; and basal breccia (Fig. 1.2).

The obsidian layer envelopes the central rhyolite core, the latter being characterised by a finely crystalline groundmass in contrast to the glassy groundmass of the obsidian. The upper obsidian and the finely vesicular pumice layers denote the flow carapace or outer skin of the flow which is usually structurally complex. Explosion breccias, or the coarsely vesicular pumice of Fink (1983), interrupt the top two flow units and autoclastic breccias may occur throughout the flow stratigraphy (Manley and Fink, 1987).

1.7. Thesis Outline.

Chapter 2 outlines the regional geologic setting for the Ben Lomond region and describes the regional stratigraphy (objective 1), flow morphology and stratigraphy and a composite profile throughout the flow sequence is assembled. Physical profiling of the textural stratigraphy (objectives 2 and 3) is interpreted in chapter 3 and with structural and petrographic data an emplacement history is assembled for Ben Lomond (objective 4). Major and trace element chemistry and estimates of temperature and water contents are presented in chapter 4. As subsurface data is not available, the results of the Inyo Drilling Project and a degassing model for rhyolite magmas is used to interpret processes at depth for the Ben Lomond magma. The means of estimating the flow viscosity are critically outlined and two viscosity profiles are constructed for the Ben Lomond flow, during emplacement and late flow phase. Thus chapter 4 satisfies objectives 5 and 6. Chapters 5 and 6 outline the emplacement history from physical volcanological studies, and the chemical variations and viscosity of the pantelleritic lavas of Mayor Island respectively, repeating the approach developed in chapters 2-4. The emplacement model for calc-alkaline lavas from chapters 3 and 4 is applied to two other lavas in chapter 7 fulfilling objective 10. The Ben Lomond and Mayor Island flows are placed within the wider picture of effusive rhyolitic volcanism in chapter 8. Parameters that can act as suitable approximations to temperature and viscosity are outlined and the three major questions listed in section 1.4 are addressed, thus satisfying objectives 7 - 9. Chapter 9 presents an overview of the results of this research project for both lava types and contrasts their respective modes of emplacement. The paper in Appendix I illustrates the application of lava flow studies by remote sensing within the wider framework of planetology, to elucidate the composition of extra-terrestrial lavas and to provide insights into the thermal evolution of the terrestrial planets.

Fig. 2.1 A generalised geological map of the northern Taupo region. The inset (top left) locates the area with respect to the North Island, New Zealand. This region includes the arbitrary boundary between the Taupo and Maroa Volcanic Centres (indicated far right) and the detailed mapping area in Fig. 2.2. Kinloch settlement is located in the Whangamata Graben between two northeasterly trending rhyolitic complexes of the Taupo Volcanic Centre. Major NE-SW faults with upthrown (U) and downthrown (D) sides are indicated. The relative stratigraphy and key to the geological units is shown below:

ta = Taupo Ignimbrite and pumice alluvium (1.8 ka age);
Ab = Acacia Bay rhyolite dome (10 ka age);
P = Puketarata rhyolite domes and tuff ring (14 - 15 ka age);
20ka= 20 ka Ignimbrite;
th = Tauhara Dacite (37 ka age);
ha = Haparangi Rhyolite;
M = Mokai Ignimbrite (c.140 ka);
Ktb = K-Trig basalt and other basalts (< 140 ka age);
wg = Whakamaru Group Ignimbrites (330-230 ka);
Kb = Karangahape Basalt (290 ka).
Other units are Orakonui Ignimbrite (Or), Wairakei Breccia (w), Waitahanui Breccia (wt) and the Huka Formation (hg).

The map was compiled from Grindley (1960), Grindley (1961); and Wilson et al. (1986)

CHAPTER 2.

BEN LOMOND RHYOLITE: REGIONAL GEOLOGICAL SETTING, FLOW MORPHOLOGY AND STRATIGRAPHY.

2.1. Regional Geological Setting

The Ben Lomond Station rhyolite dome is approximately 10 km north of Kinloch, Lake Taupo and is one of a number of rhyolite domes in part of the boundary zone between the Taupo Volcanic Centre and the Maroa Volcanic Centre. The northern Taupo domes cluster to form two elongate northeast trending complexes: one from Te Kauae Point to T17/680862; and the other from Te Tuhi Point to T17/693810. Structurally the area is dissected by predominantly northeast trending faults with displacements decreasing northwards away from the Taupo Caldera. Faulting is everywhere normal (Grindley, 1965) with throws both northwest and southeast generating numerous horst and graben structures (Grindley, 1960; Healy et al. 1964; Grindley, 1965; Grindley, 1982; Healy, 1984). The Whakaipo-Te Tuhi Point horst is a northeast aligned accumulation of rhyolite domes where the ridge morphology is partly due to block faulting and partly to the extrusion of lavas along fissure zones (ref. Fig. 2.1). Whangamata graben faults were displaced as recently as 1922 (Grange, 1937).

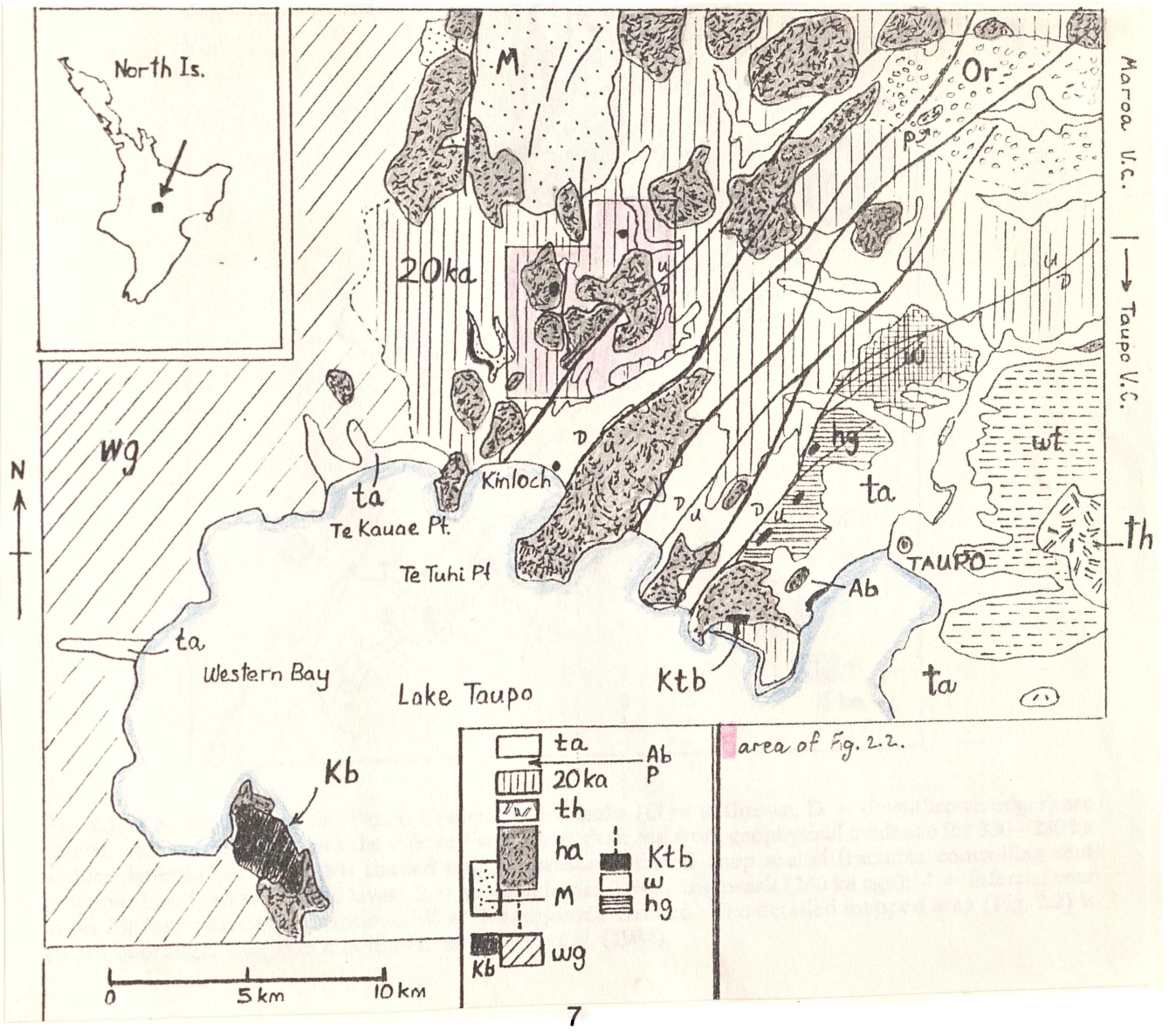

The geological history of the Taupo Volcanic Centre has been previously discussed (Froggatt, 1982; Northey, 1983; Wilson et al. 1984.) in terms of two major periods of activity: (a) 230 - 20 ka B.P.; (b) 20 ka B.P. to present.

From 230 to 20 ka B.P. the eruptive history is poorly understood. The relative and absolute chronologies of eruptive events are poorly established. Also in the field, preserved upper, basal and lateral contacts between units are rare. The 50 - 20 ka eruptives (Vucetich and Howorth, 1976b) and the well documented eruptive history from 20 ka to the present (Topping and Kohn, 1973; Vucetich and Pullar, 1973; Vucetich and Howorth, 1976a; Walker 1981; Froggatt,1981a,b; Self, 1983; Wilson 1986; Wilson et al. 1986) will not be discussed further.

Fig. 2.2 shows a regional geological map of the horst to the west of the Whangamata Graben. The geological history may be subdivided into: early ignimbrite (Otaketake Gorge); rhyolite domes - Holyoake Station, Ben Lomond, and Marotiri; K-trig basalts; and 50 - 20 ka pyroclastics.

2.1.1. Ben Lomond rhyolite dome and related deposits.

The Ben Lomond rhyolite outcrops as two flow lobes comprising an eroded dome, dissected by the Whangamata Fault which exposes up to two thirds of the flow stratigraphy. The flow stratigraphy for Ben Lomond outcrops will be described in section 2.3. The Ben Lomond rhyolite has been K-Ar and glass fission-track dated at 110 ± 1 ka; 95 ka; 120 ± 2 ka (Stipp, 1968; Kohn, 1973).

The northeastern margin of the Ben Lomond dome is buried by 20ka ignimbrite and this is illustrated by the exposures of s59, s7, and a site north of Poihipi Road where a drill hole intersected obsidian at 72 m below the surface.

Deposits associated with Ben Lomond lavas include possible pre-dome pyroclastics 0.5 m thick above K-trig basalt at s22, and late-flow ballistic non-vesicular obsidian blocks with bomb sag structures (Froggatt oral comm. 1988) from explosion breccia formation. Similar non-vesicular obsidian clasts were found at s46 below a sequence of 50-20 ka tephras and 20 ka ignimbrite.

At s50 (Fig. 2.3) an epiclastic breccia 4.4 m thick underlies 20 ka ignimbrite and overlies a gently dipping sequence of airfall lapilli of 1.85 m thickness. The obsidian clasts are highly porous (60% porosity) with low aspect ratio voids (long axis / short axis = 1.5) and angular equant clast shapes with breadcrusted margins. Other clasts are more andesitic and also include devitrified rhyolite. However, all obsidian, rhyolite, and pumice comprising the bulk of the clasts contain 5 - 7.5% phenocrysts in contrast with the aphyric Ben Lomond lavas. This evidence alone precludes an origin as a marginal avalanche breccia or explosion pit-originated breccia for the Ben Lomond flow. With only one exposure, the source of this deposit is problematic.

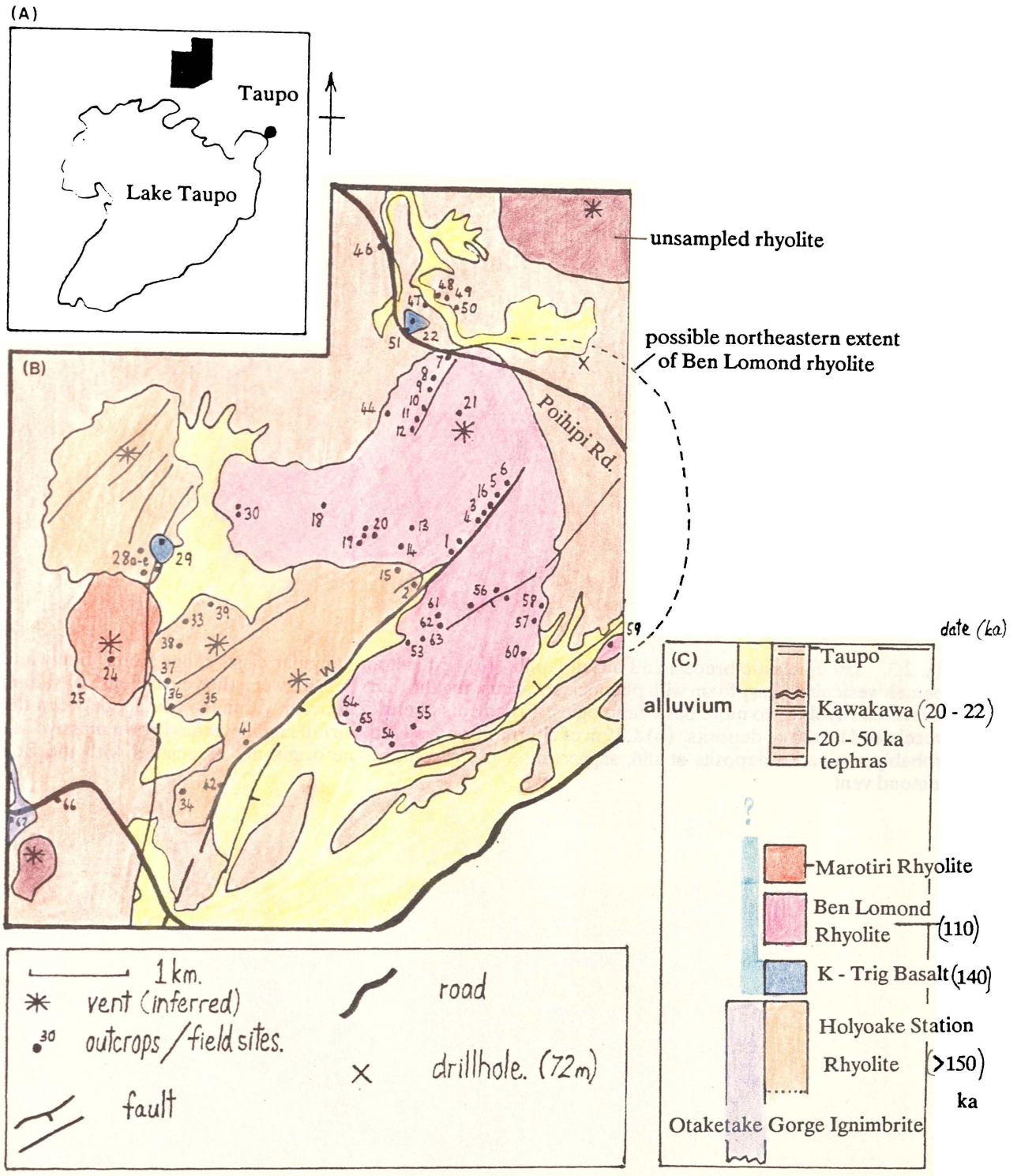

Fig. 2.2. Ben Lomond - Whangamata horst region showing location (A), geology and field sites (B), and stratigraphy (C).

Fig. 2.3. s50 epiclastic breccia and airfall lapilli. (a) Equant and angular clasts range from: finely and coarsely vesicular glassy foam with phenocrysts occupying the thin septa between the voids; dense obsidian; devitrified rhyolite; to more basic lithologies. Fragments of obsidian occur within the contact between the breccia and the 20 ka deposits. (b) 1.85 m of alternating coarse/fine airfall lapilli overlies brown massive ash probably similar to deposits at s66, suggesting a pre-rhyolite dome origin not associated with the Ben Lomond vent.

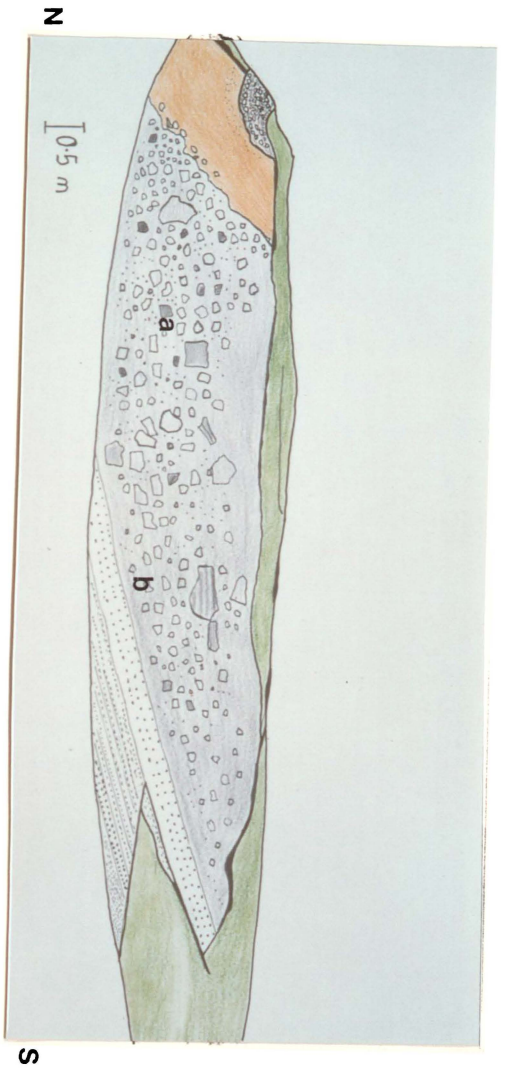

(a)

(b)

2.1.2. Holyoake Station rhyolite domes.

Other exposed rhyolites include the Holyoake Station domes, older than the 110 ka Ben Lomond rhyolite because:

a. the two Ben Lomond flow lobes to the north lap around the Holyoake Station domes;
b. only one outcrop has been identified as finely vesicular pumice suggesting extensive erosion of the dome carapace;
c. the rhyolite is weathered and spherulitic, with vestiges of inter-spherulite glass, originally having been fresh obsidian (as at Ben Lomond).

Outcrops are sparse but the pumice at s15 has been interpreted as finely vesicular pumice (FVP). The densely spherulitic rhyolite and obsidian (at s33-42) represents the upper obsidian (OBS) layer of the flow model (refer Fig. 1.1). At s2, lithophysal foliated rhyolite with moderate to widely spaced shrinkage joints define the rhyolite (RHY) zone of the flow stratigraphy. The vent position is assumed to be under the highest point of the dome.

Site 28a-e represents an eroded rhyolite dome consisting of spherulitic rhyolite with inter-spherulite obsidian, spherulitic clasts (formerly obsidian) with grey 1 - 2 mm diameter spherulites, in an orange-brown pumiceous glassy matrix, and an autoclastic breccia, representing OBS and FVP zones in a flow-dome stratigraphy. Flow banding dips 35° to 72° E to NE toward an inferred vent area near the summit (618 m) of the dome.

2.1.3. K-Trig basalt

At s29, the Holyoake Station rhyolite has been intruded by K-trig basalt which is exposed as a small eroded scoria cone. K-trig basalt is also exposed northeast at T17/667871 (s22). Two distinct units occur at s22:

unit a. steeply dipping (153/27° WSW) poorly bedded oxidised sub-spherical lapilli and bombs, with poor lateral continuity suggesting that the material was emplaced by avalanching down a building scoria cone (Houghton and Wilson, 1986);

unit b. non-bedded variably oxidised scoria consisting of from loose to densely welded material with large rhyolite xenoliths that are usually fused.

In unit a, the ubiquitous accidental rhyolite fragments (unlike s29 where none were observed) have an adhering crust of basalt lapilli. Often the rhyolite has been fused to form beads of glass between the basalt lapilli. Therefore the basalt must have intruded through older rhyolite (e.g. s49) at depth.

The basalt outcrops at s29 and s22 trend northeasterly parallel to the Whangamata Fault and have been grouped with the K-Trig basalt west of Taupo (Grindley, 1961; Cole, 1972; Cole, 1973). Although s22 and s29 are undated, the relative age of the basalt at s29 appears younger than the Holyoake Station rhyolite. The age of s22 with respect to the Ben Lomond flows, is more uncertain. One interpretation occurs in section 2.1.1(p.8). Alternatively, this weathered unit may be unrelated to the Ben Lomond rhyolite. The age for the K-trig basalt has been determined by Stipp (1968) as c.140 ka by K-Ar dating. Other basalts in the Maroa Centre such as the Ongaroto Basalt are younger (c.80-90 ka)(Houghton et al. 1987). Thus, a younger age for s22 and s29 basalts cannot be ruled out.

2.1.4. Marotiri dome

Of the three rhyolites of the Whangamata horst between Poihipi Road and Whangamata Road, the youngest is Marotiri dome. The dome is not dissected and outcrops are sparse, comprising columnar blocks of devitrified pinkish-grey spherulitic rhyolite (containing elongated pumiceous blebs) below a thin, rubbly, vesiculated rhyolite.

2.1.5. Otaketake Gorge Ignimbrite and possible pre dome deposits.

A moderately welded ignimbrite of more than 100-150 ka B.P. age (Houghton and Wilson, 1986) outcrops at the bottom of the Otaketake Gorge showing well developed columnar jointing and 15-55 mm sized crudely aligned flattened pumice clasts.

At T17/631816 (s66), a non-vesicular orange tuff, rich in obsidian fragments occurs below an irregular contact, with well-bedded white pumiceous lapilli and fine brown ash. Low angle pinch and swell structures occur in this unit.

These obsidian-bearing airfall, pyroclastic flow and surge deposits are probably associated with Marotiri and perhaps some other domes west of the Whangamata Fault and may represent subordinate explosive activity probably preceding or associated with dome growth (Houghton and Wilson, 1986).

2.2. Ben Lomond Flow Morphology

The Ben Lomond Rhyolite consists of two exposed flow lobes - the southwestern and southern flows, with the northeastern margin buried by 20 ka deposits. Even though the dome is covered with grass and scrub with at least 10 m of the carapace stratigraphy missing in some places, sufficient outcrop exists (41 sites) to measure flow banding orientations and to use surface grooves, flow striations, flow marks, and cracks as local flow indicators.

Flow marks are formed from stretching and subsequent compaction of elongate vesicles (Bonnichsen and Citron, 1982; Bonnichsen and Kauffmann, 1987) and occur sporadically in the upper and marginal parts of flows. The more elongate the flow mark (i.e. the greater length / height or aspect ratio), the earlier their formation (Bonnichsen and Kauffman, 1987). Their dip and direction indicate the vector of local tensile stresses (stretching) of cooling lava in the outer carapace during the formation of rampart structures - projecting ridges of obsidian between zones of FVP (Cas and Wright, 1987). The silicate skin of an obsidian ridge chills on contact with air and distorts while the interior is still plastic from differential flow localised in narrow zones (Shaw, 1969; Lawless, 1975; Best, 1982). Striations on flow band surfaces also record local secondary extrusion directions of the cooling viscous carapace, while the hot, insulated interior part of the flow lobe flows slowly downslope.

The orientations of surfaces parallel to the strike of foliation planes is also a useful indicator of lava flow direction, particularly for ancient eroded poorly preserved flows. Fig. 2.4 shows that most dip measurements from the deeper parts of the southwestern flow incline predominantly towards s21. In addition, as the surface slope of the southwestern flow is about 4^{o}, the vent position may be confidently inferred to be near the highest point on the Ben Lomond station (744 m) near s21. Dips from obsidian

outcrops interpreted as being near to or part of the flow carapace, are steep and more variable in direction. For example, at s8, steeply inclined divergent flow bands in an outcropping rib of obsidian and associated FVP breccia, suggest the projection of an obsidian ridge (or rampart structure), tensile fracture, and brecciation occurred in a cooling carapace. Grooves and striations on folial surfaces along the airstrip section (s8 - 12), are orientated obliquely (commonly about 50° ± 20°) to the strike of flow banding recording local or small-scale directional information during late-flow phases.

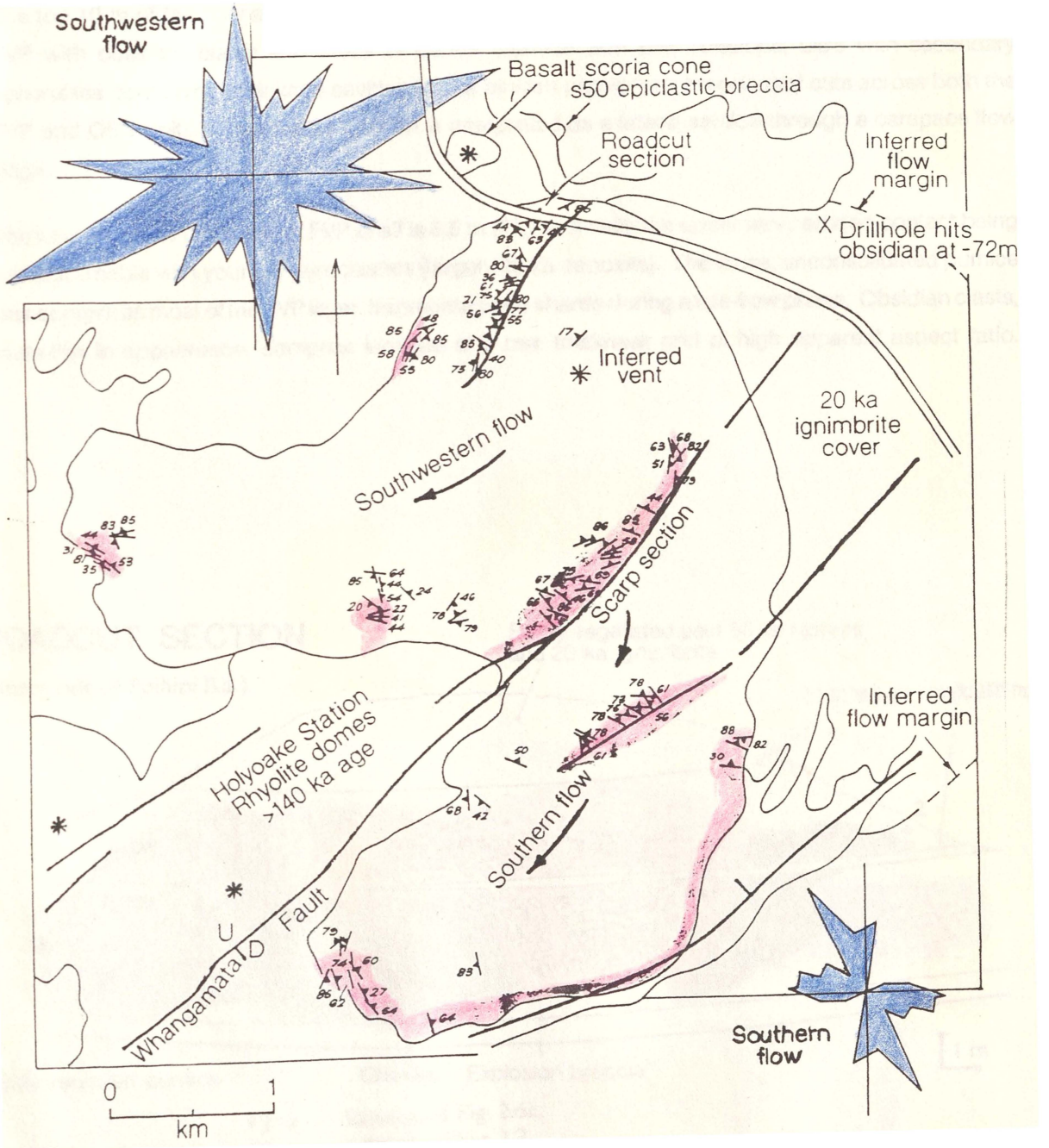

Fig. 2.4. Flow banding of deeper parts of both flow lobes (O) dip toward the inferred vent. Near surface carapace outcrops have a more variable dip direction. Rosettes measure the strike of flow banding and flow surfaces for both flow lobes. By analogy with the Inyo domes (refer to Suemnicht and Varga, 1988) the data for the southwestern flow does not seem inconsistent with an origin from a circular vent. The southern flow may show a preferred orientation for flow banding strike, but this may be due to a smaller data base and the elongate geometry of the flow lobe.

2.3. Ben Lomond Flow Stratigraphy

The stratigraphy of three primary outcrops: roadcut; airstrip; and scarp; from the southwestern flow are described. Together with information from secondary sites (s14, 19, 21, 30 and 44) and from sections comprising the southern flow, a composite flow stratigraphy may be assembled.

2.3.1. Roadcut section (s7).

The top 10 m of the flow stratigraphy is best observed at the Poihipi road cut (Fig. 2.5), comprising: FVP with obsidian plates and areas of denser pumice with flow striations; OBS with secondary spherulites containing shrinkage cavities; and a pinkish pumiceous breccia that cuts across both the FVP and OBS units. The roadcut section is interpreted as a lateral section through a carapace flow ridge.

The total exposed thickness of FVP at s7 is 6.5 m (Fig. 2.6), with the upper wavy eroded contact being unconformable with younger pyroclastics (largely 20 ka deposits). The loose, unconsolidated pumice that comprises most of the FVP layer, fragmented into shards during a late-flow phase. Obsidian clasts, plate-like in appearance, comprise laminae of 5 mm thickness and of high apparent aspect ratio.

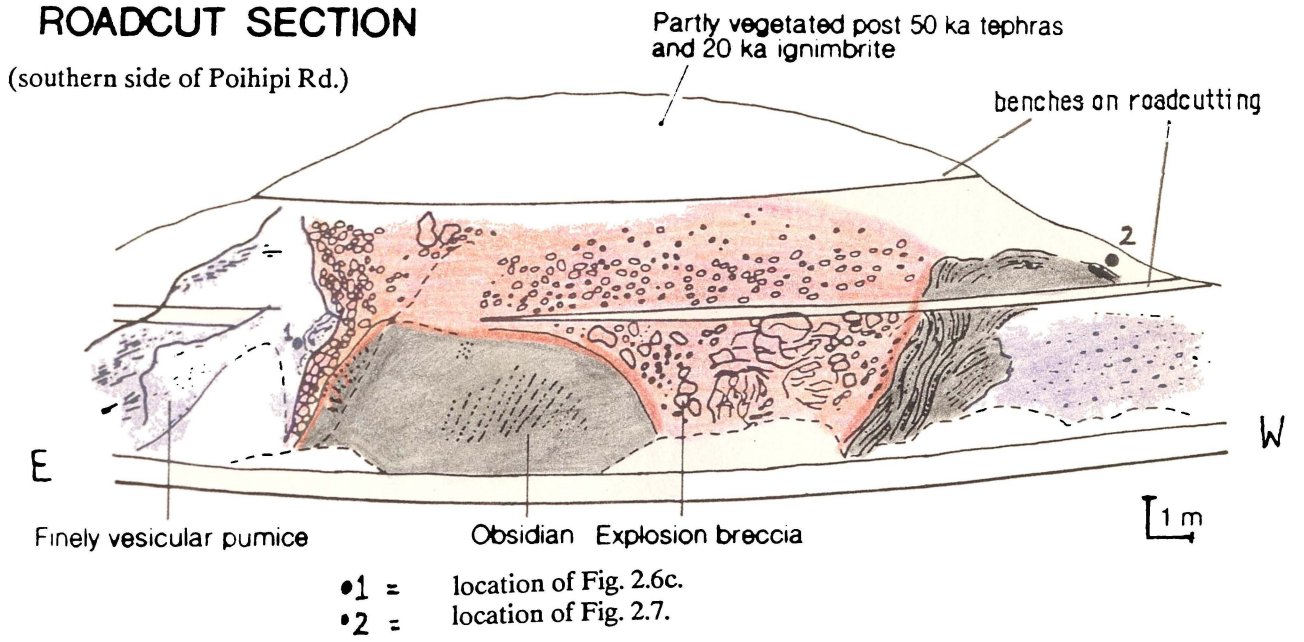

Fig. 2.5. Road cut section s7 showing finely vesicular pumice, obsidian and breccia fabrics below a mantle of 20 ka and 50 - 20 ka ashes.

Fig. 2.6. (a) obsidian plates and clasts within unconsolidated fragmental pumice shards, comprise the upper exposed 1.33 m of the northern cut, Poihipi Road. (b) unconsolidated fragmental pumice (lower 5.2 m of section) showing irregular contact with the explosion breccia. (c) dense pumice (density = 1.2 - 1.5 g/cm^3) showing flow striations (southern cut).

a

b

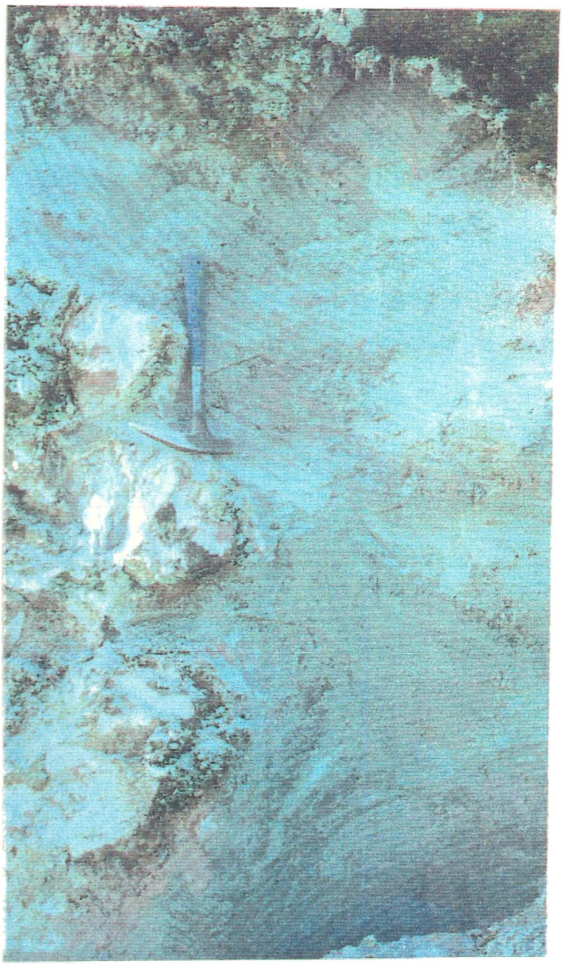

c

Inter-laminae zones are rich in voids with bubble septa oriented perpendicular to plate surfaces. The clasts are oriented generally northeast.

The obsidian unit dips from 028/63° NW to 144/27° NE and outcrops as part of a rampart structure or ridge disrupted by a breccia that cuts across both OBS and FVP units. The obsidian is black, aphyric and spherulitic, and contains (at s7) no primary voids that distort flow banding. Spherulites contain hollow shrinkage cavities with a pale grey disrupted margin comprising finely radiating acicular needles. The irregular shrinkage cavities have a long axis approximately parallel with the flow banding dip. Foliation surfaces show fractured surface rinds and surface cracks approaching a sigmoidal form oblique to flow striations (Fig. 2.7).

The explosion breccia unit consists of large angular to subrounded pale pink, pale grey, and white finely pumiceous blocks up to 1.2 m size, and grey perlitic obsidian, set in a matrix containing three

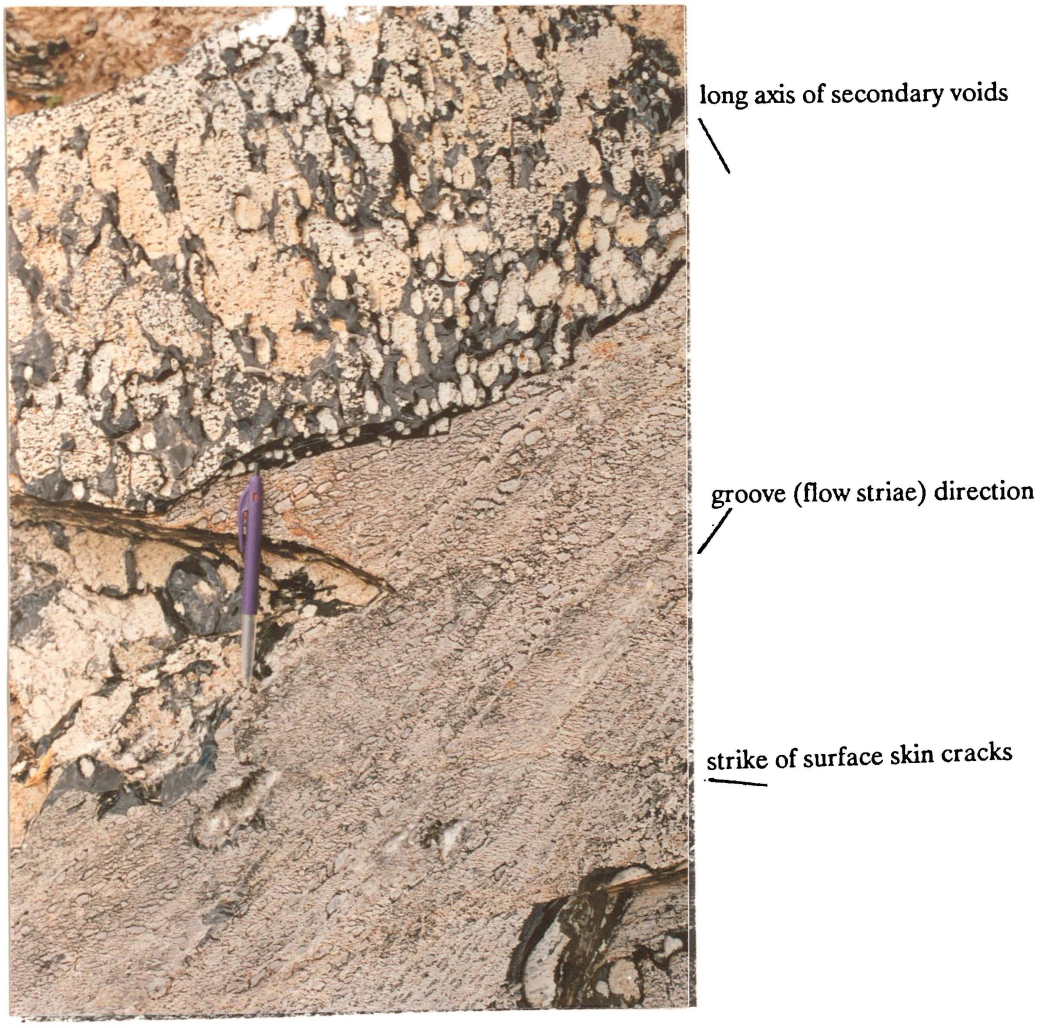

Fig. 2.7. Foliation surface (location in OBS unit, Fig. 2.5) orientated 065/58°N, showing flow striation directions on a cooling surface, oblique to the long axis of interfolial secondary voids.

sizes of material: c. 60 mm and c. 3 - 10 mm sized black, grey, pink, and brown glassy clasts; in a fine ash-sized loose white material. The origin of this unit is discussed in chapter 3.8.

2.3.2. Airstrip section (s8 - 12).

The airstrip section is a scarp, approximately 300 m long and 25 m high, interpreted as being fault controlled (Lloyd, oral comm., 1988).

At the northern end of the section nearest s7, the outcrops at s8 and s9 cut FVP and OBS, and are interpreted as being near the basal part of the flow carapace. Divergent flow banded zones in the OBS unit formed from tensional stresses operative during late flow and cooling phases. The OBS layer contains primary voids that distort the flow banding, flow striations and tubes, and polygonal cooling fractures (Fig. 2.8a).

a

b

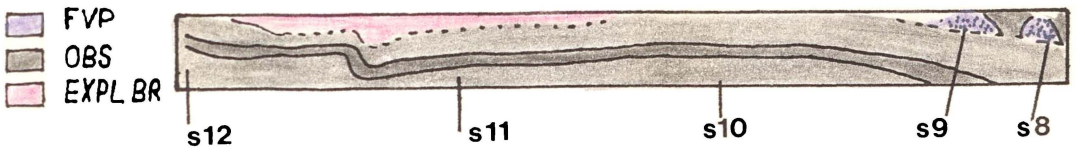

Fig. 2.8. (a) Polygonal cooling fractures that have cut across surface striations and tubes (flow marks) on the divergent limb of an obsidian ridge, s9. (b) Schematic diagram of the airstrip section locating sites s8-12. The dark band in the OBS unit represents dense grey lineated obsidian and the paler grey band spherulitic obsidian with a secondary porosity attaining 20%.

Steeply dipping zones of alternating grey lineated obsidian and spherulitic obsidian, where the secondary voids overprint the primary flow banding, crop out down the airstrip scarp face between s10 and s12 (Fig. 2.8b). Spherulites occur preferentially in the grey bands. The section also has poor exposures of pinkish-grey pumiceous breccia, similar to the explosion breccia at s7.

2.3.3. Scarp section (s1 - 6)

The Whangamata fault scarp, approximately 65 m high at s1, and 20 m high 1600 m to the northeast at s6, provides a continuous section into the upper two-thirds of the flow stratigraphy, including the central core of the Ben Lomond flow. Nowhere is the base of the flow exposed. At s6, a small exposure of FVP (0.4 m thick), conformable with the underlying OBS zone, is the only occurrence of FVP along the entire scarp. This suggests that at least 6 m of the carapace is missing (6.5 m is observed at s7). This estimate provides a lower limit for the thickness of the FVP layer. At s3, a pocket of breccia disrupts the OBS unit, and lies above a spherulitic transition zone (which includes lenses of brown glass), and a crystalline rhyolite core, best seen at s1 (Fig. 2.9). The flow units will now be described, from the OBS layer to the central RHY core.

The OBS unit (15 - 20 m thick) is characterised by medium-spaced, near-vertical jointing, black aphyric obsidian passing downwards into grey flow banded fabrics, and spherulite-rich and -poor discontinuous layers parallel to the steeply dipping flow banding. Within the top 5 m rare gas blisters occur. The largest, at s6, contain interior septa perpendicular to cooling surfaces (ie. the blister margins),

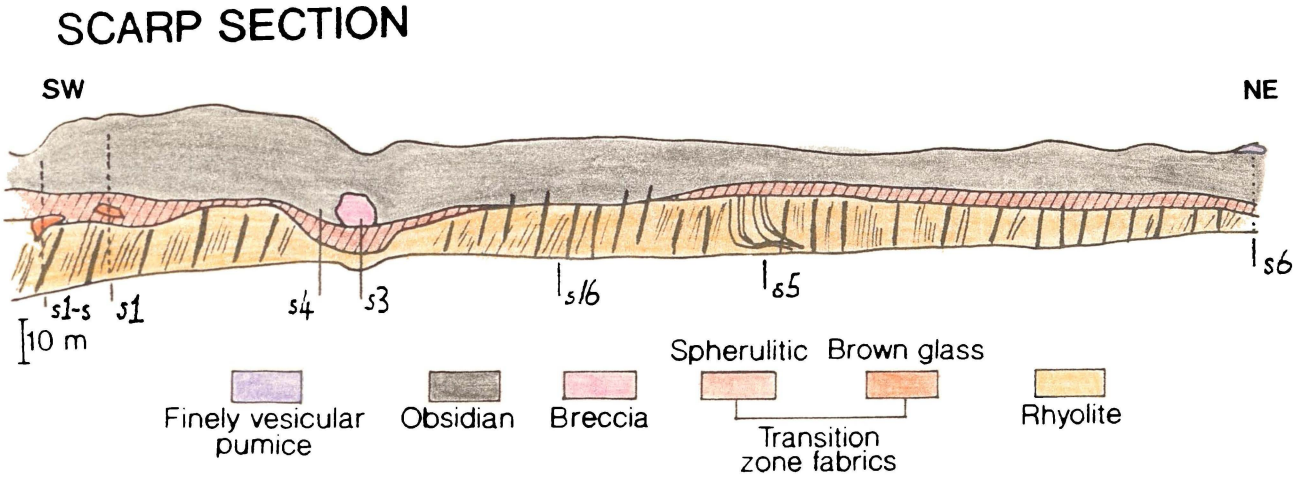

Fig. 2.9. Schematic diagram of the Whangamata Fault Scarp section. Shrinkage joints (medium to wide joint spacing) and flow banding orientations are shown best at sites 16 and 5 respectively. Joint spacing in the OBS unit is less than that of the central RHY unit and flow banding is steeply dipping toward the inferred vent. Approximately 90% of the scarp section is obscured by vegetation.

similar to those of the OBS unit in the Haumingi flow, Okataina Volcanic Centre. At s3, spherulites preferentially occur in the grey flow bands, suggesting that nucleation sites for spherulite growth are more common in these bands. At s5 and s3, the flow banding declination steepens from about 26° (base) to 85° (top), dipping north to northwest toward the inferred vent.

A pod of explosion breccia, consisting of pale grey and white angular pumice blocks, and obsidian clasts, disrupts the lower half of the OBS unit and occurs above a transition zone to the central RHY core. The breccia pod margin is jagged consisting of platy OBS clasts with plastically deformed primary voids, and fractured clasts of grey lineated obsidian. Unlike the breccia/OBS margin of s7, perlitic brown glass is virtually absent. The explosion breccia contains angular clasts, with elongated, tapered voids of high aspect ratio.

The transition zone (TZ), of variable thickness, is dominated by secondary spherulites up to 30 mm diameter. Relict glass between discrete spherulites is less than 5% by area. Associated with the spherulitic transition zone are axiolite tubes (350 mm length and 20 mm width at s3b), and lenses of brown glass 1.5 - 10 m at s1-south, occasionally with black flame-like obsidian clasts. Between the brown glass and the spherulitic transition zone, the contact is sharp. However the TZ/OBS and the TZ/RHY contacts are gradational over a one metre extent.

The rhyolite unit is the central crystalline core of the Ben Lomond flow. Lithophysae and spherulites with well developed shrinkage cavities attain 140 mm diameter. These voids are secondary as they partly cut the primary foliation, although they deform the flow bands around their outer margins. The rhyolite is yellowish-brown and flow-banded with a resinous lustre indicating partial devitrification. The rhyolite is annealed along joint surfaces and is characterised by widely spaced shrinkage joints that formed after devitrification during cooling to ambient temperatures.

2.3.4. Secondary outcrops; southwestern flow.

Five other sites are briefly noted, confirming the flow unit descriptions from the three main sections.

At s44on the northwestern margin, foliation orientations in the OBS unit steepen from 58° - 85°, E to SE, toward the inferred vent near s21. This latter site has pink devitrified rhyolite, dipping at 17°WNW, typically partly brecciated with rare associated hydrated interstitial obsidian. Site 14 shows thin tube-like voids in finely lineated black OBS, indicating closeness to the c. 10 m carapace zone. Site 19a-d is a section on the southern slopes of the flow, exposing weathered FVP breccia (outcrop extent 1m) and OBS with tight disharmonic flow folds (s19c) that generally dip towards the vent. Site 19d is typified by a train of voids (aspect ratio = 2.66), whose parallel long axes are aligned obliquely to and cross-cut the flow bands implying that they are secondary features. Finally, s30 at the eroded toe of the southwestern flow, is characterised by an OBS/TZ succession similar to that at s1. Flow band orientations, highlighted by lenses of brown glass less than 2 m thick, steepen from 30° - 81° NNE up the cliff face.

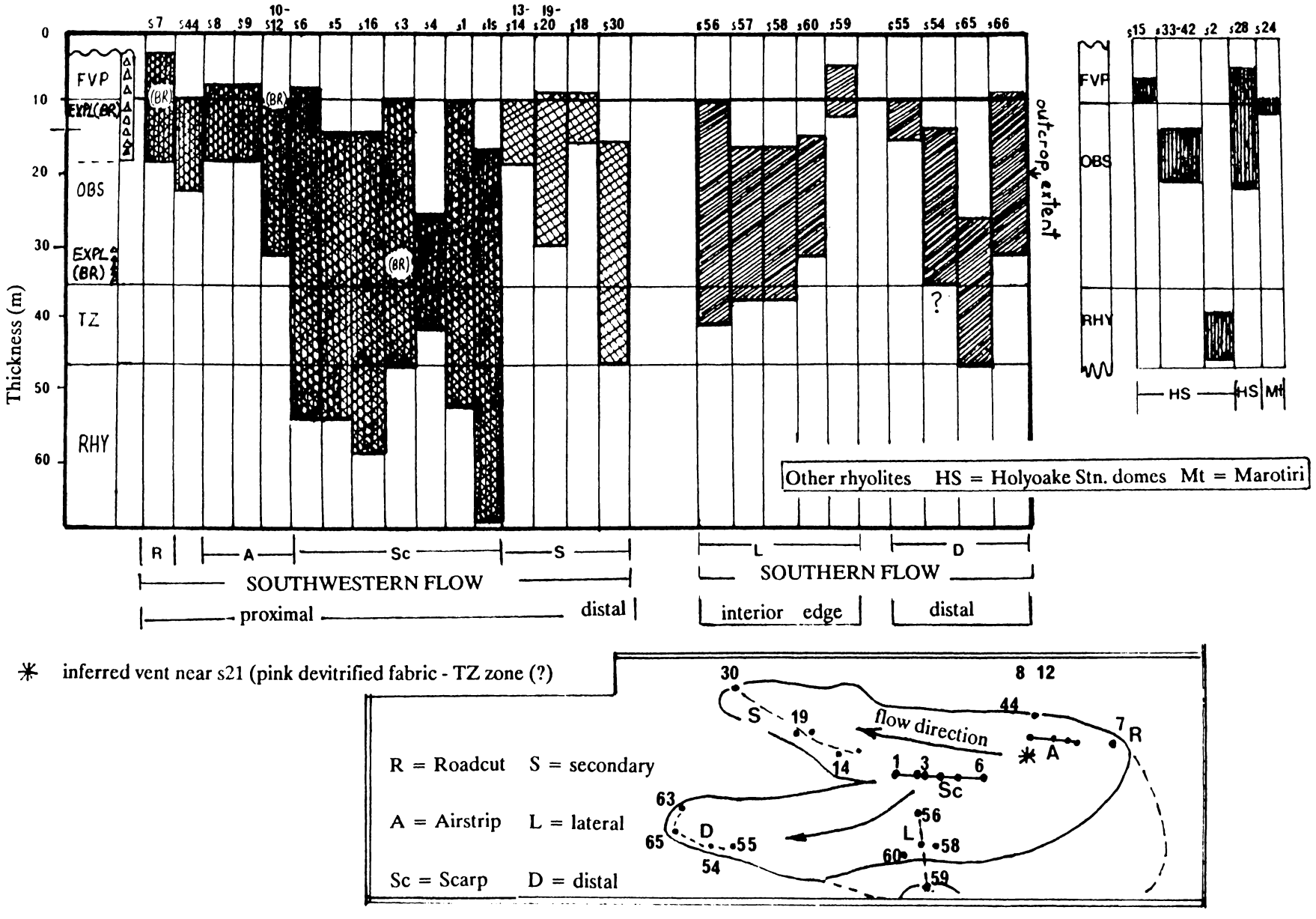

Fig. 2.10. Composite column of the flow stratigraphic units compiled for Ben Lomond flow lobes and a schematic column for other rhyolites of the area.

2.3.5. Southern flow.

At s54 - 56 and s64 - 65, prominent outcrops of aphyric obsidian form the eroded margin of a second flow, the southern flow. The total flow length extends for 3.8 km, from an infered vent just north of s21 (Lloyd pers. comm., 1988). North of a line adjoining s56, s58, and s59, no outcrops were observed as the flow is draped by 20 ka ignimbrite. The eastern margin of the flow extends from s59 to T17/684863 where a drillhole intersected obsidian 72 m below the surface. Evidence for a tapering flow margin at s59 is that FVP with obsidian clasts containing primary voids outcrop at an equivalent topographic level to the deeper OBS layer exposed at s57-58 and s60. At s56, a fault-controlled valley dissects the entire exposed thickness of the OBS unit (25 m). The fault is downthrown to the southeast as there is no OBS/TZ contact on the southeastern side of the valley. Remanent FVP occurs at s64 between projecting obsidian ribs with an arcuate strike surface, similar to s8 and hence formed by processes described in section 2.2. Sites 53 and 56 are inferred to be close to the FVP/OBS contact, based on a textural similarity to the spherulitic black obsidian at s7. The contact, although largely missing (except at s64), is inferred to slope approximately parallel to the present surface of the flow. When matching the inferred FVP/OBS and OBS/TZ contacts with those same contacts on the s1-6 scarp of the southwestern flow, a throw of about 50 m is suggested for the Whangamata fault, which increases toward Lake Taupo. This displacement would have occurred after the emplacement of the southern flow. Explosion breccia associated with the OBS layer is poorly exposed at s56 and s64b. At s64b, a sharp contact with the 20ka ignimbrite is delineated by non-vesicular obsidian fragments, perhaps related to carapace disruption by the emplacement of an explosion breccia nearby. As at s1, s3, and s30, brown glassy lenses at s65 are associated with axiolitic and spherulitic fabrics that mask or overprint primary flow fabrics - namely the obsidian that was formed from rapid cooling of the original lava.

2.3.6. The Development of a Composite Stratigraphic Column.

From the evidence in section 2.3, for the roadcut, airstrip and scarp sections, supported by observations from secondary sites and the southern flow outcrops, a composite column can be compiled representing the complete accessible stratigraphy exposed for the Ben Lomond dome flow lobes (Fig. 2.10). The upper two-thirds, or 65 m of the flow comprises: an eroded FVP top; OBS; explosion breccia; TZ (with spherulitic fabrics and brown glass); and a central core of RHY. A variety of fabric parameters, outlined in chapter 3, were measured down the flow profile providing information on emplacement processes and properties.

CHAPTER 3.

AN EMPLACEMENT HISTORY FOR BEN LOMOND RHYOLITE.

3.1. Introduction.

A composite profile, compiled for the Ben Lomond flow (chapter 2&3.6)from the roadcut, airstrip and scarp sections, provides a basis for fabric profiling: the measurement of parameters such as density, porosity, primary void aspect ratio, volatile content, autoclast aspect ratio, spherulite diameter and proportion, and microlite size. From these profiles, an insight can be gained on both the emplacement history and the physical properties of the Ben Lomond rhyolite flows.

3.2. Density and Porosity.

The density and porosity of the Ben Lomond flow lithologies was determined by the following equation:

$$\rho = \rho_w m_{dry}/(m_{sat} - m_{sub}) \qquad (3.1)$$

where m_{dry} = dry mass

m_{sat} = saturated mass of sample in air

m_{sub} = saturated mass of sample while submerged in water

ρ_w = density of water

Both profiles (Fig. 3.1), provide indirect information on the distribution of volatiles in the emplacing lavas (Fink and Manley, 1987). For the FVP and explosion breccia pumices, the porosity is entirely from primary voids, wheras for the OBS and RHY layers, porosity is largely from secondary spherulites with shrinkage cavities. True porosity (from primary voids) is determined from the following equation:

$$V_p = (1 - m_{dry}/\rho_g V_{tot}) \times 100\ \% \qquad (3.2)$$

where m_{dry} = dry mass, ρ_g = grain density and V_{tot} = total volume. For the OBS layer, ρ_{dry} (the dry bulk density) may be considered as follows:

$$\rho_{dry} = (\rho_{obs} \cdot \alpha_{obs}) + (\rho_{air} \cdot \alpha_{voids}). \qquad (3.3)$$

As primary voids are volumetrically negligible it is assumed that the proportion of obsidian (α_{obs}) is equivalent to $1 - \alpha_{voids}$ where α_{voids} is all secondary voids.

$$\text{Therefore } \rho_{obs} = \rho_{dry} \div \alpha_{obs}. \qquad (3.4)$$

Thus when secondary porosity is removed by the above procedure, profiles may be derived that are characteristic of the emplacing lava. Below 10 m depth, there is a suppression of vesicularity, due to the weight of the overlying lava (Manley and Fink, 1987).

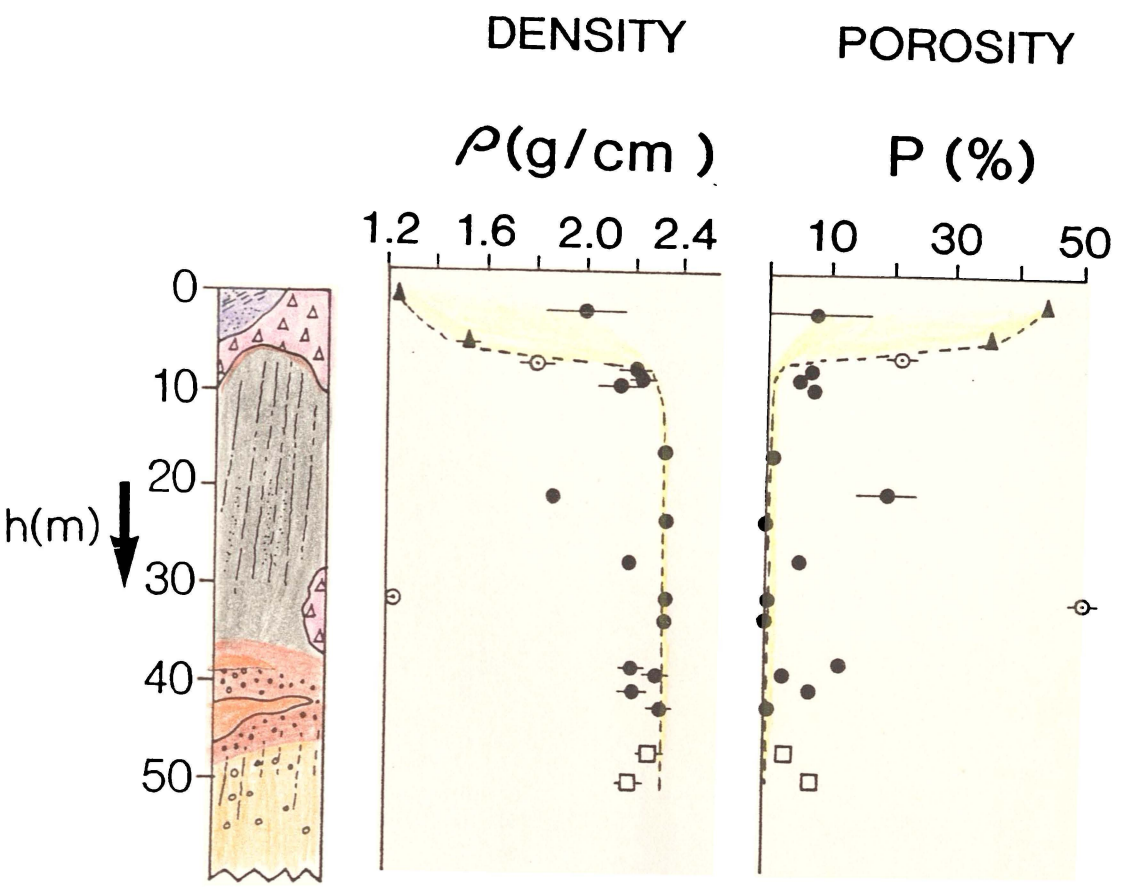

Fig. 3.1. Density and porosity profiles for Ben Lomond rhyolite flow, showing mean density and porosity (▲ FVP, ● OBS, ⊙ explosion breccia, □ RHY, including secondary porosity) and deduced primary density / porosity at emplacement (- - -). Error bars represent one standard deviation. The total number of determinations was 163, with at least three repeat determinations per level. Data are listed in Appendix II.

3.3. Void Aspect Ratio.

Variations in the void aspect ratio - namely the long axis length:short axis length measured from scanning electron microscope (SEM) and petrographic thin-section slide, provide information on:

a. stress directions in the lava during cooling, where principle stress parallels void long axis;

b. the rheology of the surrounding fluid (molten lava);

c. the vapour pressure in the voids.

Points b and c are linked in the following way. If the vapour pressure of the void is exceeded by the pressure of the surrounding liquid lava exerted on the void, deflation of bubbles occurs. The opposite case is true for bubble inflation, but this may be prevented by the viscosity of the melt and the overlying weight of the lava (Sherman, 1968; Fink and Manley, 1987). For fluid basaltic lavas, void aspect ratios are low because gas bubbles rise to the surface and are quickly deflated (Moore, 1987). The low viscosity of the lava does not record the stress directions within the cooling carapace, unlike more viscous lavas.

Vesicles in the FVP are tapered and elongated (Fig. 3.2) with high void aspect ratio (Rv) values between 15 - 30. Within the obsidian clasts of the FVP layer, there are three populations of voids corresponding to: central low aspect ratio (Rv = 1.5 - 2.5); surface blisters (Rv = 2.5); surface flow marks or tubes (Rv ≈ 30). Intraclast voids occur as large blisters near plate surfaces and between plates suggesting rapid cooling of plate surfaces and local foaming during volatile loss from clast interiors, during middle to late flow phases. Supporting evidence for this interpretation is the low Rv value of the interplate foam compared to the high Rv value for the tapered elongated deflated vesicles of the dense pumice. This suggests that the viscosity of the lava (that later cooled to form glass), was lower during the deflation of the dense pumice and higher during the local foaming forming the interplate voids. Alternatively, local tensile stresses were less intense during interplate void formation. In addition, intraplate cracks occur in some instances perpendicular to cooling surfaces as do most interplate void septa.

In contrast to the high mean Rv value and its large standard deviation exhibited by the void populations of the FVP carapace, those of the explosion breccia tend to be lower (Rv = 10). Rare gas blisters in the upper black obsidian of the OBS layer, have aspect ratios of less than 5.

3.4. The LOI - H_2O^+ profile.

Loss on ignition (LOI) values include some adsorbed water (H_2O^-), bound H_2O^+ (as hydroxyl groups) and a mass component from the oxidation of Fe^{2+}(Lechler and Desilets ,1987). LOI was determined by the standard method (Maxwell, 1968; in Hutchinson, 1974) using a tetraborate flux bead. The LOI component from the oxidation of Fe^{2+} is additive to the observed LOI value, hence may be ignored. Accurate Karl Fischer titration by Westrich (1987) on water-poor obsidians, show that adsorbed H_2O exists at less than 400°C,and at high temperatures)400°C, OH groups are dissolved within the glass. Thus, the proportion of mass lost by furnace heating of a powdered sample between 400 - 1000°C approximates to the bound water (H_2O^+) in the glass. In addition LOI between 500 - 1000°C was measured. All LOI results are listed in Table 3.1.

The difference between LOI (400 - 1000°C) and LOI (500 - 1000°C) values for the FVP and explosion breccia pumices (Fig. 3.3a), is attributable to the upper tail of a large H_2O^- mass peak. Low temperature non-magmatic H_2O^- is easily adsorbed to the surfaces of pumices with an inherently high surface area/volume ratio. Water contents are uniform throughout the OBS, TZ, and RHY layers except for an enriched value on the upper carapace FVP and the explosion breccias of the scarp (s3) and roadcut (s7). Values determined from LOI (500-1000°C) from obsidians compare very favourably with those from Karl Fischer water analyses. For example, an obsidian from s7 contained 0.11% water when heated between 500-1000°C. A value of 0.10 ± 0.006 wt% total water was obtained from Karl Fischer titration from three duplicate analyses on an obsidian from the same site (Westrich writt. comm., 1989), and a plot of wt% water versus pyrolysis temperature is illustrated in Fig. 3.3b for this sample, and three others from the Ben Lomond flow. Distal flow samples of obsidian from s30 and s59 have 0.08% and 0.06% total water respectively. Although these values are lower than that of s7, a proximal sample, the limited number of results precludes an interpretation on degassing losses, with increasing

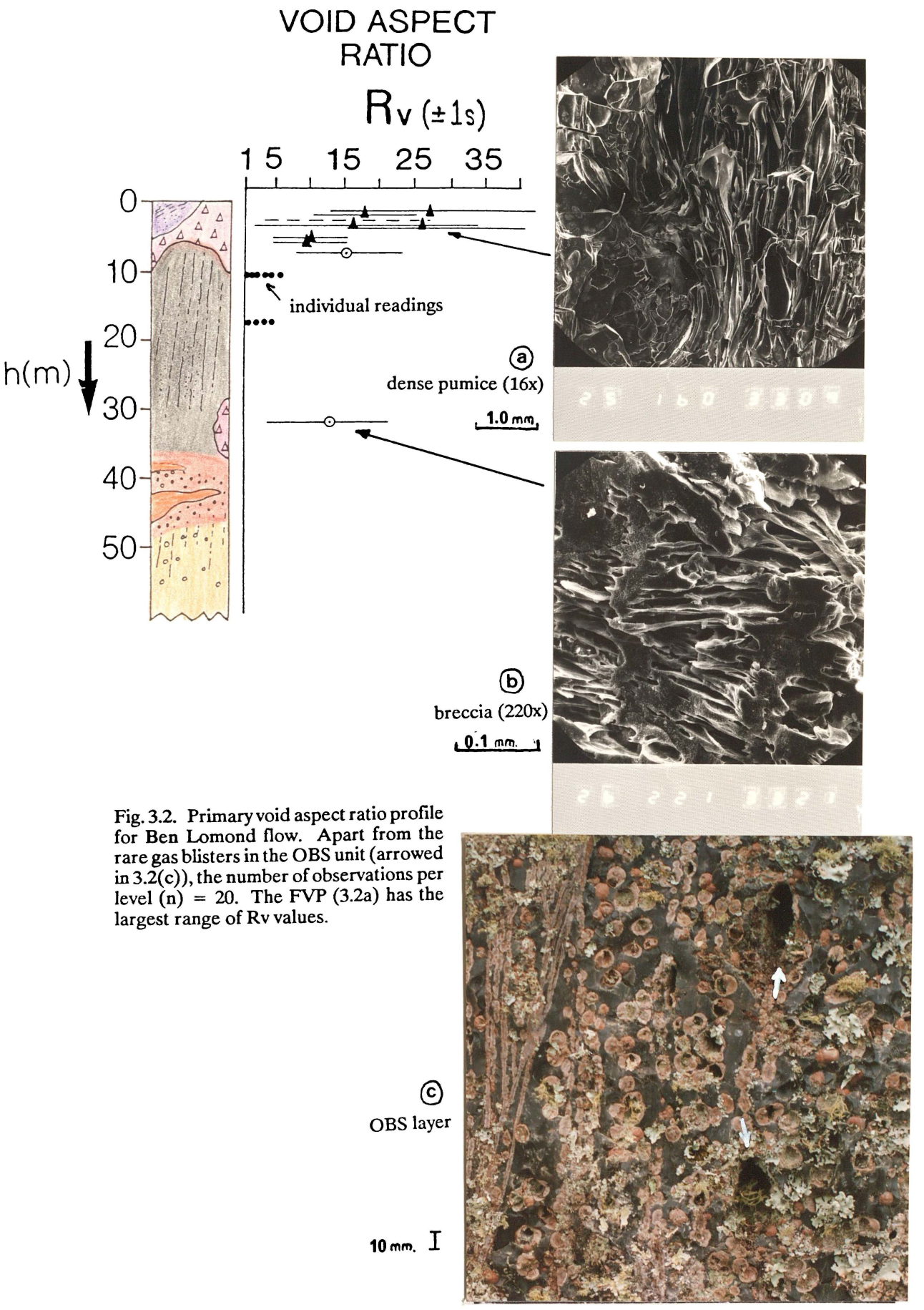

Fig. 3.2. Primary void aspect ratio profile for Ben Lomond flow. Apart from the rare gas blisters in the OBS unit (arrowed in 3.2(c)), the number of observations per level (n) = 20. The FVP (3.2a) has the largest range of Rv values.

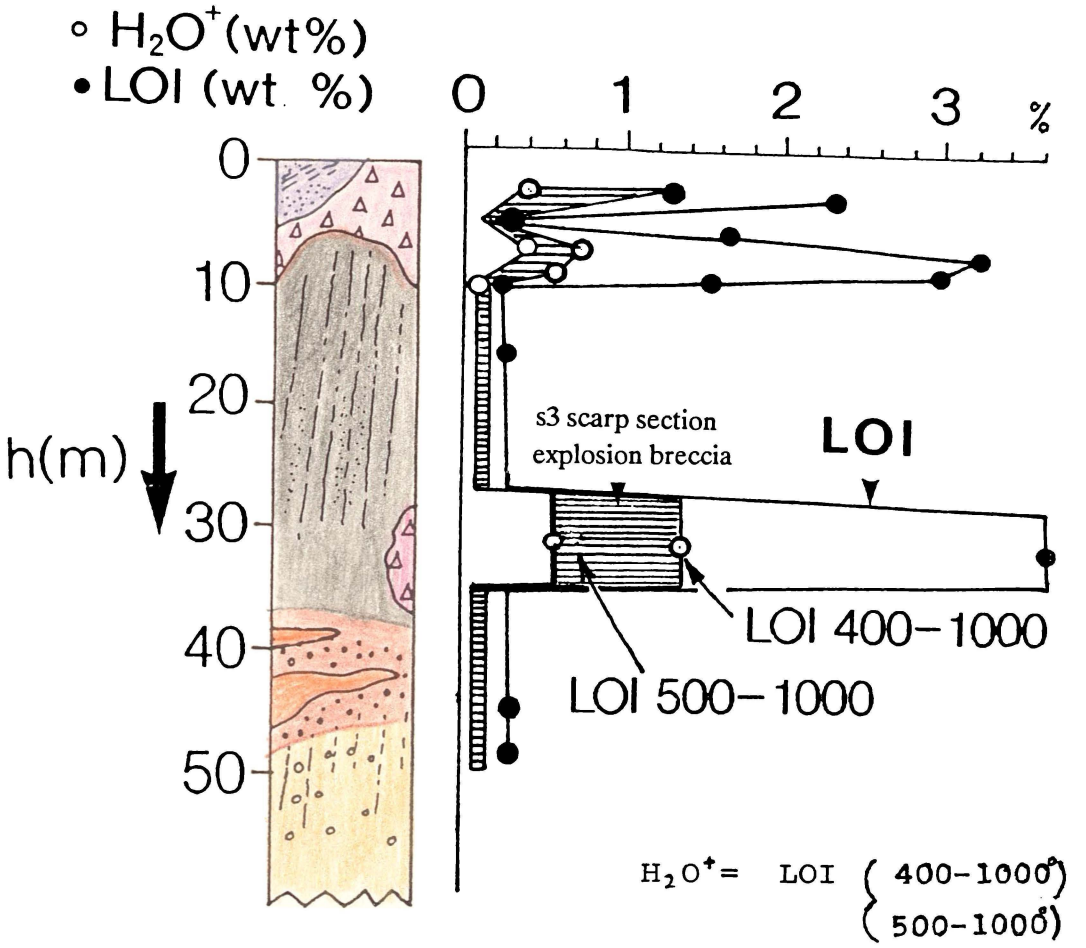

Fig. 3.3a Loss on ignition (total), LOI (400-1000°C) and LOI (500-1000°C) for the Ben Lomond flow section.

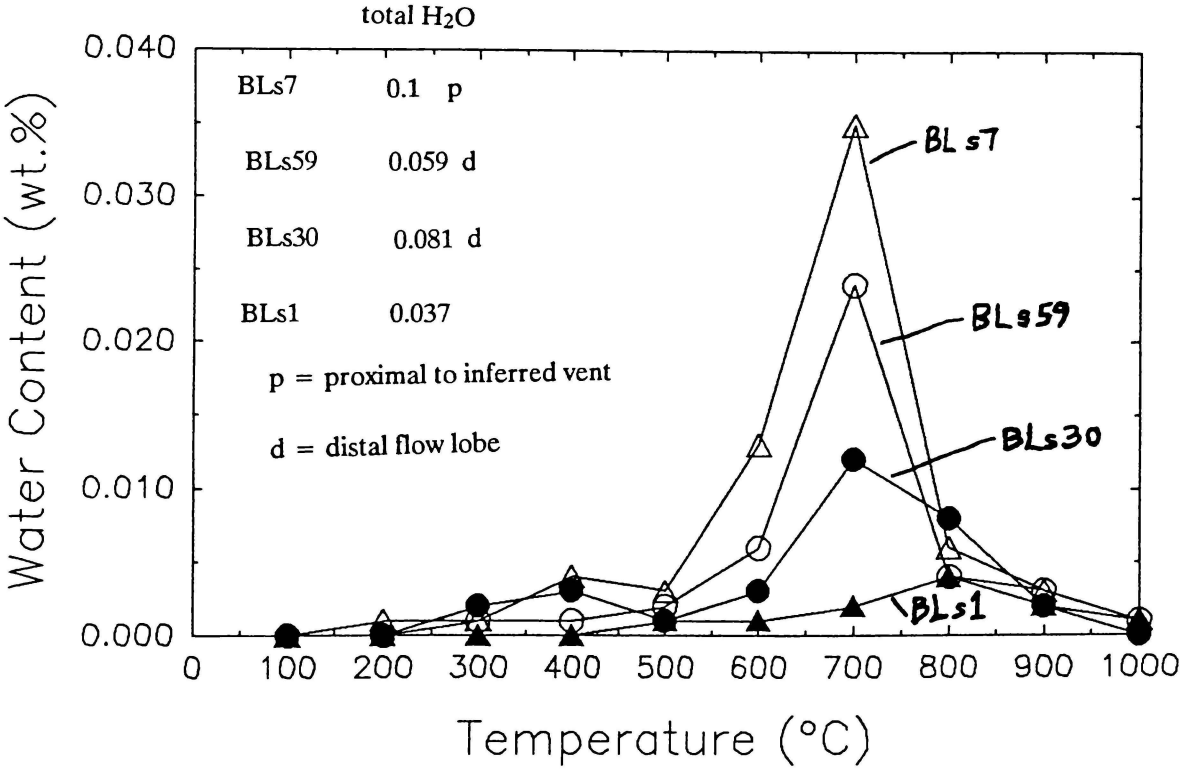

Fig. 3.3b Water content (wt%) versus pyrolysis temperature for four Ben Lomond samples. BLs1 is an oxidised brown glass from the TZ layer, characterised by a small high temperature pyrolysis peak, 100°C higher than those typical of the other fresh black obsidians. Samples were analysed via Karl Fischer titration by H.R. Westrich, Sandia Laboratories, Albuquerque U.S.A.

Table 3.1 Loss on ignition determinations for Ben Lomond flow fabrics

sample	unit	LOI	LOI (400 - 1000)	LOI (500 - 1000)
BL#1 (1)	FVP	2.37	1.33 ± 0.3 (n = 2)	0.37
-----(2)	obs plate,FVP layer	0.22	-	0.06
-----(3)	"	0.29	-	0.11
-----(4)	FVP	1.61	0.65 ± 0.2 (n = 2)	0.49
-----(5)	obs plate,FVP layer	0.32	-	0.06
-----(6)	EXPL BR	3.12	0.71 ± 0.1 (n = 2)	0.32
-----(7)	hydrated brown glass	1.41	-	0.16
-----(8)	OBS	0.22 (n = 2) (.27)*	0.25 ± 0.03 (n = 2)	0.05
-----(9)	hydrated brown glass	1.46	0.59	-
-----(10)	EXPL BR	2.92	-	0.18
-----(11)	glassy clast, EXPL BR	1.92	-	0.15
-----(12)	OBS	0.34	-	0.10
-----(13)	OBS (airstrip section)	0.30 (n = 2)	0.23 ± 0.01 (n = 2)	-
BL#2 (7)	EXPL BR	3.64 (3.32)*	1.35 ± 0.15 (n = 3)	0.51
BL#2 (9)	brown glass TZ layer	n.d	0.30	0.02
BL#2 (10)	RHY	0.17	n.d	n.d
s50	epiclastic br.	0.91	-	0.72

OBS	Av. LOI, (VUW)	n = 8	0.28 ± 0.05
	sequential furnace	n = 4	0.59 ± 0.04
	LOI (105 - 1000) WU	n = 5	0.34 ± 0.07
	LOI (400 - 1000) WU	n = 4	0.24 ± 0.02
	LOI (500 - 1000) WU	n = 4	0.07 ± 0.03
	H_2O^+	Ewart et al. (1968)	0.18
	H_2O	Taylor et al. (1986)	0.14

* LOI 105-1000 , furnace University of Waikato
All others determined at VUW.

distance from the vent during the flow emplacement. According to Westrich (writt. comm., 1989), there appears to be no difference in the water contents between proximal and distal parts of the flow.

The Karl Fischer analytical values compare favourably with 0.14% water determined by Taylor et al. (1986) for Ben Lomond obsidian, and appears more precise than the value of 0.2% H_2O^+ from sample P28361 in Ewart et al. (1968).

3.5. Development of Primary Vesicularity.

Before a silicic magma is extruded, it loses most but not all of its dissolved volatiles at a depth of 1 kilometre or less (Taylor et al. 1983). Eichelberger et al. (1986), proposed that degassing occurs on magmatic ascent, the magma expanding on decrease in pressure into a permeable foam within the conduit, and that collapse of the foam occurs during flow across the surface. My observations suggest that collapse must occur within the upper conduit, and that effervescence during effusion recurs in the upper part of the flow. Supportive evidence includes the wide range of aspect ratios of pumice vesicles, and the enrichment of H_2O^+ in the FVP layer in contrast with the OBS and RHY units. Additional physical evidence is from s9 where the FVP contains grey lineations between coarsely pumiceous zones, characterised by tear-drop shaped gas blisters (20 mm length) with intra-void fibrous septa. These vesiculated zones point to local collection of volatiles, squeezed out from deeper parts of the

carapace, migrating through cracks (via a decompressional process) perpendicular to cooling planes (e.g. lineation or flow-layer surfaces).

These observations are supported by those of Manley and Fink (1987), and Houghton (oral comm., 1988) for other flows. The overburden pressure of the carapace FVP is negligible, being insufficient to balance the vapour pressure of the dissolved water. Bubbles expand in the primary stress direction of the moving lava, becoming elongated and tapered. On rapid cooling, the surrounding liquid comprising the inter-void septa becomes plastic as the viscosity increases causing the voids to deform and deflate. The base of the FVP layer represents a horizon below which the vapour pressure is insufficient to counteract the load pressure, and so marks the lower limit of effervescence. Thus the beginnings of deflation of the upper conduit foam forming an OBS layer must have been an early pre-extrusion event. Any rare gas blisters (primary voids that distort pre-existing primary flow banding), must then exist owing to local slight increases in dissolved water content. Their low Rv value is a result of:

a. large (cm - m scale) intervoid distance through which flow stresses are propagated;
b. lower interior viscosity and higher overburden pressures acting to increase the surface tension of the developing gas blisters.

The anomalous high aspect ratio voids and volatile content of the explosion breccia will be explored in section 3.8.

3.6. Clast Aspect Ratio.

The apparent clast aspect ratio is defined as Rc = long axis length/short axis length (Peterson,1979), as measured from a two dimensional outcrop face. The apparent clast aspect ratio (Fig. 3.4a) is high for obsidian clasts and plates in the FVP carapace, indicating a rapidly cooling outer flow skin undergoing brittle fracture and rafting down the edges of flow ridges and rampart structures. At s7, avalanching of clast-rich parts of the FVP carapace caused fragmentation of pumice and deformation (asymmetric folds and small-scale laminae folds) of the still partly plastic obsidian clasts. Carapace clast groove directions (Fig. 3.4b) are predominantly between 070° - 080°, supporting an avalanching process occurring adjacent to a projecting obsidian ridge, near the margin of the flow lobe.

For a lateral transect across the explosion breccia of s7 where the sample number (n) equals 100 (rather than the usual n = 20 per sampling quadrat), the Rc values and standard deviation (s) values are uniformly low and may reflect violent late-flow brittle fracture during violent emplacement.

3.7. Spherulite Diameter and Proportion Profiles.

Mean spherulite diameter decreases up the profile from more than 30 mm (RHY layer lithophysae and TZ spherulites) to less than 10 mm in the OBS layer (Fig. 3.5.). The proportion of spherulites is greatest above the central RHY layer, where spherulitisation overprints primary flow fabrics such as flow banding. The acicular crystals that form spherulites (alkali feldspar and quartz) are anhydrous, so as a spherulite crystallises around a nucleation point (for example, a microlite), volatiles diffuse away

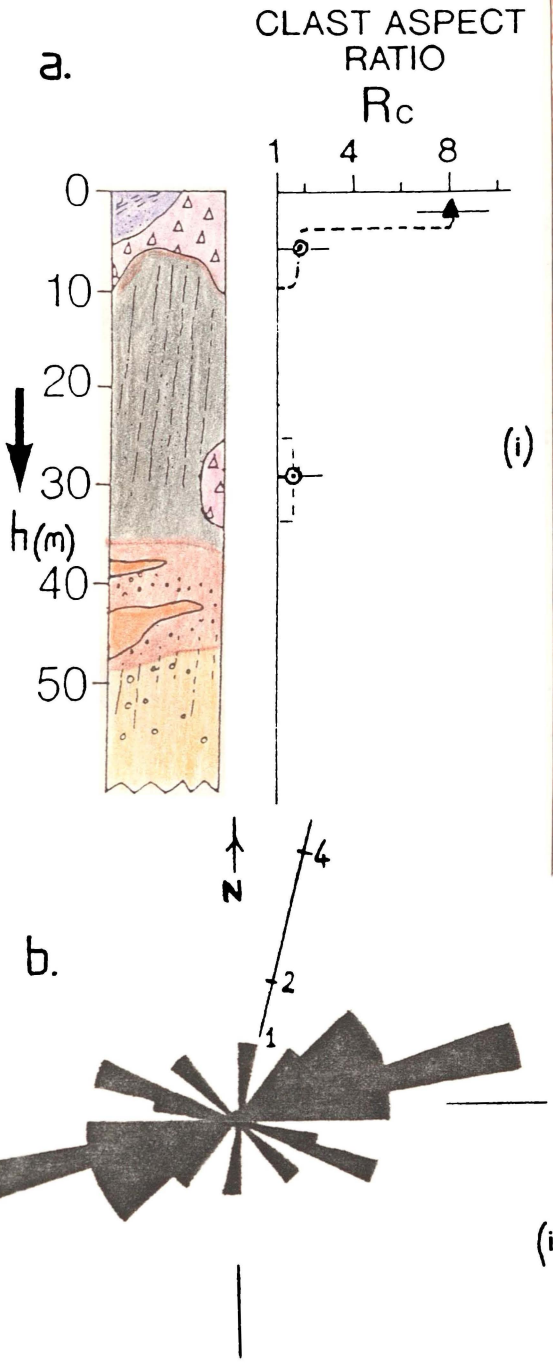

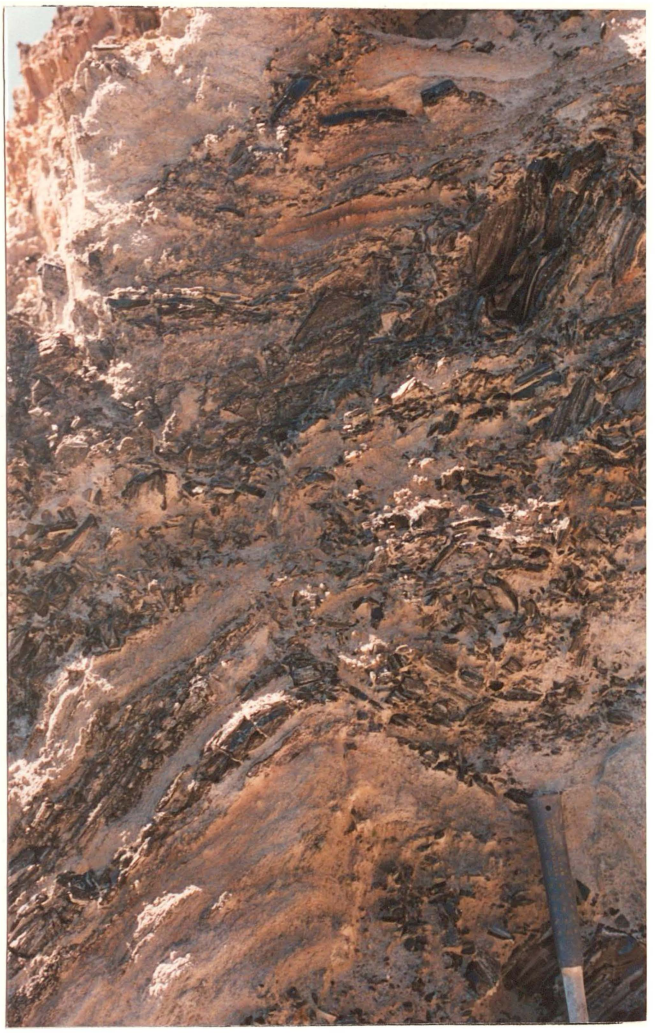

(i)

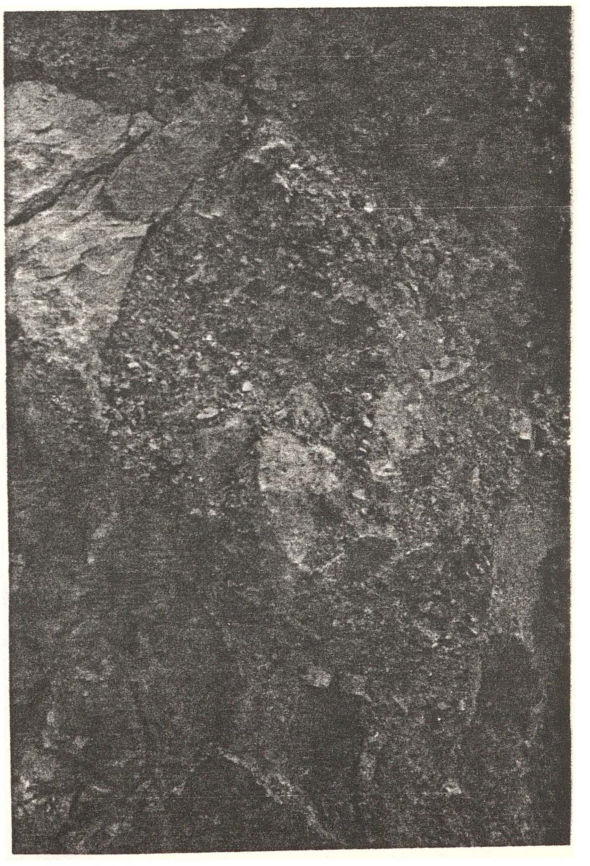

(ii)

Fig. 3.4a. Clast aspect ratio, Ben Lomond, for the two breccia types:
(i) obsidian clasts and plates (FVP), and
(ii) the pink pumiceous explosion breccia.

Fig. 3.4b. Groove directions on the obsidian plates of the FVP carapace, s7.

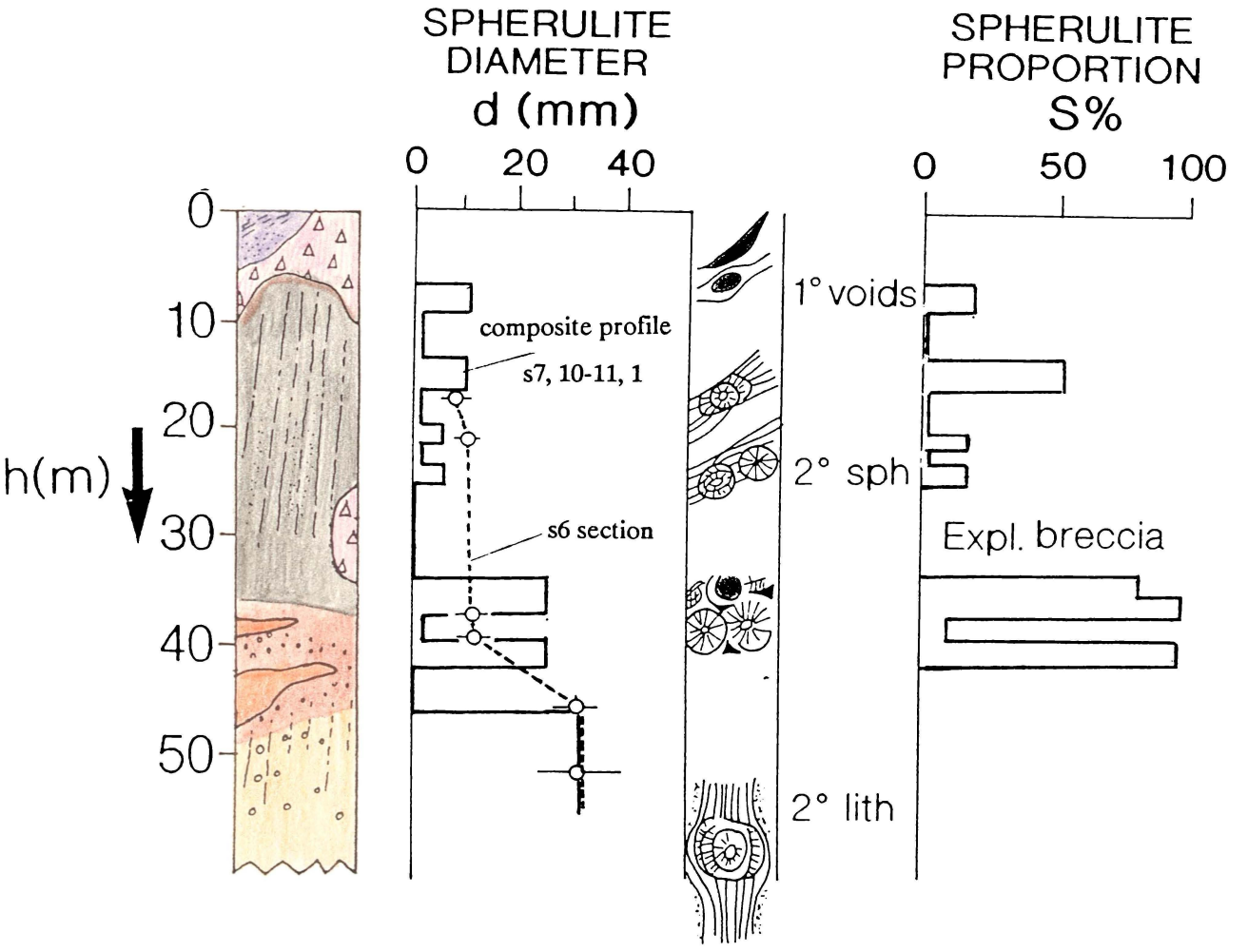

Fig. 3.5. Spherulite diameter and proportion profiles compiled from field measurements and observations from the Ben Lomond flow unit section. The inferred step-function of the composite profile for d is the result of an apparent layering in outcrop, where foliation occurs perpendicular to measurement faces, whereas the profile from s6 is parallel to foliation. S% is compiled from the composite profile (s7, 10-11,1) and s3 from field estimates and from $S = 1 - \alpha_{OBS}$ where α is the proportion of glass.

(Best, 1982; Cas and Wright, 1987; Manley and Fink, 1987). Secondary lithophysae nucleate, overprinting primary flow banding and inflate in a devitrifying RHY layer plastically distorting flow lineations during the slow cooling of the interior of the flow. Once the vapour pressure is exceeded by the load pressure, lithophysae collapse as volatiles are expelled along cracks within the RHY layer. Some are also deformed by later localised flowage within the central thermally insulated flow core that remains mobile for the longest time. This local heating could be a response to thermal feedback, a mechanism postulated by Nelson (1981).

The RHY layer volatiles from secondary lithophysae and the initiation of groundmass crystallisation, form a halo around the core where the TZ layer spherulites grow, virtually masking any original primary fabric such as obsidian. Therefore, the profile describing the proportion of spherulites is an indicator of secondary volatile migration.

3.8. The Origin of the s3 and s7 Explosion Breccias

A breccia pod occurs at s3 directly above the spherulite-rich transition zone. The presence of elongated vesicles in the breccia is a problem as the breccia at s3 lies below the depth at which primary effervescence took place. With an H_2O^+ content approximately five times greater than the adjacent OBS and RHY units, an origin associated with a local vapour pressure increase caused by the migration of gas through lava is suggested. At s3, the marginal obsidian breccia has lower aspect ratio voids (Rv $\leq$ 7:0). Usually, the weight of the overlying lava (more than 35 m) would preclude the formation and stability of primary voids, unless there was a secondary volatile enrichment (Fink and Manley, 1987). The breccia then fragmented either owing to movement of the surrounding flow, or was related to the explosive release of volatiles.

The origin of s7 as an explosion breccia during late flow-phase is supported by the following lines of evidence:

a. the breccia cross-cuts both FVP and OBS units;
b. the inverted conical shape of the breccia outcrop, suggesting an origin from below the base of the section (road level), and explosive release via at least two fissures;
c. the largest of the clasts occurs in the central part of the major exposed fracture or pipe(Fig. 3.6);
d. the irregular contact with the FVP unit, suggesting explosive projection of clasts into, and disrupting the FVP;
e. the breccia-OBS contact is delineated by a brown perlitic glass, containing angular and lenticular fragments of black aphyric spherulitic obsidian from the adjacent OBS unit;
f. the brown perlitic margin has a volatile content intermediate between the volatile-poor obsidian and the volatile-rich breccia pumice and grey perlitic obsidian, suggesting localised hydration of the obsidian margin during explosive volatile release.

The contrast in morphology between s3 and s7 explosion breccias indicates that s3 represents an early phase - namely a pod-shaped volatile enrichment zone in a halo above the central devitrifying rhyolite. Later during flow, tension fractures opened in a brittle carapace acting as pathways for the explosive release of volatiles forming an inverted cone shaped deposit (in cross-section) as at s7.

3.9. Microlite Morphology and Size Profile: Implications for Emplacement Thermal Regime.

Microlites occur throughout the FVP and OBS layers as well as the interspherulite glass of the TZ layer. They are entirely absent from the pumice of the explosion breccia. Their identification is difficult in the RHY unit as groundmass devitrification textures and limonite staining tend to mask any birefringence exhibited by existing small crystal laths ($\sim$50 μm long) and microlites. Concentrations of microlites in the OBS layer delineates the primary flow banding (Fig. 3.7a). Two populations of microlites exist, best seen in the OBS layer: tabular laths or plates including thin cross cutting platelets (a:c = 2:1, $\bar{l}$ = 125μm); and elongate rods (a:c = 10 - 15, $\bar{l}$ = 14μm). Experimental studies in the literature (Lofgren, 1974; Swanson, 1977; Muncill and Lasaga, 1988) indicate tabular microlite formation during a low undercooling (ΔT < 50°C) regime, whereas the elongate rods formed at higher undercoolings (ΔT > 150°C), at temperatures exceeding 600°C (Swanson et al. 1985). Crystallisation occurred under isothermal

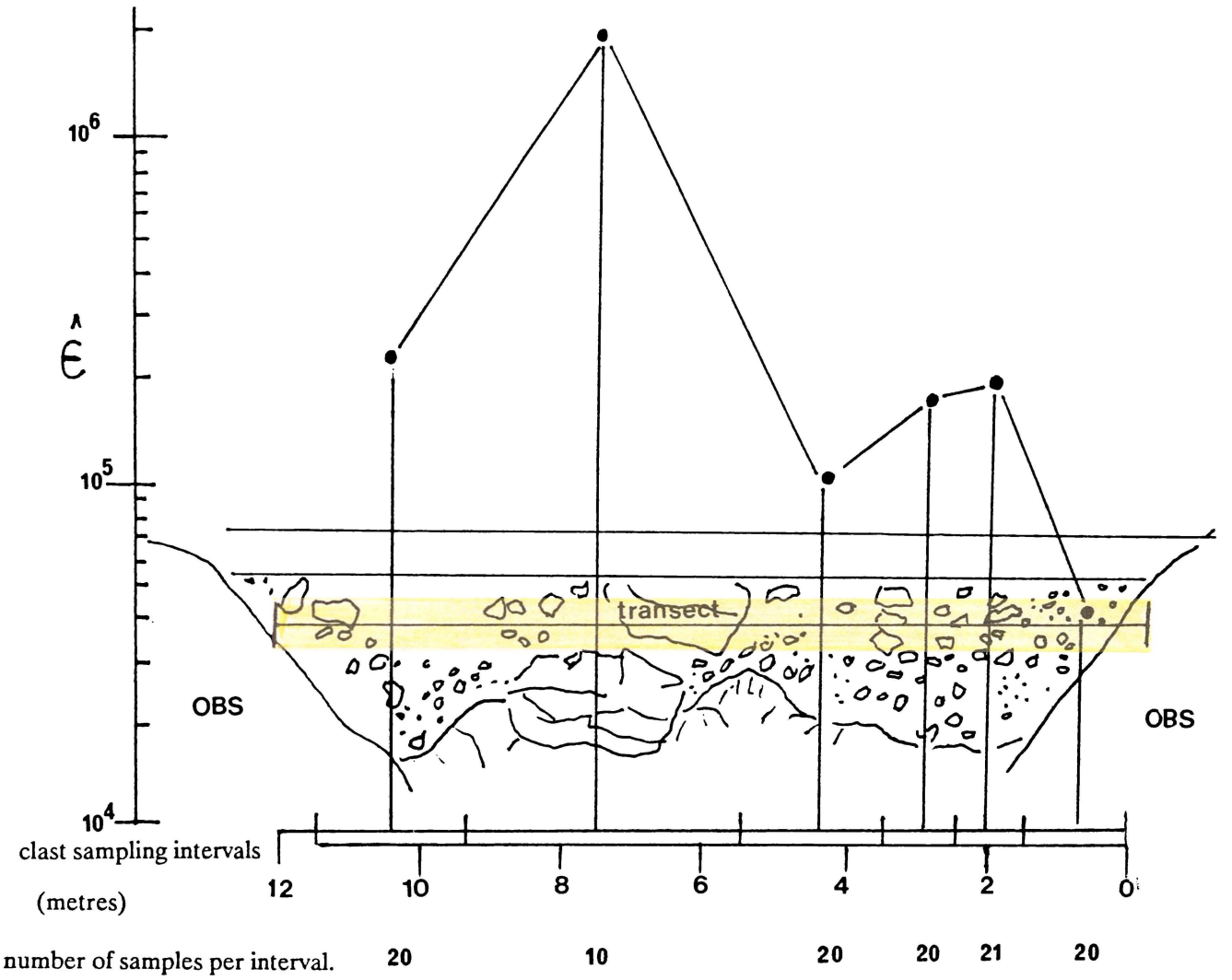

Fig. 3.6. Transect across the breccia 'pipe' at s7 where $\epsilon = 2\chi_1 - \chi_2$, χ_1 = largest clast and χ_2 = second largest clast within the clast sampling intervals and χ_n = log (length x height) (method from Robson and Whitlock, 1964).

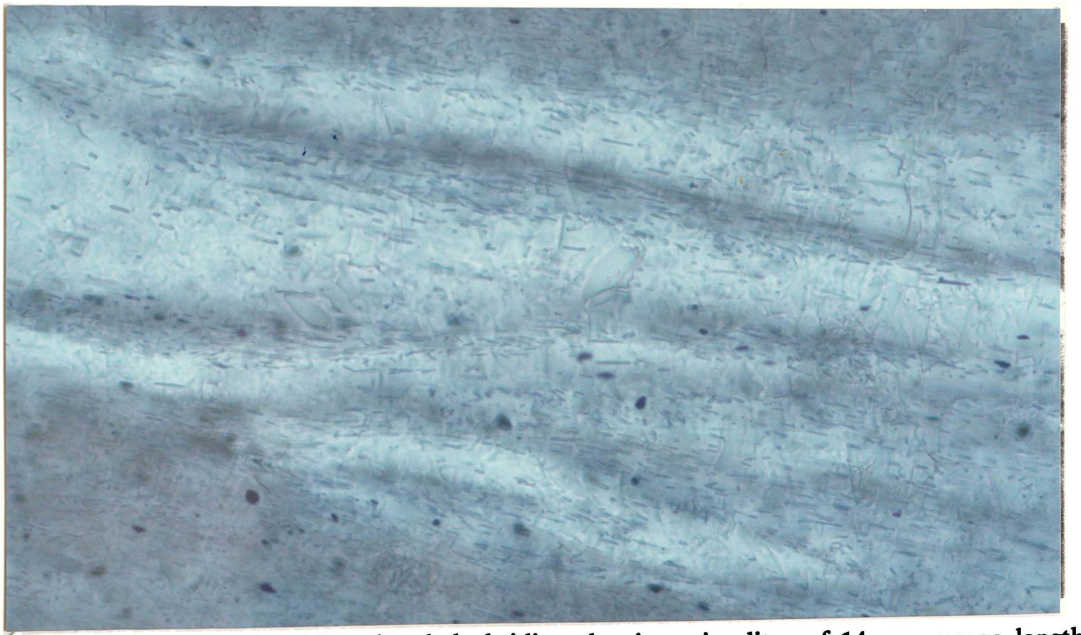

Fig. 3.7a. Photomicrograph of flow banded obsidian showing microlites of 14 μmaverage length with flow-aligned long axes. (400x magnification)

conditions during near-complete dewatering while undergoing magmatic decompression on ascent (Westrich et al. 1988). The elongate rods also formed later than the tabular microlites, as the rods flow around rotated tabular laths. Therefore the tabular microlites formed at low undercoolings nearest the magma chamber, whereas the rods formed at higher undercoolings away from the magma chamber. The regularity of length of the rod-like microlites throughout the flow section suggests that their crystallisation history is independent of post-eruptive cooling (Fig. 3.7b). Hence their locus of formation is constrained between the magma chamber and the surface, that is, in the conduit prior to eruption.

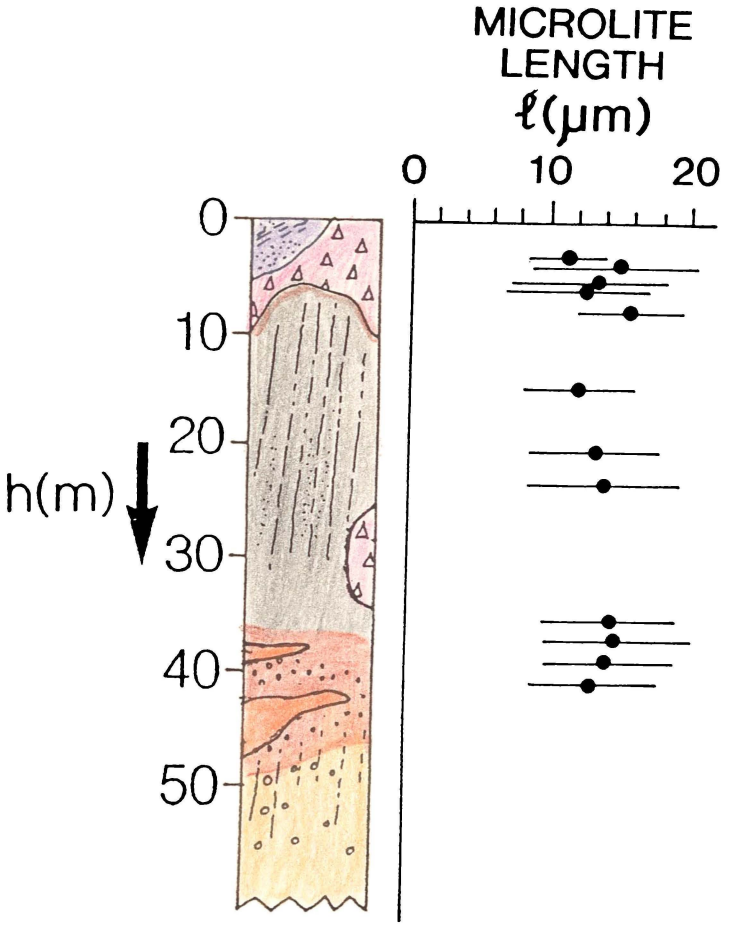

Fig. 3.7b. Microlite length profile, Ben Lomond flow.

3.10. The Emplacement History of the Ben Lomond Flow.

From fabric profiling and structural data, a sequence of events (Fig. 3.8) is proposed. Aspects of such a model may be tested for example, by trace element chemical data from samples taken throughout the flow profile, discussed in chapter 4.

Rare phenocrysts (plagioclase and Fe-Ti oxides), and 50 μm length laths of plagioclase and biotite) formed in the chamber. Microlites formed between the chamber and the surface within the conduit, and during ascent segregated into bands that later deformed during eruption and flowage. Vesiculation occurred in the upper 300 m of the conduit giving rise to possible pre-lava pyroclastic activity from the fragmentation of a gas rich silicic foam although no clearly identifiable outcrops exist of a pre-lava

pyroclastic sequence. Collapse of an inflated foam occurred in the upper conduit followed by effervescence and elongation of vesicles in the FVP carapace during flow. Primary vesiculation was largely suppressed at depths greater than 10 m. As the carapace cooled, the flow stratigraphy was disrupted by the still molten moving lava beneath, stressing the carapace forming flow ridges, rampart structures, and fracturing and rafting of obsidian clasts within the FVP. The formation of the explosion breccia was a later flow feature, connected either with local volatile enrichment from a halo surrounding a devitrifying flow interior, or from interaction with ground water. Disruption of the FVP and OBS layers took place from decompressional opening of carapace tension cracks, causing the explosive release of volatiles. Spherulites formed associated with small gas cavities in zones of volatile enrichment within the TZ layer. Those that formed around such cavities in the OBS layer, before and after the emplacement of the s7 explosion breccia, cross-cut primary flow banding and were only slightly deformed by compression (Rv $\leq$ 2.5) when the vapour pressure of voids was exceeded by pressure from the overlying thickness of lava. Single spherulites without associated gas cavities and with aspect ratios of 1, formed after flow cessation and later joints formed during cooling to ambient temperatures.

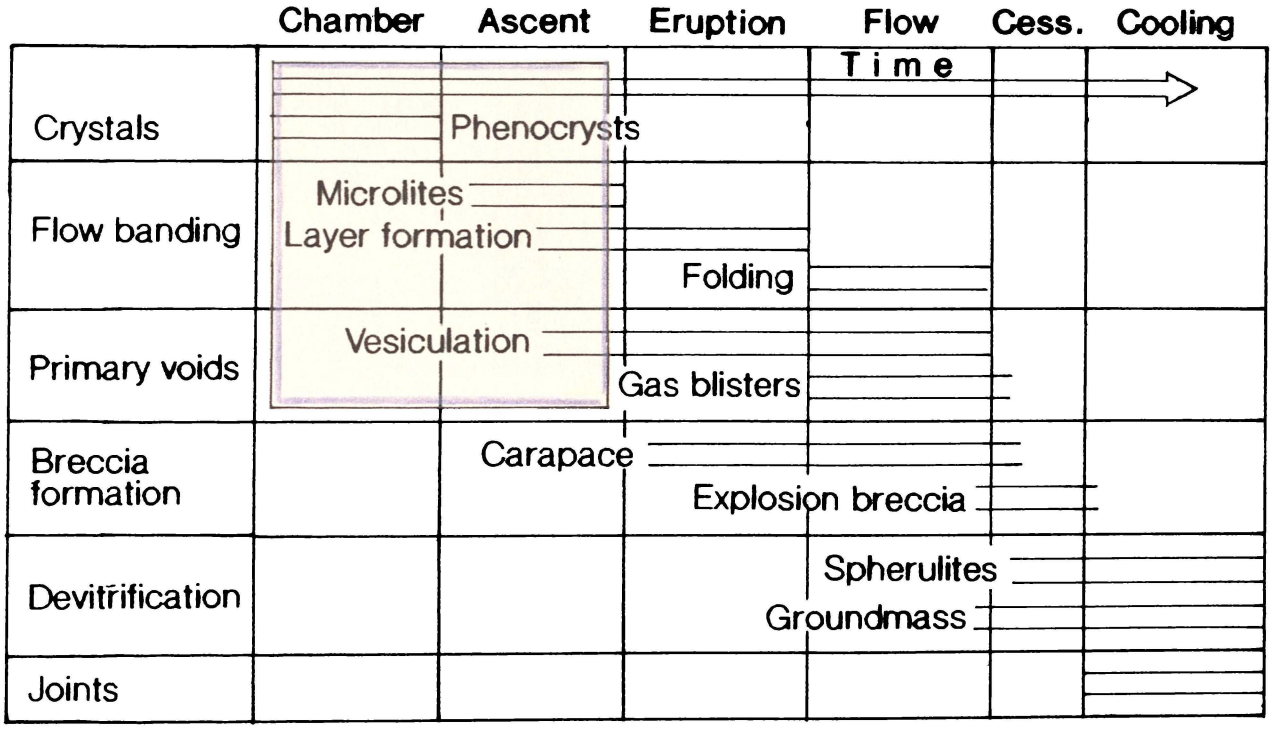

Fig. 3.8. Emplacement history of events, Ben Lomond flow.

CHAPTER 4.

DEGASSING HISTORY, CHEMISTRY, AND INFERRED VISCOSITY OF THE BEN LOMOND RHYOLITE FLOW.

4.1. Introduction.

Viscosity is a fundamental property of magmas, contributing to eruption style and landform morphology. During eruption, the viscosity of lavas is affected by its crystallinity, volatile content, temperature, chemistry (or degree of polymerisation), yield strength and morphological factors such as basal slope and flow thickness. As the viscosity of rhyolite lavas has rarely been measured directly in the field, viscosity of emplaced lavas can be estimated using two approaches: a method based on the chemistry and physical properties of the magma after Shaw (1972); and a method based on the morphology of the arrested flow after Hulme (1974), Wilson and Head (1983); Zimbelman (1985), assuming a Bingham rheology.

Microlite form and petrography provide some information on pre-eruption magmatic processes at depth. Estimated magma temperature and volatile content, from a well constrained degassing model for rhyolite lavas (Westrich et al. 1988) is critically assessed, and provides a framework for interpreting the degassing history of the Ben Lomond magma. Major and trace element chemistry for a composite section through the Ben Lomond flow is outlined, and comparisons are made between the relative mobility of soluble trace elements and fabric variations within the lava. A review of the methods of estimating viscosity and inferring the rheological behaviour of the flow is followed by the calculation of the viscosity of the Ben Lomond flow and the generation of a flow viscosity profile during early and late flow phases.

4.2. Inferences on Subsurface Processes.

Below is a summary of results pertaining to the pre-eruption history of the Ben Lomond magma:

a. the magma is essentially aphyric, with very rare phenocrysts of plagioclase, Fe-Ti oxides including augite and hypersthene with laths of plagioclase and biotite less than 50 μm long;

b. volatile contents are low in the OBS layer;

c. microlites exist in 2 populations - tabular and elongate, and delineate the primary flow banding;

d. a regularity of length of elongate microlites occurs in the FVP and OBS layers.

The above results provide a window on processes operative at depth. Biotite crystallised in the magma chamber under hydrous conditions with water contents greater than 4.3% (Ewart et al. 1975; Dunbar and Kyle, 1989; Hervig et al. 1989). Paradoxically, the low water content within the surface OBS layer (less than 0.2%) suggests a significant degassing between the chamber and the surface. For lavas that are largely aphyric, the magma crystallisation temperature is a good approximation to the lava

temperature (Carmichael, 1974). Rare phenocrysts of plagioclase (approximately 5 observed in 100 thin sections) crystallised in the chamber. The small plagioclase and biotite laths crystallised in the chamber later than the rare large plagioclase phenocrysts, as the laths are flow-aligned around the margins of the phenocrysts. The uniformity of length of the elongate microlites suggests that their crystallisation proceeded independently of the post-eruptive thermal history, implying formation in the conduit. From laboratory based crystallisation studies (eg. Swanson, 1977; Muncill and Lasaga, 1988), the two microlite populations crystallised at different undercooling temperatures - the tabular population at 50°C and elongate at 150°C. Although such laboratory experiments were performed at higher pressures (1 kbar) and water contents (20 - 30%) (Lofgren pers. comm. 1989) to facilitate rapid crystallisation, the form of the crystals approximates that of natural conditions. The undercooling temperatures for both populations above, would be considered maxima, as these were determined for synthetic binary silicate solutions. Minimum undercooling estimates would be 25°C and 100°C respectively for natural silicate systems (Lofgren pers. comm. 1989).

The tabular population formed first and thus closest to the magma chamber as the rod-like elongate microlites flow around the margins of the tabular laths. Therefore the undercooling temperature - the difference between the magma temperature and the water-saturated liquidus, increases on magmatic ascent in the conduit as the pressure decreases and volatile contents decrease. The lack of reaction rims and resorption on the margins of the biotite laths and rare plagioclase phenocrysts respectively suggests an uninterrupted ascent of the Ben Lomond rhyolitic magma.

4.3. Magma Temperature Estimation.

For basalt lavas, temperatures have been measured directly by thermocouples or optical filament pyrometers, and comparisons have been made with Fe-Ti oxide geothermometry and glass geothermometry (Helz and Thornber, 1987).

For viscous rhyolite lavas, no lava flows have been observed hence direct temperature measurements have not been obtained. Laboratory measurements to determine liquidus and solidus temperatures as an upper and lower limit to emplacement temperatures of silicic lavas is extremely difficult (Carmichael, 1974). An uncertainty is introduced by the water content which can strongly affect the liquidus temperature.

For example, an attempt was made to estimate the glass transition temperature (solidus) of the Ben Lomond rhyolite by fusing powdered obsidian in the DTA furnace at a heating rate of 10°C per minute. The heat applied to grains of polymerised glass, being from the outside-in, was the reverse of original conditions. Tack welding occurred near 1000°C; this exceeds temperature estimates and stability temperatures for crystals determined from mineral-pair geothermometry for the rhyolites (Ewart et al. 1975), and measured glass transition temperatures of approximately 670°C (Navrotsky, 1981). A possible reason for the high tack-welding temperature was that the heating rate (at 10°C / minute) and run time (30 minutes) was too rapid. Additional physical constraints include differences in the physical nature of the obsidian - a continuous cooling fluid versus grain-to-grain contacts of a rapidly heated powdered sample.

Any endothermic peaks associated with possible changes of state or release of volatiles above 300°C in DTA were subtle and difficult to interpret. Liquidus temperatures are also difficult to determine from furnace-type experiments. For example, the bulk composition of an anhydrous obsidian with plagioclase and biotite crystals, is not quite the same as that of subsurface crystallisation from a hydrous liquid (approximately 4% water) under pressures exceeding 2000 bars. The heating and quenching of samples in the laboratory by this method, would not give reliable results for a viscous calc-alkaline lava.

Laboratories for determining T_g (glass transition temperature) and T_f (fusion temperature) under varying pressures and volatile contents, are unavailable in New Zealand.

For a nearly aphyric lava, the temperature is inferred as approximating closely, the crystallisation temperature in the chamber (Carmichael, 1974; Cas and Wright, 1987). Certainly, for slowly cooling aphyric lavas, this assumption seems valid. For example, Wright et al. (1968) measured via thermocouple, the temperature of a basalt lava lake as 1160°C. By extrapolating the chemical composition of older pumice, an initial temperature of 1200°C is inferred. For the Inyo domes, Vogel et al. (1985) calculated from Fe-Ti oxide geothermometry, variations of ± 50°C within the conduit bisected by the drill hole. The range of estimates of 884-948°C exceeds the mineral pair error suggesting that differences in crystallisation within the conduit occur owing to co-mingling of two magmas. Glass from the pre-dome plinian phase and lava, give the same estimates of temperature, suggesting that no significant variation in temperature occurs during ascent of the magma in the upper 600 m of the conduit. Therefore, the low cooling or conduction rates of glass (Gable & Shankland, 1984) formed on quenching via dewatering during decompression (Westrich et al. 1988) preclude significant variations in the temperature of the magma on ascent. However, the significant decrease between the water contents of the magma (4%, Naney, 1983) and lava (0.2%) points to considerable differences in the rheology of the melt between magma chamber and surface, a rising water saturated liquidus and increased undercooling of the melt.

As only two crystals of "opaques" were observed in approximately 100 thin sections, magnetite - ilmenite geothermometry by the method of Buddington and Lindsley, (1964) and Andersen and Lindsley (1988) is not feasible. Fe-Ti oxide temperatures are closure temperatures (Lofgren oral comm. 1989). Thus the previous thermal history of the magma such as the separation of the Ben Lomond magma from the other rhyolite magma in the chamber, is unknown. As P H_2O is unknown, the plagioclase-glass geothermometry method of Kudo and Weill (1970) cannot be used either.

Temperature can only be inferred for Ben Lomond lavas from crystallisation experiments of granitic fluids under changing temperature, water content and pressure from laboratory studies by Piwinskii and Wyllie (1968), Whitney (1975), Naney (1983) and Whitney (1988).

Fig. 4.1 shows a phase diagram of a synthetic granite at a pressure of 200 MPa, in particular the stability field for biotite + plagioclase + clinopyroxene (augite) ± orthopyroxene (hypersthene).

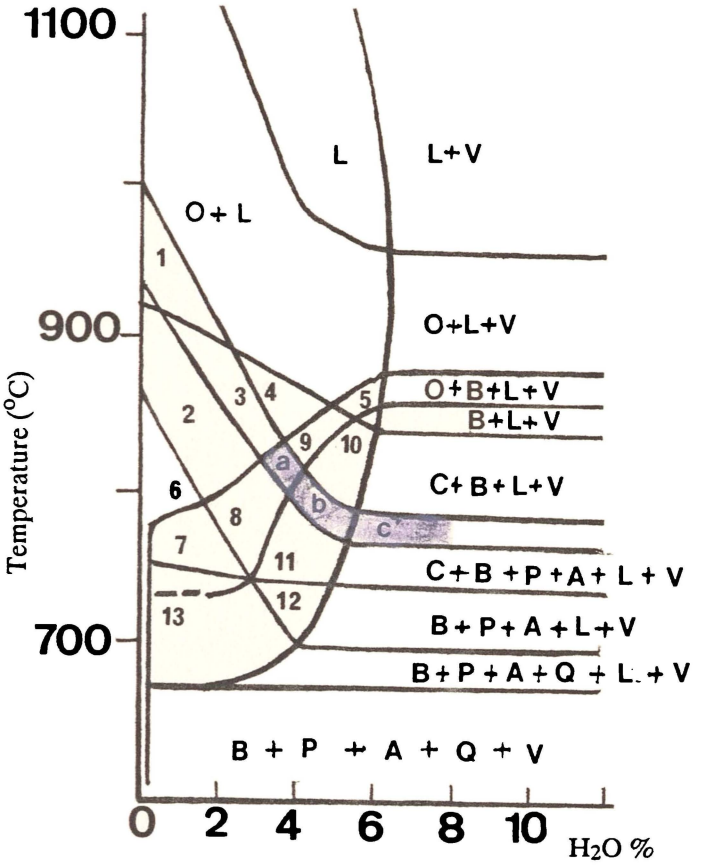

a = O + C + B + P + L
b = C + B + P + L
c = C + B + P + L + V

1 = O + P + L
2 = O + C + P + A + L
3 = O + C + P + L
4 = O + C + L
5 = O + B + L
6 = O + C + P + A + Q + L
7 = O + C + B + P + A + Q + L
8 = O + C + B + P + A + L
9 = O + C + B + L
10 = C + B + L
11 = C + B + P + A + L
12 = B + P + A + L
13 = B + P + A + Q + L

A = alkali feldspar
L = liquid
V = vapour
Q = quartz

Fig. 4.1. Temperature H_2O phase diagram for a synthetic granite at 200 MPa pressure showing the region of stability of co-existing biotite (B), orthopyroxene (O), clinopyroxene (C) and plagioclase (P) (from Naney, 1983).

For Ben Lomond, only one crystal of hypersthene was observed and less than three augite phenocrysts. At 200 MPa, the upper limit of biotite crystallisation under hydrous conditions is 880°C, and with co-existing plagioclase at approximately 825°C. The lower limit for co-existing plagioclase biotite and clinopyroxene is 775°C at water contents exceeding 3.5%. The sparse distribution and small size of biotite laths suggests that few nucleation sites were available for crystal growth. This may be caused by a short residence time of the Ben Lomond magma in the chamber and inadequate time for phenocryst nucleation and/or the arresting of diffusion controlled crystal growth by the decrease in H_2O on ascent. Unlike the phenocrysts of site 50, there is no evidence of resorption or reaction rim formation. Plagioclase phenocrysts lack oscillatory zoning. Thus a temperature estimate of the Ben Lomond magma of between 775°C - 825°C (average approximately 800°C) appears reasonable, and is consistent with other Taupo Volcanic Zone biotite-bearing lavas (via Fe-Ti oxide geothermometry of Ewart et al. 1971; 1975) and those from other rhyolites (e.g. Warshaw and Smith, 1988).

4.4. A Degassing Model of Rhyolite Magmas: the Inyo Domes.

From drillhole and surface data from glass inclusions, airfall tephra, conduit and dome samples, Westrich et al. (1988) documented a complete record of the degassing history of a rhyolite magma (via measurements of H_2O, Cl, S, and F) at Obsidian dome in the Inyo Chain, northern California. Their evidence suggests two processes by which magma can lose its volatiles: isothermal decompression; and isobaric crystallisation.

Available evidence suggests that the two processes are sequential. That is, the dome/flow glass compositions represent melt compositions at the end of the decompression stage and prior to second boiling, this being prior to dome emplacement and during early flow.

The initial volatile content was at least that required for the stability and crystallisation of hornblende in the magma chamber (4% Naney, 1983, at temperatures of 930°C, Vogel et al. 1985). The dome magma (0.2% H_2O) lost 97% of its original water by decompression, strongly undercooling the magma and inhibiting further crystallisation. Degassing and isothermal decompression occur over days within an eruptive timescale (Eichelberger et al. 1986). However, as the decompression of the magma during ascent occurred, H_2O is reduced from 4 to 0.1% and the liquidus (Naney, 1983; Westrich et al. 1988) rises to 1100°C at 1 MPa water pressure (Fig. 4.2). Therefore the dome magma is strongly undercooled relative to the water saturated liquidus. The 4% to 0.1% H_2O decompression would cause a $\sim$ 4 orders of magnitude increase in viscosity between the chamber and the surface.

Magma with 4% water began to vesiculate on ascent as the confining pressure declined below 100 MPa or 4 km depth. At porosities more than 60%, rhyolite becomes highly permeable to gas flow. By diffusion, H_2O^+ in silicate polymers diffuses into inflating voids. Void interconnection allows porous gas flow, achieved as the magma approaches 500 m depth (Eichelberger et al. 1986). Wet magma begins to leak gas prior to reaching the surface into a permeable breccia-filled vent funnel, formed during the initial explosive phase of the eruption. The inflation of the magma into a foam (60% porosity, 1.2% H_2O at 500 m depth) would cause a further increase by two orders of magnitude (in addition to

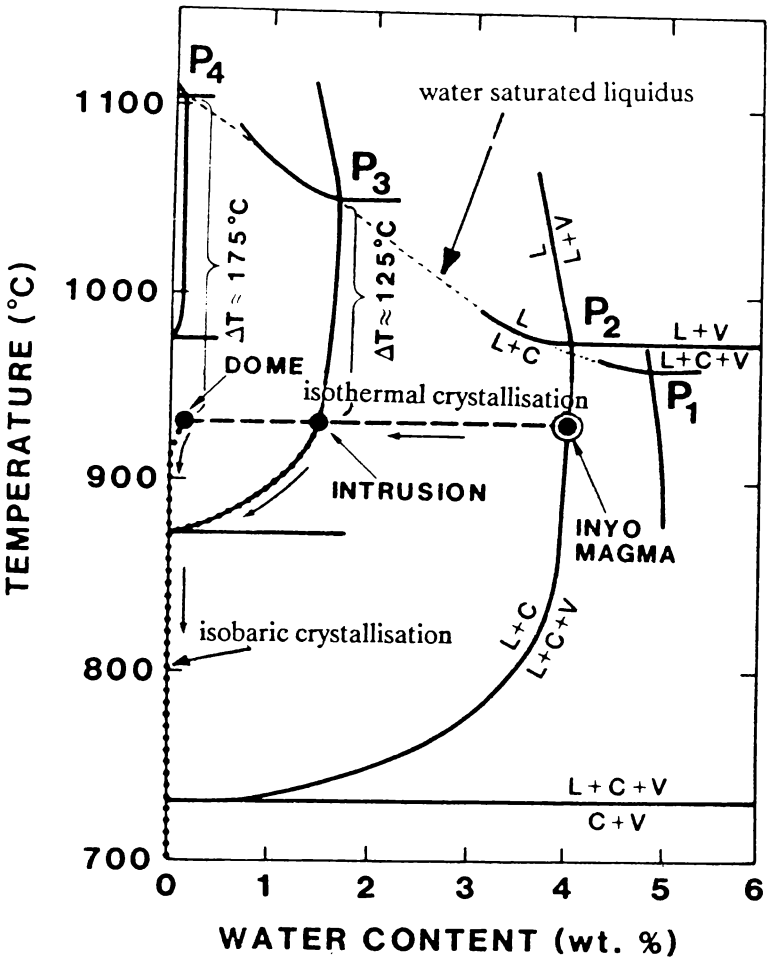

Fig. 4.2. Polybaric TX phase diagrams for a hydrous magma undergoing decompression. The inferred paths of the Inyo magma are superimposed (Westrich et al. 1988). Phase boundaries are labelled for 100 MPa pressure. The water saturated liquidus rises from P1 (200 MPa), to P4 (1 MPa). P2 and P3 represent pressures of 100 and 20 MPa respectively. L = liquid V = vapour C = crystals.

the four orders of magnitude viscosity increase from dewatering alone between chamber and surface), as bubbles would act as rigid spheres impeding shear (Roscoe, 1952).

Low H_2O at near surface levels would suppress further isothermal crystallisation forming microlites. Swanson (1977) measured nucleation and growth rates for common rhyolite liquidus phases (quartz and feldspar) in water undersaturated granitic melts at high pressure which suggested that larger undercoolings in dome/flow magma would result in more nucleation sites than in the intrusion (conduit). The abundance of microlites imparting a flow banded texture in the Inyo dome indicates that nucleation occurred immediately prior to the extrusion of the dome magma, within the upper conduit.

The vapour pressure throughout the dome bled off to near atmospheric pressure before bubble collapse began. The degassed foam then collapsed during extrusion. The pumiceous carapace did not undergo collapse because of rapid cooling and a load pressure of less than two bars. The interior

of the dome collapsed during extrusion to form obsidian. Hence collapse of the stiff inflated foam during flow, would give a net viscosity increase of four orders of magnitude between the chamber and the surface.

4.4.1. Supportive physical evidence for the degassing deflated foam emplacement model based on Obsidian dome.

The degassing model and collapse of a foam to form obsidian is a scenario for the emplacement of rhyolitic lavas that is the reverse of the traditional view: that the flow pumice is foamy lava (Eichelberger, 1989); and that the magmatic source is stratified as a dry magma with a wet top and sides (Friedman, 1989).

The following evidence provides the supportive basis for the degassing and emplacement model of Eichelberger et al. (1986) and Westrich et.al. (1988).

Firstly the presence of vesiculated glass at about 600 m depth in the conduit with bubble contents attaining 60% and volatile contents of approximately 1.15% on fresh unaltered glass suggest: the presence of a volatile-rich magma; the inflation of the magma during ascent; and the lower water content compared to that of the chamber.

According to Eichelberger et al.(1988), deflation of the foam could only occur with the presence of a permeable pyroclastic funnel. Such a funnel is present under Obsidian dome (Vogel et al. 1985). Existence of a vent funnel is also evident by an increase of accidental lithics toward the top of the pre-dome plinian sequence (Miller oral comm. 1989).

Secondly, the deflation of the emplacing foam at the surface is supported by the following lines of evidence:

a. decrease in H_2O content of glasses from the vent area hole RDO 2B to the distal flow (hole RDO 2A);
b. the lack of obsidian around the vent area in contrast to the flow margin (Swanson et al. 1989);
c. the decline of bubble content with increasing depth into the flow.

In addition, Westrich and Eichelberger (1989) conducted some experiments vesiculating samples of glass at 900°C for 30 minutes after which they were heated at 900°C for two days at 0.1, 0.2, 0.4 and 1 MPa presssures. The results indicated that bubbles in a magmatic foam could be completely resorbed at pressures as low as 0.4 MPa. Resorption is incomplete at lower pressures. Thus these tests (according to Westrich and Eichelberger) demonstrate that a permeable magmatic foam can collapse to a dense obsidian without preservation of relict vitroclastic textures found in welded tuffs.

4.4.2. Objections to the degassing - deflated foam model.

Objections to the degassing and deflated foam emplacement model have arisen from Friedman (1989), and, on physical grounds (particularly associated with the emplacing lava) from Fink, Manley and Ondrusek (oral comm. 1989).

Friedman's (1989) major objections are concerned with the mechanism of degassing, the explanation for vesicularity in flows and domes, and the formation of obsidian. His contentions are:

a. that the magma body was dry (0.3% H_2O) but that a water-rich selvedge developed in the magma chamber at the margins from water uptake from the environment;
b. that kneading of water-rich and water-poor magma accounts for obvious zoning of vesicularity in flows and domes, as well as chemical heterogeneity of the magmas (rhyolite and dacite);
c. that a lack of evidence exists for the rewelding of the foam to form obsidian.

The above three contentions were all effectively countered by Eichelberger (1989). Firstly, biotite and hornblende crystals in the Inyo magmas would not be stable in a magma with 0.3% water. Secondly, excess water cannot be generated over lithostatic internal vapour growth necessary for bubble growth. Friedman's explanation is not supported by bulk water contents (Westrich et al. 1988) intrusion derived H_2O, or the isotope data of Taylor et al.(1983). Thirdly, the lack of physical evidence in the obsidian layer for the rewelding of the former foam is beyond the ability of the petrographer as complete resorption occurs.

Fink, Manley and Ondrusek's objections are based primarily on textural evidence from detailed fabric studies of both drill holes carapace and flow front exposures. Their evidence points to the collapse of the foam in the conduit and effervescence during emplacement to account for layers like the coarsely vesicular pumice (CVP). Westrich does not consider the upper 10 m comprising the flow carapace (Westrich oral comm. 1989). However, within the carapace textures, evidence of void elongation in the direction of flow, and effervescence from sudden overburden removal during overturning of the upper flow stratigraphy (Manley pers comm. 1989) runs counter to the deflation of the foam during flow. The basis of Eichelberger and Westrich's observations and theoretical model is derived from only two holes. The CVP is not taken into consideration, and mentioned only briefly associated with one of the figures in Eichelberger et al. (1986). In addition, the porous flow model of Eichelberger (1986) is based on the permeability of nitrogen gas through pumice. The inferred permeability of gas through interconnecting bubbles has not been directly measured for magmatic materials although Whitham and Sparks (1986) inferred high permeability of pumice in water. In a magmatic foam, the permeability of gas through interconnecting voids would in part be a function of the viscosity of the void walls not taken into account by Eichelberger (1986) in his porous flow model.

Unlike the statements of Eichelberger et al. (1986) and Swanson et al.(1989) that no obsidian layer (upper OBS) occurs near the vent, Fig.1 of Manley and Fink (1987) show a column representing RDO 2B with an upper obsidian layer present. However, a lack of OBS (above the CVP) at the drill hole site occurs. The rigid surface plug (equivalent to the thickness of the FVP) is less than half the thickness of the plug at the distal RDO 2A hole site. According to Manley and Fink, these thickness variations may reflect the proximity of the core to the vent area where locally high heat flux could have acted to decrease the lavas yield strength, thus minimising the thickness of the upper OBS layer.

4.4.3. Summary: Some modifications for the model.

In contrast to the traditional stratified chamber model, the degassing model of Eichelberger et al. (1986) and Westrich et al. (1988), although based on limited core-hole sections, best explains the physical changes accompanying decompression of a hydrous rhyolitic melt. However, textural interpretations of the flow stratigraphy, particularly in the carapace zone, point to modifications in the scenario of Westrich and Eichelberger - namely collapse in the conduit and elongation of voids during flow.

Several pertinent questions can be posed. Firstly, can void aspect ratio profiles distinguish between deflating of the magmatic foam at the surface during flow or in the upper conduit? Secondly, would collapse during flow, or in the upper conduit be decipherable given that post- and syn-emplacement effervescence by either model would obscure textural evidence and clear definition between each scenario?

If the outer layer according to Eichelberger et al.(1986) did not collapse because of rapid cooling, and a load pressure of less than 2 bar, then the FVP layer should have low aspect ratio voids and a more limited range of void populations. Westrich and Eichelberger have not looked at textural variations, aspect ratios, void size and shape variations or void populations suggesting stages of effervescence. Their main line of evidence is purely textural - the vent area is more vesicular than the distal flow core.

Void aspect ratio studies should help support the expanding foam scenario from examination of conduit samples within the South Inyo Crater. Conduit geometry between both the South Inyo Crater and Obsidian dome conduits should be different as the former magma fragmented but did not reach the surface and the latter formed a dome. Differences in the behaviour of the magma is probably more a function of conduit geometry, permeability of country rock rather than H_2O content. The approximate 33% porosity of South Inyo Crater samples assuming equilibrium between vapour pressure and lithostatic load, and an overburden density of 2.5 g/cm^3 should give a water content of 2.2% (Eichelberger et al. 1988). This is higher than the H_2O content determined for Obsidian dome of 1.15% in the conduit at a comparable level. Further implications for degassing are discussed in chapters 8 and 9.

Void aspect ratio profiling through the scattered Ben Lomond outcrops support the modification of Eichelberger and Westrich's model that collapse occurs within the conduit and re-effervescence during flow.

4.5. Ben Lomond Degassing History and Implications for the Rheology of the Magma.

As no drillhole data and feeder conduit samples are available for Ben Lomond, information on subsurface degassing processes and the rheology of the ascending magma is fragmentary. The degassing model of Eichelberger et al. (1986) and Westrich et al. (1988) takes into account the physical changes in the magma between chamber and surface and is thus the best current model which explains the paradox posed by dry massive obsidian lavas and petrologic evidence for their high pre-eruptive water contents. Therefore the subsurface degassing history of the Ben Lomond magma is here initially interpreted using the model of Westrich et al. (1988) (Table 4.1).

Table 4.1. Subsurface degassing history of the Ben Lomond magma. Subsurface evidence (*) points to the degassing of an originally hydrous magma and collapse of an inflated foam just prior to emplacement.

Location	Depth	Microlite shape	ΔT	Min	T_C	H_2O%	Porosity	Comments
Upper conduit	<500m					0.14–.2	FVP 35% Obsid 0.2%	Foam collapse/ effervescence
Conduit	500m	Elongate rods Tabular	≥150° ≤50°			≈1.15%	60% + (e.g. s50)	Foam inflation rising water–saturated liquidus
Chamber	>6000			Bt Rare pl	780°	>4.0		

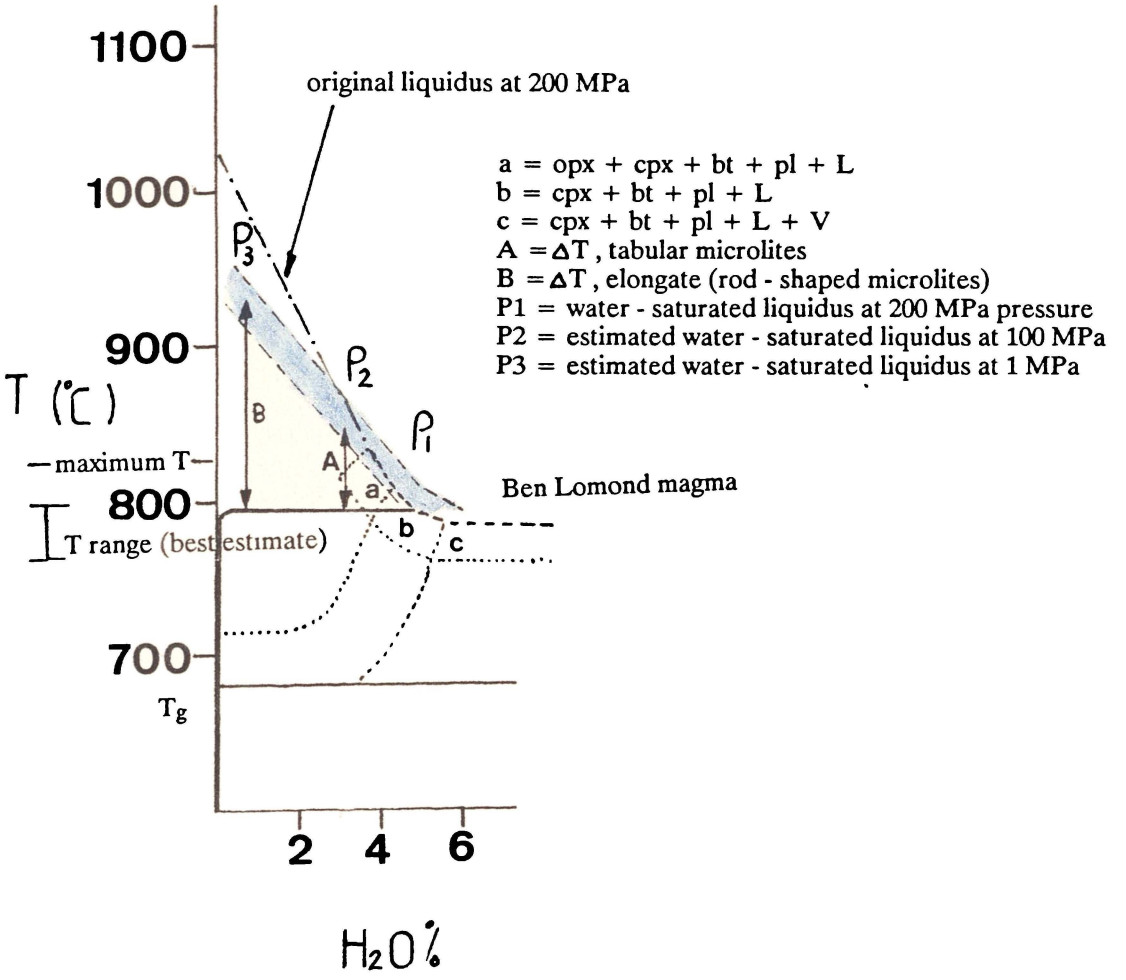

Fig. 4.3. Estimated decompression paths for the Ben Lomond magma. The range of inferred magma-lava temperature is from Fig. 4.1. The water saturated liquidus at pressure P3 has not been measured for Obsidian dome or Ben Lomond. However, the shaded region (rising water-saturated liquidus) has been adjusted from Fig. 4.2 and is a best estimate. The degree of undercooling (refer A and B) has an approximate error of ± 50° Lofgren pers. comm. (1989).

The initial magmatic water content for Ben Lomond lava is unknown but a value of 4.5 ± 0.8 wt% has been determined from melt inclusions in phenocrysts from the Taupo ultraplinian event (Hervig et al. 1988). This compares favourably to the estimates based on thermodynamic calculations of P H2O and f H20 by Ewart et al. (1975) to infer minimum conditions near water saturation of 5% for cummingtonite phenocrysts (for lavas of the Okataina Volcanic Centre) at estimated temperatures of crystallisation. The thermodynamic approach would be the simplest and most generally applicable if not for the present lack of reliable experimental and thermodynamic data for micas and amphiboles (Clemens, 1984).

The difference in morphology of the two microlite populations point to a rising water saturated liquidus and increased undercooling with decreasing water content and confining pressure, thus suppressing further crystallisation and yielding a glassy rhyolite lava (Fig. 4.3).

Evidence of the original vesiculation of the foam is lacking owing to the unavailability of conduit samples. Circumstantial evidence for the existance of such a foam may come from the epiclastic breccia at s50 that consists of vesicular to dense glassy clasts of porosities between more than 50% and 0%. The s50 breccia is crystal-rich with respect to the aphyric Ben Lomond lava, and thus represents a fragmental deposit of a different batch of magma from a different vent. The morphology of the low aspect ratio voids at s50 is similar to those of the main breccia zone adjacent to the conduit at a drillhole slant depth of 643 m, and the ejecta from the South Inyo Crater (Eichelberger et al. 1988). The main difference is that the ratio of void diameter to intervoid distance is larger for the clasts at s50, suggesting near surface void expansion and fragmentation from shallow steam explosions. The lack of any other exposures of this deposit prevents more definitive interpretation.

The physical data, particularly void aspect ratio (Rv) values from Ben Lomond supports collapse of a foam within the upper conduit and re-effervescence during flow. Supportive evidence is from at least 3 - 4 populations of voids in the carapace FVP and highly elongated and tapered shapes. Those primary voids of highest aspect ratio within the glassy lineations of the dense FVP layer (s7) and the uppermost OBS layer (s14, s44) are interpreted as representing early-formed and collapsed vesicles. Collapse occurred as the exterior of the foam was deformed by flow within the upper part of the conduit. Effervescence of the FVP occurred also within the upper conduit on collapse of the foam and also during early flow phase. Voids were able to be preserved as the vapour pressure exceeded the ambient pressure from the surrounding carapace during increasing viscosity on cooling. The OBS unit formed from collapse of the foam where the overburden pressures exceeded the vapour pressure of the voids causing either disappearance of the voids to beyond the detection of the petrographer, or highly compressed lineations (Rv ≥ 60) where the short axis was at or beyond resolution to measure.

4.6. Ben Lomond Chemistry.

Analyses of major element oxides and trace elements by X-ray fluorescence at the analytical facility at Victoria University of Wellington on 33 samples was undertaken to provide a lateral section at site 7 across three fabric units representing a carapace section, and to compile a composite section through the Ben Lomond lava flow. From 10 analyses of fresh obsidians, variation in the OBS unit and

between proximal and distal sections can be tested and the trace element chemistry of both flow lobes can be compared. Also, this new data adds to previous analytical data on other rhyolites in the Ben Lomond region.

The major element chemistry may be used in the calculation of viscosity via the method of Shaw (1972), and the trace element chemistry, to further constrain the migration of secondary volatiles. Two ideas may be explored:

a. the aphyric OBS layer best represents the chemistry of the original magma prior to secondary boiling;

b. the difference between the OBS and RHY layer chemistry points to the partitioning of elements during isobaric crystallisation via secondary volatile migration.

Table 4.2. Major and trace element geochemistry of the Ben Lomond region rhyolites. Major elements (wt %), where t = total FeO + Fe_2O_3 expressed as Fe_2O_3, and * = original analytical values are tabulated on a volatile free basis. For the trace elements, duplicate pellets were made for each sample giving 4 measurements of trace element concentration (in ppm) per sample. Concentrations are tabulated as mean ± 2 standard errors. n.d. = not detectable. Analyses 1 - 33 are listed below with sample description, fabric unit, sample site and Waikato University number.

	1	2	3	4	5	6	7	8	9	10	11	12	13
SiO_2	75.46	77.08	77.03	76.84	77.10	77.03	77.26	76.93	76.92	76.79	76.78	77.06	76.99
TiO_2	0.20	0.18	0.18	0.17	0.18	0.19	0.18	0.17	0.18	0.18	0.18	0.18	0.18
Al_2O_3	14.32	12.47	12.52	12.78	12.49	12.74	12.44	12.59	12.53	12.58	12.82	12.51	12.47
$Fe_2O_3^t$	1.60	1.40	1.40	1.44	1.39	1.44	1.39	1.38	1.40	1.43	1.45	1.41	1.41
MnO	0.05	0.05	0.05	0.05	0.05	0.05	0.05	0.04	0.05	0.05	0.05	0.05	0.05
MgO	0.25	0.25	0.23	0.22	0.22	0.23	0.21	0.21	0.23	0.25	0.24	0.23	0.24
CaO	1.04	1.10	1.11	1.10	1.10	1.10	1.11	1.10	1.10	1.10	1.10	1.09	1.10
Na_2O	3.82	3.98	4.03	3.92	3.96	3.69	3.85	3.90	3.87	4.14	3.88	3.99	4.08
K_2O	3.29	3.46	3.45	3.46	3.49	3.52	3.49	3.65	3.66	3.46	3.48	3.46	3.46
P_2O_5	0.02	0.02	0.02	0.02	0.02	0.02	0.02	0.03	0.02	0.02	0.02	0.02	0.02
Total*	100.00	99.44	99.77	99.70	99.44	99.78	99.73	100.00	100.16	99.12	100.22	100.19	99.77
LOI*	2.37	0.22	0.29	1.61	0.32	3.12	1.41	0.22	0.22	1.46	2.92	1.92	0.34

	14	15	16	17	20	21	23	24	27	28	29	30	31	32	33
SiO_2	77.02	77.03	77.10	75.86	77.20	77.06	77.12	77.08	77.22	76.36	76.69	77.10	48.39	75.01	78.16
TiO_2	0.18	0.18	0.18	0.19	0.17	0.18	0.17	0.18	0.18	0.20	0.19	0.19	1.10	0.25	0.10
Al_2O_3	12.49	12.46	12.49	13.84	12.46	12.48	12.59	12.61	12.48	13.16	13.26	12.96	17.23	13.50	12.28
$Fe_2O_3^t$	1.36	1.37	1.39	1.52	1.38	1.40	1.38	1.37	1.31	1.59	1.52	1.34	10.34	1.83	1.11
MnO	0.05	0.05	0.04	0.04	0.04	0.04	0.03	0.03	0.04	0.03	0.04	0.02	0.17	0.05	0.04
MgO	0.24	0.24	0.30	0.29	0.28	0.30	0.21	0.19	0.29	0.15	0.26	0.22	7.44	0.46	0.18
CaO	1.10	1.11	1.13	1.08	1.11	1.12	1.09	1.08	1.13	1.09	1.00	1.07	12.61	1.57	0.68
Na_2O	4.11	4.11	4.01	3.79	3.78	3.94	3.84	3.92	3.95	3.84	3.60	3.73	2.43	3.89	3.90
K_2O	3.43	3.43	3.35	3.37	3.56	3.47	3.55	3.51	3.40	3.54	3.41	3.34	0.16	3.42	3.54
P_2O_5	0.02	0.02	0.01	0.01	0.01	0.01	0.01	0.02	0.01	0.02	0.02	0.02	0.13	0.02	n.d
Total*	99.44	100.32	99.21	99.74	99.22	99.57	99.49	99.44	99.24	99.85	99.17	99.19	99.93	99.31	99.36
LOI*	0.31	0.28	0.36	3.64	0.17	0.32	0.30	0.35	0.74	0.49	1.04	0.76	0.39	2.84	0.91

	1	2	3	4	5	6	7	8	9	10	11	12	13	14	15
Sc	4.2	3.5	4.3	3.3	3.7	4.3	4.4	4.0	3.6	3.1	3.9	3.8	3.9	3.3	4.9
V	8.2	9.9	10.0	9.7	9.5	8.8	9.0	8.0	9.0	8.6	8.6	9.1	8.5	8.8	9.0
Cr	n.d	n.d	n.d	n.d	0.1	n.d	0.2	n.d	n.d	0.2	n.d	n.d	0.2	0.6	n.d
Ni	0.6	0.7	1.0	1.5	0.7	1.0	1.2	1.7	1.5	1.2	1.9	1.5	1.8	1.1	1.4
Cu	2.4	2.9	2.3	2.2	2.9	2.4	2.9	2.9	2.9	2.3	2.2	1.6	2.8	2.1	2.6
Zn	42	36	35	36	36	36	34	36	35	35	36	36	36	36	35
Ga	14	13	12	12	12	13	13	13	12	13	13	13	11	13	12
As	2.4	3.1	3.4	2.8	2.9	3.2	2.8	3.2	3.4	3.0	2.1	3.5	2.8	2.7	2.6
Rb	113	121	122	118	123	118	121	127	126	121	117	120	123	122	122
Sr	79	83	84	81	84	81	83	85	86	85	82	83	84	85	84
Y	23	20	21	19	21	20	19	21	22	21	21	21	22	22	21
Zr	176	156	156	156	156	156	156	157	158	159	159	157	157	158	157
Nb	7.0	6.2	6.3	5.2	6.2	5.9	6.8	5.0	6.7	6.5	6.7	6.5	6.6	7.0	7.0
Ba	777	665	666	677	665	663	658	670	671	667	667	656	663	667	663
La	21	20	19	21	19	21	20	20	20	20	19	19	21	19	19
Ce	43	39	40	40	40	40	40	40	39	43	43	43	41	39	41
Pb	17	14	14	15	16	13	15	15	14	14	17	14	15	15	16
Th	14	13	13	13	14	11	14	13	12	12	13	13	12	12	13
U	3.6	3.0	3.0	3.0	3.2	3.5	3.4	3.3	3.7	3.5	3.3	2.7	3.5	2.9	3.1

	16	17	18	19	20	21	22	23	24	25	26
Sc	3.9 ± 0.9	4.2 ± 0.9	3.5 ± 0.7	4.2 ± 0.5	3.7 ± 0.3	4.0 ± 0.6	3.7± 0.5	3.5 ± 0.5	2.9 ± 0.3	3.5 ± 0.4	3.7 ± 0.5
V	7.2 ± 0.2	7.9 ± 0.7	8 ± 0.5	7.7 ± 0.5	7.8 ± 0.5	7.9 ± 0.3	7.3 ± 0.6	7.8 ± 0.7	8.5 ± 0.4	7.6 ± 0.4	7.9 ± 0.3
Cr	0.2 ± 0.4	0.3 ± 0.3	0.2 ± 0.2	0.6 ± 0.4	0.6 ± 0.3	0.2 ± 0.2	0.4 ± 0.1	0.2 ± 0.1	0.3 ± 0.2	0.1 ± 0.2	0.2 ± 0.3
Ni	n.d	0.1 ± 0.6	n.d	0.2 ± 0.6	0.7 ± 0.8	0.2 ± 0.4	n.d	0.4 ± 0.3	0.3 ± 0.5	0.5 ± 0.1	0.5 ± 0.5
Cu	3.7 ± 0.3	5.2 ± 0.5	4.0 ± 0.5	3.8 ± 0.3	4.3 ± 0.5	3.5 ± 0.3	3.3 ± 0.2	3.5 ± 0.1	3.9 ± 0.3	3.9 ± 0.1	3.7 ± 0.2
Zn	35.4 ± 0.3	49.6 ± 0.6	40.1 ± 0.3	33.0 ± 0.2	30.9 ± 0.3	35.8 ± 0.6	31.9 ± 0.6	37.4 ± 0.4	34.8 ± 0.3	35.1 ± 0.5	34.2 ± 0.2
Ga	13.2 ± 0.3	13.3 ± 0.4	12.5 ± 0.6	12.8 ± 0.3	12.1 ± 0.6	13.0 ± 0.5	12.9 ± 0.5	13.2 ± 0.4	13.5 ± 0.5	12.9 ± 0.7	12.4 ± 0.6
As	2.9 ± 0.2	2.8 ± 0.6	2.9 ± 0.8	2.7 ± 0.3	2.5 ± 0.7	3.2 ± 0.3	3.3 ± 0.2	3.2 ± 0.5	2.8 ± 0.6	3.6 ± 0.4	3.0 ± 0.3
Pb	123.3 ± 0.9	115.3 ± 0.7	117.3 ± 1.4	112.3 ± 1.0	119.5 ± 1.7	123.2 ± 0.6	118.5 ± 0.3	121.3 ± 0.7	121.3 ± 0.2	123.4 ± 1.1	120.8 ± 0.4
Sr	85.6 ± 0.3	81.2 ± 0.5	83.1 ± 1.6	84.4 ± 0.9	82.9 ± 1.6	84.7 ± 0.7	85.0 ± 0.1	85.2 ± 0.5	85.6 ± 0.4	85.0 ± 0.6	83.4 ± 0.6
Y	23.1 ± 0.3	21.7 ± 0.8	20.6 ± 1.26	22.8 ± 0.7	20.0 ± 0.6	23.3 ± 0.6	20.5 ± 0.3	20.0 ± 0.1	18.3 ± 0.6	22.6 ± 0.7	22.3 ± 0.4
Zr	156.7 ± 0.4	170.6 ± 2.4	160.0 ± 2.3	158.6 ± 1.4	161.0 ± 1.0	157.6 ± 0.8	155.6 ± 1.1	159.3 ± 0.5	157.8 ± 0.4	158.3 ± 0.9	155.1 ± 0.8
Nb	6.7 ± 1.0	6.5 ± 1.0	6.7 ± 0.6	6.4 ± 0.8	6.9 ± 0.7	6.7 ± 0.8	6.6 ± 0.9	6.4 ± 0.8	6.4 ± 0.8	6.9 ± 0.1	6.9 ± 0.1
Ba	664.0± 2.4	721.9 ± 9.6	662.2 ± 12.9	665.0 ± 7.2	672.5 ± 13.8	665.5 ± 2.1	653.6 ± 2.6	660.9 ± 9.1	662.8 ± 3.2	664.8 ± 2.0	655.9 ± 2.4
La	17.8 ± 0.3	17.9 ± 0.7	17.5 ± 1.3	18.9 ± 0.3	18.0 ± 0.5	17.9 ± 0.4	17.3 ± 0.5	16.7 ± 0.5	15.9 ± 0.2	17.6 ± 0.5	18.4 ± 0.5
Ce	40.3 ± 1.7	42.6 ± 1.0	39.8 ± 1.2	41.3 ± 1.6	40.4 ± 0.2	41.5 ± 1.3	40.1 ± 2.9	40.1 ± 1.0	36.9 ± 1.2	41.7 ± 1.2	41.3 ± 1.0
Pb	15.7 ± 0.4	15.0 ± 0.7	18.6 ± 0.5	15.3 ± 0.4	14.6 ± 1.0	14.8 ± 1.2	16.1 ± 0.5	14.1 ± 0.2	14.7 ± 0.9	15.3 ± 1.0	14.8 ± 0.9
Th	13.3 ± 0.4	13.7 ± 0.3	12.8 ± 0.8	13.1 ± 0.6	12.8 ± 0.7	13.0 ± 0.2	13.1 ± 0.7	13.1 ± 0.3	13.3 ± 0.5	12.9 ± 0.1	12.6 ± 0.6
U	3.3 ± 0.2	3.0 ± 0.4	3.0 ± 0.6	3.1 ± 0.5	2.9 ± 0.4	3.0 ± 0.2	3.0 ± 0.2	2.9 ± 0.2	3.1 ± 0.1	3.0 ± 0.4	3.3 ± 0.2

	27	28	29	30	31	32	33
Sc	3.9 ± 0.5	5.8	4.2 ± 0.4	2.7 ± 1.0	42.4 ± 0.9	4.9 ± 0.6	3.2 ± 0.3
V	7.9 ± 0.4	8.4	8.4 ± 0.7	9.5 ± 0.9	278.9 ± 0.8	10.2 ± 0.7	4.2 ± 0.4
Cr	0.3 ± 0.2	0.2	0.4 ± 0.3	0.7 ± 0.3	172.8 ± 0.5	0.2 ± 0.1	0.2 ± 0.4
Ni	0.5 ± 0.2	1.2	1.9 ± 0.2	0.4 ± 0.4	53.9 ± 1.0	0.1 ± 0.3	n.d
Cu	2.3 ± 0.4	2.8	6.2 ± 0.8	4.0 ± 0.4	63.0 ± 0.3	3.2 ± 0.2	3.4 ± 0.1
Zn	43.9 ± 0.2	28	105.7 ± 0.1	28.6 ± 0.2	102.3 ± 0.7	50.1 ± 0.4	36.0 ± 0.4
Ga	12.6 ± 0.5	14	13.0 ± 0.6	13.8 ± 0.5	17.4 ± 0.6	13.8 ± 0.4	13.3 ± 0.6
As	2.9 ± 0.5	1.8	3.8 ± 0.3	9.7 ± 0.5	0.8 ± 0.5	3.1 ± 0.4	3.7 ± 0.2
Pb	121.9 ± 0.5	124	118.8 ± 0.5	121.4 ± 0.3	4.7 ± 0.2	114.9 ± 0.8	141.1 ± 1.1
Sr	84.4 ± 0.5	101	80.1 ± 0.6	85.6 ± 0.4	347.0 ± 1.3	124.6 ± 0.3	45.3 ± 0.3
Y	22.5 ± 0.5	15	18.9 ± 0.8	18.9 ± 0.5	18.9 ± 0.6	22.9 ± 0.1	27.8 ± 0.4
Zr	158.1 ± 1.1	186	172.2 ± 2.4	169.1 ± 10.1	58.9 ± 0.7	192.9 ± 1.8	103.4 ± 0.9
Nb	6.6 ± 0.2	6.4	7.4 ± 0.9	7.1 ± 0.6	2.0 ± 0.9	7.0 ± 0.5	6.2 ± 0.6
Ba	665.7 ± 3.5	687	742.5 ± 3.6	627.8 ± 23.2	67.6 ± 2.7	706.5 ± 3.0	721.7 ± 1.7
La	17.7 ± 0.6	21	16.2 ± 0.6	17.3 ± 1.0	n.d	17.7 ± 0.5	20.8 ± 0.7
Ce	40.8 ± 0.3	41	37.6 ± 2.0	36.9 ± 0.7	20.9 ± 1.7	40.7 ± 1.3	47.9 ± 1.2
Pb	15.5 ± 0.8	16	16.5 ± 0.6	13.9 ± 0.6	2.3 ± 0.8	15.5 ± 0.7	16.5 ± 0.7
Th	13.5 ± 0.5	13	13.6 ± 0.4	13.1 ± 0.5	1.9 ± 0.5	12.4 ± 0.2	15.0 ± 0.6
U	3.2 ± 0.3	2.5	2.9 ± 0.3	3.2 ± 0.3	n.d	2.9 ± 0.1	3.8 ± 0.6

1 unconsolidated pumice (FVP) s7, (WT.26800)
2 obsidian plate (FVP) s7, (WT.26801)
3 obsidian plate (FVP) s7, (WT.26802)
4 dense pumice (FVP) s7, (WT.26803)
5 vesiculated obsidian clast (FVP) s7, (WT.26804)
6 pumice clast (EXPL BR) s7, (WT.26805)
7 brown perlitic margin (EXPL BR/OBS contact) s7, (WT.26806)
8 spherulitic black obsidian (OBS) s7, (WT.26807)
9 (duplicate of 8) (WT.26808)
10 brown perlitic margin (OBS/EXPL BR contact)s7, (WT.26809)
11 pumice (EXPL BR) s7, (WT.26810)
12 grey perlitic obsidian clast. (EXPL BR) s7, (WT.26811)
13 foliated black spherulitic obsidian (OBS) s7, (WT.26812)
14 grey foliated obsidian (OBS) s11, (WT.26813)
15 duplicate of 14 (WT.26814)
16 grey foliated obsidian (OBS) s3, (WT.26815)
17 pumice (EXPL BR) s3, (WT.26816)
18 spherulitic rhyolite (TZ) s1, (WT.26817)
19 brown glass (TZ) s1s, (WT.26818)
20 flow banded rhyolite (RHY) sls, (WT.26819
21 black obsidian (OBS) s6(.14), (WT.26820)
22 spherulitic obsidian (TZ) s6(.9), (WT.26821)
23 brown flow banded rhyolite (RHY) s6(.1), (WT.26822)
24 brown flow banded rhyolite (RHY) s16, (WT.26823)
25 black obsidian (OBS), southern flow s64b, (WT.26824)
26 brown perlite (duplicate of analysis 7) (WT.26825)
27 TO standard (Auckland University), (WT.26826)
28 pink spherulitic rhyolite, Marotiri dome s24, (WT.26827)
29 pale brown pumice, Holyoake Stn. rhyolite s15, (WT.26828)
30 pink flow banded lithophysal rhyolite, Holyoake Stn. rhyolite s2, (WT.26829)
31 vesiculated basalt, K-Trig Basalt, s29 (WT.26830)
32 orange pumiceous autobrecciated glass rhyolite, s28 (WT.26831)
33 obsidian clast epiclastic breccia, s50 (WT.26832)

4.6.1. Major element variations

Major element oxide data for the Ben Lomond flow and other rhyolites are listed in Table 4.2 recalculated on a volatile free basis. Real intrafabric variation occurs when variation exceeds that from duplicate determinations from two obsidians and one perlite fabric.

Fig. 4.4 illustrates the SiO_2, Al_2O_3, Na_2O and K_2O profiles compiled from a composite section comprising the roadcut, airstrip and scarp sections. Owing to difficulties in XRF bead preparation, major elements could not be reported for transition zone (TZ) fabrics.

The SiO_2 profile, shown in Fig. 4.4, is uniform for OBS and RHY fabrics. A depleted value occurs in the unconsolidated pumice within the uppermost part of the FVP layer, and the explosion breccia pod. However, the SiO_2 value for the less porous explosion breccia of the roadcut section is similar to that of the obsidian.

The Al_2O_3 profile appears to be the reverse of the SiO_2 profile in that the breccia pod exceeds the value for the explosion breccia at the roadcut section. In addition the weight percentage of Al_2O_3 is slightly greater in the RHY layer compared to the OBS layer. The slight difference in chemistry may occur during isobaric crystallisation when Al_2O_3 was preferentially incorporated into groundmass feldspar - quartz crystals - the former containing more Al_2O_3 than the original glass (cf. Smith, 1974).

The Na_2O profile shows a depletion of $\sim$ 0.2% between the RHY and OBS units, a depletion of $\sim$ 0.3% at the s3 breccia pod, and a variable amount of Na_2O within the breccia pipe at s7. The slight depletion in the RHY layer and s3 pod may reflect the mobility of dilute sodic secondary vapour-phase fluids and will be examined further in section 4.6.2.

The K_2O profile shows a small peak at within the upper OBS of the roadcut section and within the RHY layer. The former site contains approximately 20 % spherulites consisting of K-feldspar and quartz (cf. Carmichael, 1982).

The uniformity of the major element profiles particularly within the OBS layer attests to the tapping of one magma and emplacement of the flow en-masse, in contrast with the wide chemical variations owing to co-mingling of two magmas that formed some of the Inyo flows, northern California (Sampson and Cameron, 1987; Vogel et al. 1987).

4.6.2. Trace element variations.

For each sample, duplicate beads were prepared to give four sets of analyses, whereby a mean and 2 standard errors ($2s / n^{0.5}$ or 95% confidence interval) could be plotted. Hence in order to reliably detect interfabric and intrafabric variability, variations must exceed 2 standard errors. Variations within the machine detection limits of 5 ppm (eg. U, As, Cr, Ni, Cu, Sc) are ignored.

Trace element profiles are plotted in Fig. 4.5.

A depletion at the breccia pod of 4 and 7 ppm occurs for Sr and Rb respectively (3.7 and 6.9% with respect to OBS layer). The depletion zone also coincides with the TZ layer for Rb. Variations are subtle

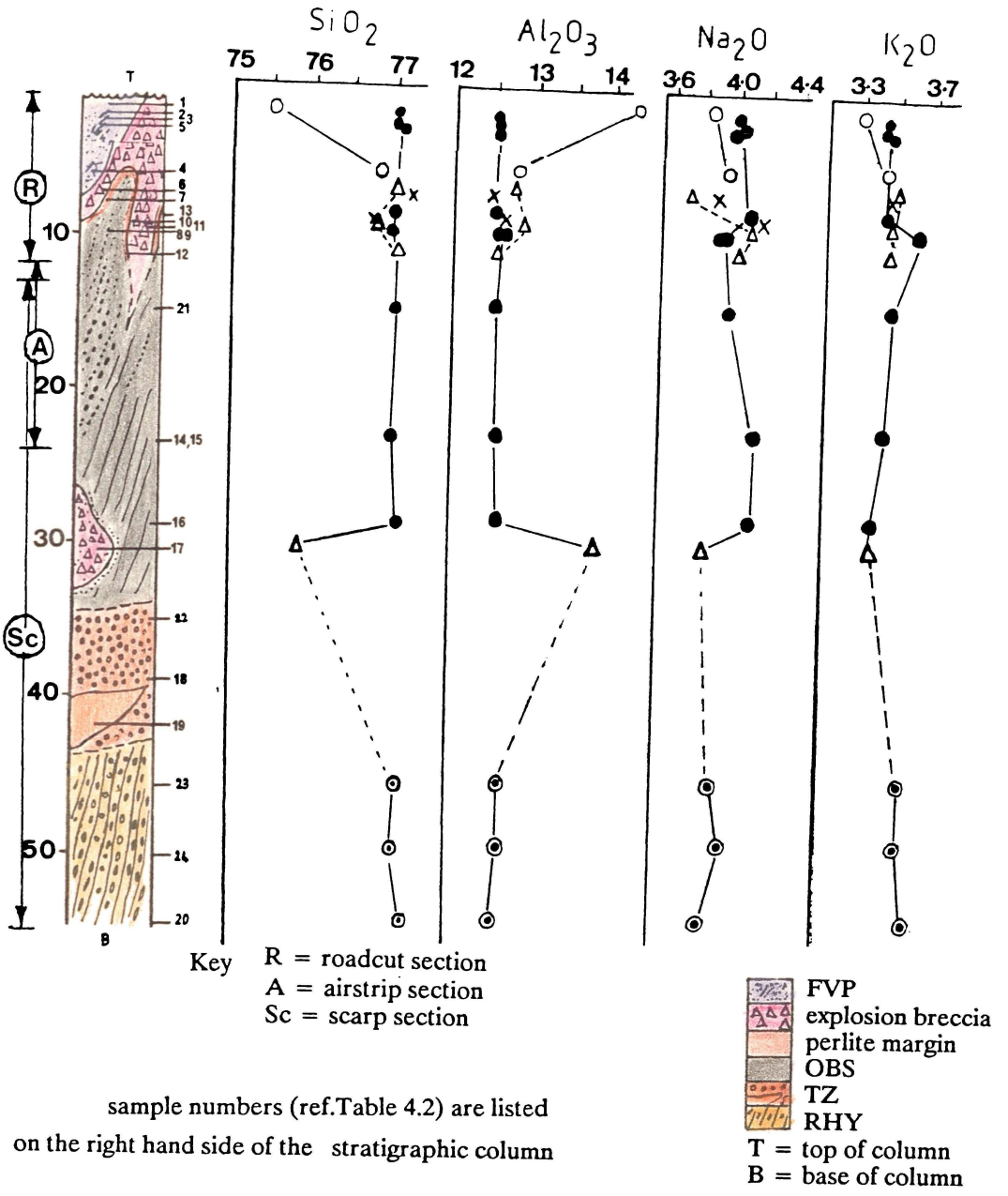

Fig. 4.4. Major element oxide variations (wt %) within the Ben Lomond flow. Oxides are plotted on a volatile free basis.

and inconclusive within the Y profile, whereas, for the RHY layer intrafabric variation of ~ 2 ppm exceeds interfabric variation of ~ 1 ppm. La and Ce both gradually decrease down profile. The Zn profile is typified by wide intrafabric variation (~ 7 ppm) below the s3 breccia pod in the TZ and RHY layer, and pronounced enrichment in the breccia pod, not mimicked by the explosion breccia of the roadcut. Trends within the Zr profile show a peak of ~ 12 ppm or an 8.5% enrichment in the pod with respect to the OBS layer. For Ba, a peak in the s3 breccia pod and the unconsolidated FVP is the only distinguishing feature. For Pb, a peak of 3 ppm (21.6% with respect to the OBS layer) in the spherulitic TZ layer exceeds intrasample or intrafabric variation of 0.5 - 1 ppm. Thus the uniformity of the trace element chemistry of the OBS layer is the best representation of the eruption chemistry of the lava.

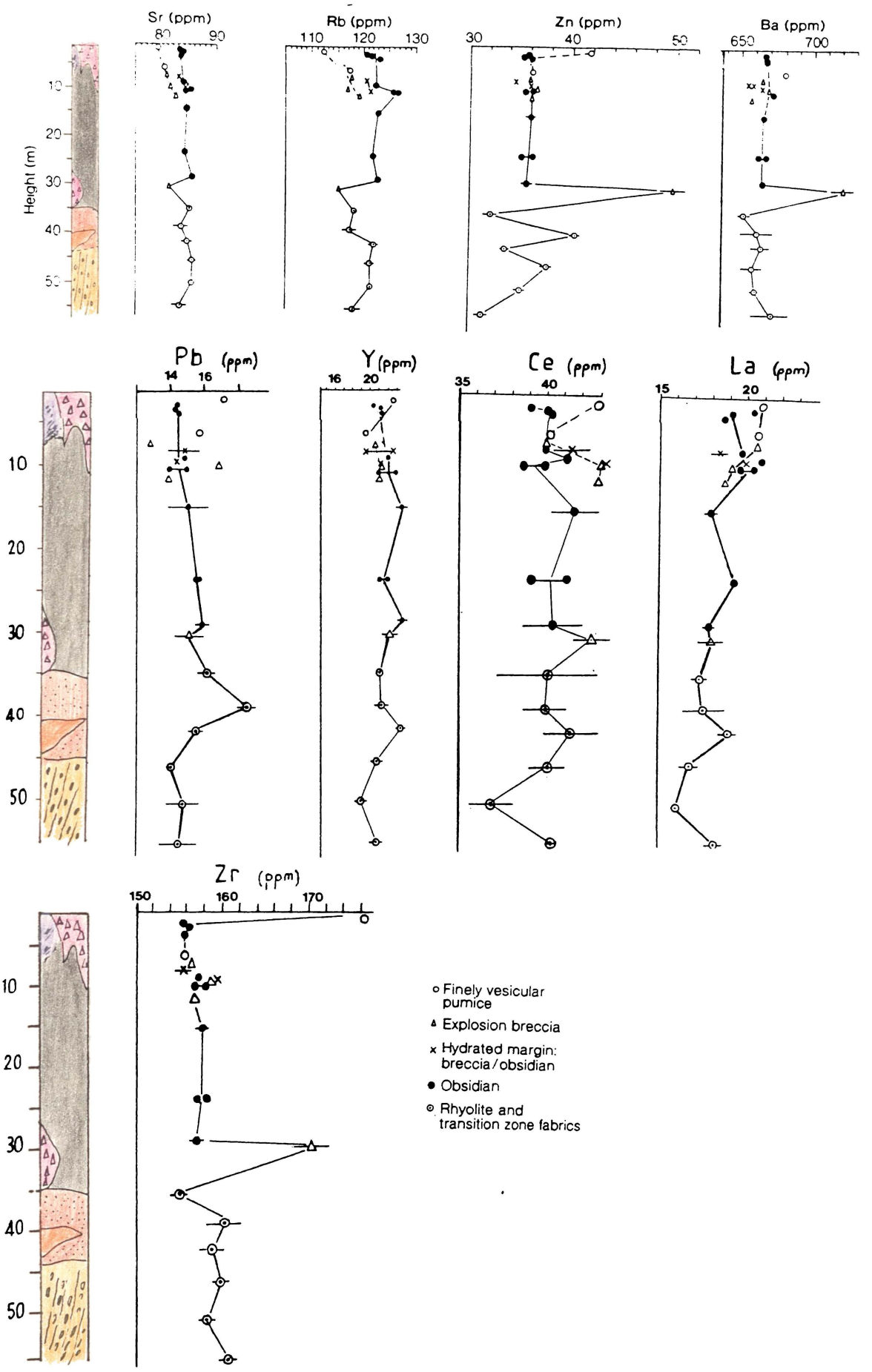

Fig. 4.5. Trace element variations within the Ben Lomond flow. Error bars represent 2 standard errors or the 95 % confidence interval of the mean of 4 measurements of trace element concentration per sample.

Trace element concentrations are identical between both proximal and distal sections, and also when the obsidians of both flows are compared. Hence effusion of the lava forming both flow lobes must have come from the same vent, or that both lobes emplaced at the same time.

Down-profile variations in Na_2O, Sr, Rb, Zn, Ba, and Zr appear to coincide with zones of secondary fabric (i.e. RHY, TZ, and explosion breccia layers) and are also correlative with variations in water content. An interpretation for the variations in trace element chemistry is as follows. Once isobaric crystallisation of the metastable glass began, secondary vapour-phase fluids migrated in a front, out of the thermally insulated central parts of the flow. Spherulites were able to nucleate and crystallise around rare phenocrysts or microlites within the volatile rich zone. But on formation of the K feldspar and quartz comprising the spherulite needles, volatiles were excluded, thus collecting into pockets at approximately 35 m below the flow surface. Vesicles inflated under 8 bar confining pressures, forming a stiff foam being 4 - 5 times more volatile rich than the surrounding lava. From the Inyo study other volatile phases present included 500 ppm Cl and 500 ppm F (Westrich et al. 1988), and 0.2 ppm CO_2 (Newman et al. 1988) from Mono lavas.

Table 4.3. Cl analyses, Ben Lomond.

sample	location	unit	H_2O^+ (%)	LOI (%)	[Cl] (ppm)
BL#1 (4)	s7	FVP	0.4	1.61	890
BL#2 (7)	s3	EXPL.BR	0.5	3.64	860
BL#2 (11)	s6	OBS	0.1	0.32	900
BL#2 (10)	s1	RHY	< 0.1	0.17	520

BL#1(4) analysis 4, Table 4.2; BL#2(7) analysis 17; BL#2(11), analysis 21; BL#2(10) analysis 20. H_2O^+ is estimated from LOI (500 - 1000°C). LOI values determined at the analytical facility Victoria University of Wellington. Cl analyses were performed by Dr Steve Weaver, Geology Department, University of Canterbury, and have an accuracy of ± 30 ppm.

For a comparable calc-alkaline system such as Ben Lomond, halogens were present within the vapour phase of the lava during emplacement (Table 4.3). From Fig. 3.8, secondary textures formed late in the emplacement history at high undercoolings of between 200 - 400°C (Swanson, 1985), below the glass transition temperature ~ 670°C (Navrotsky, 1981). Therefore volatile migration at inferred temperatures of 700 - 500°C was via diffusion and crack decompression. At the cessation of flow, secondary volatiles were explosively released, forming inverted cone-shaped deposits as explosion pits.

Fig. 4.5 may be interpreted as follows:

a. localised depletions occur in response to migration of hot fluids through the cooling upper OBS layer and brittle FVP carapace;
b. localised enrichment (e.g. in the breccia pod) occurs from upward migration of volatiles within the central units of the flow.

Very little geochemical data exists on the vapour phase mobility (e.g. diffusion) of trace elements at high temperatures.

Assuming that H_2O behaves as a bipolar fluid at temperatures of 700 - 500°C (the temperature estimated for post flow cessation and cooling from Figs. 3.8 and 4.3), the solubility of fluoride and chloride salts in hot water may approximate the actual mobility of the trace elements as displayed in Fig 4.5. The solubilities of RbCl and $SrCl_2$ are comparable, exceeding that of RbF, $SrCl_2.6H_2O$ and SrF and thus may be likely agents of transport for Rb and Sr which exhibit similar depletion proportions in the explosion breccia. Both $YCl_3.6H_2O$ and the less soluble YCl_3 have low solubilities in contrast to RbCl. Y shows more subtle interfabric variations. Down profile variations within the RHY and TZ layers of the Zn profile may occur in response to the high solubility of $ZnCl_2$ accounting for the maximum enrichment of Zn within the explosion breccia pod at s3.

However, the coefficient of D_{R-O} and D_{E-O} which represent the partitioning of an element between RHY/OBS and explosion breccia/OBS respectively, when plotted against solubility (Fig. 4.6), is somewhat inconclusive and may suggest that at temperatures above the critical point of H_2O, that transport of trace elements may occur as complex ions (Hodder oral comm. 1989).

A cautionary note in interpretation of down-profile trace element variability, is the separation of effects of low-temperature groundwater metasomatism, and high-temperature secondary volatile migration discussed above. Enrichments, with respect to the OBS layer, are greatest for the high-porosity unconsolidated pumice of the FVP (analysis 1, Table 4.2). The magnitude of these enrichments is as

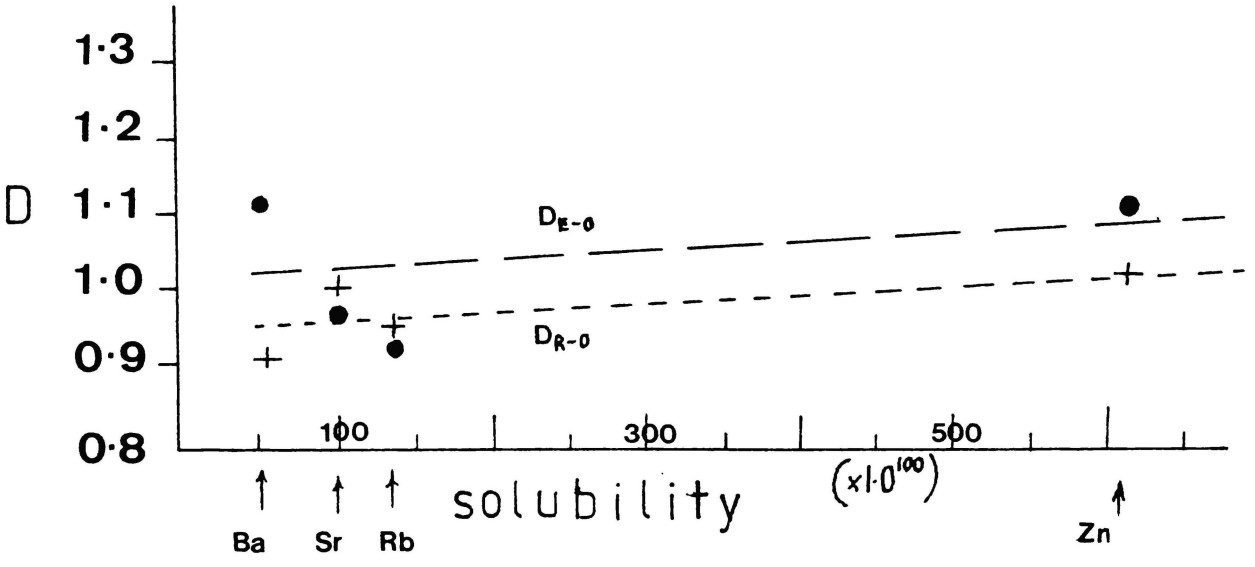

+ D_{R-O} = $x_{i(RHY)} / x_{i(OBS)}$

● D_{E-O} = x_i explosion breccia / x_i(OBS),

where x = concentration of trace element i.

Fig. 4.6. Depletion / enrichment coefficients D_{R-O} and D_{E-O} versus the solubility of trace element chlorides for Ben Lomond flow.

follows: Ba, Zn, Zr, Al_2O_3 in decreasing order, and are not matched in the dense pumice (analysis 4, Table 4.2).

Similarly, enrichments within the explosion breccia pod of the scarp (porosity = 50%), are not matched with values from the explosion breccia of the roadcut (porosity = 21%). The magnitude of these enrichments declines in the following order: Zn, Al_2O_3, Zr, Ba.

For both unconsolidated pumice and explosion breccia pod samples, depletions of 2.1% and 1.6% in SiO_2 occur with respect to the OBS layer.

Metasomatic effects may arise from groundwater perculation in a slip section near a stream channel where the pumice clasts of the explosion breccia pod were sampled. However, in order to verify these trends, more chemical analyses from the clasts of the explosion breccia pod, and the FVP fabrics would need to be undertaken. For the explosion breccia of the roadcut section, two pumice and one fractured obsidian clast were analysed, and show small chemical variations that are internally consistent, and less dependent on porosity variations. Thus, trace element variations occur in response to isobaric crystallisation and are overprinted by metasomatic effects that are greatest in zones of high porosity.

4.6.3. Regional variations.

Major and trace element chemistry of four other rhyolites in the Ben Lomond region was obtained. Together with pre-existing published and unpublished chemistry for the North Taupo region, X / X and X / SiO_2 plots (Fig. 4.7), provide an insight into the nature and compositional changes of the magma chamber with time. However, the temporal control is poor in that absolute dates exist only for the Ben Lomond rhyolite, K-Trig basalt, and the young Acacia Bay rhyolite. The relative ages of other rhyolites is unknown given that lateral and basal contacts between different domes within a massif are poorly exposed, obscured, or eroded.

Intervent variation within the Whangamata vent lineation zone suggests a subtle progression in chemistry with time between the Holyoake Stn. rhyolite, Ben Lomond rhyolite and Marotiri dome. The differing phenocryst proportions and assemblages suggests the tapping of differing levels within a stratified magma chamber or tapping of discrete batches of magma from separate sources of smaller volume. Intravent variation (i.e. within Ben Lomond) is minimal and not equivalent to the Inyo case where magma mixing is evident.

The source of the aphyric Ben Lomond magma was tapped at near-liquidus temperatures. In contrast to the magma that formed the deposit at site 50, with 7.5% phenocrysts, the Ben Lomond magma is inferred to have had a shorter residence time in the magma chamber. The presence of K-Trig basalt within a rhyolitic sequence points to an immiscible uprise of hot fluid basalt from depth into a relatively cooler rhyolite chamber and final ascent along fault-controlled fractures. The scoria cone at s22 contains abundant rhyolite xenoliths that became incorporated from conduit wall crustal assimilation during ascent of the basaltic magma.

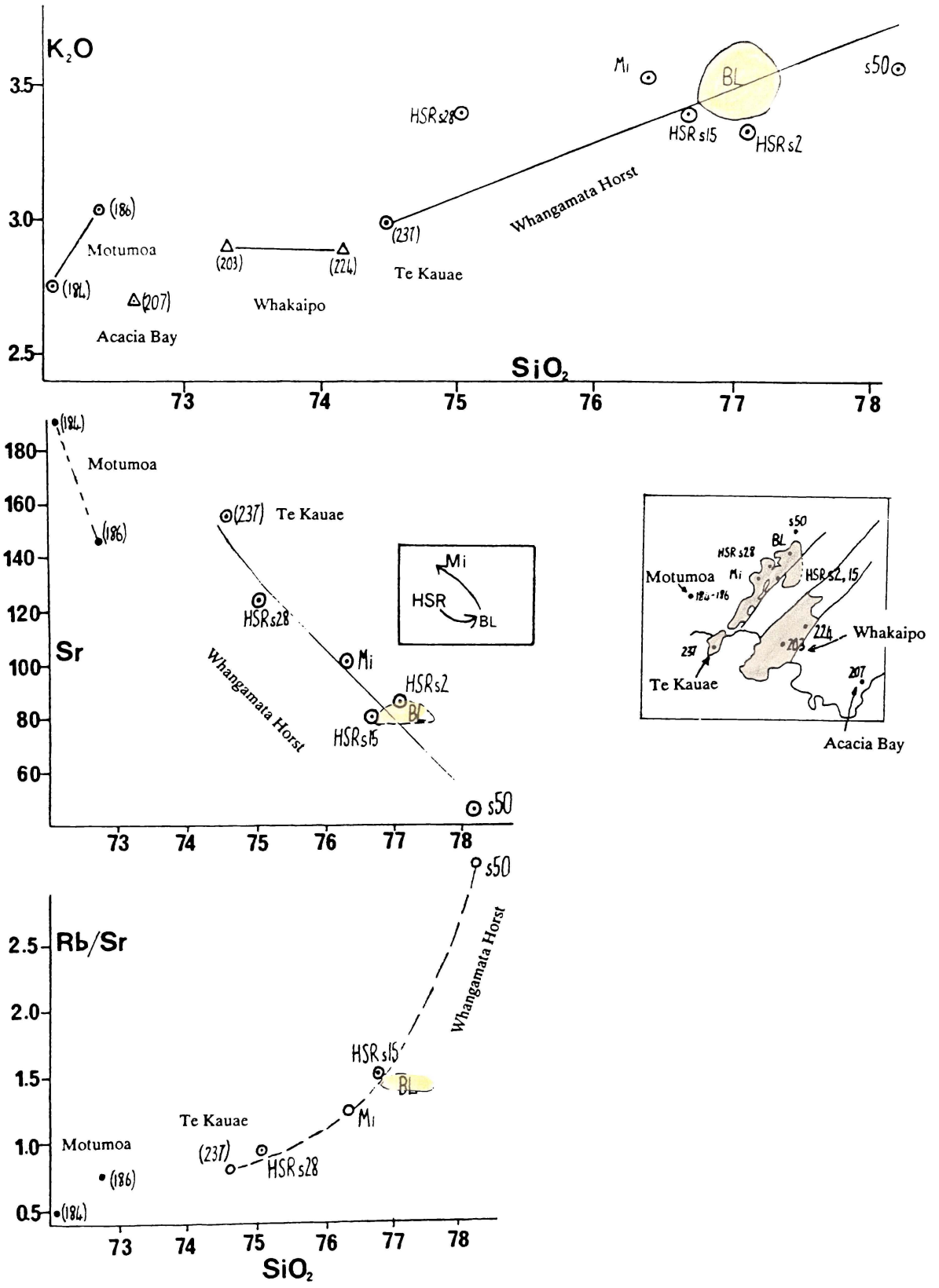

Fig. 4.7. K_2O / SiO_2, Sr / SiO_2, and (Rb/Sr) / SiO_2 plots for rhyolites of the Ben Lomond region. For the K_2O / SiO_2 plot, the trend may represent a mixing line between high- and low-silica end members. This is supported by the hyperbolic trend for the (Rb/Sr) / SiO_2 diagram. Alternatively, fractionation of plagioclase may have occurred causing a decrease in Sr with increasing silica content. Additional data is from Cole (1979).

4.7. Viscosity of Magma: a Review.

Knowledge of the viscosity of magmas is necessary for the evaluation of hazards associated with volcanic eruptions, the understanding of the evolution of magma bodies, and the behaviour of lava flows. The fundamental properties of the liquid (or melt) can be either measured directly for active basalt flows in the laboratory, or using indirect means. The rarity of closely studied rhyolite flows severely hampers knowledge of the rheological properties. Currently in New Zealand, there is no appropriate laboratory apparatus to measure the viscosity of rhyolite glass over temperature ranges of 1000 - 600°C and a $\log_{10}$ viscosity range of 7 - 14 poise (10 poise = 1 Pa.s). Thus lava flow viscosity can only be determined by indirect means.

The presence of steep flow fronts on lava flows suggest that lavas behave as non-Newtonian fluids, that is, they possess a yield strength (Hulme, 1974). Yield strength is a quantity of stress that must be exceeded prior to lava deformation (Shaw et al. 1968). Lava flows may behave as Bingham plastics or exhibit non-linear behavior as a power law fluid, termed pseudoplastic, defined in Fig. 4.8. Fluid basalt flows usually display several types of rheological activity but the high viscosity of rhyolite flows may be expected to show a more limited range of rheological behaviour (Chester et al. 1985).

Lava viscosity may be calculated using two independent approaches: one dependant on the morphology of the feature, the other on its chemical composition. Viscosity based on the morphology of arrested flows can be calculated in the following way after Johnson (1970), Hulme (1974), Wilson and Head (1983), and Zimbelman (1985) involving the estimation of Y (yield strength):

$$Y = \rho g h \sin\theta \qquad \text{(Johnson, 1970) (4.1)}$$

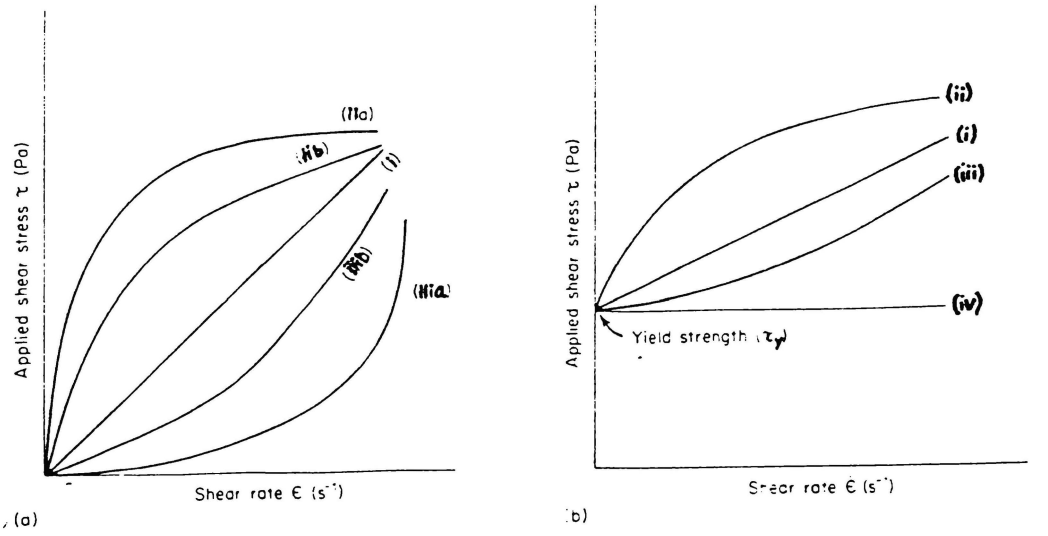

Fig. 4.8. Rheological flow curves or phenotypes.
(a) The principal flow curves of power-law liquids. (i) Newtonian fluid. (iia) Pseudoplastic fluid - ideal. (iib) Pseudoplastic fluid - real. (iiia) Dilatant fluid - ideal. (iiib) dilatant fluid - real.
(b) The principal flow curves of plastic materials. (i) Bingham plastic. (ii) General plastic. (iii) Dilatant plastic. (iv) Ideal plastic (flows with zero viscosity when yield strength has been exceeded.) τ is applied shear stress; τ_y is effective yield strength ; ε is ambient shear rate, (from Chester et al. 1985).

$Y = \rho g h^2 / R$ (Orowan, 1949; Moore et al. 1978) (4.2)

$Y = \rho g \sin^2\theta (w1 + w2)$ (Hulme, 1974) (4.3)

where ρ = density, h = flow thickness, θ = basal slope

R = radius and w1 and w2 = width of levees

Methods (4.1) and (4.2) are equally applicable for rhyolite lavas but (4.3), which includes flow levee widths is more applicable to basalt flows. Effusion rate is calculated as follows:

$F = 300 \kappa W L / h$ (Hulme and Fielder, 1977) (4.4)

where κ represents thermal diffusivity ($\sim 5 \times 10^{-7}$ m^{-2} s^{-1}).

W = flow width and L = flow length

Y and F are substituted into the following expressions for viscosity:

$\eta = w^3 Y \sin^2\theta / 24 F$ (4.5)

for basalt flows with confining leves,and

$\eta = w^{11/4} Y^{5/4} \sin^{6/4}\theta / 24 F g^{1/4} \rho^{1/4}$ (4.6)

for low aspect ratio rhyolite flows.

This method cannot be used for eroded flows owing to the compounding of error up to 25%, from the difficulty in obtaining accurate cross-sectional dimensions. It does not take into account rheological variations within the flow stratigraphy. Also, the overriding of the flow front and basal breccia is not considered (Moore et al, 1978). Even recent sophisticated models of lava flow behaviour (Dragoni et al. 1986; Dragoni, 1989) rely on a detailed knowledge of the lava flow shape and-or its change in shape with time - values which are best known for recent or observed basaltic flows. In contrast, rhyolite flows have never been scientifically observed (Manley, 1989).

The second approach incorporates the molal proportions of the major element oxides, temperature and water content in the following expression from Shaw (1972) and based in form on the method of Bottinga and Weill (1972):

$\ln \eta o = s(10^4 / T) - c_T.s + c_\eta$ (4.7)

in which $s = X_i (s^{io}. X_{SiO2}) / 1 - X_{SiO2}$ (4.8)

and ηo = viscosity of the liquid, T = temperature,

c_T and c_η are constants, and X_i = mole fraction of oxide i

Slope intercept s^{io} values derive from Arrhenius slopes from the mixing of binary silicate liquids (Shaw 1972).

One of the problems inherent in Shaw's method (as representing the viscosity of a superliquidus Newtonian fluid) is the memory effects of glass with a pre-existing annealing history (a difficulty for laboratory based direct viscometer measurements). Hence, Shaw expects that his simple correlations would not be valid because they assume a unique T / viscosity function depending only on composition. A limitation pointed out by Murase and McBirney (1973, p. 3570) is stated:

"Shaw (1972) and Bottinga and Weill (1972) attempt to relate viscosity of molten silicates to simple chemical relations by empirical linear projection of experimental data. The only way a viscosity calculated from such relations can be tested is by comparing them against measured values which are of course the original basis of the calculations. Therefore it is not surprising that their results are consistent"

Such an objection, however, may be made to all science when an empirical relationship is used as a prediction. Viscosity when measured directly (Shaw, 1969; Pinkerton and Sparks, 1978), may be compared with Shaw's basis for calculation only for basalts, as no active rhyolite lavas have been observed. Direct field based measurements for active basalt lavas are difficult and the lava is usually behaving in a non-linear manner characterisic of subliquidus fluids. Notwithstanding these difficulties, Shaw's method has been the most widely applied method to date.

Below the liquidus, the presence of bubbles and crystals will considerably increase the viscosity of the magma. The effective viscosity (ηs) for crystal-rich magmas is commonly estimated from the Einstein Roscoe equation written as either:

$$\eta s = (1 + 2.5\,\phi)\,\eta o \qquad (4.9)$$ or

$$\eta r = \eta s / \eta o = (1 - \phi)^{-2.5} \qquad (4.10)$$

where ηo = viscosity of liquid (from Shaw's method)

ηs = viscosity of suspension

ϕ = volume fraction of crystals (or suspended spheres as bubbles)

ηr = relative viscosity

When taking into account the immobilised fluid between the spheres:

$$\eta r = (1 - 1.35\,\phi)^{-2.5} \qquad (4.11)$$

As these equations were formulated for emulsions with suspended bubbles within, they may be equally applicable to void-rich foams as demonstrated by Sibree (1933):

$$\eta r = 1 / (1 - (1.2\phi)^{1/3}) \qquad (4.12)$$

On measuring the viscosity of a froth Sibree (1933) found it to be a function of the volume percentage of bubbles, increasing by up to 2 orders of magnitude to a porosity attaining 70%. Observations made during the heating of a water-rich obsidian in the laboratory indicate that the viscosity of a lava decreases during frothing, but that after the liberation of gases, the foam becomes stiff and resists further deformation. On reheating the intervoid septa collapse and flow resumes. Hence the rheological difference between a flow pumice and a bubble free obsidian arises primarily from the presence of vesicles in the pumice (Fink, 1984). With increasing porosity the bulk density of the pumice decreases while its viscosity increases (Williams and McBirney, 1979).

For crystal-rich suspensions, Murase et al. (1984) found that large differences existed between measured laboratory based values for the effective viscosities of Mt. St. Helens dacite, and values from equation (4.9) above. The discrepancies were attributable to the sizes and high concentrations of crystals, both of which exceed the range of values for which equation (9) was derived. If the viscosity of the liquid fraction, can be estimated from the composition of the glass via Shaw's method, then the effective viscosities (ηeff) of such magmas can be calculated according to the expression:

$$\log \eta_{eff} = \log \eta o + 0.019\ Dm / [(1/\phi)^{1/3} - 1) \qquad (4.13)$$

where ηo = viscosity of the original liquid (Shaw, 1972)

Dm = diameter of crystals (μm)

ϕ = the proportion of crystals

Sherman (1968) examined the effects of a wide range of crystal concentrations of different sizes and found that the relative viscosity increases with mean diameter of crystals (Dm) and concentration of crystals (ϕ) according to the relation:

$$\ln \eta o = \ln (\eta_{eff} / \eta o) = [\alpha\ Dm / (\phi_{max} / \phi)^{1/3} - 1] - 0.15 \quad (4.14)$$

where ηo = viscosity of a crystal free fluid,

α = constant that varies with mean diameter of crystal Dm (μm),

ϕ_{max} = the concentration of solids at maximum packing

ϕ = the concentration of suspended crystals.

This equation assumes that the solid fraction has no physical or chemical relation to the liquid in which it is suspended. McBirney and Murase(1984) state that ϕ or Dm do not necessarily increase on cooling as large numbers of small crystals growing from the groundmass more than offset the slight increase in phenocryst size. For phenocryst-poor rhyolites, crystallites appear first. Dm may be arrested because of the impeded diffusion by ions in fluids of high viscosities, or a lack of nucleation sites may preclude crystal growth.

For a crystal-rich pumice the viscosity may be calculated by the following procedure. For superliquidus Newtonian viscosity characteristic of water rich magma chambers, equation 4.7 may be applied. The effective viscosity of subliquidus crystal-bearing suspensions is calculated using equation 4.13 (or 4.14). After adjusting the water content to that of a lava flow pumice (e.g. 0.2%), hence altering the result of equation 4.7 and 4.13, the proportion of voids is accounted for with equation 4.12.

Equation 4.13 or 4.14 may also be used for voids as its form originated from laboratory experiments on the rheology of emulsions. However, at high rates of shear, bubbles become distorted (Spera et al. 1988). The rheological behaviour of deflating, stretching and elongating bubbles in the FVP layer, can only poorly be modeled using ϕ (equation 4.12) or ϕ and mean diameter (Dm) (equation 4.14). The three dimensional shape of the bubble is not taken into account.

The relative effects of suspended bubbles and crystals to the viscosity of the suspension are considered similar (Shaw, 1965).

Other estimates of viscosity such as surface fold analysis (Fink and Fletcher, 1978; Fink, 1980) and gravity instability between two layers of contrasting rheology from the spacing of coarsely vesicular pumice diapirs (Fink,1980; Baum et al. 1989) are of applicability only if sufficient carapace exposure is available. This is not the case for either Ben Lomond or the Mayor Island lavas. For the former method,a discrepancy between laboratory measured values (by using a viscometer within an enclosed furnace) and fold analysis viscosity of $\sim$2 orders of magnitude occurs. The latter method includes the presence of carapace heterogeneity in the form of rafted FVP and obsidian blocks. Surface fold analysis was attempted for the Waiti flow, Okataina Volcanic Centre. However, carapace exposure was inadequate for either fold analysis or gravity instability analysis for Ben Lomond or the Mayor Island flows.

Structures on lava flow carapaces constitute a type of natural laboratory where qualitative estimates of rheological deformation is observed from a variety of small scale structural observations, namely: flow banding deformation; changes in the aspect ratio of primary voids; interlayered obsidian and pumice folds; and regularly spaced intra-layer tension cracks. Simple folded flow layers of constant thickness and a wavelength to thickness ratio of less than 10, exhibit pseudoplastic power law rheology. The periodic spacing of tensile necking cracks within crystallite-rich obsidian layers is also evidence of pseudoplastic rheology (Fink, 1984). Tensile necking cracks occur if local layer-parallel strain rates exceed local tensile strengths. Also, provided that sufficient areal exposure of an uneroded carapace occurs, then the depth of tension cracks as a function of distance from the vent can be used to estimate the cooling rate of the flow surface and to infer thermal conductivity (Fink, 1984).

4.8. The Viscosity of Ben Lomond flow.

Calculation of the viscosity of the Ben Lomond rhyolite lavas may be undertaken using the chemistry of the aphyric black obsidian of the OBS layer as being most representative of the pre-emplacement composition of the liquid, employing the method of Shaw (1972) and varying the water content (and hence making adjustments to the weight percentages of the major element oxides), and temperature

for three different environments: magma chamber, conduit, and flow. For the latter case, a viscosity profile can be constructed for early and late flow situations, constrained by sufficient physical data previously outlined in chapter 3.

Firstly, for the magma chamber, the hydrous rhyolitic fluid is assumed to have a Newtonian rheology at water contents of 3% or more at temperatures of 1063 K (790°C). Calculated superliquidus viscosity is 2.4×10^7 poise. The less than 0.5% crystals and the occasional rare phenocryst does not significantly influence the effective viscosity for the virtually aphyric magma because for the small biotite and plagioclase laths. Dm is beyond the lower limit for the modified Einstein-Roscoe equation (eq. 4.14).

Secondly, for the conduit, under isothermal conditions, and an estimated water content of 1.5% the viscosity of the liquid component is 1.2×10^9 poise. During inflation of the ascending magma into a foam of approximately 60 - 70% porosity (Eichelberger et al. 1986) above a conduit depth of approximately 600 m (Eichelberger, 1988), the relative viscosity of the Ben Lomond magma is inferred to increase 2 orders of magnitude to $\sim 10^{11}$ poise.

Thirdly, for the collapsed, non-vesicular flow centre, originally entirely obsidian prior to the post-flow isobaric crystallisation, at a temperature of approximately 790°C, and a water content of 0.2%, the viscosity of the flow centre is 1.3×10^{11} Poise. The voids comprising the emplacing foam collapsed in the upper conduit with effervescence in the FVP during eruption and flow. Primary vesiculation was supressed at depths of greater than 10 m.

4.8.1. Generating a thermal profile throughout the Ben Lomond flow

Manley (1989) generated a numerical model for flow temperature and calibrated it for Obsidian Dome, Long Valley Caldera, northern California. The model was then applied to investigate the emplacement of hot large-volume rhyolite lava flows in southwestern Idaho. Boundary conditions for the model (generated from a finite difference approximation to the heat conduction equation), are set for a constant flow surface temperature of 0°C at time $t = 0$, while the basement temperature is set at half the emplacement temperature of the lava at time $t = 0$. Geometrical constraints are assumed as follows:

(a) the glass zones at the top and bottom of the flow cooled below T_g (glass transition temperature) before sufficient time had passed for crystallisation to begin;

(b) the crystalline RHY layer should be the last portion of the flow to cool through T_g;

(c) isochrons should be symmetrical around the centre of the RHY zone.

Fracturing of the upper carapace and convective movement of air preferentially cools the upper part of the flow. The textural profile nomenclature of the cooling curves of Manley (1989) was matched with the columns in Fig. 1 of Manley and Fink (1987). Unlike Obsidian dome, Bruneau - Jarbidge flow or the Banco Bonito flow, the total flow thickness of the southwestern lobe of Ben Lomond is unknown. However, the thickness can be estimated by:

$$\frac{h\ RHY}{h\ U.OBS}_{(Ben\ Lomond)} = \frac{h\ RHY}{h\ U.OBS}_{(Banco\ Bonito)} \qquad (4.15)$$

The total thickness (h) of the RHY layer (of which the upper 16m is exposed at s1, Ben Lomond) is 43 m. Thus the total thickness of the Ben Lomond southwest flow (hBL) may be expressed as:

$$hBL = hBB \times hoBL/hoBB \qquad (4.16)$$

where hBB = total flow thickness (Banco Bonito),

hoBL = thickness of upper obsidian (Ben Lomond)

hoBB = thickness of upper obsidian (Banco Bonito)

Hence hBL is ~105 m assuming that up to 10 m of the FVP comprising the carapace is removed by erosion.

Table 4.4. Parameters involved in estimating cooling time (t) for the Ben Lomond flow.

	Obsidian Dome	Ben Lomond	Bruneau Jarbidge
To	850	~ 790 (est)	~ 930
ΔT	180	120	260
h	55	105 (est)	150
t	6	?	50
To / h	15	7.5	6
ΔT / t	20	?	5.2

To = initial flow temperature; $\Delta T = To - T_g$ where T_g is the glass transition temperature
h = total flow thickness; (est) = estimated. Data for Obsidian dome and Bruneau-Jarbidge from Manley (1989).

Both the Banco Bonito and Ben Lomond flows have similar ages (140 ka and 110 ka respectively) and hence show thicker crystalline RHY zones than Obsidian dome (0.6 ka age). Data listed in Table 4.4 was used to estimate the time (t) taken for the central RHY layer of the Ben Lomond flow to cool below the estimated glass transition temperature (~670°C). When To/h and ΔT/t were plotted for Bruneau-Jarbidge and Obsidian dome data of Manley (1989), an expression:

$$To/h = 0.608\ \Delta T/t + 2.84 \qquad (4.17)$$

was derived that may be used to calculate t.

For Ben Lomond, if To/h = 7.5, then ΔT/t = 7.66, and as ΔT is estimated as 120°C, the time taken for the flow centre to cool below the glass transition temperature (t), becomes ~16 years. Fig. 4.9 illustrates the inferred temperature profile at t = 0.1, 1 = 1 yrs and t = 16 years.

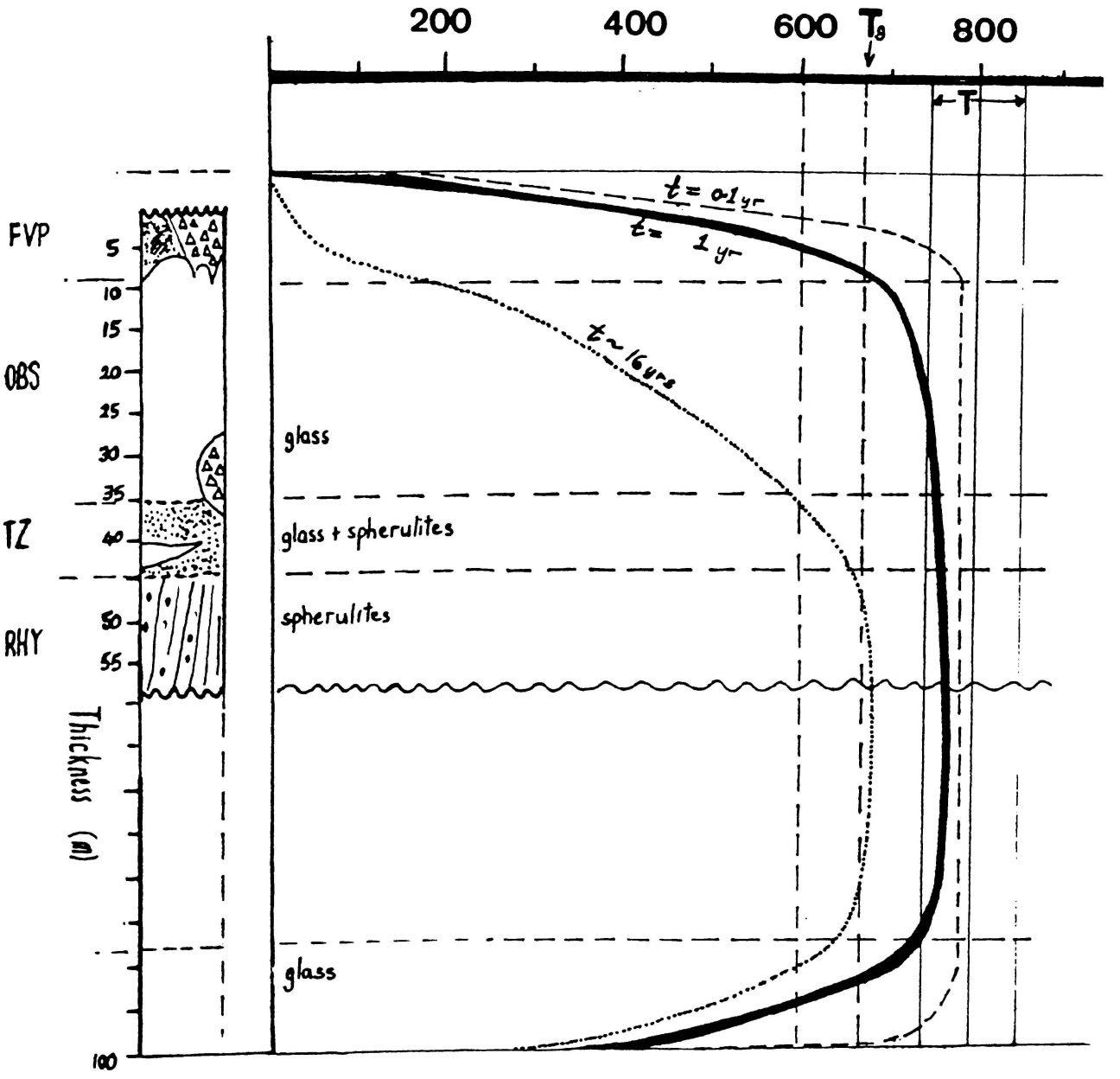

Fig. 4.9. Inferred thermal profile for the Ben Lomond flow after 0.1 yr, 1 yr, and 16 years.

4.8.2. Generating a viscosity profile for Ben Lomond flow.

Within the c.10 m thickness of the carapace comprising FVP and broken OBS clasts, a large temperature gradient between 790°C and ambient atmospheric temperature (~20°C) is inferred. The inferred viscosity of the finely vesicular pumice at a temperature of 730°C and a water content (H_2O^+ or LOI 400-1000) of 0.65% using equation 4.7 (after Shaw, 1972) and taking into account a porosity of 35% with average void diameters of 74 μm (via equation 4.12 or 4.14), the effective viscosity becomes 1.03×10^{12} poise. The viscosity of a carapace obsidian clast such as those at s7, at a subsolidus sub glass-transition temperature of 873 K after brittle fracture with a water content of 0.2% is 2.1×10^{14} poise. With this information a viscosity profile may be constructed for the early flow history of the Ben Lomond flow (Fig. 4.10a). During the middle and late flow stages, secondary isobaric crystallisation commenced in the central part of the flow. Pockets of volatile-rich areas developed above the TZ layer with water contents c.4 times greater than the 0.2% H_2O^+ typical of the remainder of the central flow. When incorporating an adjusted void diameter of 35 μm (assuming the voids on inflation were originally spheres) and a porosity of 50%, the effective viscosity of s3 pod explosion breccia is estimated as 2.9 $\times 10^{11}$ poise. In a cooling lava at 35 m depth the overlying pressure is 8 bar and with a water content 4 times greater than the overlying OBS layer and a porosity 10 times that of the OBS, gravity instability of a more viscous froth would occur. The relative viscosity of the explosion breccia pumice and the OBS layer is calculated using equation 4.12.

The viscosity of the explosion breccia increases from 1.6 to 2.7 times the viscosity of the denser OBS unit at a pressure drop of 8 to 1 bar from an increase in the specific volume of water by about six times (Friedman et al. 1963; Kennedy and Holser, 1966 in Fink, 1983). On the explosive release of volatiles via tension cracks, the primary voids would deflate and the breccia pumice fragment, forming an

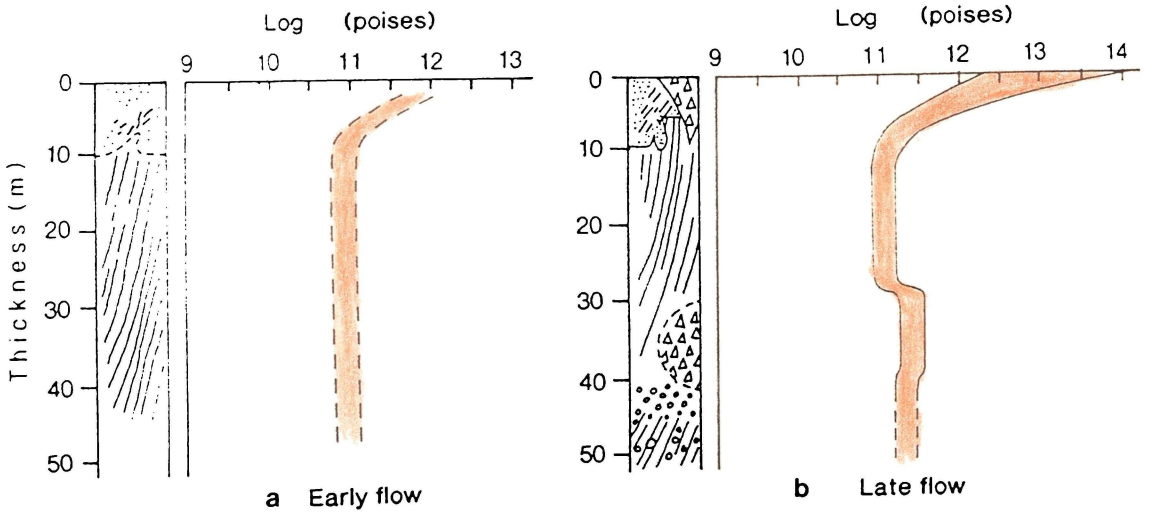

Fig. 4.10. Profiles of inferred viscosity for the Ben Lomond flow: (a) early flow; (b) late flow.

inverted cone shaped deposit like at s7. With this information a viscosity profile characteristic of the late flow history of the Ben Lomond flow may be compiled (Fig. 4.10b).

The morphological method (equations 4.1 - 4.6) may be used with much less confidence for the southwest flow of the Ben Lomond dome as:

a. the carapace (or FVP) is virtually stripped, with approximately 10 - 15m estimated missing;

b. flow fronts are not obvious;

c. as no carapace flow ridges are areally preserved, the width of the active channel is in doubt;

d. flow slope can only be measured as the average slope of the OBS/FVP contact which is coincident with the topographic surface;

e. the dome is draped by 20 ka ignimbrite.

Thus a large measurement uncertainty exists for w (flow width), L (flow length), and h (flow thickness) of at least ± 20 m, when measured from air photographs and topographic maps. Y may be calculated best from equation 4.1 as levees (in 4.3) are not preserved. Two values of Y may be estimated by substituting two different estimates of density (ρ).

Fink and Zimbelman (1986) calculated viscosity from different cross-sections down the 1983 Royal Gardens basalt flow, generating a range of estimates for Y, F and η. Such an approach to calculating F was attempted for Ben Lomond, with four measurements of w corresponding to four estimates of F from 3.94 - 8.14 m^3/s. When F is substituted into eq. 4.6, the range of η estimates (Table 4.5) is not significantly different from each other and are within a measurement error of ± 25%. The morphology

Table 4.5. Viscosity of the Ben Lomond flow based on the morphological method.

			Y1 (ρ 1)	Y2 (ρ 2)
log η 1	w 1	F 1	11.26	11.06
log η 2	w 2	F 2	11.21	11.01
log η 3	w 3	F 3	10.71	10.51
log η 4	w 4	F 4	10.10	10.90

Notes: Four different flow widths from near-vent to distal flow lobe (w1 - w4) are 1550 m, 1450 m, 750 m and 1250 m respectively. The two different densities $\rho 1$ and $\rho 2$ represent a collapsing pumiceous foam (density = 1.5 g / cm^3) and a dense obsidian respectively (density = 2.35 g / cm^3), giving two estimates of yield strength (Y) via equation (4.1). The greatest factor influencing F (effusion rate) is flow width w and hence flow cross-sectional area.

method may be applied with greater reliability for the young flows of the Okataina Volcanic Centre where both Shaw's method and the morphological method are compared.

4.9. Summary

Evidence from two microlite populations point to a rising water-saturated liquidus and an increase in undercooling of an ascending hydrous magma that emplaced as the Ben Lomond dome. The degassing model of Eichelberger et al. (1986) and Westrich et al. (1988) was critically assessed. Evidence from void aspect ratios in the finely vesicular pumice of the Ben Lomond flow point to deflation of the magma in the upper conduit and its re-effervescence during flow causing a range of void populations. Major element chemistry is fairly uniform throughout the obsidian layer and subtle interfabric variations together with trace element depletions/enrichments, varying H_2O^+ and Cl concentrations are consistent with the development of post-flow secondary fabrics in the rhyolite layer, transition zone and explosion breccia units. The viscosity of the Ben Lomond flow was calculated using major element oxides, a range of water contents and temperature estimates based on a numerical model of Manley (1989). The time for the central rhyolite layer to cool below the glass transition temperature when brittle rheological behaviour commences was estimated as ~16 years. Viscosity profiles during early and late-flow phases were generated, taking into account the primary vesicularity of the finely vesicular pumice and the anomalous vesicularity of the late-flow explosion breccias.

CHAPTER 5.

MAYOR ISLAND PANTELLERITE LAVAS - PHYSICAL VOLCANOLOGY AND EMPLACEMENT HISTORY.

5.1. Introduction.

Mayor Island is a Quaternary pantelleritic volcano rising 700 m from the sea floor from a 15 km wide base, 26 km north of Tauranga, Bay of Plenty, northeastern New Zealand. The island is 4 - 4.5 km wide, characterised by a 3 km wide breached caldera, with caldera walls up to 105 m height (Fig. 5.1). The island lies in a back arc setting of a convergent plate margin, 100 km behind the Taupo Volcanic Zone (TVZ) in a continuation of the Ngatoro Basin (Cole, 1978).

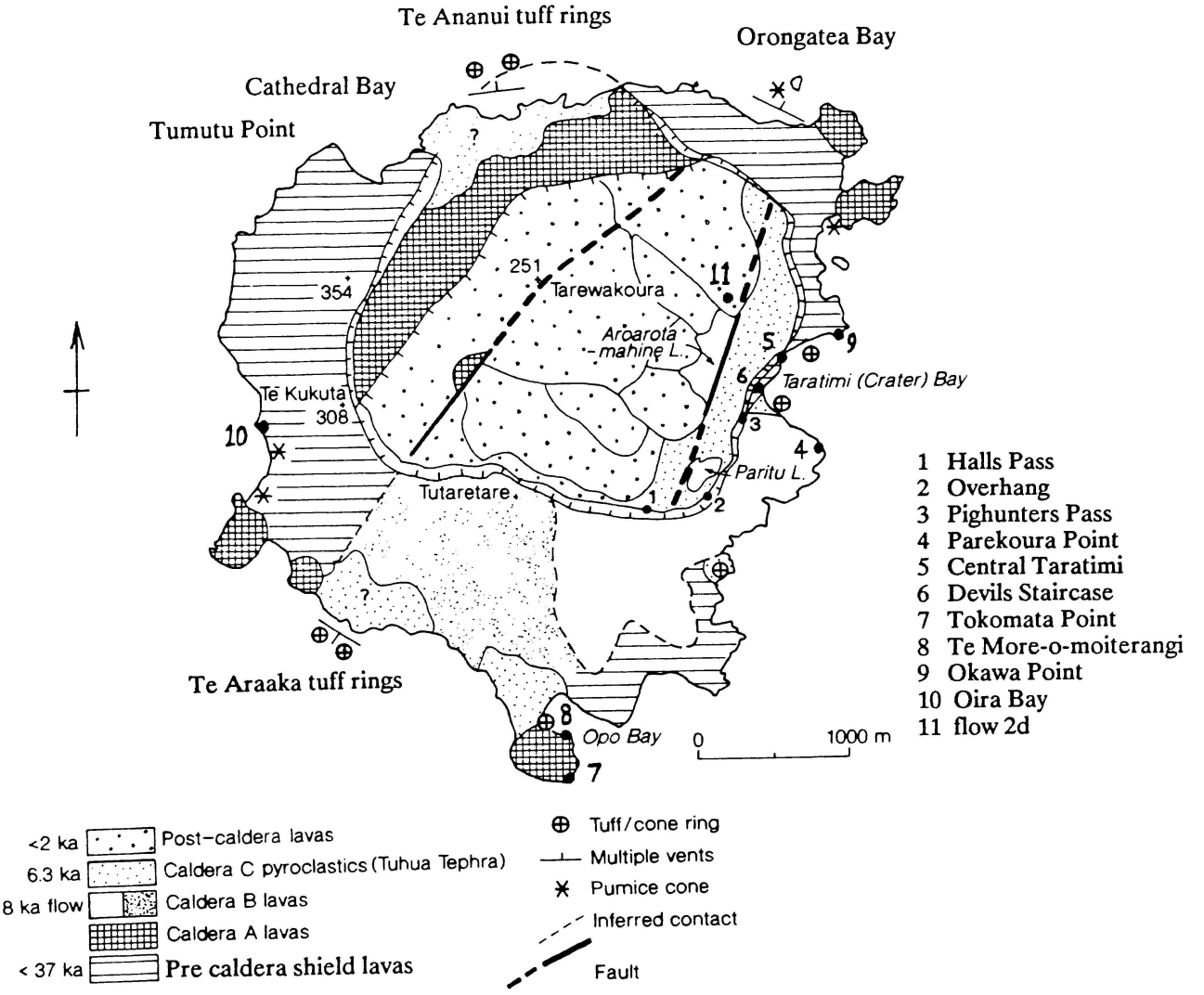

Fig. 5.1. Mayor Island geology, showing field study locations. Exposures are along the coast and around the caldera wall, and hence inland contacts are inferred as the slopes are draped with c.6.3 ka tephras. The Te Araaka and Te Ananui deposits have not been placed within the post Caldera A chronology. Map and column assembled from Houghton and Wilson (1986).

5.2. Physical Volcanology and Eruptive History; Previous Work.

Brothers (1957) presented a morphological account of the volcano based on exposed landforms and a chronology of eruptive history including, from air photo interpretation, that of the intracaldera lavas. Buck (1978) and Buck et al. (1981), described the pyroclastic successions and provided new radiocarbon dates for the Tuhua tephra and the 8 ka tuff. Recently, Houghton et al. (1985a;b), Houghton and Wilson, (1986), and Houghton et al. (1987), have re-evaluated the eruptive history of the island, and have identified, largely from pyroclastic sequences, "basaltic" eruption styles and inferred from field evidence, fluid rheological behaviour from gas-poor pantelleritic magmas.

5.3. Objectives.

Until this study, no detailed profiling of the physical properties of lava sequences on Mayor Island, in contrast to those of the pyroclastic sequences, had been undertaken. Three flows were profiled: Panui; Pre-8 ka (central Taratimi Bay); and 8 ka flow. The following properties were measured; density, porosity, apparent clast aspect ratio (Rc), void aspect ratio (Rv), microlite length, and flow directional information. Together with structural information, a flow emplacement model is assembled.

5.4. Volcanic History.

The volcanic history of Mayor Island is separated into three distinct phases:

a. pre-caldera volcanism;
b. caldera collapse ;
c. post-caldera volcanism (Fig. 5.1).

The oldest lava at north Oira Bay overlies the TVZ-originating Rotoehu Ash. Grey finely vesicular pumice breccia (FVP) occurs above interlayered selvedges of black obsidian of 1 - 2 m thickness and glassy pink FVP breccia. The obsidian layers contain voids of low aspect ratio (Rv = 2.07 ± 0.86) and dip northwest. Columnar foliated rhyolite (RHY) outcrops below the obsidian zone and is locally brecciated with lenticular clasts (Rc = 5.01 ± 1.62), with an average aspect ratio exceeding the Rc value for pink breccia (2.06 ± 0.59).

Prior to caldera development, both lava shields were dissected with considerable metres relief (Houghton and Wilson, 1986). Flows such as that at Okawa point, showed considerable mobility and flowed down steep eroded slopes (slope angle = 26°). Below the Tumoe Pa site where rubbly pumice and obsidian occur, the flow is made up largely of steeply dipping flow banded rhyolite (028/53° NW). The flow banding is dipping toward the inferred vent, now obliterated by caldera development. The basal parts of the devitrified RHY layer have subhorizontal to low angle (22°) foliation formed by basal shear during flow (cf. Fink and Manley, 1986). The RHY layer is columnar jointed with five sided blocks of wide joint spacing (Jsp = 3.73 ± 0.77 m, n = 6) and bow outwards near the base, passing downwards into a 13 m thick wedge of basal breccia. Fig. 5.2 highlights the uniformity of Rc values of a 5 m section through the breccia and low strain analysis (Rs) value of 2.5 for a two-dimensional column face. The apparent long axis of most clasts lies within 20° of the mean alignment axis, subparallel to the breccia/RHY contact and local flow base.

Fig. 5.2c Rc vs. ϕ scatter plot where ϕ = final angle between long axes and principal strain direction ϕ, for initial shape ratios (Ri = 1 - 4). Theoretical curves of Rc vs. ϕ are from Dunnet (1969) and Elliot (1970). The visual best fit of these curves is used to obtain the value of the strain ratio Rs = 2.5. This section was from a vertical column face striking 160°. The long axes of autoclasts at Okawa Point are aligned approximately ± 35° about the mean of -6°. The negative value indicates the apparent dip of long axes landward (E) toward the inferred vent now obliterated within the caldera.

True strain ratios require 3 mutually perpendicular faces. Measurements from only one face limits any detailed interpretation. Rc values are apparent aspect ratios. Clasts appear to show similar shapes, Rc values and alignments on a vertical face striking 079°, mutually perpendicular to the face where the values in Fig. 5.2c were measured. If apparent long axes of clasts vary between 079° - 160°, random alignment of clast long axes along a surface parallel to the base of the flow is inferred. Such a section was not available for measurement. The above results indicate that deformation of the Okawa Pt. basal breccias is only compactional.

Although this method was used by Sparks and Wright (1979) to measure the strain ratio of fiamme from welded airfall tuffs, the applicability of this method to lava flows is more doubtful. Elliot and Dunnet used strain analysis methodology for sedimentary sequences (e.g. oolites). Other limitations as stated by Dunnet (1969) include ductility contrasts and the presence or absence of initial preferred orientation of fabrics. For lava flows, additional forces other than compactional are likely to influence the shape ratios and orientations of autoclasts.

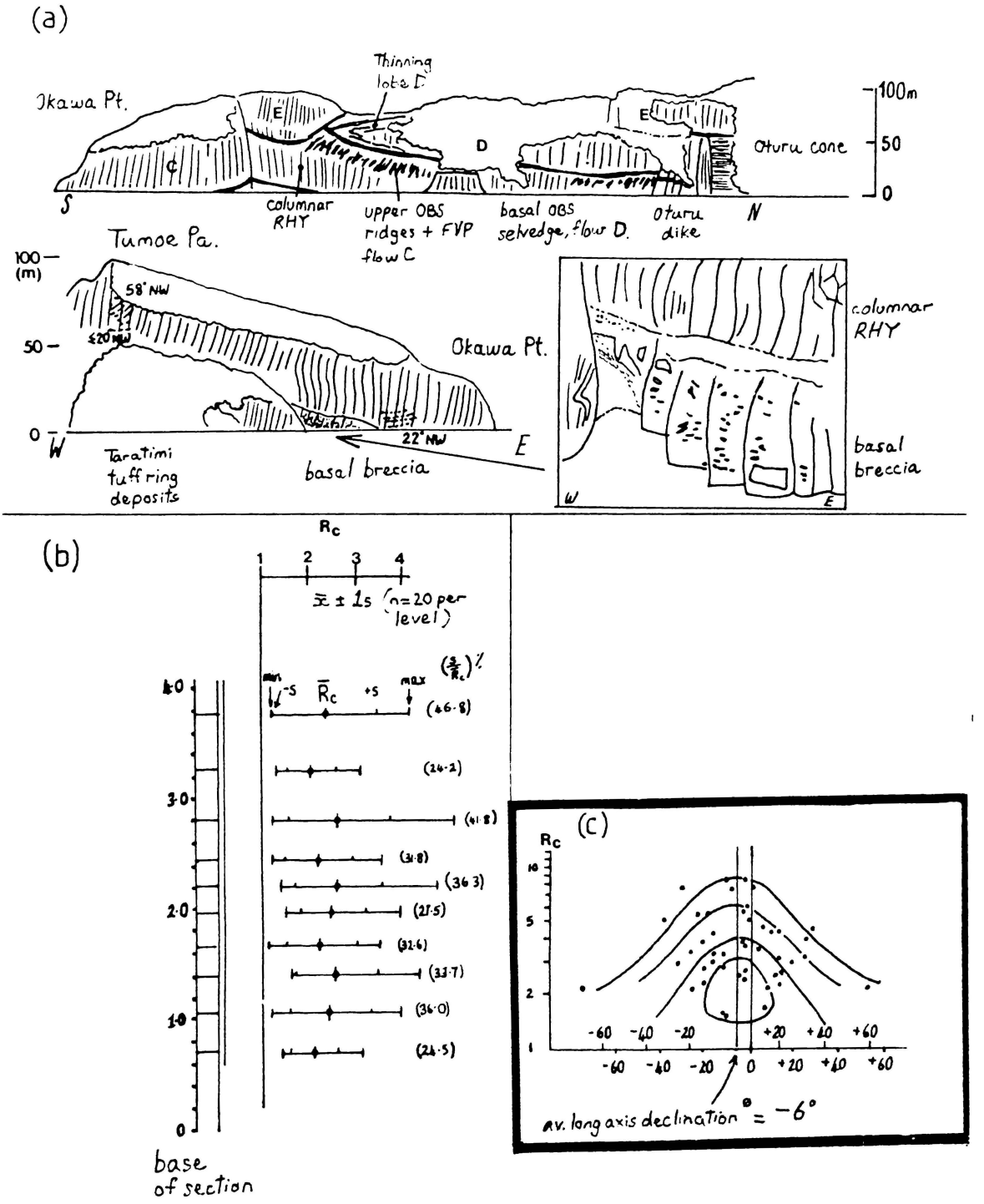

Fig. 5.2.

a. Okawa Point flow cliff section sketch.

b. Basal breccia apparent clast aspect ratio (Rc): mean ± 1 standard deviation, range and $(s/x^{0.5})\%$ for number of samples (n) = 20, over the outcrop coverage indicated. Clasts are angular to tapered and comprise black obsidian, greenish-grey lineated obsidian, green devitrified rhyolite and minor reddish brown clasts of basaltic composition.

The Pre-8 ka flow at central Taratimi Bay and Pighunters Pass, is interpreted as being an eroded remnant of a pre-caldera phase lava shield flow. The Panui flow is equivalent to an extra-caldera segment A lava, and the 8 ka flow post-dates caldera B preceding caldera C and the Tuhua tephra.

Post-caldera volcanism has occurred from vents within the caldera. A succession of petrographically uniform flow lobes and domes were extruded probably less than 1000 years ago. The flow carapaces such as flow 2d, north edge of Lake Aroarotamahine, are characterised by flow ridges of ≥ 6 m height and steep flow margins 18 - 27 m in height (Brothers, 1957). Blocky FVP and vesiculated obsidian (density = 0.42 - 1.52, porosity = 35 - 85%) contain primary voids of high aspect ratios (Rv = 15.55 ± 14.14, n = 20).

5.5. Panui Flow.

The Panui peninsula forming the southern tip of Mayor Island comprises eroded remnants of a 10 m + high tuff cone and associated lavas, joined to the remainder of the island 6340 years ago by a fan of unwelded ignimbrite (Houghton et al. 1987).

The Opo Bay tuff cone only exposed near Te More-o-moiterangi headland has been described by Houghton et al. (1987) who examined the stratigraphy, granulometry, clast morphology and density of the deposit.

Sections through the lava flow were profiled at Tokomata Point, and Te More-o-moiterangi headland. Lava is exposed around the coast for 900 m between south Omapu Bay and the Opo Bay tuff cone, suggesting that the lava, post-dating the tuff cone, may have either been originally ponded within the tuff cone or could have overwhelmed its southern wall. The radial strike pattern of flow banding (Fig. 5.3) results from steeply inclined obsidian ridges that formed by compressional deformation of the lava flow during cooling. Similar patterns from several of the Inyo-Mono domes were inferred by Suemnicht and Varga (1988) to originate from a circular vent opening. A circular vent opening is similarly postulated for the Panui dome and the feeder conduit is inferred to lie near to or beneath the summit of the Panui peninsula.

The Tokomata Point section consists of basal Tuhua beds (6340 yrs B.P., Hogg and McCraw, 1983) overlying an orange sandy paleosol (0.6 - 1.1 m thickness) with loose carapace pumice blocks from the carapace of the underlying lava flow unit. Within the flow sequence, finely vesicular pumice blocks (FVP) of 55 mm average width occur as pockets up to 6 m thickness between steeply dipping ribs of obsidian (upper OBS) of variable thickness. The upper OBS unit lies above a rhyolite core at least 5 m thick. Flow banding steepens from 23° to 74° up the section oblique to joints (Jsp = 0.9 ± 0.4 m) that form four-sided columns.

The Te More-o-moiterangi profile occurs through a thinning wedge of lava that laps up over the apex of the Opo tuff cone, providing an inclined section through: upper OBS (1.5 m thickness); RHY 4 m, increasing southwards to 15 - 20 m; basal OBS (2.1 m thickness) and basal breccia (~ 6 - 8 m). Thus a composite section from both localities provides a profile through the entire flow.

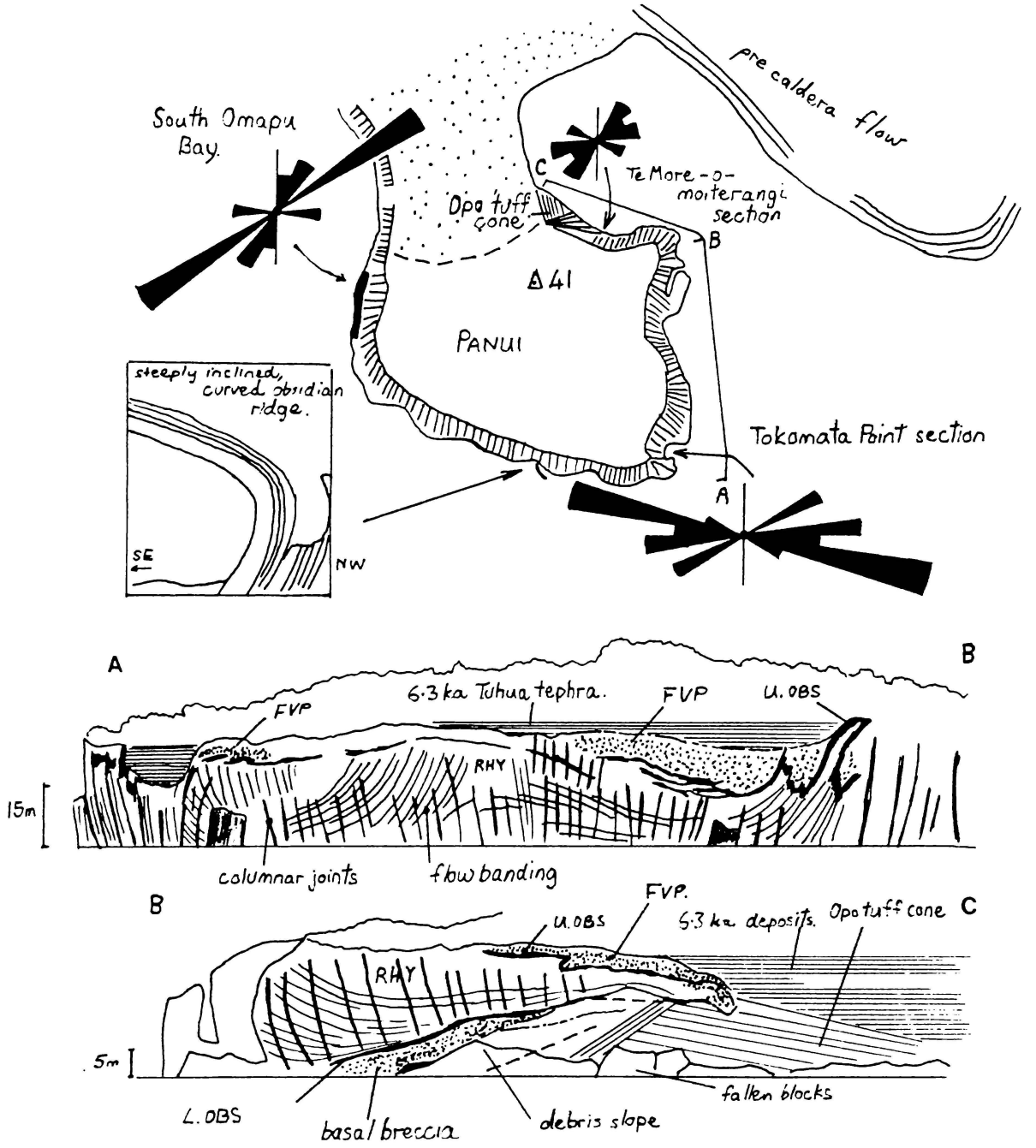

Fig. 5.3. Map of the Panui flow showing flow banding strike rosettes and cliff sections:
A - Tokomata Point to Te More-o-moiterangi;
B - Te More-o-moiterangi to the Opo Tuff Cone

Fig. 5.4a,b illustrates the dry bulk density and porosity profile for the Panui flow, highlighting:

a. uniform moderately vesicular FVP (porosity = 25 - 33%, density = 1.5 - 1.8 g. cm^{-3}), (Fig. 5.4c);
b. a transition zone of 1 - 10 cm thickness between non-brecciated intact FVP at the top of the upper OBS layer, grading into non-vesicular dense obsidian;
c. uniform high density, low porosity OBS layers;
d. a transition zone between OBS and devitrified RHY with both fabrics interfingering (Fig. 5.4d);
e. the 10% porosity of the RHY core, being largely intergranular void space within the groundmass and larger secondary voids, partly cross-cutting the foliation;
f. a range of clast densities within the basal breccia from 1.7 (pumice) to 2.4 (obsidian), (bulk sample = 2.1).

Clearly interfabric variation exceeds intrafabric variations.

Primary porosity for the FVP is lower than the airfall and blast-derived pyroclastics (some breadcrusted) from the Opo tuff ring (25 - 33% vs. 35 - 45%) suggesting a decrease in total volatiles between the emplacement of the Opo tuff ring and the Panui flow. Vesiculation in the lava was suppressed at more than 6 m from the top of the cooling flow carapace.

Apparent void aspect ratio (Rv) values in Fig. 5.4f are highest for the FVP layer, resulting from vesiculation of the outer skin of the lava prior to and during emplacement. Several populations of voids are present; those smallest voids of highest aspect ratio ($\bar{R}v \sim 22$) having formed earliest (Bonnichsen and Kauffman, 1987), were deflated and elongated during gas escape and tensile stretching from carapace flow processes. Deformation of early-phase voids occurred on the margins of larger lower aspect ratio (Rv = 11 - 18)$_{voids}$ that formed later, inflating in a more viscous magma. The upper OBS layer has rare primary voids (Rv = 2, Rv = 7.3) suggesting that either: (a) primary vesiculation was inhibited at depth as the overlying pressure exceeded the vapour pressure of the voids; or (b) the lava was initially gas poor. The secondary voids of the RHY layer (at Tokomata Pt.) cut across and partly distort the flow banding being subdivided into two populations - tapered and rounded with void long axes paralleling foliation dip. However, the RHY layer Rv values are uniform throughout the Tokomata Point section. Rv values are low (<3) for the basal OBS layer, and for pumice clasts of the basal breccia (Rv = 8, refer Fig. 5.4e and contrast with Fig. 5.4c).

Clast aspect ratios are uniform throughout the upper FVP and basal breccia, with the exception of a zone of lenticular clasts compressed against a large dislodged portion of obsidian at the exposed base of the Te More-o-moiterangi section. Uniform clast aspect ratios suggest late flow phase brittle fracture followed by avalanching down flow ridges, and the advancing flow front prior to incorporation within the basal breccia wedge.

Loss on ignition values (LOI) for the upper OBS; OBS/RHY contact and basal OBS; best representative of the original magma, are uniformly low - 0.23 - 0.24% (cf. H_2O^+ = 0.18%, Ewart et al. 1968). Values for the FVP and a sample best representative of the basal breccia are inferred to have a high H_2O^- (low temperature $<400^{\circ}C$) component owing to a high surface area-volume ratio and short diffusion pathway lengths (Eichelberger and Westrich, 1981; Westrich, 1987). LOI values from fresh obsidian

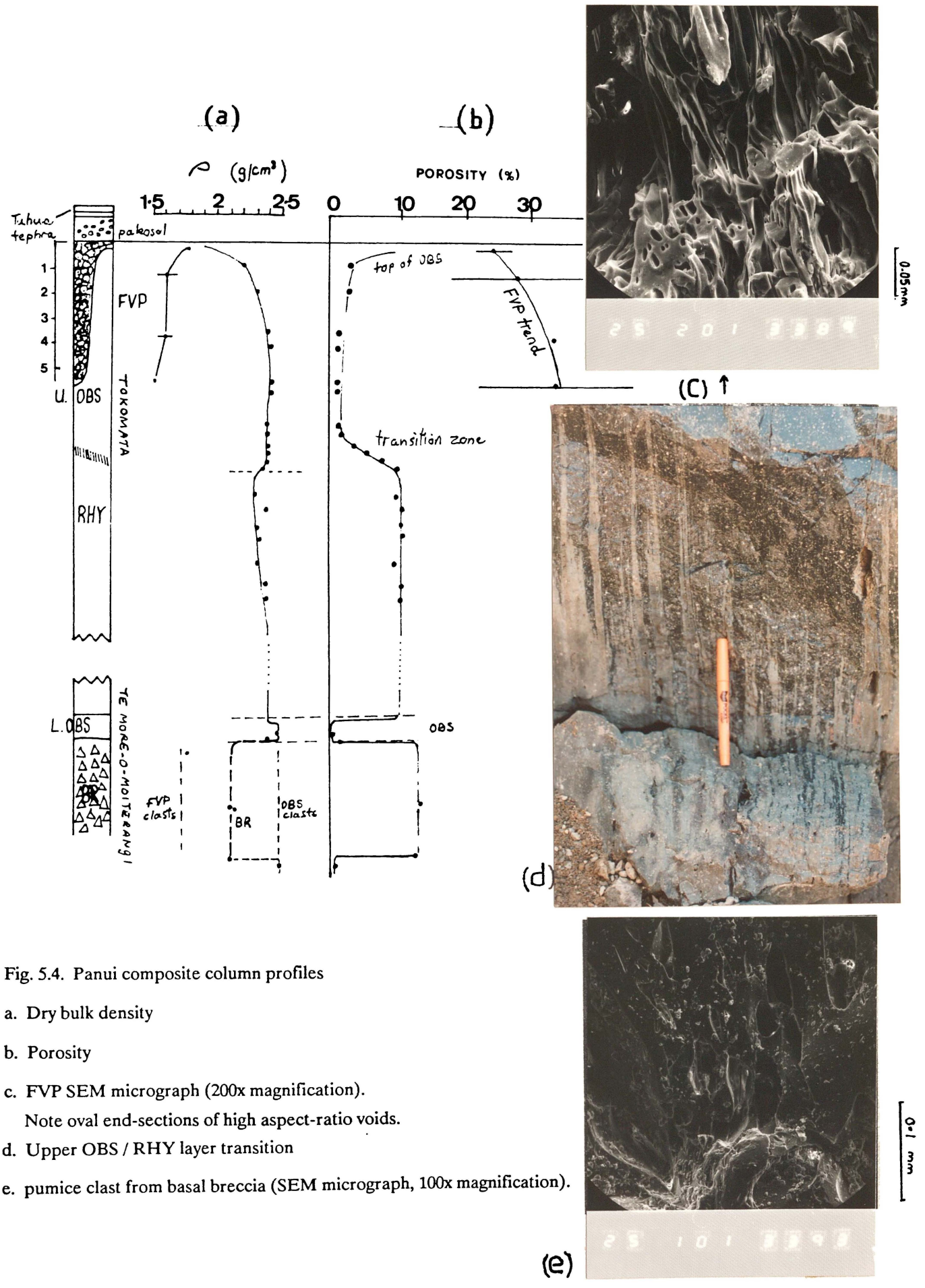

Fig. 5.4. Panui composite column profiles

a. Dry bulk density

b. Porosity

c. FVP SEM micrograph (200x magnification).
Note oval end-sections of high aspect-ratio voids.

d. Upper OBS / RHY layer transition

e. pumice clast from basal breccia (SEM micrograph, 100x magnification).

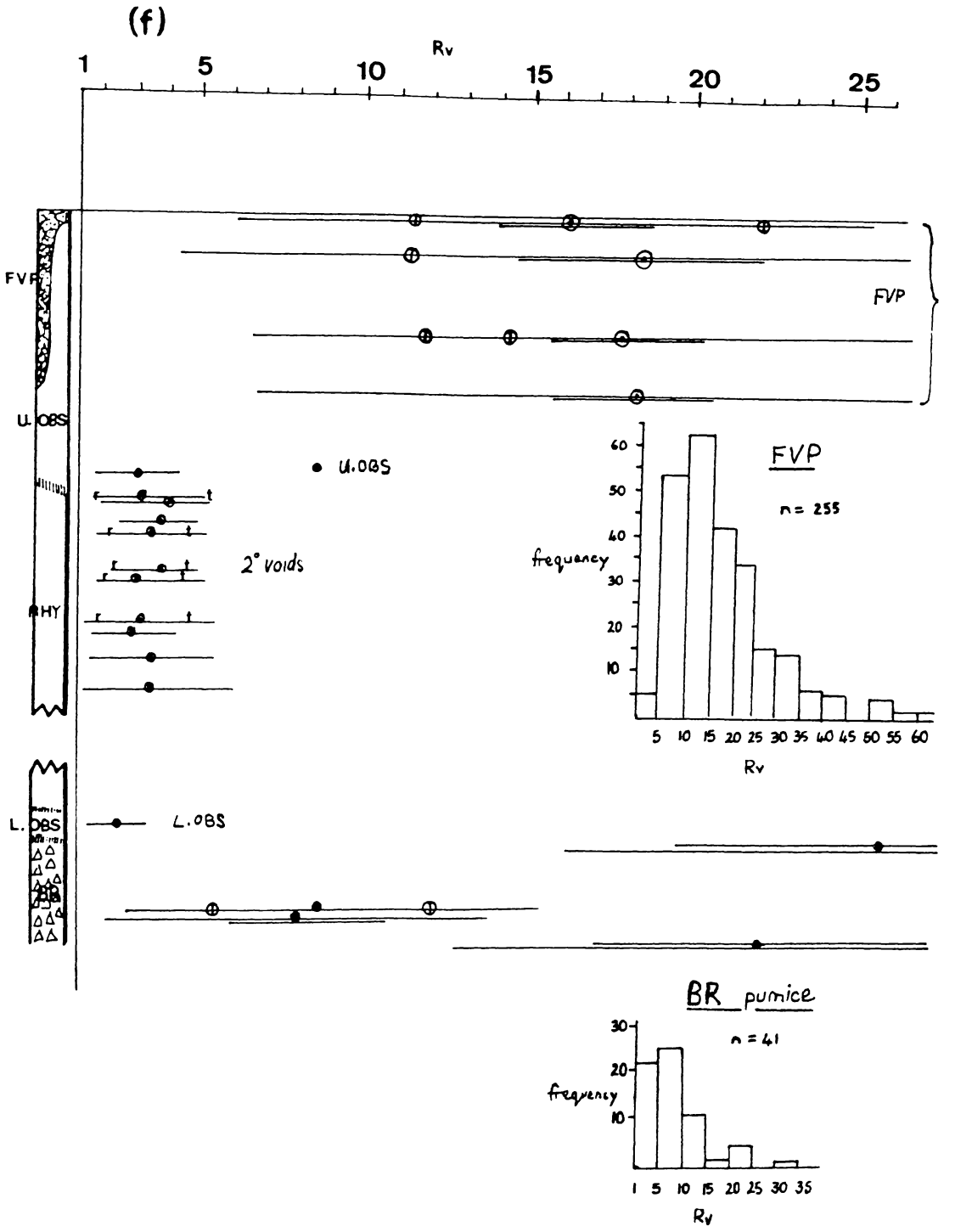

Fig. 5.4f. Rv profile, Panui. Several populations of primary voids occur in the FVP layer. High aspect ratio voids cause asymmetry of the histogram. The low aspect ratio secondary voids in the RHY layer at Tokamata Point, partly superimpose and deform the flow banding and are rounded (R) or tapered (T).

and pumice clasts in the Opo tuff cone vary between − 0.6 and +0.46% (Weaver oral comm. 1989). Negative values indicate that more oxygen is gained on oxidation of Fe^{2+} to Fe^{3+} than the loss of volatiles (H_2O^+, H_2O^-) during heating to 1000°C. Alternatively, the low water content was within the analytical error of determination so that negative values represent magmatic water contents close to zero. Thus, true H_2O^+ is interpreted as being low (less than 0.18%) for both tuff cone and lava.

However physical evidence from the tuff cone (in Houghton et al. 1985) suggest an additional non-magmatic volatile source was responsible for shallow steam explosions that fragmented the emplacing tuff cone magma.

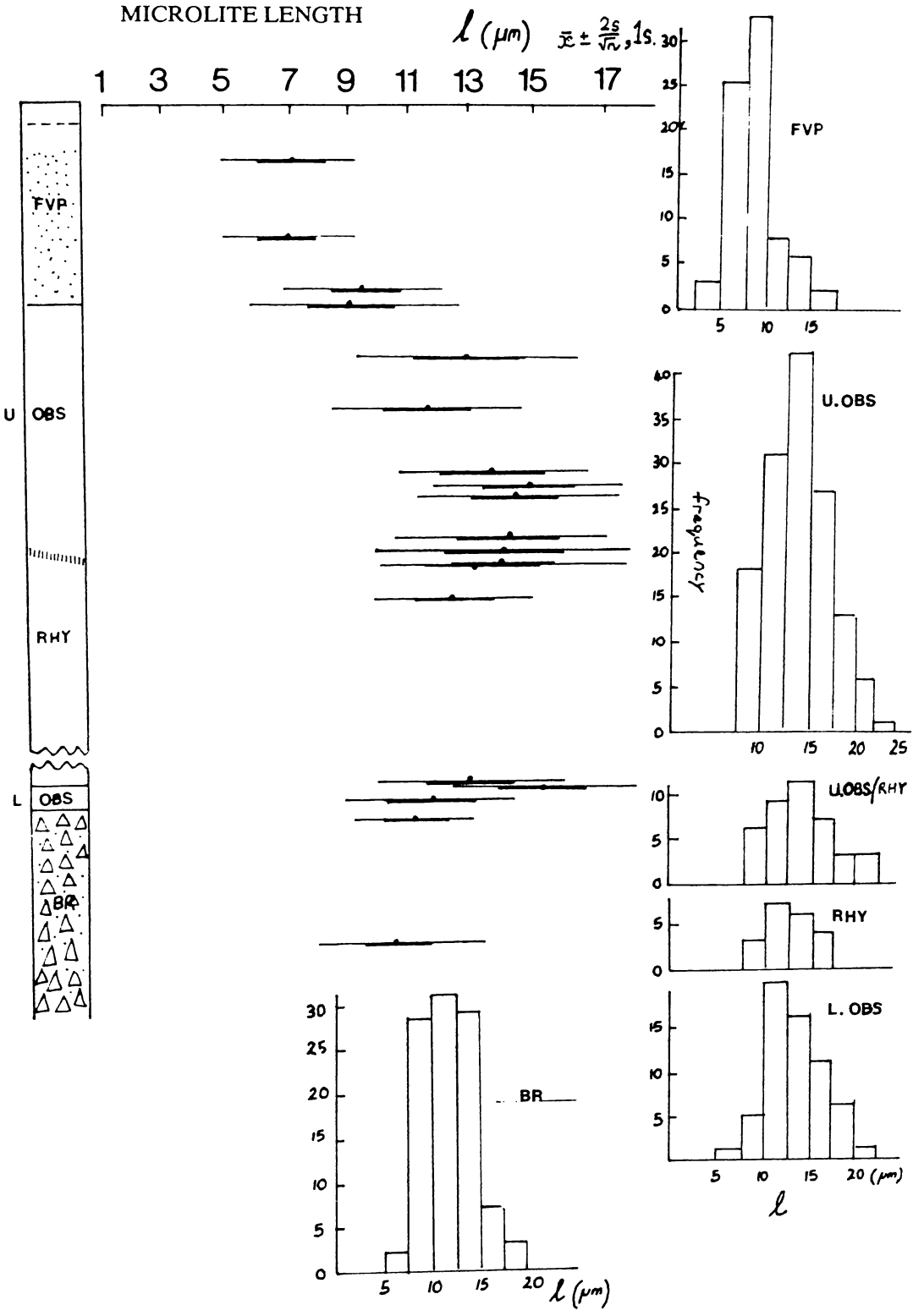

Fig. 5.5. Microlite length variations throughout the Panui flow column. Histograms illustrate the pronounced difference between the mean and modes of the FVP and upper OBS populations, and the similarity of the upper OBS, RHY and lower OBS populations.

Average microlite length (Fig. 5.5) varies from 7 μm (FVP) to 14 μm (upper OBS), with groundmass devitrification largely obscuring any microlites in the RHY core. The rod shaped morphology suggests an undercooling of 100 - 150°C. Tabular microlites formed at depth under lower undercooling conditions. The microlites delineate flow banding within the OBS and flow around phenocrysts indicating that their formation occurred during the conduit ascent of the magma. However, their crystallisation history appears in part to be dependent on the post-eruptive cooling history of the lava. The FVP microlites (6.99 ± 2.15 μm) are significantly smaller than the OBS microlites (12.48 ± 3.38 μm) suggesting that their growth via ionic diffusion was inhibited by both the low water content and the increasing viscosity of the cooling carapace of the flow. The flow interior remained thermally insulated, and hence less viscous, for the longest period of time and thus conduit-formed microlites were able to grow longer. Thus the microlite length may be used as an indicator for the flow temperature profile (refer to Carslaw and Jaegar, 1959; and Fink et al. 1983), as a lack of magnetic minerals preclude using paleomagnetism to provide estimates of flow temperatures as described in Audunsson and Levi, (1988).

Phenocryst width (Dm) and proportion (ϕ) vary little throughout the Panui flow (Fig. 5.6). Sanidine and anorthoclase are the largest phenocrysts and the most abundant (Dm = 0.350 mm, ϕ = 5.0%), with anorthoclase occasionally occurring as intergrowths with anhedral quartz up to 2.5 mm size. Lesser amount of aenigmatite (ϕ = 0.8%, Dm = 0.130 mm) and aegerine (ϕ = 0.3%, Dm = 0.124 mm) form a minor part of the total phenocryst proportion of 6 - 7% and average diameter of 0.4 mm. These values may be substituted into the Einstein-Roscoe equation to calculate the effective viscosity of the Panui lava, outlined in chapter 6.

5.6. The Pre-8 ka Flow.

The Pre-8 ka flow (named in Houghton and Wilson, 1986), outcropping on the eastern caldera wall, extends from central Taratimi Bay, to Pighunters Pass and represents an eroded slice through a pre-caldera shield lava flow. Profiles at the following locations provide the basis for a composite column: (a) Central Taratimi Bay (Fig. 5.7a)exposing the upper stratigraphy of the flow (~1 m FVP breccia, ~3 m OBS, 5 m RHY); (b) Pighunters Pass (Fig 5.7b) exposing basal flow stratigraphy (5 m RHY, 0.5 m basal OBS, 2.2 m basal breccia). A secondary site at the Devils Staircase is an oblique section across the top of a fossil sea cliff (Houghton and Wilson, 1986).

5.6.1. Taratimi Bay section.

The Taratimi section is a cross-section bisecting the northern edge of the Pre-8 ka flow, cutting across longitudinal flow ridges, and inter-ridge embayments comprising pink pumiceous FVP breccia. The RHY layer is columnar jointed with basal foliation shallowly dipping (e.g. 057/21°SE) steepening to 64° declination near the RHY/OBS spine zone. Flow folds are characteristically isoclinal and asymmetric, common in the upper OBS and RHY layers but rare in the planar foliated basal portion of the RHY layer. Voids are generally rare, except for those confined to narrow finely vesiculated layers on platform sections. Together with folial grooves and flow band dip surfaces, orientations of the long axes of voids may be used as local flow directional indicators. For example, flow marks on ridge

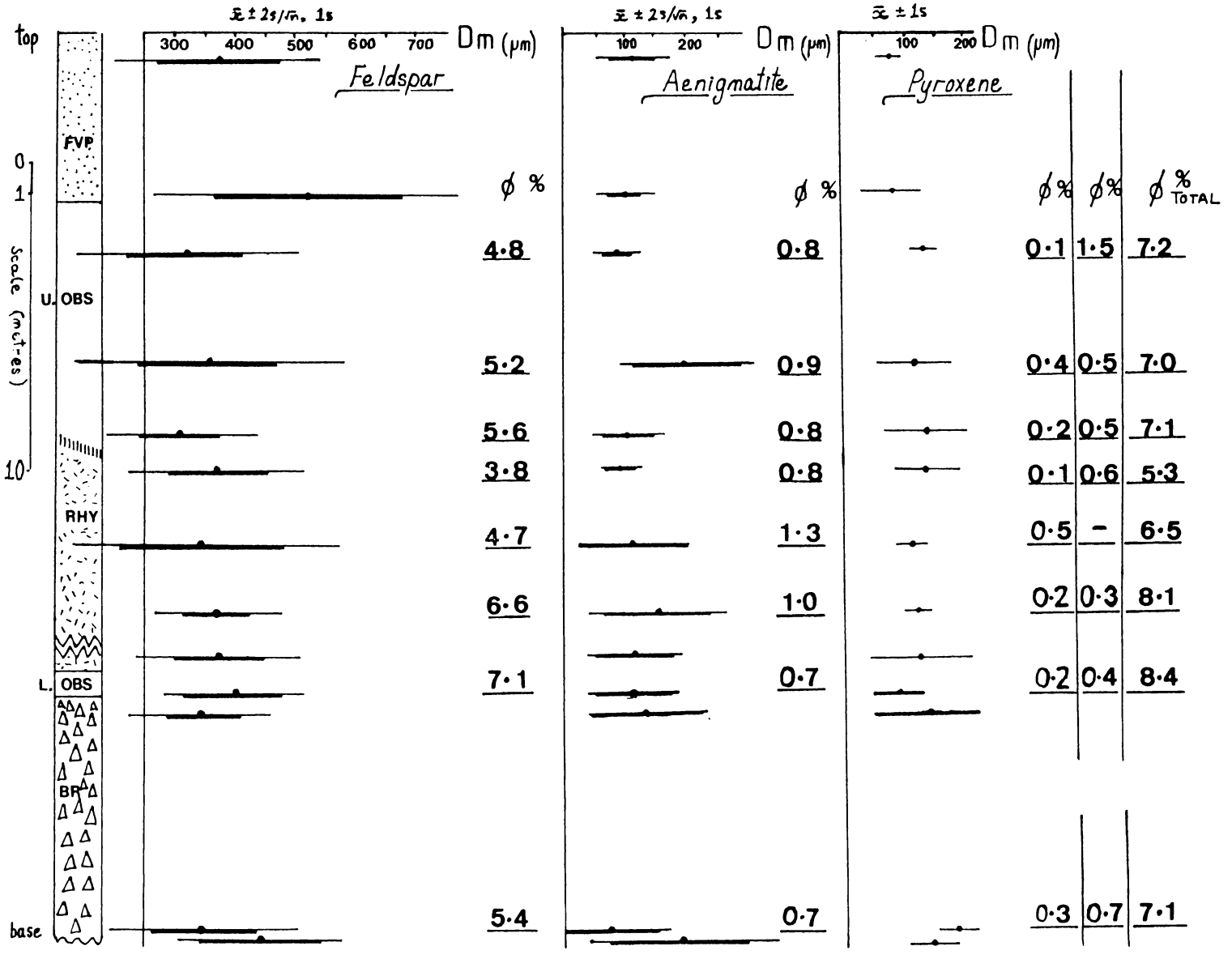

Fig. 5.6. Crystal size (Dm) profiles and crystal % for feldspar (sanidine), aenigmatite and pyroxene (aegerine-augite) phenocrysts, Panui flow.

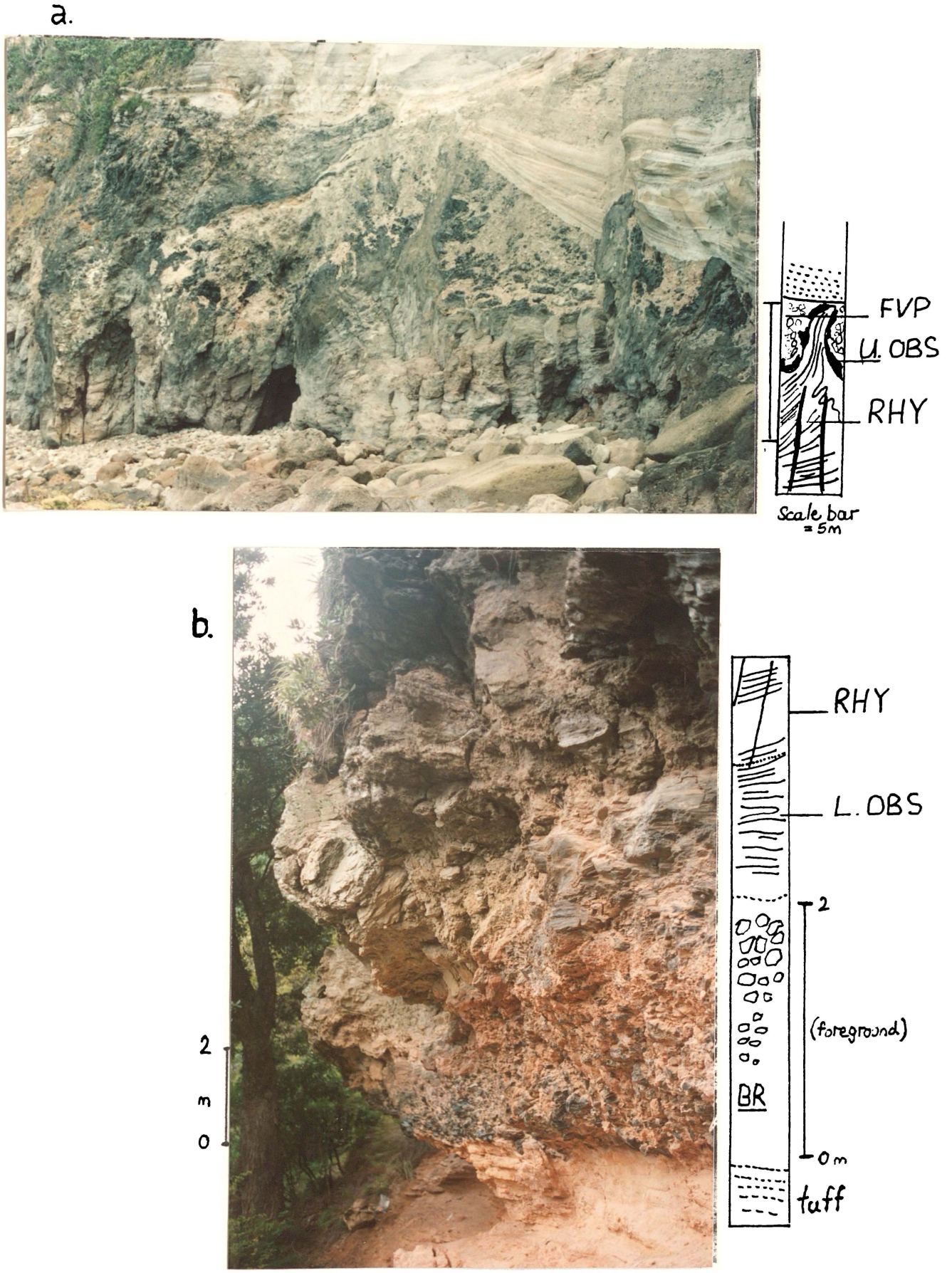

Fig. 5.7. Pre-8 ka flow top and basal sections: a. Central Taratimi Bay; b. Pighunters Pass (lower level).

surfaces are parallel with flow band or unit contact strike, (140/65°SW) suggesting local lateral flow edge movement eastward from a vent now obliterated by calderas A - C.

5.6.2. Pighunters Pass.

The Pighunters Pass section lies below a northward thinning lobe of the 8 ka flow and above an ancient tuff ring deposit consisting of coarse-fine grained successions similar to those below Paretu Ash at the Overhang.

The clast-supported basal breccia of variable thickness consists of angular grey lineated obsidian blocks that are highly flow folded and are less than 0.3 m size, pink pumiceous FVP, and grey-green foliated rhyolite. All blocks in the basal breccia have a random long axis orientation. Obsidian blocks tend to be more angular than pumice clasts. Reddish-brown vesiculated basalt occurs as xenoliths within breccia pumice, obsidian, and at the base of the RHY layer. Distortion of flow banding occurs around xenolith margins caused by its rotation induced by flow shear stresses. In thin section, the basalt consists of vesicles of low aspect ratio (Rv = 1.5), surrounded by Fe oxide-rich dendritic or feathery groundmass textures from quenching. Well developed sieve textures are characteristic of the plagioclase phenocrysts. Surfaces of obsidian blocks within the basal breccia show polygonal cooling cracks and some rhyolite blocks show late-phase brittle deformation. These may be possible dislocation planes parallel to fold axial planes (Fig. 5.8) and small fractures parallel to flow band surfaces. The base of the RHY layer appears to consist of formerly disrupted and re-fused rhyolite clasts in locations where the basal OBS selvedge is not continuous. The basal RHY layer is therefore a source for the rhyolite clasts of the basal breccia.

The basal OBS selvedge is 0 - 0.5 m thick sometimes with largely subhorizontal fold axes, with folds also appearing as tubular cross-sections, where the axial plane is sub-parallel to the inferred flow direction. At the margins of the OBS layer, yellow glass occurs adjacent to joint block surfaces originating from microvesiculation and elongation-deflation of the long axes of voids, as well as incipient groundmass devitrification. Where the basal OBS layer is missing, alternating pink vesiculated and dark green glassy layers occur sometimes with dislocation planes offset by about 1 cm.

The upper contact between Pre-8 ka and 8 ka flows is poorly exposed. However track-side obsidian outcrops usually occur with steeply dipping foliation planes unlike the basal OBS, and represent small exposures of the upper OBS layer.

5.6.3. Devils Staircase.

The Devils Staircase section is an oblique traverse through the upper-central part of the Pre-8 ka flow at the flow's maximum point of thickness of approximately 50 m. The five fabric zones, described in Fig. 5.9, represent an eroded section through upper OBS, RHY and FVP zones.

5.6.4. Flow emplacement history and composite profile interpretation.

Fig. 5.10 a,b illustrates the density and porosity profiles of a composite section comprising the central Taratimi and Pighunters Pass localities of the Pre-8 ka flow. Vesiculation is primary for the FVP and basal breccia zone. However, the upper and lower OBS layers are interpreted as being undercooled

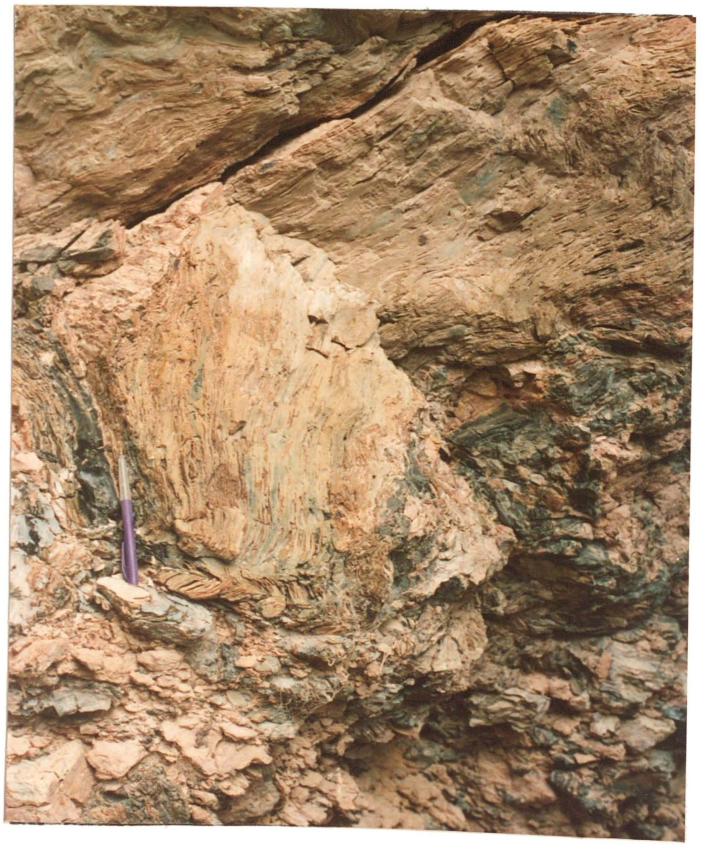

Fig. 5.8. Pre-8 ka flow, Pighunteers Pass RHY/basal breccia contact. Late phase rhyolite clast deformation is indicated by the fracturing to the right of the pen. At this locality, the basal OBS layer is within the upper part of the breccia.

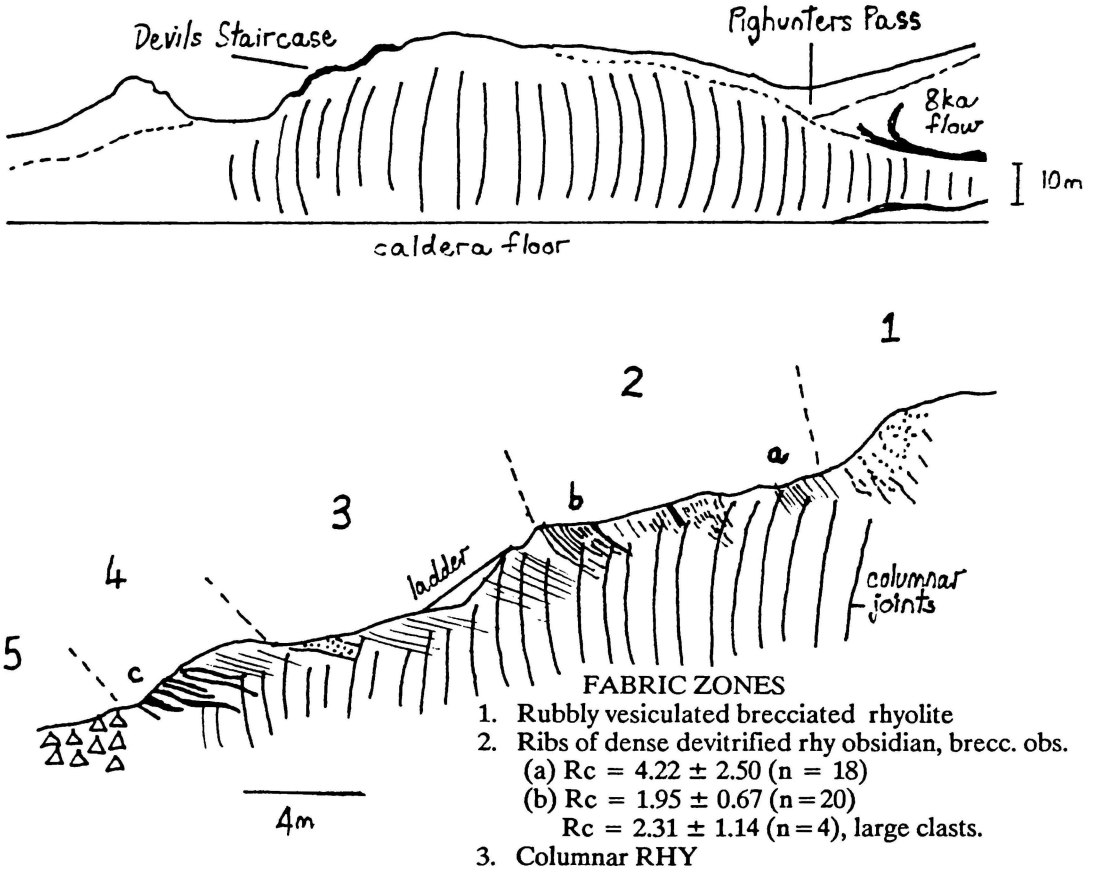

FABRIC ZONES

1. Rubbly vesiculated brecciated rhyolite
2. Ribs of dense devitrified rhy obsidian, brecc. obs.
   (a) Rc = 4.22 ± 2.50 (n = 18)
   (b) Rc = 1.95 ± 0.67 (n = 20)
   Rc = 2.31 ± 1.14 (n = 4), large clasts.
3. Columnar RHY
4. Obsidian lineations and interlayered pumiceous glass, brown glass
   (c) Rv = 2.45 ± 0.4 n = 10
5. blocky pumice + obsidian breccia.

Fig. 5.9. Devils Staircase Section.

examples of the original magma, subjected to a further cooling over a large thermal gradient between the central thermally insulated core and the surface. The central RHY layer originally had a density and porosity identical to the OBS layers, but was modified by secondary vesiculation during isobaric crystallisation (or devitrification) after emplacement. Low density pockets of devitrified auto-brecciated rhyolite occur adjacent to the basal OBS/RHY boundary and within the RHY layer suggesting late flow disruption and re-fusion of clasts.

Several populations of voids (Fig 5.10d) are present suggesting that vesiculation occurred throughout the latter phase of ascent, eruption and flow, during increasing viscosity, and decreasing gas pressure and temperature. Thus the void aspect ratio decreased with time. In contrast to the FVP zone, the ratio

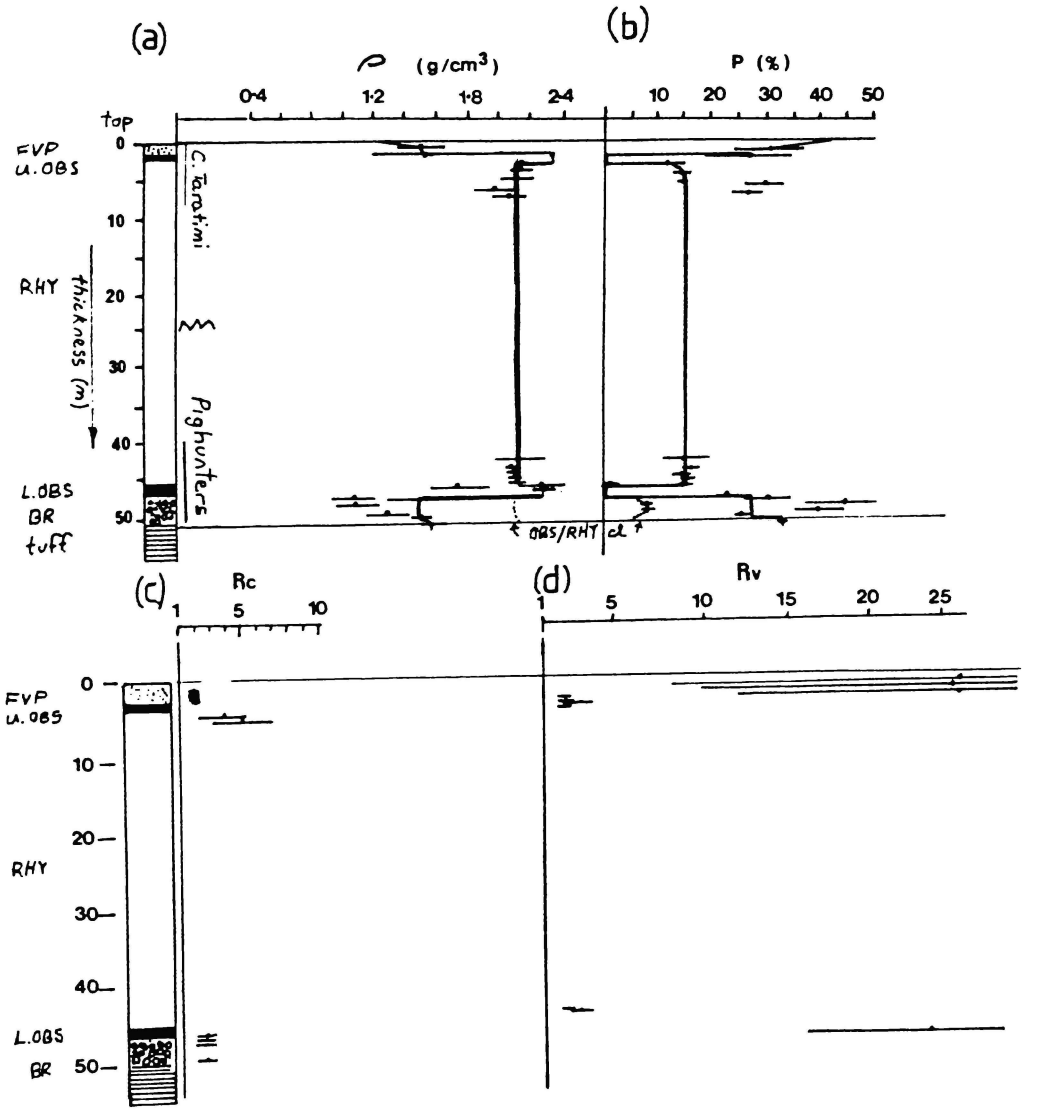

Fig. 5.10. Pre-8 ka physical volcanology:
a. dry density (ρ_{dry});
b. porosity (P%);
c. clast aspect ratio (Rc);
d. void aspect ratio (Rv).

of the tensile forces to the pressure exerted by the overlying lava within the upper OBS layer was lower. Voids were thus less able to elongate in the OBS layer where vesiculation of the gas-poor lava (LOI = 0.18%) was largely inhibited evident from rare gas blisters or primary voids.

Clast aspect ratios throughout the FVP and basal breccia (Fig. 5.10c) are uniform although higher values of 3 - 5 occur owing to localised compression in a pocket between OBS layers flanking the RHY spine core. Therefore, minor local variations exist but close sampling shows little down-profile variation.

As in the Panui flow, average length of elongate rod-shaped microlites, varies between units (Fig. 5.11) suggesting that microlite length was affected by the postemplacement flow thermal history.

The basal breccia, whilst containing 3 different clast types, formed from avalanching of blocks from the FVP and upper OBS carapace. Also, incorporation of banded obsidian from the basal OBS zone

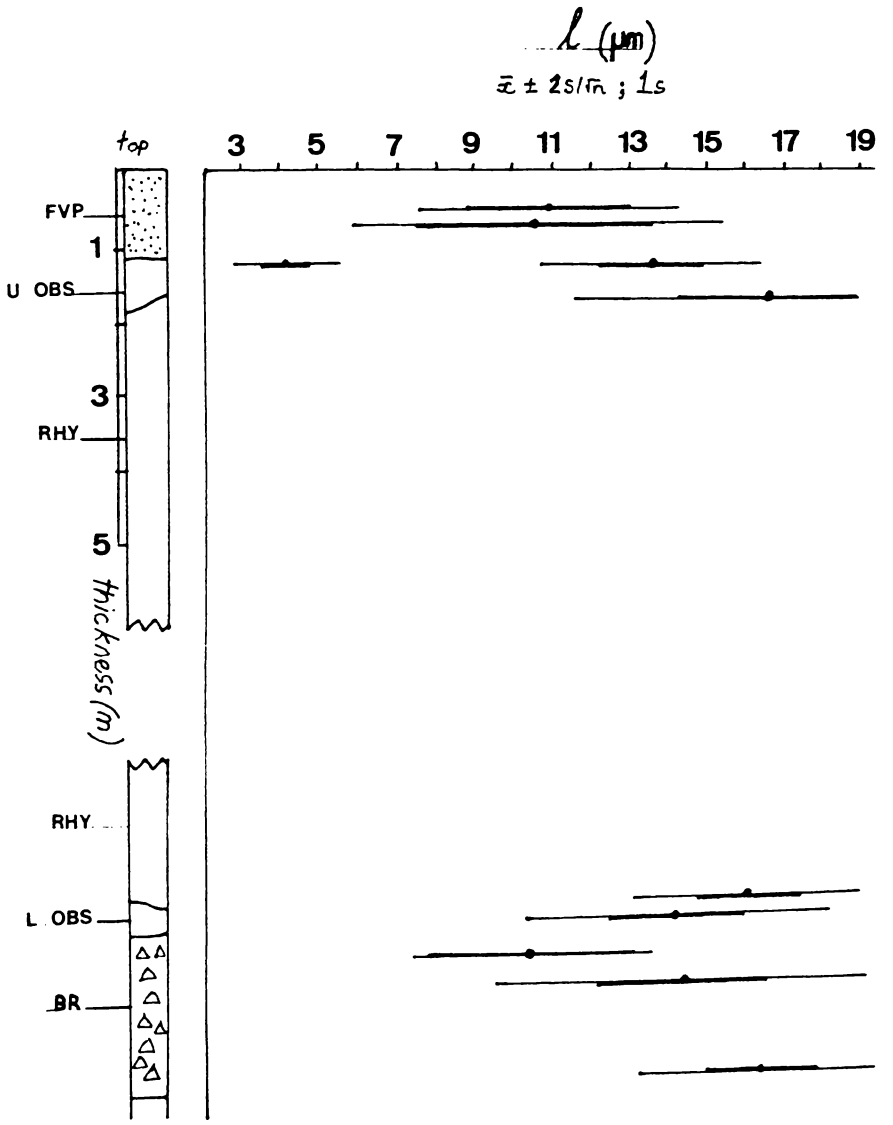

Fig. 5.11. Microlite length profile; Pre-8 ka flow.

into the breccia is suggested by a discontinuous basal selvedge thickness. The presence of rhyolite blocks in the upper part of the basal breccia layer also suggests incorporation into the flow base from the RHY layer during a late flow phase but that devitrification of the groundmass was initiated prior to flow cessation at high temperatures (Weaver et al. 1985).

The sharp boundaries between the upper two fabric units occurs owing to the suppression of vesicularity, where the vapour pressure of the voids is exceeded by the pressure exerted from the overlying lava causing differing rheological behaviour of both FVP and OBS units. The demarcation between OBS and RHY is primarily the result of secondary vesiculation during groundmass devitrification resulting in angular voids several millimetres in size of low aspect ratio. Low density pockets of devitrified autobrecciated rhyolite occur adjacent to basal OBS/RHY boundary and within the RHY layer supporting late flow-phase disruption and re-fusion of clasts.

Unlike other pre-caldera shield lavas (e.g. Tumoe - Okawa Pt.) that flowed down steep slopes, were very mobile and are traceable for at least 500 m, the longitudinal extent of the Pre-8 ka flow is limited - Crater Bay being the possible source of a thick sequence of 6.3 ka Taratimi tuff ring deposits (Houghton and Wilson, 1986). The basal slope (θ) cannot adequately be estimated. Houghton and Wilson (1986) infer that at least the most recent of the pre-caldera shield lavas were spatter fed, on the basis of steep flow slopes and diminishing flow thicknesses away from source. There is no physical evidence for the spatter feeding of the Pre-8 ka flow. Further discussion on this emplacement mechanism will be outlined in the following sections.

5.7. The 8 ka Flow.

The 8 ka flow (Fig. 5.12) is a lava sheet extending from the base of Tutaretare to Pighunters Pass, overlying an airfall lapilli dated at 8 ka B.P. (Buck et al. 1981). The 3 caldera section sites studied at the 8 ka flow were:

a. Halls Pass, a complete profile through the flow below the overlying Ruru Pass welded tuff (Houghton et al. 1985b);
b. The Overhang, comprising basal RHY, OBS, and the 8 ka fall layer, in a section above Te Paritu Lake;
c. Pighunters Pass, the northern most margin of the 8 ka sheet, above the Pre-8 ka flow.

In addition, at Parekoura Pt., on the southern margin of Taratimi (Crater) Bay, a well developed distal carapace section is observed.

5.7.1. Halls Pass.

The top 6 m of the Halls Pass column is characterised by flow-lineated finely vesicular obsidian. Individual lineations are 2 - 2.5 mm width and are distorted around the margins of rare rotated pumiceous clasts. Some clasts also have long axes oriented obliquely to the apparent dip of the flow banding and are rotated by the flow. Between lineations, the long axes of primary voids are 15° oblique to the flow banding, trending 274° with a 3° dip inwards toward the caldera. Mean Rv varies from 8.6

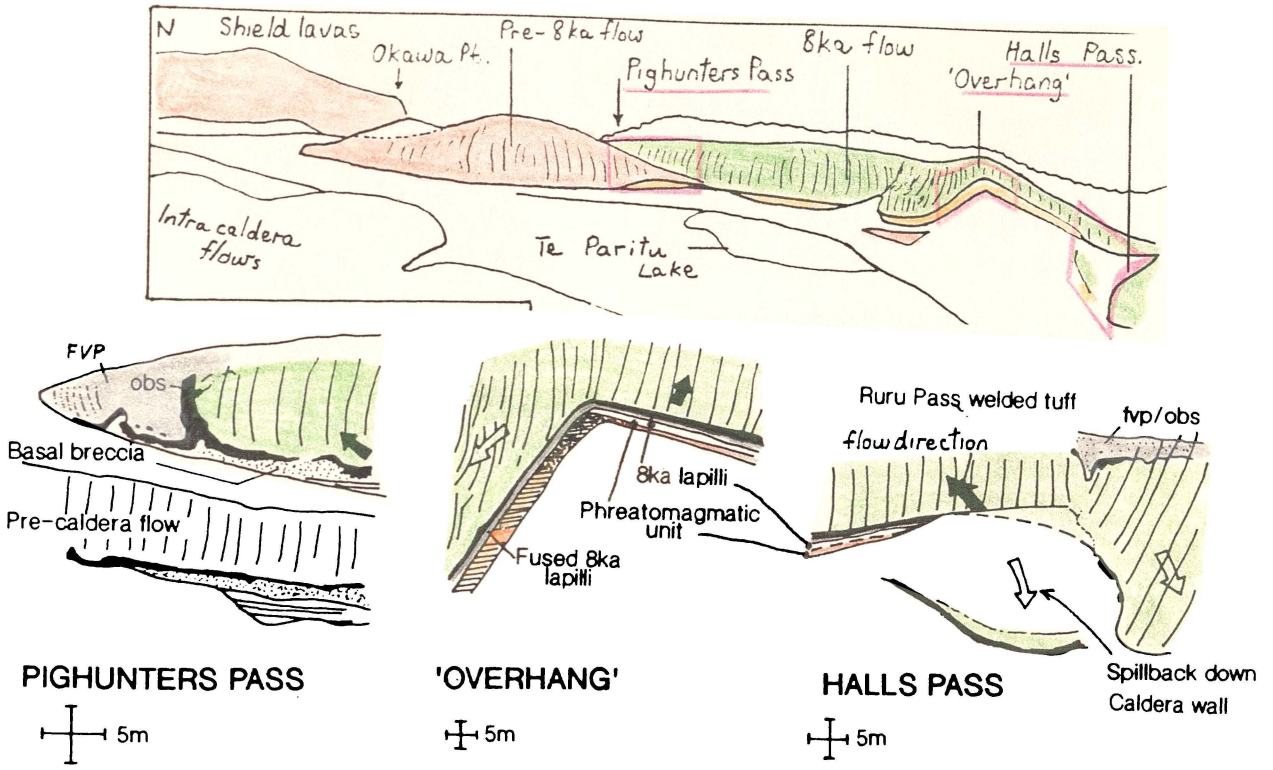

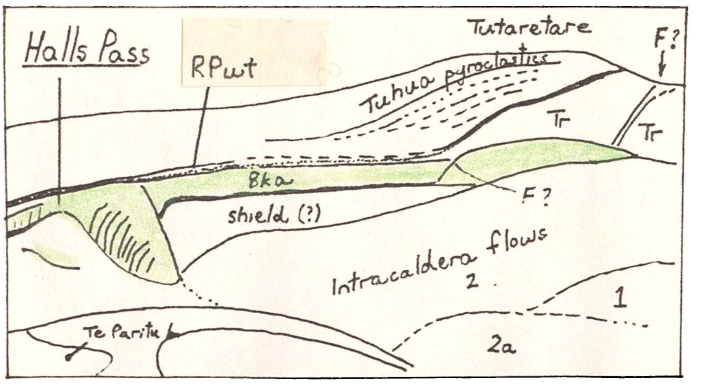

Fig. 5.12. Location and aspect of the caldera wall sections of the 8 ka flow. The sections above are plan views and are located on the diagram at the top of the page. Symbols for the lower photo and explanatory sketch are as follows: RPwt = Ruru Pass welded tuff; Tr = Tutaretare pantelleritic lava flows.

to 6, and, together with porosity (Fig. 5.13) decreases with increasing depth within the intact upper FVP/OBS layer. The finely vesicular obsidian/RHY contact is undulating over a 2 m vertical extent.

The RHY layer is characterised by medium spaced columnar jointing dipping 70°SE and steeply dipping foliations (0.5 - 10 mm) with interfolial angular secondary voids of low aspect ratio less than 3.5. On the western margin of the Halls Pass track, near the apex of a blocky talus slope, small obsidian wedges contain flow bands dipping 40°NW. The basal OBS layer is exposed downslope on the eastern margin of the track of 1.8 m in thickness, locally brecciated into angular lozenges (Rc = 2.15 ± 0.6, to 3.14 ± 1.15).

Fig. 5.14a shows the flow stratigraphy of the Halls Pass area.

Halls Pass is interpreted as being the lateral equivalent of the Overhang section in that the best model to explain the outcrop stratigraphy is that the 8 ka flow spills inward over the caldera rim in addition to flowing away from the inferred vent now obliterated by caldera C. Evidence for this scenario includes:

a. joints in section A bow outwards toward the caldera (dipping southeast) indicating formation by tensile fracture during progressively inward propagation on cooling and block contraction, perpendicular to the inclined basal cooling surfaces of the flow;
b. no lateral equivalent of the 8 ka fall deposit (in C) occurs in A, but an equivalent of basal OBS of similar contact dip occurs in B, being correlative with the wedges in A;
c. lava overlies both the 8 ka fused fall lapilli and non- fused older pyroclastics.

In segment B, the basal OBS layer is locally brecciated (Rc = 3.21 ± 2.00, n = 20; 2.03 ± 0.50, n = 20) favourably comparing with the same unit upslope in C (3.30 ± 1.13, n = 19). The basal OBS/RHY contact is sharp and marked by broken obsidian lineations and both rhyolite and obsidian clasts.

Fig. 5.14b describes a section through the basal OBS layer, and the 8 ka fall lapilli layer. At 0.75 m below the lower flow contact, a fine-grained unit, of phreatomagmatic origin, contains fossil pohutukawa leaf moulds, orientated subparallel to the contact (020/31°E) with the 8 ka fall lapilli, but not preferentially aligned within the unit. The bulk of the 8 ka lapilli, both above and below the phreatomagmatic unit comprises a coarse grained (5 - 10 mm), fines-free unit suggesting an open vent fountaining style of eruption. The uppermost 0.4 m is marked by alternating coarse- and fine-grained fused lapilli of higher density (2.22 $g.cm^{-3}$) and 12% porosity, compared to 1.6 $g.cm^{-3}$ and 26.5% for the density and porosity of the basal coarse grained 8 ka fall unit. Rare gas blisters with long axes orientated into the outcrop face may be used as local indicators of flow direction. These occur mainly within the upper fused lapilli just beneath the lava-lapilli basal contact, suggesting that the fall lapilli was hot and contained volatiles.

5.7.2. The Overhang.

This section, 50 m above Te Paritu lake best shows the spatter fed nature of the 8 ka lava sheet. The 8 ka lava during or shortly after emplacement cascaded down the caldera wall to unconformably overlie all older units, i.e. 8 ka fall lapilli, paleosol, Paretu Ash, and two older taalian tuff ring deposits separated

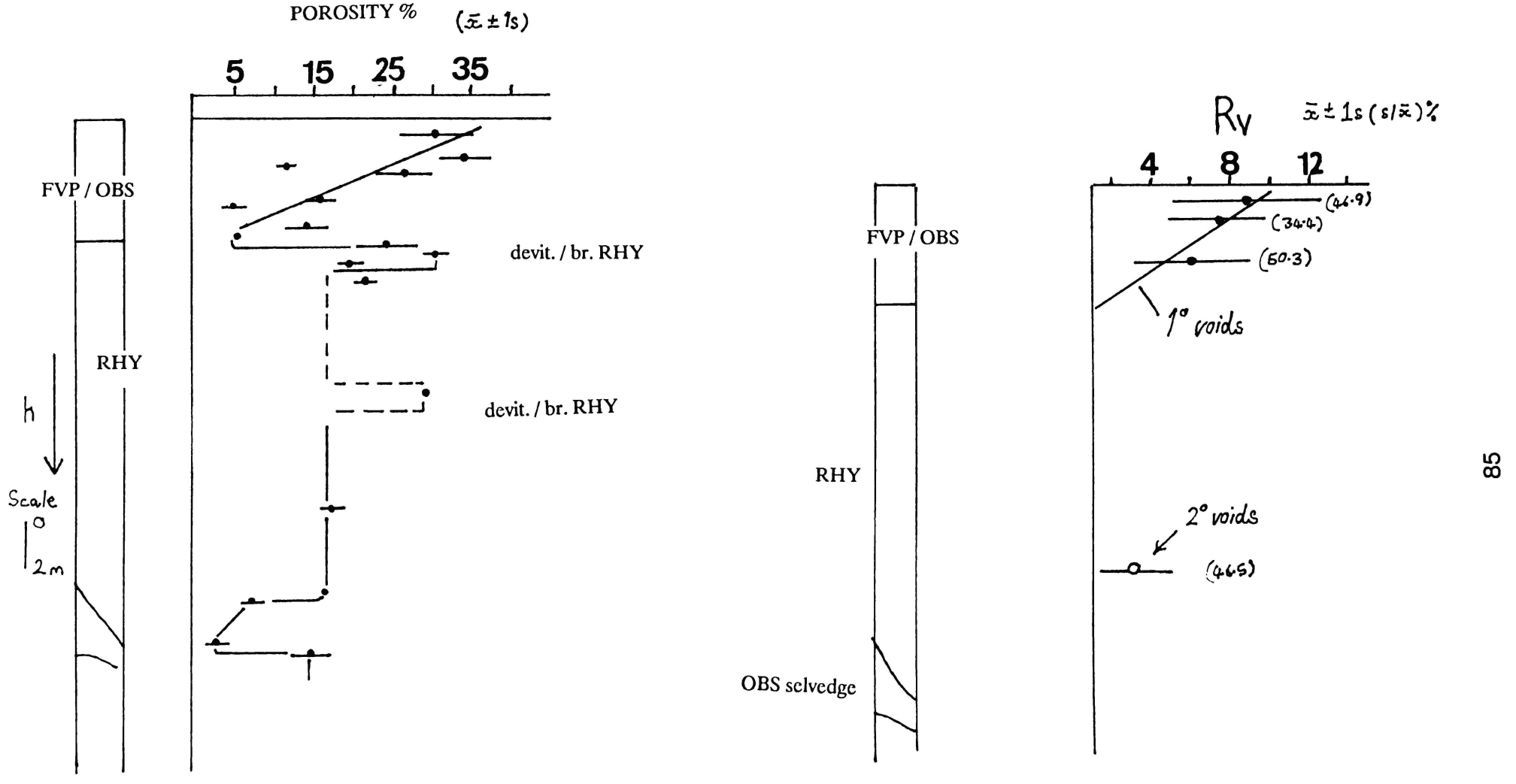

Fig. 5.13. Porosity and void aspect ratio (Rv) profiles for the 8 ka flow at Halls Pass.

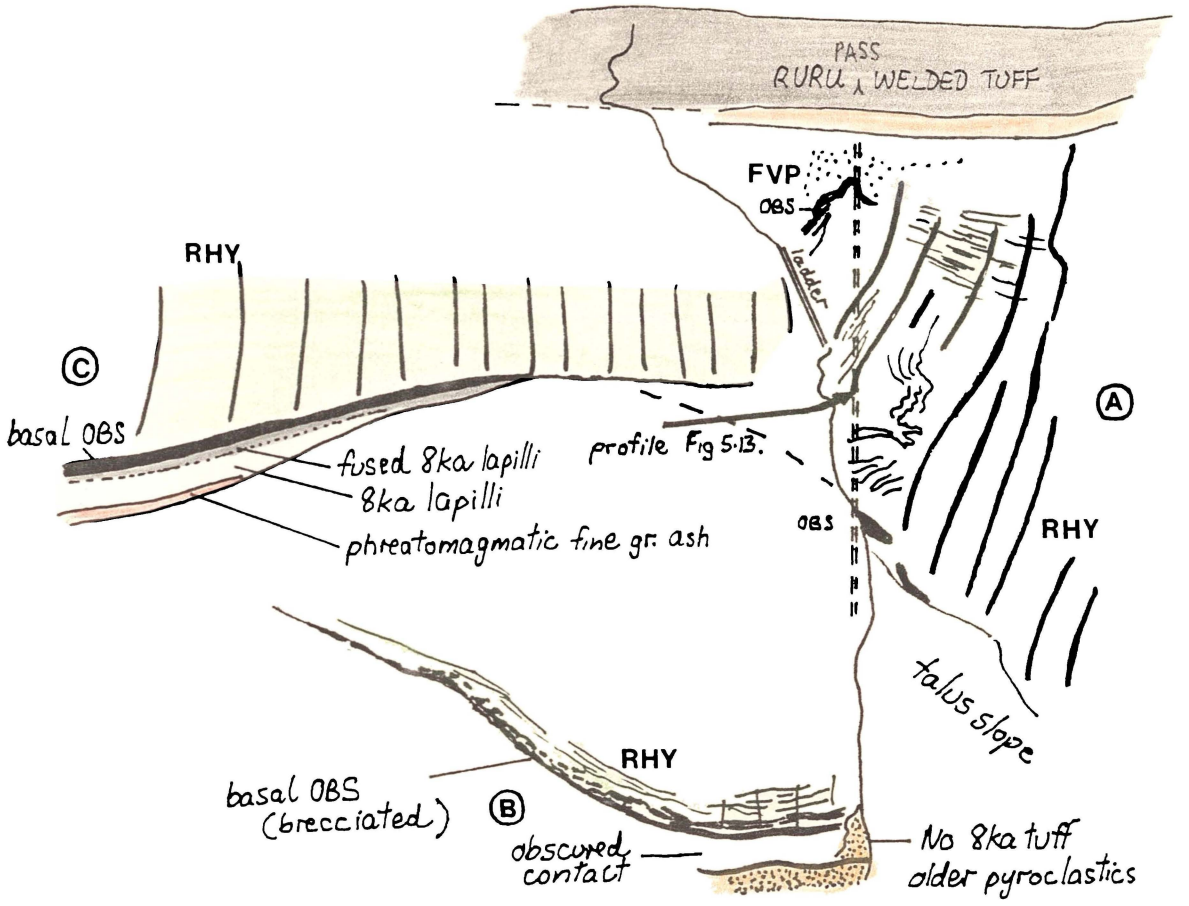

Fig. 5.14a. Halls Pass stratigraphy. (plan view)

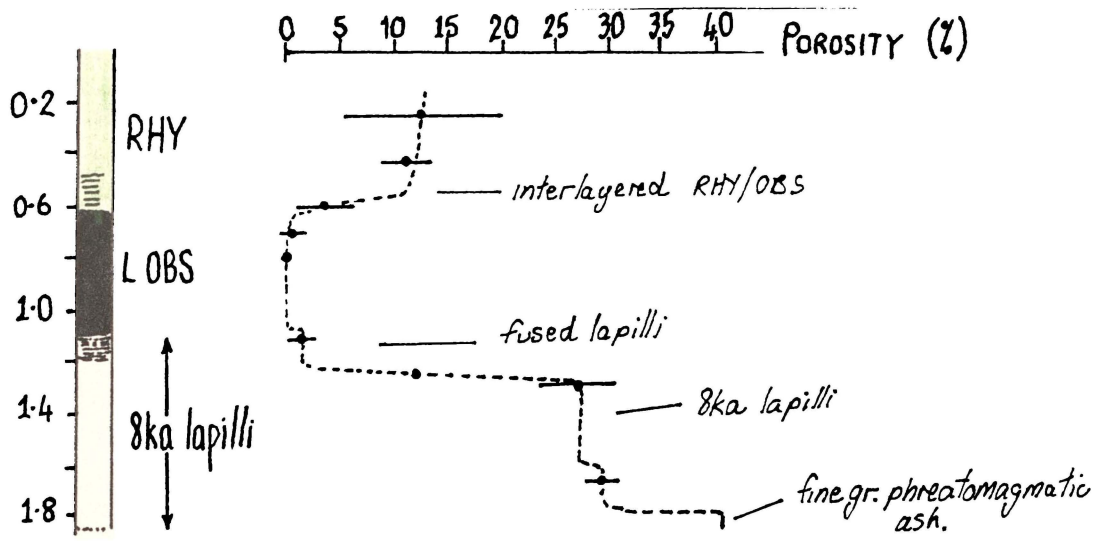

Fig. 5.14b. Porosity profile and stratigraphy of the basal part of the 8 ka flow and fall lapilli layer.

by a deep orange paleosol (Houghton and Wilson, 1986). Underlying this sequence is an older rhyolite lava of probable pre-caldera shield origin.

Houghton and Wilson (1986) conclude that the 8 ka lava sheet is spatter fed because the lava unconformably truncates older deposits draping caldera segment B. The inference here is that either the vent lay on the caldera rim, which means that it must have been an arcuate fissure extending to Pighunters Pass of which there is no evidence, or that the vent was within caldera B and is now obliterated by caldera C. Further evidence against a vent origin on the caldera rim is no vent related pyroclastic facies, such as a breccia funnel occur(cf. Eichelberger et al. 1986). Additional evidence for a spatter fed eruption mode is the fusion of the co-eruptive 8 ka fall deposits. Thermal effects are absent when the 8 ka lava overlies older pyroclastics.

Residual volatiles and heat in the fall deposits may have played a role in promoting interclast fusion. The 8 ka fall deposits are only fused within the top 0.1 - 0.2 m below a ~20 m thickness of lava at the top of the Overhang and 1.35 m below a greater overlying thickness of lava (~ 70 m +) on the eastern wall, where the lava truncates the Paretu Ash and two ancient tuff rings with an intervening paleosol. At section 1 (Fig. 5.15) the upper contact of the fine grained unit underlying the 8 ka lapilli is plastered against charcoal-lined holes from former logs. Therefore the fine grained deposit was cold and cohesive supporting a phreatomagmatic origin. The log holes occur largely within the basal coarse grained lapilli of the 8 ka fall layer suggesting that the airfall unit was hot (300°C) but not hot enough to fuse. The top 0.1 - 0.2 m is fused and gas blisters at the contact between the lapilli and the basal OBS selvedge of the lava may be used as directional indicators of flow. Their presence suggests that the lava was emplaced shortly after the upper 8 ka fall lapilli and that during fusion, largely by heating from the overlying lava, volatiles from the lapilli collected into pockets. In contrast, vesiculation of the overlying lava would have been completely suppressed within the basal parts of the flow. The flattening ratio of the fall lapilli clasts increases from the basal coarse-grained unit (Rc = 2 - 3) upwards to 5 - 9 in the fused zone with a density of 2.22 $g.cm^{-3}$ suggesting an increasing temperature and decreasing clast viscosity, influenced by the overlying lava.

At the eastern edge of the Overhang at section 2 (Fig. 5.15), the following basal sequence occurs below a discontinuous basal OBS layer of the lava:

a. a 0.95 m thick fused lenticular unit (Rc = 5 - 10, clast size = 2 - 3 mm) . Joints (022/84°W) continue from the base of the OBS selvedge into this unit;
b. a fine grained fused unit (0.16 m thickness);
c. a less fused coarse grained deposit (0.24 m thickness) with a range of clasts from underlying deposits such as the pinkish orange inter-tuff ring paleosol.

The contact between unit c and the underlying truncated older pyroclastics dips 31°W.

Thus the fusion layer is caused from the baking of the co- eruptive fall tephra. Only the top part of the fall lapilli is fused suggesting that its emplacement from a pulsating eruption column (Houghton pers. comm. 1988) shortly preceded that of the lava. Older pyroclastics on the caldera wall such as those below segment B, Halls Pass, were not fused. However these deposits were incorporated into the

basal unit c as the lava spilled down the caldera wall after eruption. Further evidence of spill-back of the 8ka sheet is from a tight asymmetric fold whose crest dips 36° upslope, boudinage of obsidian foliations at the basal OBS/RHY contact and clast rotation on the basal OBS/fused 8 ka lapilli boundary.

The lower 0.45 m of the 0.9 m thick basal OBS layer of the 8 ka flow is a clast-supported breccia where foliated clasts have been rotated, stretched, tapered (subrounded morphology) and re-fused, resulting in a range of Rc values between 2.5 - 5. This piece of physical evidence alone suggests a high thermal gradient, flow temperature and a relatively mobile flow base (Fig. 5.15).

5.7.3. Pighunters Pass.

The Pighunters Pass section lies above the Pre-8 ka flow and forms the northern edge of the 8 ka sheet (Fig. 5.16). On the northern margin of the FVP,the orientation of the long axes of voids is 65° SW (Rv = 12.82 ± 4, n = 20) occurring obliquely to spines of obsidian projecting 8 m from the basal selvedge of the flow.

The OBS layer shows the following characteristics:

a. an alternating dense and vesiculated margin suggesting pockets of continuing effervescence during flow;
b. void long axes dipping 78° SW toward the flow centre parallel to foliation dip;
c. gas blisters or pockets of vesiculation with glassy intravoid septa, useful as flow directional indicators;
d. three fold axial plane orientation populations - two low angle (basal) and one high angle paralleling the limbs (at the base) of the projecting OBS spine;
e. disharmonic tight asymmetric flow folds plus tubular fold cross sections (including boudins on fold limbs);
f. local brecciation along the base of the flow resulting in an irregular OBS layer thickness, with flow-orientated long axes of obsidian clasts.

The lower OBS layer occasionally includes clasts of FVP (Rc = 2.58 ± 0.90, n = 20), forming a breccia up to 0.68 m in thickness, lying above a thin pyroclastic unit consisting of a succession of coarse and fine-grained fall units (8 ka fall lapilli) less fused than at the Overhang or Halls sections.

Thus the Pighunters Pass section represents a transverse basal slice through a southwards thickening 8 ka flow sheet consisting of a margin of intact and brecciated FVP also incorporated into the basal portion of the flow, enveloping an OBS unit of variable thickness with flow margin obsidian spines projecting from the basal selvedge. The RHY layer consists of widely spaced columnar jointing bowing outwards in the direction of the flow trend. The Pighunters Pass section, like the Overhang and Halls Pass sections provide proximal exposures through the 8 ka flow sheet. The arcuate caldera wall trends from 068° to 270°. The average trend of the long axes of basal gas blisters is 146° ± 20° (n = 9) for Halls-Overhang and 090° - 120° (n = 2) at Pighunters Pass. These values indicate that the flow originated from a vent or northeasterly aligned fissure within the southwestern corner of the caldera.

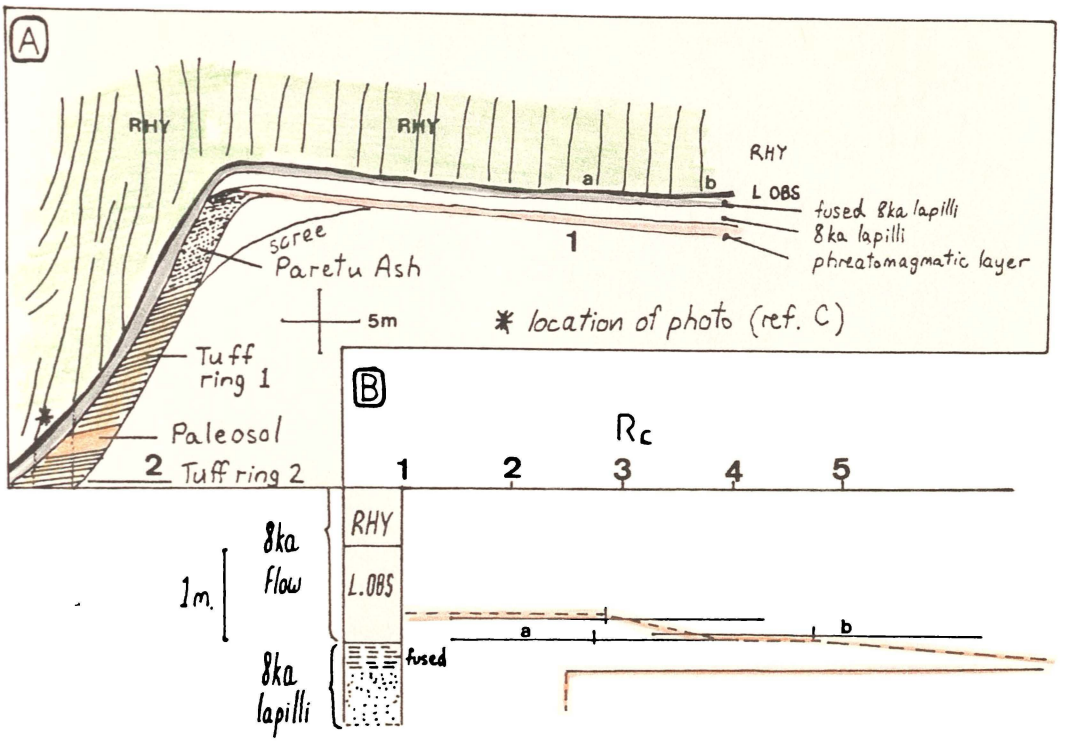

C

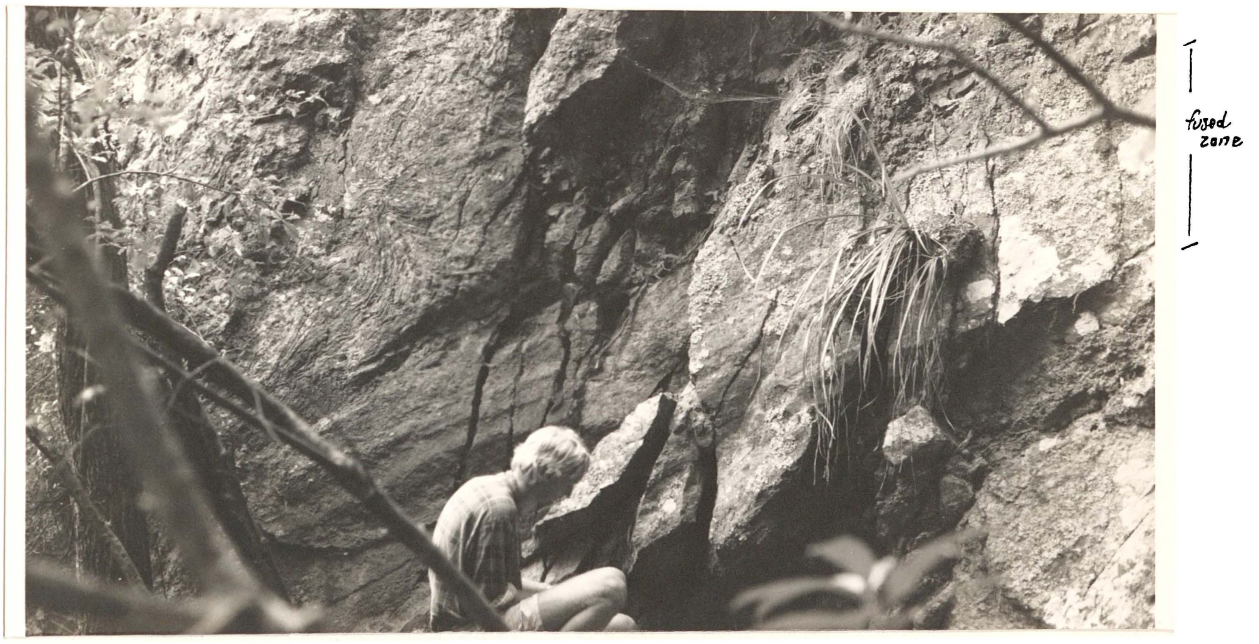

Fig. 5.15. The Overhang Section

(A) Plan view showing location of sections 1 and 2.

(B) Clast aspect ratio, (section 1) through lower OBS, fused layer and 8 ka lapilli. The orange dashed line represents the average Rc value increasing to 5 - 9 in the fused zone towards its base. The brecciated part of the lower OBS unit is discontinuous and varies in Rc as is shown by dissimilar values at locations a and b.

(C) Photograph of Section 2 showing an increased thickness of fused 8 ka lapilli below an interfoliated L.OBS/RHY zone marked by an asymmetric flow fold dipping upslope. (photograph courtesy T. Clemm)

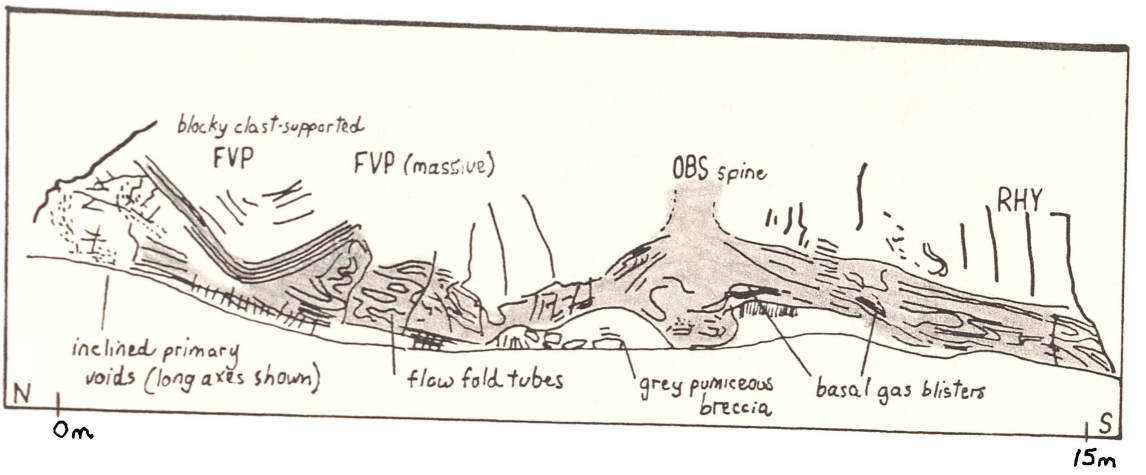

Fig. 5.16. Pighunters Pass Section, 8 ka flow.

5.7.4. Parekoura Point.

Parekoura Pt. (Fig. 5.17a) is the most well developed flow carapace section on Mayor Island, underlying a thick sequence of proximal Tuhua deposits (described in Houghton and Wilson, 1986). The upper flow stratigraphy exposed comprises: FVP breccia; OBS; and RHY.

The FVP breccia comprises angular clasts of pumice filling structural synclinal troughs between obsidian spines or ridges. Void size varies from coarsely vesicular(1 - 2 mm) to finely vesicular (0.2 mm). The FVP/Tuhua sequence contact is marked by a dry plinian tuff (unit A of Houghton and Wilson, 1986) dipping 22° N marking the tapering northern edge of the 8 ka flow, and also dips 3° E parallel to the longitudinal flow axis. The maximum thickness observed for the clast supported FVP breccia is 12 m (Fig. 5.17b). The contact between the FVP and OBS comprises broken or semi detached clasts of interfoliated obsidian and finely vesiculated pumice, and dense obsidian blocks.

The OBS layer stratigraphy is best shown at section C (Fig 5.17c) largely comprises dense black obsidian, vesiculated with high aspect ratio voids marginal to FVP-derived breccia pockets, and with pinkish-brown and finely microvesicular yellow glass and spherulitic obsidian (spherulites ≤ 1 mm diameter) bordering the RHY layer. The OBS layer contains abundant primary voids and tubes, and well preserved grooves and surficial cracks. In cross-section, the longitudinal OBS ridges usually have a devitrified rhyolite centre with a vesiculated obsidian margin containing high aspect ratio voids, and gas blisters with glassy intravoid septa interlayered with dense obsidian or brecciated obsidian and rhyolite. The latter forms corridors between flow ridges (Fig. 5.17d) representing either:

a. tension cracks in the original carapace, where during flow the stratigraphy overturned, and marginal RHY/OBS fabrics became brecciated. As the breccia arose through the cooler more rigid OBS layer, the obsidian fragmented and sections were rafted; or
b. fractured synclinal troughs in which obsidian avalanched down rising flow ridges and mixed with vesiculated obsidian and flow banded rhyolite from the OBS/RHY boundary.

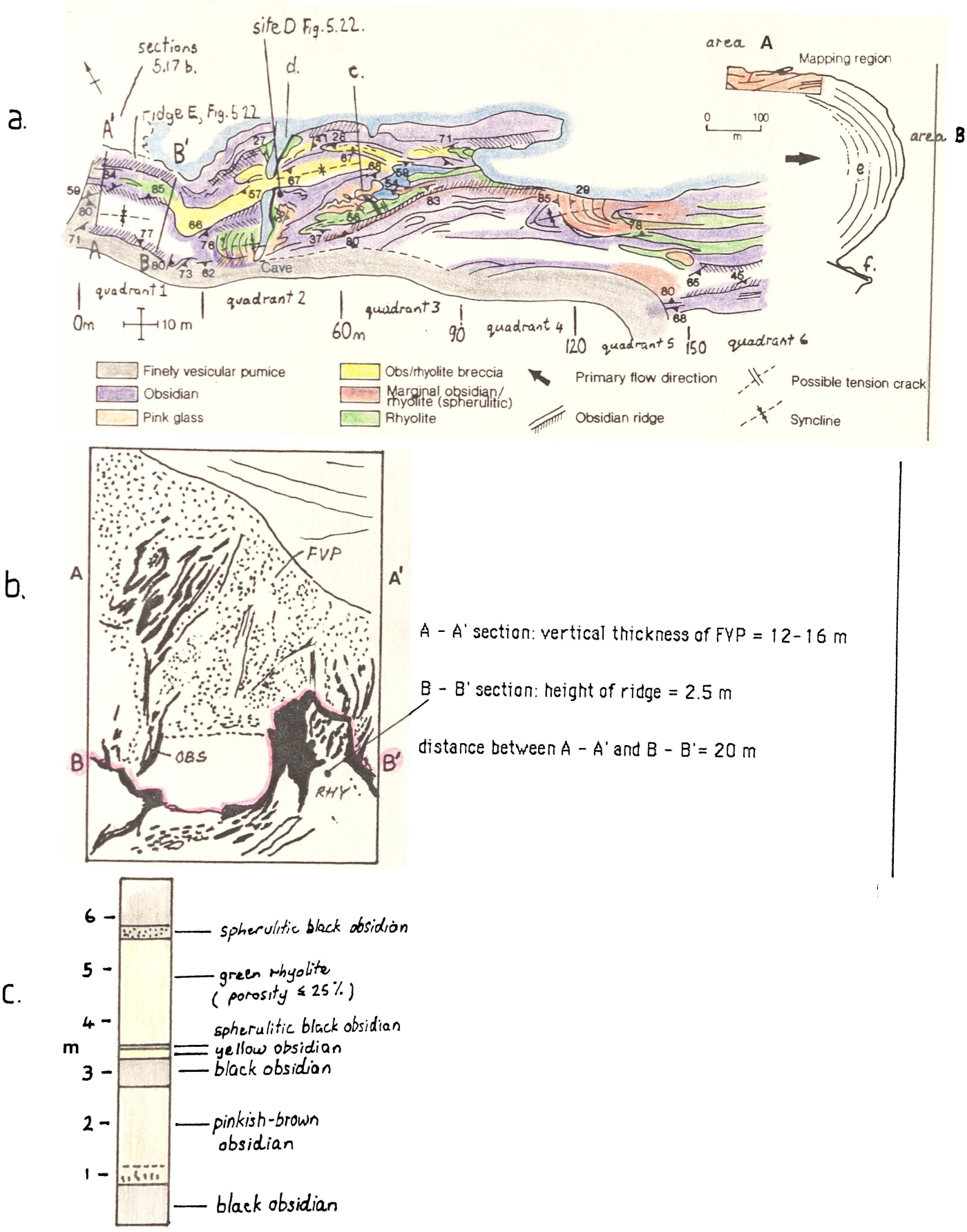

Fig. 5.17. Parekoura Point

a. Structural map of the northern margin of Parekoura Point.

b. Transects A and B; a trough containing FVP breccia between two obsidian ridges with a central rhyolite core (B'), quadrant 1

c. Transect C, quadrant 3; a lateral transect showing contact relations on the margin of a brecciated rhyolite core.

d.

e.

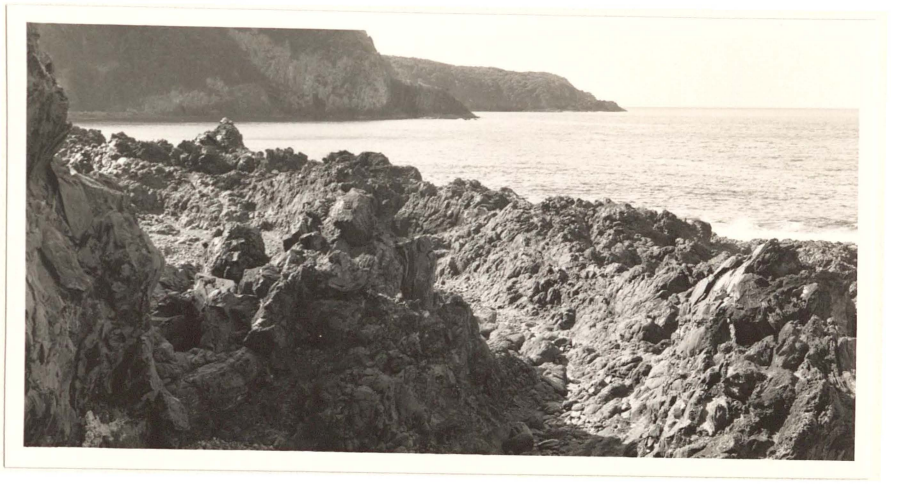

f.

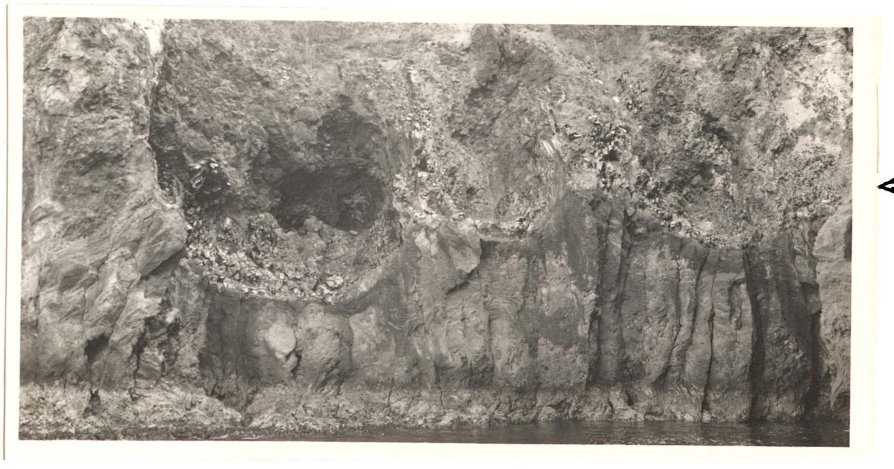

d. Transect D, quadrant 2; - a fractured syncline showing brecciated obsidian and rhyolite along the synclinal hinge-line between two flow ridges capped with obsidian.

e. Curvilinear obsidian and rhyolite flow ridges as fractured synclines and rampart structures.

f. Cliff section parallel to the central flow line (primary flow direction) showing the folded structure of the upper flow stratigraphy: FVP in troughs, lined with obsidian (compressed anticlines as spines), and columnar jointed rhyolite. Photographs courtesy of T. Clemm.

The outcrops of rhyolite occur either in exposed sections across ridge ends (e.g. section B-B') or as elongated exposures flanked by obsidian parallel to flow ridges. Usually the foliation is steeply dipping or the rhyolite brecciated, suggesting the fluid injection of lava as spines (that later brecciate) between the more brittle crust, or fracturing and compression of structural anticlines with the fold axial plane and fracture plane coinciding (cf. Fink, 1980; 1983). Foliation is steeply dipping usually toward the central flow line.

Beyond quadrants 1 - 6 the flow ridges change strike direction from 089° to 024° and dip inland toward the inferred vent (Fig. 5.17d). Texturally the pantellerites are less varied than those of the mapped zone on the northern margin of Parekoura Pt., and the OBS spines of the upper carapace generally contain fewer primary voids with rare gas blisters up to 0.65 x 0.28 x 0.27 m size steeply inclined (e.g. 045/53° NE).

The cliff section south of Parekoura Pt. (Fig. 5.17f) represents a longitudinal section through part of the 8 ka flow confirming the folded structure of the upper flow. Thus area B of Parekoura Point (Fig. 5.17a), represents a section across basal OBS and upper foliated RHY, through a series of rampart structures (cf. Cas and Wright, 1987), as fractured folds, whereas area A is a compressional flow margin comprising longitudinal ridges with a complexity of flow structure (ie. greater brecciation and vesiculation).

A model describing the sequence of events primarily from structural evidence at Parekoura Point carapace section will be outlined in section 5.8.

5.7.5. Composite profile interpretation - 8 ka flow.

The following locations provided data from which the composite profiles are composed: Parekoura Point - a composite section providing the best exposure of FVP, upper OBS, and upper RHY; Halls Pass - upper OBS, RHY lower OBS, and 8 ka tephra; and Overhang - lower RHY, OBS and fused upper 8 ka lapilli.

Fig. 5.18 shows the wide range of porosities (5 - 50%) for the FVP breccia (average density, 1.1). The wide range of clast porosities implies a mixing of originally equant blocks during avalanching into structural troughs. The wide range of vesicularity is also evident by the variable Rv values suggesting locally variable vesiculation in the FVP layer giving rise to differing void populations. For example, the obsidian-rich lineations in the flow lineated FVP contain voids of lower aspect ratio (Rv $\leq$ 5) and a larger inter-void distance in contrast to the higher porosity zones with at least 2 populations of voids. Those with the highest aspect ratio deflated earlier in the flow history and are deformed around the margin of the later lower aspect ratio voids that inflated in a more viscous froth.

The clast aspect ratio values are uniform suggesting that fracture of the FVP occurred within a fairly narrow time interval late in the flow history.

Between the FVP and OBS layer, a sharp increase in density and decrease in porosity shows as a marginal zone with contrasting inferred rheological properties. For example, at section B at Parekoura

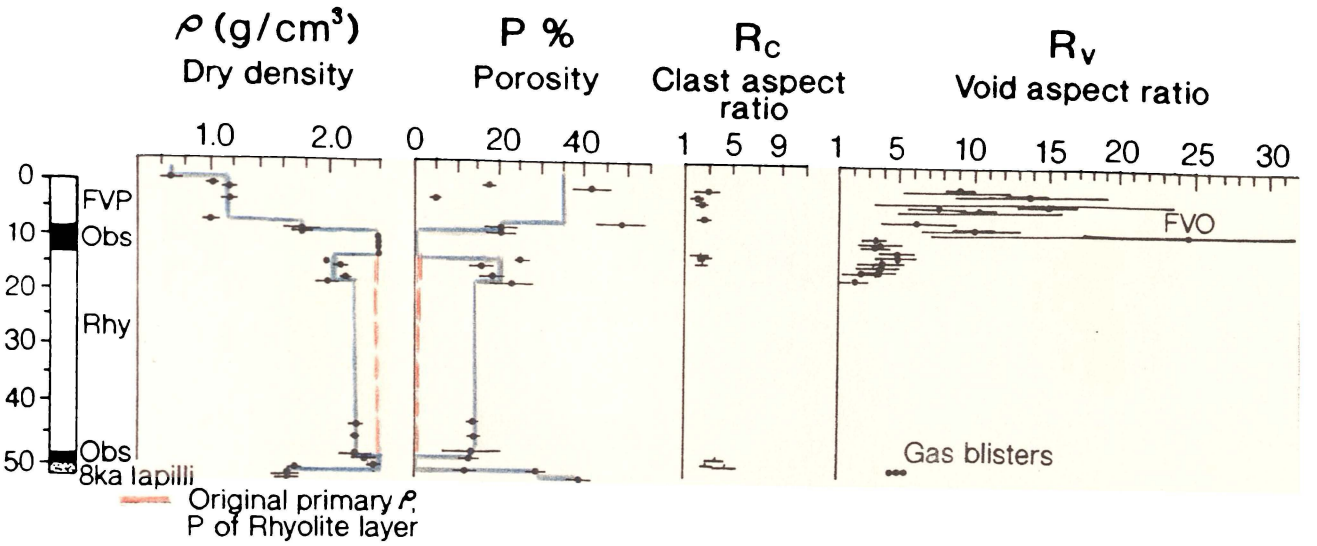

Fig. 5.18. Dry density, porosity, clast aspect ratio and void aspect ratio profiles for the 8 ka flow.

Pt., a finely vesicular obsidian with large Rv values occurs sandwiched between dense OBS and pink glassy microvesicular breccia. These vesiculated layers act as zones of differing rheological behaviour. From larger-scale flow movements, both layers may be deformed. However, the obsidian layer may show small amplitude tight disharmonic folds whereas the pumiceous layer of higher viscosity from surface tension forces between suspended gas bubbles, shows lesser intralayer deformation. Rv values within the OBS layer (of 3 - 4) decrease in the upper RHY/basal OBS layer breccia, to values of about 1 - 2. Below this level (10 m depth) primary vesiculation is suppressed. The only other evidence of primary vesiculation within the entire flow thickness is basal gas blisters, formed from volatiles within the upper 8 ka lapilli during fusion by the overriding lava. The 15% difference in porosity between the OBS layers and the central rhyolite is due entirely to secondary vesiculation on devitrification of the groundmass. Clast aspect ratios within the RHY layer in zones of local brecciation are uniformally low (Rc = 2) in contrast to the basal clasts at the Overhang and those in the fused upper 8ka fall lapilli unit under high temperatures and thermal gradients. While small scale deformation of clast shapes occurred at the base of the 8ka flow, rheomorphism of the fused basal lapilli did not occur, unlike the Ruru Welded Tuff at Halls Pass where mean Rc ~ 20 - 22 and standard deviations are large. Here, the dark glassy fiamme have tapered ends and deform around angular vesiculated clasts of 3 - 5 mm size. Initial aspect ratios are unknown but Ri values of 1 - 4 may be appropriate for two mutually perpendicular two-dimensional surfaces (Fig. 5.19). However high Rc values of between 7 - 60 with long axis declinations deviating less than 10° indicates that the Rc values are greater than from compaction alone and hence rheomorphism must have occurred. A more detailed account of the Ruru Pass welded tuff may be found in Houghton et al. (1985b).

Microlites (Fig. 5.20) appear to be subdivided into 3 discrete populations corresponding to the FVP, OBS and RHY layers respectively. Rod-shaped elongated microlites occur sparsely in the FVP layer

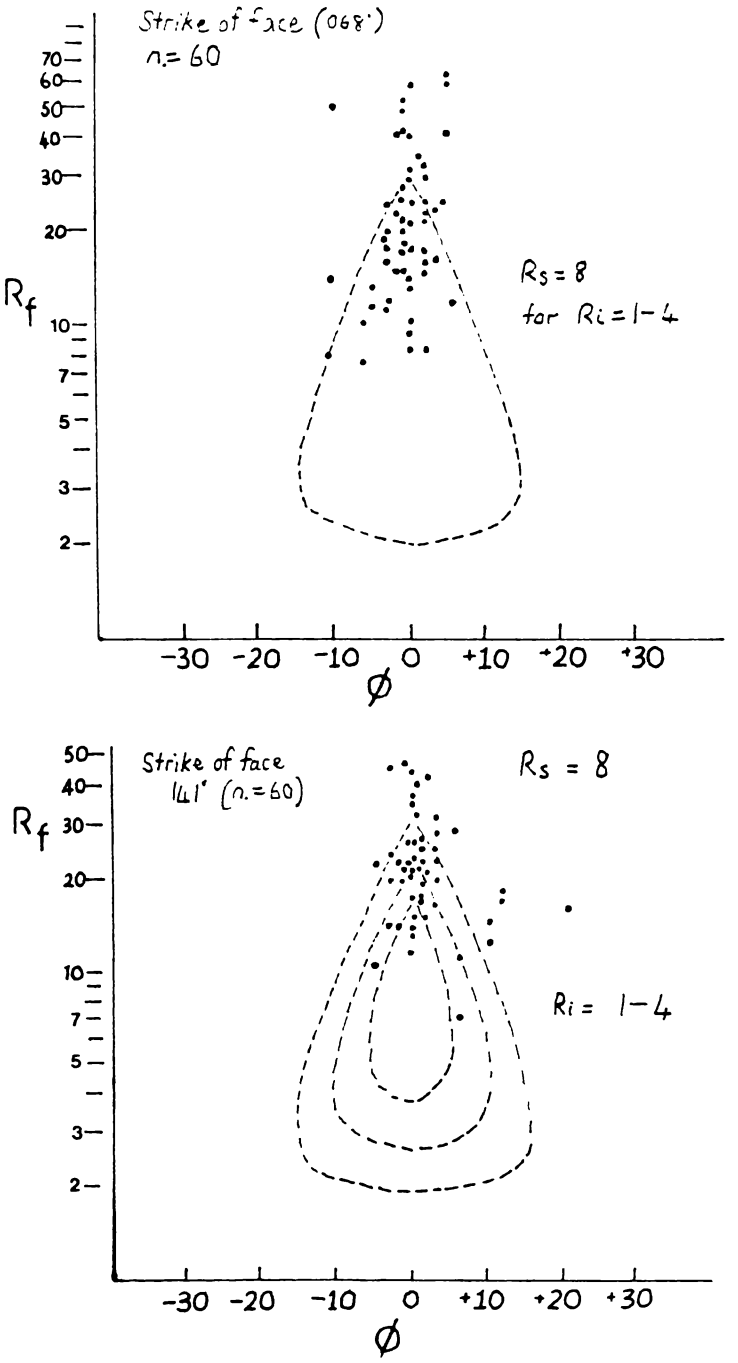

Fig. 5.19. Rf/ϕ for two mutually perpendicular vertical faces of the Ruru Pass welded tuff. Theoretical curves of Rf vs. ϕ are from Dunnet (1969). Ri values of 1 -4 represent the initial shape ratios of the distribution for Rs (the value of the strain ratio) of 8. The Rf/ϕ data for the Ruru Pass welded tuff exceeds the field constrained for maximum strain from compaction alone for Rs = 8.0. Samples removed from outcrop and cut parallel to bedding planes also show a preferred orientation of long axes of fiamme. Thus, rheomorphism of the tuff must have occurred during emplacement or after emplacement. This contrasts with the Thera welded tuff in Fig. 12 of Sparks and Wright (1979) in that its deformation was compactional only.

but several populations occur in the OBS layer. The location of large overlapping laths ~ 85 μm long in spherulitic obsidian bordering the RHY layer suggests that these crystals formed after the flow was emplaced because crystals of this type do not occur anywhere else within the flow stratigraphy. In

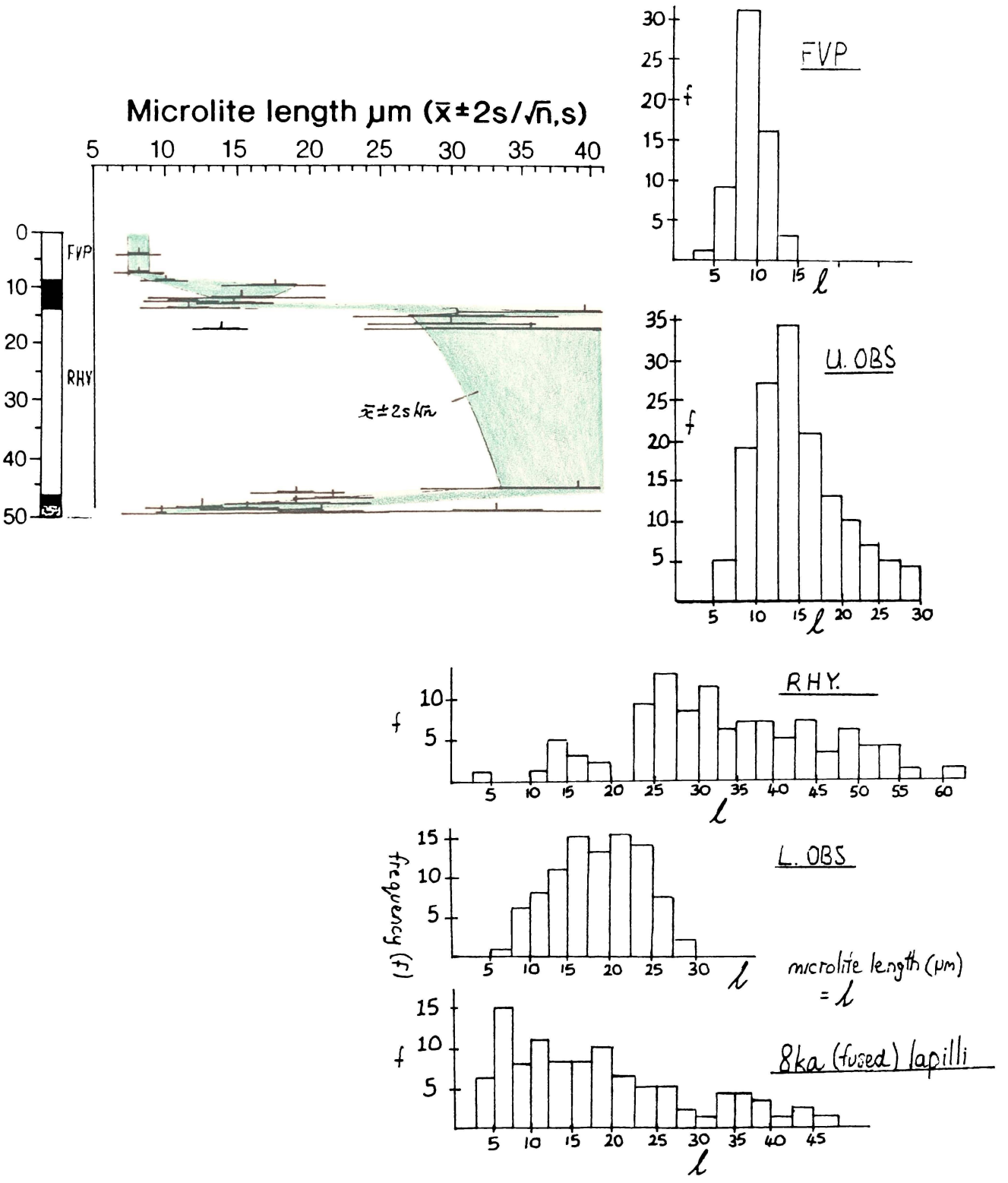

Fig. 5.20. Microlite length profile and frequency histograms for fabric units of the 8 ka flow.

addition to the population that formed during magmatic ascent, the differences in length of the elongate rod-shaped population, as for the Panui and Pre-8 ka flows, suggest that the crystallisation history is partly dependent on the thermal history of the flow.

5.8. Emplacement Model.

The 8 ka flow is inferred to be spatter fed. The flows comprising the precaldera shields (e.g. Okawa Pt., Tumutu Pt) cascaded down steep slopes and thin distally, with each flow separated by pyroclastics (possibly fused) or orange paleosols. By analogy to the precaldera shield flows, the Pre-8 ka flow may have been spatter fed. The following emplacement model summarised in Fig. 5.21 is constructed largely from the 8 ka and Pre-8 ka flows with carapace processes largely from structural observations and measurements at Parekoura Pt. Further discussion on a spatter fed emplacement mode occurs in chapter 9.

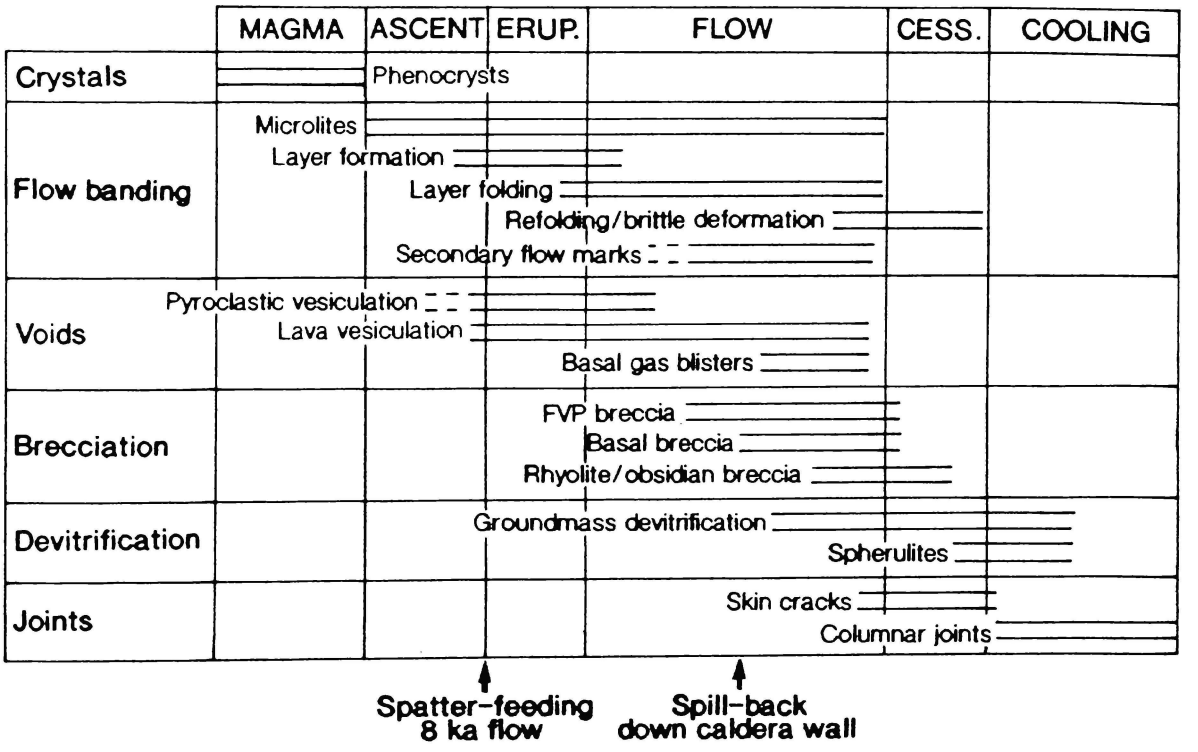

Fig. 5.21. An emplacement history for Mayor Island flows.

Phenocrysts (7.1% Panui, 3% pre-caldera lavas, 0.6 % Pre-8 ka flow) formed in the magma chamber, with quartz becoming embayed on magmatic ascent. The 8 ka flow is aphyric. Microlites formed under progressively increasing undercooling segregated into microlite-rich and -poor layers that flowed around pre-existing phenocrysts. The Panui flow and the Opo Bay tuff cone formed from the eruption of gas-poor magma that fragmented by magma-water interaction (shallow steam explosions) rather than by vesiculation alone (Houghton pers. comm., 1989). Unlike the 8 ka flow there is no physical

evidence for a spatter fed origin. However, vesiculation of the gas-poor magma occurred prior to, during, and after eruption as is evident from several populations of primary voids in the FVP zone. However vesiculation was only sustainable in the outer 6 m of the flow.

The 8 ka flow was preceded by the 8ka fall lapilli from an open-vent fountain which pulsated in height just prior to the emplacement of the lava from an hawaiian-type column. Vesiculation within the lapilli occurred within the top 300 m of the conduit. However, during magma uprise, the pantellerite did not inflate into a foam as is normal for calc-alkaline lavas such as Ben Lomond or the Inyo Domes. The very low water content precludes the formation of a foam. The Mayor Island magma was fluid enough to easily vesiculate and fire fountain, with a high but uniform textural variety and evidence of very rapid vesiculation at the time of fragmentation during strombolian and hawaiian-type eruptions (Houghton pers. comm., 1989).

As the 8 ka flow sheet emplaced, the flow carapace was thrown into a series of surface folds. The flow margin experienced circumferential tensile stresses on radial compression at the margin of the expanding flow sheet. This was responsible for the development of primary flow ridges or ogives - concentric curved ridges concave in the upflow direction, and their compression and fracture during ridge uprise. Secondary circumferential tensile stresses caused:

a. elongation of primary voids parallel to local flow directions, e.g. quadrant 2, Parekoura Pt., 248/ 10^{o} - 16^{o} E or W;
b. divergent or oblique extrusion (Fig. 5.22).

Local scale flow marks, recording secondary movement from primary compressional flow shortening of the margin in response to cooling, is evident as:

a. grooves or striae on obsidian inter-folial surfaces;
b. flow marks coincident with elongated surficial voids;
c. small-scale roller-like secondary crenulations on the limbs of primary folds as troughs or on the limbs of secondary asymmetric folds on trough limbs.

These features may have differing orientations on flow layers forming the margins of a syncline in response to differential slip during syncline formation.

Anticlines were compressed during uprise and became obsidian spines with a rhyolite core. Adjacent to zones of extension (synclinal troughs), anticlines were fractured and elongated rhyolite cores were formed. In addition, primary tension cracks parallel with synclinal troughs and flow margins locally disrupted the flow stratigraphy giving rise to brecciated OBS and RHY marginal fabrics. Some synclinal cores show compression at their hinges evident from tight asymmetric folds. Later processes caused secondary skin tension cracks perpendicular or oblique to pre-existing flow marks and shear planes bisecting or dislocating earlier flow folds. Occasionally squeeze-up structures form between polygonal skin cracks of 20 - 100 mm depth.

On lava flow carapaces (e.g. Parekoura Pt., Te Matawhero Point - correlative with the pre-caldera Pre-8 ka flow), inter-layer variation occurs in the upper OBS layer, causing zones of contrasting rheology

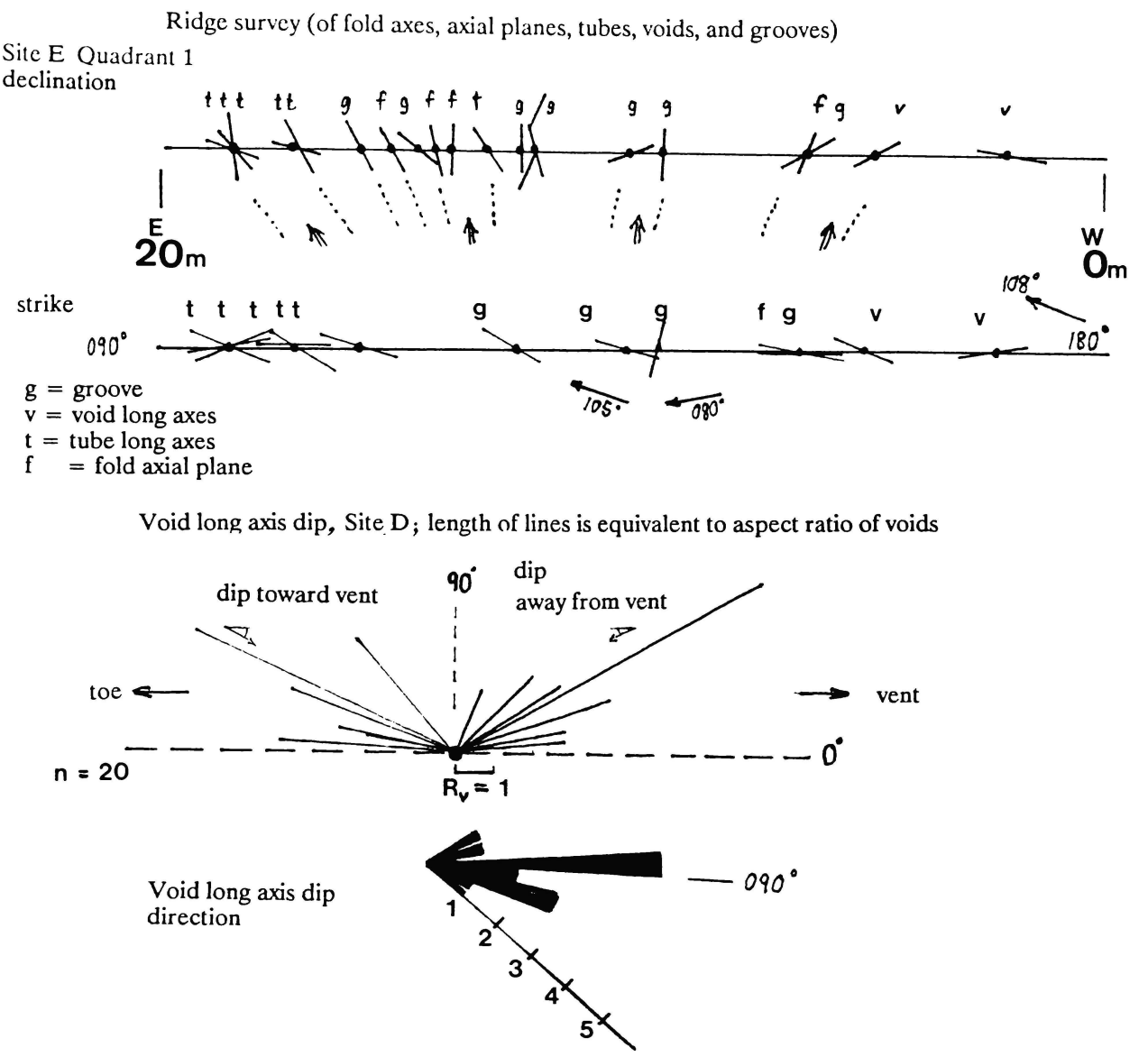

Fig. 5.22. Declination and strike of secondary flow features (e.g. long axes of primary voids, flow marks, fold axial planes) indicating localised flow movement along ridge E, quadrant 1, Parekoura Pt., (Fig. 5.17a). Locally, void long axis dip as at site D is inclined toward or away from the inferred vent in response to secondary local flow motions on circumferential compression of primary flow ridges.

from differences in vesicularity and inferred subtle differences in volatile content. Brecciated pumice and finely vesiculated pink glass occur between competent but ductile obsidian layers. Rotation of basalt xenoliths can occur between dense obsidian, vesiculated obsidian and pumice breccia from late flow phase differential slip via local tensile movements between layers of contrasting rheology.

Asymmetric flow folds and distorted primary voids in the upper OBS/RHY margin suggest that cooling and flow deformation proceded in tandem with the emplacement and compression of spines as elongate flow ridges. Brecciation of the upper margin of the carapace OBS layer occurred during and after the development of surface polygonal cracks. In addition to brittle failure of the FVP carapace, flow lineated FVP and OBS blocks avalanched down the flanks of rising spines or ridges collecting into structural troughs. The blocky flow front was overriden by the advancing lava during emplacement causing the formation of basal breccias. A mobile flow base and high thermal gradient contributed to the fusion of the upper portion of the 8 ka fall lapilli. The lapilli was initially hot and volatile-rich at

emplacement. During fusion, Rc values, glass% and density increased. Volatiles were trapped at the lapilli/lava contact as gas blisters which recorded the direction of flow of the overlying lava sheet. Also during spill-back down the caldera wall, refolding and boudinage occurred in the basal OBS/RHY interlayered contact. Available evidence indicates that spill-back occurred during the middle flow-phase of lava emplacement.

The presence of rhyolite blocks in the upper part of the basal breccia, Pre-8 ka flow and the inter-ridge rhyolite/obsidian breccias of the 8 ka flow at Parekoura Pt., suggests that devitrification of the RHY layer commenced prior to the emplacement of both late flow-phase breccias and that devitrification of the groundmass commenced before flow cessation at high temperatures. Spherulites of about 1 mm in size occur within the upper OBS/RHY layer margin that overprint primary flow textures having formed during flow cessation. No explosion breccias like those at Ben Lomond were formed, although the evidence of secondary volatile release is observable in all three flows studied and from trace element profiles described and interpreted in chapter 6.

Joints within the central RHY layer formed last from inward propagating tensile failure perpendicular to cooling surfaces. Variations in cooling within the flow centre caused the curving of interior columns.

CHAPTER 6.

INTRAFLOW CHEMICAL VARIATIONS AND INFERRED VISCOSITY OF PANTELLERITIC LAVAS.

6.1. Introduction.

In contrast to the calc-alkaline Ben Lomond lavas, the following lines of evidence from pyroclastic and lava flow sequences on Mayor Island suggest a more fluid behaviour of pantelleritic lavas. Flows have a steep basal slope and thin away from source. Spill-back of the 8 ka flow down the caldera wall and fusion of the upper part of the pre-flow airfall lapilli suggest basaltic-style spatter feeding of the flow. Unlike Ben Lomond, no significant spherulitic fabrics occur (Fig. 6.1). The lack of explosion breccia deposits indicates low volatile contents of flows. Fluidal fold structures and carapace spine structures are similar to andesitic flow features. Microlite length variations occur throughout the flow profile indicating that microlite crystallisation was influenced by the thermal history of the lava during emplacement.

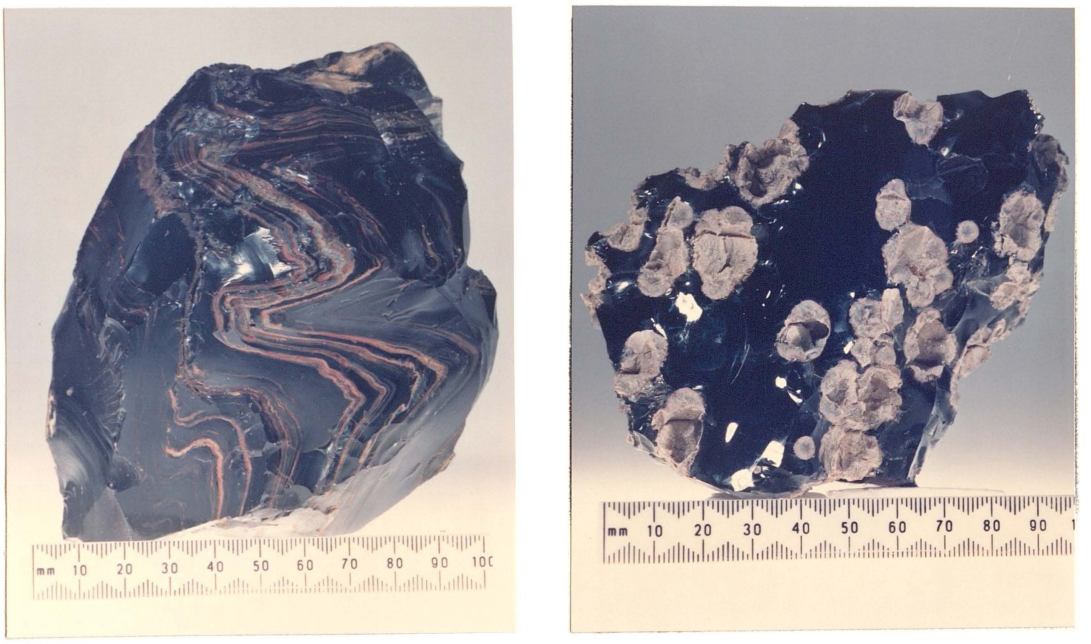

Fig. 6.1. Two contrasting obsidian fabrics:
a. flow ridge obsidian from the 8 ka flow, Parekoura Point showing tight asymmetric flow folds;
b. spherulitic obsidian, Ben Lomond.

In addition major element chemistry is significantly different from the calc-alkaline flows in that the sum of Na_2O and K_2O exceeds Al_2O_3; Na^+ and K^+ are silicate polymer bond breakers promoting a lower polymerisation of the melt. For three Mayor Island flows, Panui, Pre-8 ka; and 8 ka, 25 analyses of major and trace element oxides representative of each fabric unit enabled the identification of intraflow chemical variation. Together with estimates of temperature, water and halogen content, the viscosity

at emplacement is calculated and the rheological implications for eruptive mechanism and post-eruption emplacement history is addressed.

6.2. Flow Volatile Contents and Implications for Degassing.

Karl Fischer analyses of total water on fresh obsidians for Panui and Pre-8 ka flows, and additional estimated H_2O^+ for the 8 ka flow profile is illustrated in Fig. 6.2a. Values for OBS layer fabrics are very low, particularly for the 8ka flow where negative values suggests that either the effect of an increase in weight on oxidation of ferrous to ferric iron (total Fe ~ 6 wt.%) outweighs the loss in mass of H_2O, or additional volatiles other than water are lost, or that the water content is within the error of determination.

For the 8ka flow, enrichment in LOI occurs in the FVP owing to an increased surface area per unit volume attracting low temperature H_2O^-.

Karl Fischer values for total water of 0.05% (Fig. 6.2b) are typical of the black obsidian in upper and lower layers, and are inferred to be characteristic of the entire flow thickness prior to devitrification of the flow interior. The pink and yellow obsidians fringing the RHY layer, show a higher estimated H_2O^+ and LOI owing to incipient devitrification and a microvesiculated fabric. Volatile contents of the RHY layer are high owing to secondary vesiculation and/or hydration associated with isobaric crystallisation. Estimated H_2O^+ for the 8 ka lapilli at 0.4% approximates the bound magmatic water content prior to the eruption of the 8 ka flow. This value is in contrast to that for calc-alkaline plinian deposits. Dunbar and Kyle (1986) found high water contents in airfall obsidian (from 0.3 - 2.6 wt%), and interpreted the obsidian lithics as quenching at depth prior to total degassing, hence giving a minimum estimate of pre-eruptive volatile content of the magma. For the 8 ka lapilli, consisting entirely of pumice, the estimated H_2O^+ from LOI between 400-1000°C provides a minimum estimate of the volatile content prior to the emplacement of the 8ka flow.

The LOI trends listed in Table 6.1a for the Panui and Pre-8 ka flows are similar to that of the 8 ka flow.

Pantelleritic magmas are usually reported as being dry: bulk analyses give low water contents (MacDonald and Bailey, 1973); no hydrous phenocryst phases are observed except late arfvedsonite (Nicholls and Carmichael, 1969); eruptions are generally not explosive (Houghton et al. 1985a); the halogen content is high (Ferrara and Treuil, 1974); and petrographic textures in natural samples match well with those from experiments on dry pantellerites but not with water saturated compositions (Bailey et al. 1974). However, from ion microprobe analyses of trace elements within matrix glass and glass inclusions in anorthoclase and quartz, Kovalenko et al. (1988) reported water contents of 4.5 ± 0.5% and 0.5 ± 0.1% respectively for inclusion and matrix glasses, pointing to a wet pantelleritic melt origin. The alternatives stated by Kovalenko et al. (1988) to the dry pantellerite scenario are:

a. low water contents means that most water outgassed during eruption;
b. the stability of hydrous phases is reduced if $aH_2O < 1$ even though abundant water is present in the melt;

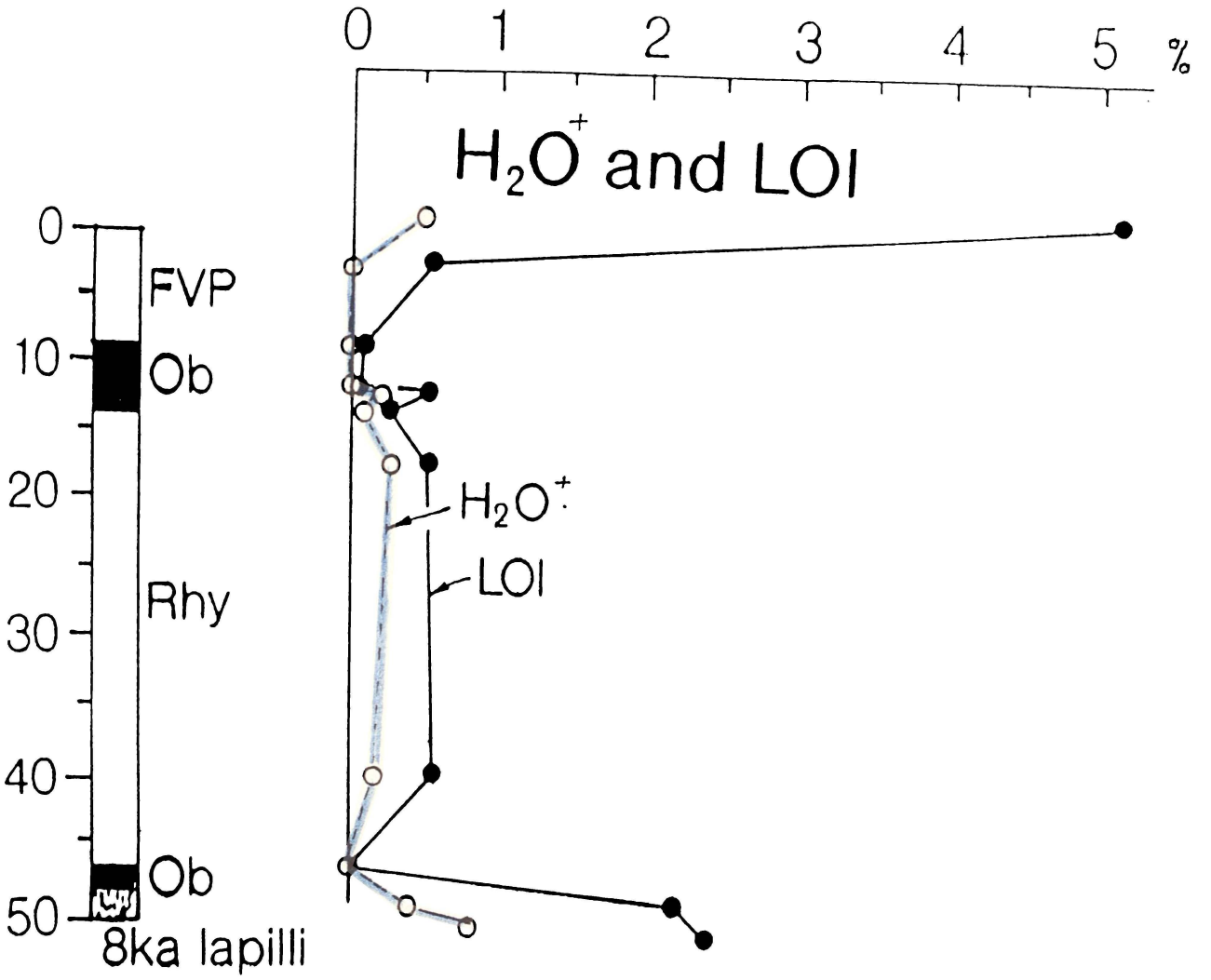

Fig. 6.2a. H_2O^+ and LOI for the 8 ka flow. H_2O^+ is estimated from LOI 400-1000°C giving an upper limit for bound water. LOI was determined via tetraborate flux bead at the analytical facility, Victoria University of Wellington.

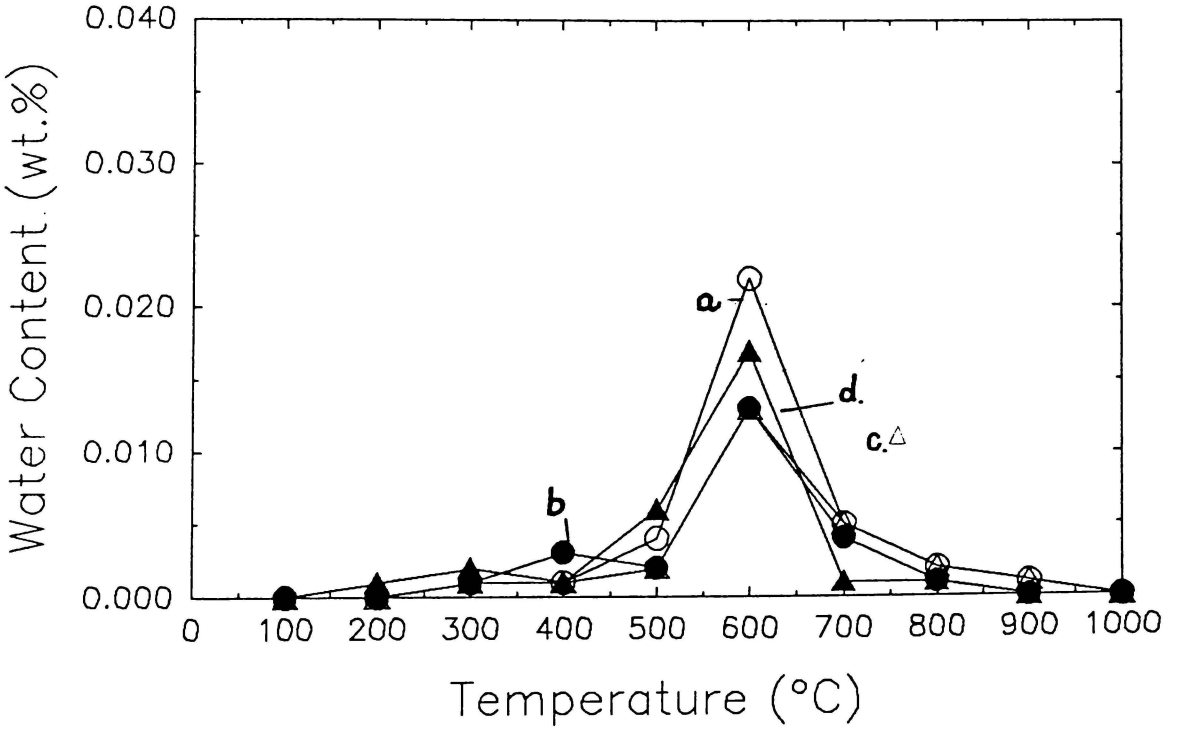

Fig. 6.2b. Water content (wt%) versus pyrolysis temperature for four Mayor Island obsidians:
(a) = upper OBS, 8 ka flow (total water = 0.059%);
(b) = lower OBS, 8 ka flow (0.057%);
(c) = upper OBS, Pre-8 ka flow (0.057%);
(d) = upper OBS, Panui flow (0.07%). The ~5% by volume crystals were not separated from the glass. Samples were analyses via Karl Fischer tetration by H.R. Westrich, Sandia Laboratories, Albuquerque.

c. the Taupo ultraplinian and the comparatively mild Obsidian dome eruptive products give nearly identical results of 4.5 and 4.1% water respectively by ion microprobe analysis suggesting that high water contents are not sufficient to produce violent eruptions;

d. because Cl as well as water has been lost from the melt during outgassing but the amount of Cl and Na loss is minor, which testifies to the high solubilities of halogens in the peralkaline melts;

Further results (Kovalenko et al. 1989) for ten different pantellerites give an average water content of approximately 1.4%, significantly lower than the 4.5% value from the preliminary study of Kovalenko et al. (1988).

One explanation for the high result of 4.5% water in the preliminary study, was that enriched water values occurred owing to ion concentration gradients (Druitt et al. 1982). Despite the limitations of fluid inclusion methodology (refer Hervig et al. 1989), no evidence of concentration gradients occurred in the sample examined (Hervig pers. comm. 1989).

Degassing of water is expected on eruption but the pantellerites studied by Kovalenko et al. (1989) did not show a loss of F and a small depletion of Cl during this event.

An upper limit in water content for the 8 ka lapilli (porosity = 30%) is approximately 2% based on the method of Sparks (1978), whereas the lower limit is based on LOI (400-1000°C) being 0.4%. Therefore the difference in volatile content between the magma chamber and the sample was between 50 - 7.5% of the total amount of degassed water inferred for the calc-alkaline Ben Lomond system.

6.3. Temperature Estimates.

As Mayor Island lavas contain no Fe-Ti oxide pairs, temperature of the magma and lava was determined by other means. The glass transition temperature determined by DTA was approximately 850°C. In contrast to Ben Lomond the hysteresis effect, between the actual glass transition temperature (T_g) during original annealing and the value determined from the reheating and fusion of a powder by DTA, is smaller.

The appearance of the sample after fusion was unlike that of the lower temperature Ben Lomond lava. Rather than being tack-fused (i.e. grain to grain contact), the samples were completely fused and had undergone viscous deformation as shown by the smoothed and rounded surfaces of the c. 2-5 mg samples. Thus, the appearance of the fused samples alone implies a more fluid lava rheology. Also, in contrast to calc-alkaline lavas of equivalent flow thickness such as Obsidian Dome, northern California, the larger thermal gradient between the central and outer flow margins would contribute to a longer time interval for viscous deformation of the flow interior. By rearranging equation (4.17), a value for t (the time taken for the RHY layer to cool below the glass transition temperature close to 700°C), is 10.5 years (8 ka flow) versus 6 years for Obsidian dome, assuming T_o = 950°C.

The dendritic groundmass textures of basaltic xenoliths within the pre-8 ka and 8 ka lavas suggest the quenching of a high temperature magma within a lower temperature pantelleritic melt. Rutherford (1978) estimated the crystallisation temperature (via the method of Mathez, 1973) of the plagioclase within the basalt xenoliths was as high as 1300°C assuming P H_2O = 0.

The ferromagnesian assemblages in peralkaline rhyolites indicate that they start to crystallise at temperatures approximately between 900 and 1025°C and with oxygen fugacities close to those defined by the fayalite-magnetite-quartz buffer (Carmichael, 1967). As the temperature decreases and peralkalinity increases, the liquids enter a no-oxide region in which aenigmatite is the common ferromagnesian phase (Fig. 6.3). Many peralkaline rhyolites will start their crystallisation within the no oxide field but this depends on temperature, oxygen fugacity, and peralkalinity (Na_2O + K_2O / Al_2O_3) or activity of $Na_2Si_2O_5$ (Nicholls and Carmichael, 1969).

Melting experiments at standard pressures were conducted on obsidian powders from the Panui and 8 ka flows at 1000 and 1050°C respectively. Partial melting of crystal fragments within the fused glass occurred for the Panui sample. The aphyric 8 ka flow sample was fused at 1050°C for three hours, showing viscous deformation and remelting of microlites. Thus both these values provide upper limits on the emplacement temperature for Mayor Island lavas, and a temperature of 950°C is a realistic estimate. This estimate assumes that the volatile content during crystallisation of the

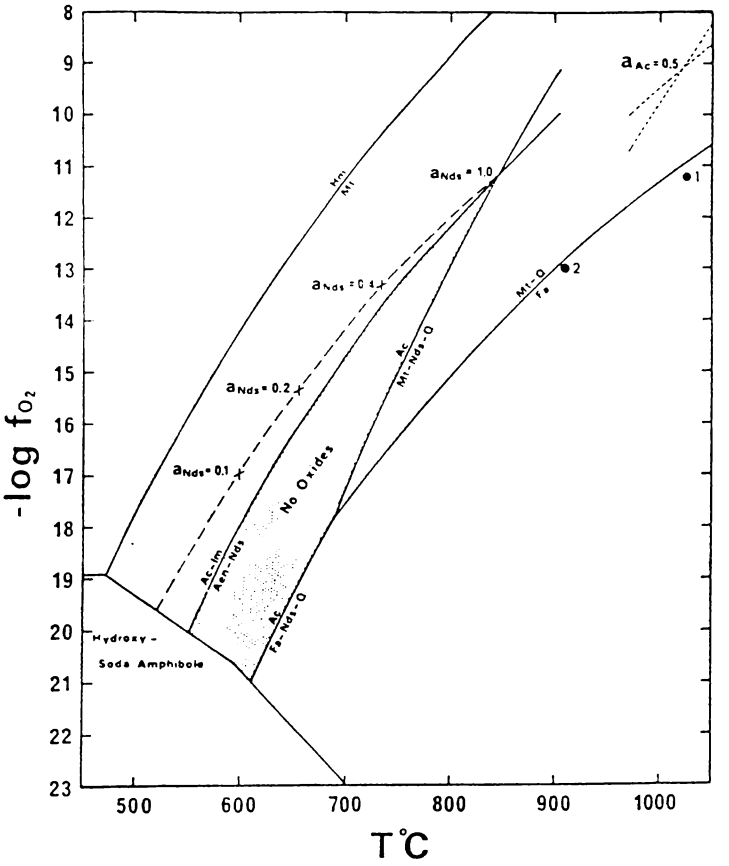

Fig. 6.3. Fugacity of oxygen vs. temperature diagram showing the 'no oxide' field. Abbreviations are Hm hematite; Mt magnetite; Ac acmite; Q quartz; Fa fayalite; Nds sodium disilicate; Aen aenigmatite; Im ilmenite. The shifting of the 'no oxide' field depends on the pyroxene composition. If the pyroxene is not pure acmite but a solid solution with an acmitic component, the intersection of the two reaction curves will shift to higher T and oxygen fugacity (Nicholls and Carmichael, 1969).

phenocrysts (sanidine, aenigmatite, pyroxene, quartz for Panui) was low, and that the volatile content at emplacement was comparable with that of the sample.

Blocks of Mayor Island obsidian when heated to 1000°C vesiculate and show evidence of viscous deformation. Mayor Island obsidian blocks expand by 370% volume and block thickness by 50% when heated to 1000°C. Inflation is initiated at temperatures of approximately 850°C. In contrast, Ben Lomond blocks expand by 600% volume and block thickness by 100% over a nine hour period after an initial lag-time of non-inflation for 2.5 - 3 hours. After inflation, the thickness of the peralkaline obsidian block collapses by 20% over a five hour period as the angular edges of the block become rounded forming a hemisphere (Fig. 6.4). Viscous deformation of the inflated Ben Lomond block is not evident.

Thus, microlite length variations, vesiculations and vesicle collapse at surface pressures can occur within the time frame of emplacement.

6.4. Intraflow Geochemical Variations.

Chemical variations in major and trace elements reflect to magma chamber origins, emplacement composition and post-flow secondary processes.

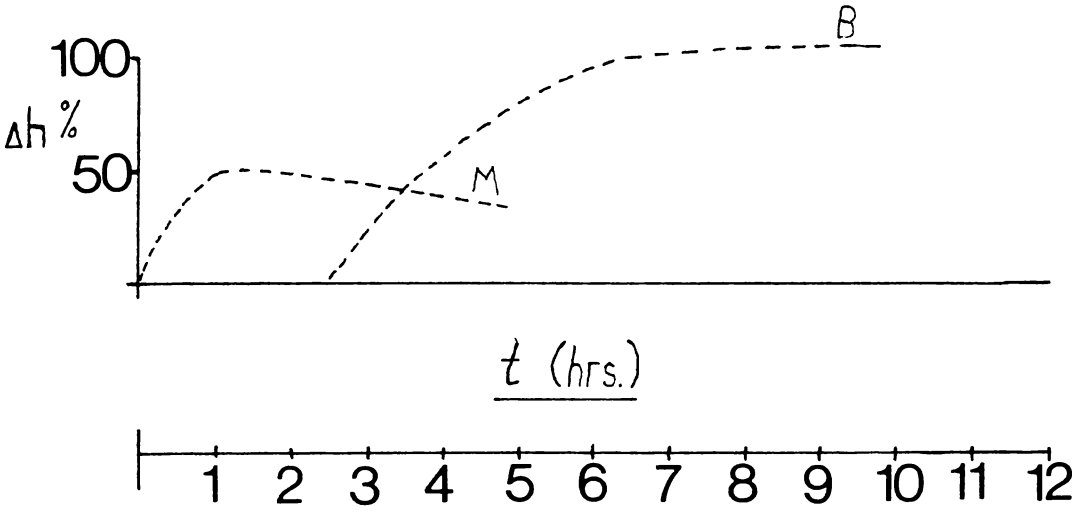

Fig. 6.4. Change in thickness (h%) during time for two obsidian blocks M (Mayor Island) and B (Ben Lomond) when heated to and held at 1000°C.

Samples selected showed no evidence of post-emplacement weathering. Samples from both coastal and caldera wall sections (Pighunters Pass exposures characterised by salt infilling joints) were washed with distilled water and oven dried at least five times. For sea water metasomatism to be manifest in chemical results, Na_2O and LOI of 7 and 5% respectively and Cl contents of 50,000 ppm (Weaver writt. comm. 1989) would be typical. Values for Cl, Na_2O and LOI were within the range of previously published Mayor Island analyses (Ewart et al. 1968; Nicholls and Carmichael, 1969; Houghton and Wilson, 1986).

The major element chemistry of the obsidian layer is significant for the following reasons. It is the unit least affected by isobaric crystallisation (for young rhyolites), and is potentially the least weathered as it has the lowest porosity.

For example, at Ben Lomond the chemistry of the OBS layer was uniform throughout the 30 m thickness of the unit. Also, apparently samples were unaffected by seawater metasomatism. For Mayor Island, the following assumptions were made to aid the interpretations of chemical profiles:

a. the chemistry of fresh black aphyric non-hydrated or non-vesicular obsidians are best representative of the eruptive composition of the lava;
b. if the chemical composition of the upper and lower OBS layers are similar then the lava flow was derived from one magma;
c. if the bulk chemistry of the OBS and RHY layers differ, then the RHY layer changed in composition from the original liquid (glass) during isobaric crystallisation.

The chemical composition of the Pre- 8ka flow closely approximates to that of the pre-caldera shield lavas (Houghton and Wilson, 1986). The 8ka and intracaldera post-C lavas have a lower SiO_2 content and higher peralkalinity (ie. $Na_2O + K_2O / Al_2O_3$) (Ewart et al. 1968; Macdonald and Bailey, 1973).

Twenty-six samples from three flows: Panui; Pre-8 ka; 8 ka were analysed by XRF for major element oxides and trace elements, and are listed in Tables 6.1a and 6.1b respectively.

6.4.1. Major element variability.

In contrast to Taupo Volcanic Zone calc-alkaline rhyolites such as Ben Lomond flow, SiO_2, Al_2O_3, Na_2O and K_2O show greater intra flow variation. All major elements have been adjusted to an anhydrous composition to eliminate variations caused by the differing LOI values between flow pumices (largely adsorbed low temperature H_2O^-) and obsidian fabrics.

For the Panui flow (Fig. 6.5), the major element concentrations comprising the upper and lower OBS layer are virtually identical, confirming that for a frozen lava unmodified by post-eruptive devitrification, the OBS layer chemistry is best representative of the eruptive composition of the lava. Also, it follows that the pre-eruptive composition of the lava is uniform. Enrichment and depletion factors for the RHY layer with respect to the OBS layer are appended to the profiles in Figs. 6.5 - 6.8. Slight enrichments occur in the RHY layers of the Panui flow for SiO_2, Al_2O_3 and K_2O. As both Fe^{2+} and Fe^{3+} comprise total Fe, and were not independently determined, profile interpretation of total Fe has limited value. The most significant variation, a 19% depletion in the RHY layer, is characteristic for the Na_2O profile.

Table 6.1a. Major element geochemistry, Mayor Island. Major elements (wt%) are tabulated on a volatile free basis. t = total FeO + Fe_2O_3 expressed as Fe_2O_3 * = original analytical values. Analyses 1-26 are listed below with sample description, fabric unit, sample site and Waikato University number.

Table 6.1b. Trace element geochemistry, Mayor Island. Duplicate pellets were made for each sample giving four measurements of trace element concentration per sample. Error bars represent two standard errors or 95% confidence interval. n.d. = not detected.

1 grey pumice (FVP) Panui flow, Tokomata Point (WT. 26833)
2 black obsidian (U.OBS) Panui flow, Tokomata Point. (WT.26834)
3 obsidian/rhyolite transition, Panui flow, Tokomata Point. (WT.26835)
4 green rhyolite (RHY), Panui flow, Tokomata Point. (WT.26836)
5 black obsidian (L.OBS), Panui flow, Te More-o-moiterangi. (WT.26837)
6 basal breccia (BR), Panui flow, Te More-o-moiterangi. (WT.26838).
7 Ruru Pass welded tuff (WT.26839)
8 Ruru Pass tack-welded basal pumice (WT.26840)
9 grey pumice (FVP), 8 ka flow, Parekoura Point (WT.26841)
10 grey pumice (with glassy obsidian bands) (FVP), 8 ka flow, Parekoura Point (WT.26842)
11 black aphyric obsidian (U.OBS) 8 ka flow, Parekoura Point (WT.26843)
12 pinkish obsidian (U.OBS), 8 ka flow, Parekoura Point (WT.26844)
13 yellow obsidian (U.OBS), 8 ka flow, Parekoura Point (WT.26845)
14 green rhyolite (upper RHY layer), 8 ka flow, Parekoura Point (WT.26846)
15 green flow-banded rhyolite (RHY), 8 ka flow, Halls Pass (WT.26847)
16 black aphyric basal obsidian (L.OBS), 8 ka flow, Halls Pass (WT.26848)
17 fused 8 ka lapilli, Halls Pass (WT.268849)
18 phreatomagmatic fine grained tuff (WT.26850)
19 pink pumice (FVP), Pre-8 ka flow, central Taratimi (WT.26851)
20 black aphyric obsidian (U.OBS), Pre-8 ka flow, central Taratimi (WT.26852)
21 dark green rhyolite (RHY), Pre-8 ka flow, central Taratimi (WT.26853)
22 rhyolite (RHY), Pre-8 ka flow, Pighunters Pass (WT.26854)
23 rhyolite (RHY), Pre-8 ka flow, Pighunters Pass (WT.26855)
24 black aphyric obsidian (L.OBS), Pre-8 ka flow, Pighunters Pass (WT.26856)
25 pink pumice (BR) Pre-8 ka flow, Pighunters Pass (WT. 26857)
26 brown tuff underlying Pre-8 ka flow, Pighunters Pass (WT.26858)

Table 6.1a. Major elements.

	1	2	3	4	5	6	7	8	9	10	11	12	13
SiO_2	74.80	74.92	75.01	75.62	74.91	74.90	73.61	73.45	73.62	73.47	73.37	73.42	73.45
TiO_2	0.22	0.22	0.22	0.21	0.22	0.22	0.24	0.25	0.22	0.22	0.22	0.22	0.23
Al_2O_3	10.08	9.89	9.92	9.97	9.92	9.92	9.48	9.42	9.75	9.73	9.72	9.66	9.66
Fe_2O_3†	5.04	4.77	4.93	4.97	4.79	4.81	6.25	6.45	6.0	6.0	5.97	6.02	6.01
MnO	0.09	0.09	0.09	0.09	0.09	0.09	0.13	0.14	0.13	0.13	0.13	0.13	0.12
MgO	0.04	0.11	0.04	0.06	0.13	0.11	0.02	0.05	0.04	0.03	0.05	0.03	0.04
CaO	0.18	0.17	0.17	0.18	0.19	0.45	0.23	0.18	0.22	0.21	0.22	0.22	0.23
Na_2O	5.20	5.51	4.90	4.44	5.42	5.24	5.75	5.55	5.71	5.91	6.03	5.99	5.96
K_2O	4.33	4.33	4.38	4.43	4.33	4.25	4.28	4.47	4.27	4.29	4.28	4.28	4.29
P_2O_5	0.01	n.d	0.01	0.01	0.01	0.01	0.01	0.02	0.02	0.02	0.02	0.02	0.02
Total*	98.45	99.65	98.09	98.44	99.83	99.50	98.47	98.07	99.93	99.83	100.01	100.09	99.69
LOI*	1.77	0.24	0.24	0.70	0.23	2.19	0.01	2.78	0.49	0.10	0.01	0.48	0.31

	14	15	16	17	18	19	20	21	22	23	25	26
SiO_2	72.86	73.66	73.57	74.05	75.00	74.71	74.88	75.01	73.38	73.65	73.37	73.49
TiO_2	0.29	0.23	0.22	0.22	0.22	0.22	0.22	0.22	0.22	0.26	0.22	0.24
Al_2O_3	10.12	9.91	9.72	9.64	9.56	10.41	10.23	10.51	9.56	9.86	9.59	9.64
Fe_2O_3†	6.14	6.13	5.98	5.92	5.47	4.47	4.47	4.49	5.93	6.10	5.93	6.06
MnO	0.13	0.13	0.13	0.12	0.10	0.08	0.09	0.09	0.12	0.13	0.12	0.13
MgO	0.32	0.24	0.06	0.11	0.40	0.09	0.04	0.10	0.06	0.20	0.05	0.09
CaO	0.49	0.28	0.22	0.26	0.23	0.28	0.19	0.20	0.23	0.37	0.19	0.28
Na_2O	5.31	5.03	5.81	5.44	4.81	5.23	5.40	4.94	6.25	5.14	6.29	5.66
K_2O	4.29	4.32	4.25	4.24	4.21	4.50	4.33	4.35	4.19	4.25	4.26	4.40
P_2O_5	0.04	0.05	0.02	0.02	0.02	0.01	0.01	0.02	0.03	0.03	0.02	0.02
Total*	99.86	100.07	99.33	99.85	99.86	99.81	100.08	98.64	99.95	99.67	99.45	100.01
LOI*	0.58	0.75	0.07	2.36	2.75	3.76	0.17	0.45	1.57	0.81	2.48	2.30

Table 6.1b. Trace elements.

	1	2	3	4	5	6	7	8	9	10	11	12	13
Sc	n.d	n.d	n.d	n.d	n.d	0.7 ± 0.6	0.4 ± 0.2	n.d	n.d	n.d	0.4 ± 0.3	n.d	0.2 ± 0.4
V	3.4 ± 0.9	3.3 ± 0.6	3.4 ± 0.4	3.1 ± 0.1	3.3 ± 0.6	4.0 ± 0.3	3.2 ± 0.6	3.3 ± 0.9	3.3 ± 0.5	3.9 ± 0.4	3.2 ± 0.4	3.7 ± 0.4	3.8 ± 0.4
Cr	0.8 ± 0.7	n.d	n.d	1.4 ± 0.5	n.d	0.9 ± 0.8	n.d	n.d	n.d	n.d	n.d	n.d	n.d
Ni	2.0 ± 0.5	1.3 ± 0.3	2.3 ± 0.1	1.6 ± 0.5	1.9 ± 0.7	1.8 ± 0.4	1.8 ± 0.4	2.1 ± 0.6	1.7 ± 0.1	2.1 ± 0.3	1.5 ± 0.6	1.7 ± 0.3	2.0 ± 0.7
Cu	9.0 ± 5.4	4.4 ± 0.2	4.8 ± 0.2	9.1 ± 0.7	4.4 ± 0.3	6.1 ± 1.6	4.6 ± 0.3	4.6 ± 0.3	5.0 ± 0.3	4.8 ± 0.4	4.3 ± 0.2	4.6 ± 0.3	4.7 ± 0.4
Zn	270.4 ± 3.2	260.4 ± 1.6	264.2 ± 1.1	283.4 ± 0.6	260.9 ± 1.7	276.9 ± 1.3	241.2 ± 6.7	250.4 ± 5.9	244.4 ± 6.6	244.5 ± 6.8	234.2 ± 2.4	243.8 ± 7.8	240.1 ± 5.5
Ga	32.2 ± 1.4	32.7 ± 0.4	33.6 ± 1.3	35.1 ± 0.6	33.1 ± 0.6	31.2 ± 0.4	35.4 ± 0.5	33.8 ± 0.9	35.4 ± 0.4	35.1 ± 0.8	35.5 ± 0.4	35.1 ± 0.9	34.6 ± 0.6
As	7.4 ± 0.6	7.9 ± 0.2	6.7 ± 0.5	3.8 ± 0.5	7.9 ± 0.3	7.1 ± 0.5	6.6 ± 0.3	7.0 ± 0.3	6.3 ± 0.2	6.3 ± 0.7	6.6 ± 0.4	6.7 ± 0.4	6.3 ± 0.7
Rb	149.9 ± 4.5	158.8 ± 0.8	157.9 ± 0.4	157.1 ± 0.8	159.7 ± 1.0	147.5 ± 0.4	132.4 ± 0.3	129.2 ± 0.4	130.6 ± 0.3	131.0 ± 1.0	131.2 ± 0.6	130.2 ± 0.7	129.0 ± 1.2
Sr	3.7 ± 0.2	3.0 ± 0.3	3.5 ± 0.3	5.5 ± 0.1	8.2 ± 0.2	5.9 ± 0.5	3.2 ± 0.2	4.3 ± 0.2	2.9 ± 0.2	3.2 ± 0.2	3.0 ± 0.2	3.9 ± 0.3	3.9 ± 0.3
Y	153.0 ± 8.5	163.3 ± 1.4	145.9 ± 0.5	104.4 ± 0.9	163.9 ± 0.8	158.2 ± 1.5	145.3 ± 0.4	148.4 ± 0.7	141.7 ± 1.3	142.9 ± 0.4	142.6 ± 0.7	142.4 ± 0.8	138.9 ± 2.7
Zr	1434 ± 3.4	1404 ± 4	1415 ± 4.9	1433 ± 11.1	1395 ± 5.3	1337 ± 3.2	1198 ± 15.7	1178 ± 0.9	1157 ± 4.1	1161 ± 4.8	1164 ± 3.6	1154 ± 2.7	1160 ± 2.7
Nb	110.3 ± 1.0	108.2 ± 1.3	108.8 ± 0.4	111.6 ± 0.6	107.5 ± 0.8	102.6 ± 0.7	97.7 ± 1.4	94.9 ± 0.7	94.2 ± 0.8	93.6 ± 0.7	93.9 ± 0.4	94.2 ± 0.3	93.0 ± 1.0
Ba	26.9 ± 3.2	28.1 ± 2.5	26.4 ± 2.3	39.6 ± 2.8	31.8 ± 3.9	30.7 ± 1.0	25.7 ± 3.2	28.8 ± 0.8	23.5 ± 0.9	24.9 ± 2.6	24.6 ± 2.2	30.5 ± 2.5	34.0 ± 2.1
La	105.7 ± 1.6	103.3 ± 1.4	94.1 ± 0.9	77.1 ± 0.9	104.3 ± 1.7	98.4 ± 1.5	91.3 ± 2.3	99.4 ± 1.0	90.1 ± 0.9	91.4 ± 1.4	89.3 ± 1.0	91.0 ± 1.1	88.7 ± 1.0
Ce	242.1 ± 3.6	236.8 ± 3.4	210.2 ± 1.9	253.4 ± 2.7	236.4 ± 1.9	230.0 ± 1.9	209.3 ± 5.7	218.0 ± 0.8	205.9 ± 1.6	207.8 ± 0.8	204.9 ± 1.1	206.6 ± 1.8	204.5 ± 2.7
Pb	30.2 ± 1.7	31.1 ± 0.6	30.3 ± 0.8	32.0 ± 0.9	30.9 ± 0.9	28.7 ± 1.1	25.1 ± 0.3	24.7 ± 1.3	25.5 ± 1.3	24.9 ± 1.2	25.0 ± 0.9	24.9 ± 1.6	24.8 ± 0.7
Th	21.4 ± 0.7	21.8 ± 0.6	21.9 ± 0.6	22.2 ± 0.6	21.8 ± 1.0	19.9 ± 0.5	18.0 ± 0.3	18.4 ± 0.6	17.3 ± 0.7	17.7 ± 0.5	18.1 ± 0.7	17.8 ± 0.4	17.7 ± 1.0
U	6.3 ± 0.5	6.4 ± 0.4	5.8 ± 0.5	3.9 ± 0.2	6.2 ± 0.1	5.9 ± 0.3	5.8 ± 0.6	5.3 ± 0.5	5.1 ± 0.8	5.1 ± 0.6	5.1 ± 0.4	5.0 ± 0.5	5.3 ± 0.3

	14	15	16	17	18	19	20	21	22	23	24	25	26
Sc	0.8 ± 0.4	0.5 ± 0.3	0.4 ± 0.4	n.d	n.d	0.5 ± 0.3	n.d	n.d	0.1 ± 0.6	0.5 ± 0.6	n.d	0.5 ± 0.1	0.1 ± 0.5
V	5.2 ± 0.6	3.5 ± 0.6	3.2 ± 0.9	3.3 ± 0.4	4.6 ± 0.6	3.4 ± 0.9	3.3 ± 0.4	3.9 ± 0.5	3.5 ± 0.8	5.0 ± 0.7	3.2 ± 0.3	3.6 ± 0.4	4.1 ± 0.2
Cr	0.3 ± 0.4	n.d	n.d	n.d	n.d	n.d	n.d	n.d	0.5 ± 0.2	1.7 ± 0.3	n.d	n.d	n.d
Ni	2.5 ± 0.3	2.3 ± 0.4	1.8 ± 0.1	1.8 ± 0.3	2.1 ± 0.8	1.2 ± 0.3	2.3 ± 0.4	1.4 ± 0.5	1.7 ± 0.4	2.5 ± 0.1	1.7 ± 0.4	1.2 ± 0.6	2.6 ± 0.3
Cu	5.2 ± 0.3	4.9 ± 3.6	4.9 ± 0.3	4.6 ± 0.5	7.0 ± 0.7	4.7 ± 0.2	4.9 ± 0.4	4.9 ± 0.4	4.9 ± 0.2	7.5 ± 0.4	5.0 ± 0.1	4.5 ± 0.1	5.0 ± 0.2
Zn	235.1 ± 1.2	244.9 ± 5	238.2 ± 5.4	238.9 ± 4.7	228.3 ± 6.7	204.3 ± 1.4	212.2 ± 1.2	212.8 ± 1.4	239.0 ± 5.1	240.9 ± 6.4	240.3 ± 3.1	236.5 ± 6.2	262.5 ± 1.0
Ga	35.9 ± 0.7	36.5 ± 2.0	35.2 ± 0.6	34.2 ± 0.8	33.8 ± 0.6	31.3 ± 0.7	32.6 ± 0.3	34.2 ± 0.5	34.9 ± 1.5	36.1 ± 0.8	35.4 ± 0.6	34.1 ± 1.2	34.1 ± 0.3
As	8.4 ± 0.5	5.4 ± 0.7	6.6 ± 0.7	6.7 ± 0.2	6.5 ± 0.4	6.3 ± 0.8	6.6 ± 0.3	4.9 ± 0.6	4.0 ± 0.3	4.6 ± 0.5	6.8 ± 0.1	6.1 ± 0.3	6.5 ± 0.7
Rb	125.8 ± 0.9	128.1 ± 0.5	130.9 ± 0.4	130.6 ± 0.3	135.5 ± 0.4	129.1 ± 0.5	134.2 ± 0.2	130.0 ± 0.5	130.5 ± 0.5	130.7 ± 0.8	131.7 ± 0.5	129.0 ± 0.5	138.5 ± 0.6
Sr	31.6 ± 0.2	12.0 ± 0.2	3.5 ± 0.3	8.0 ± 0.2	11.3 ± 0.2	12.2 ± 0.3	2.5 ± 0.1	6.6 ± 0.2	4.6 ± 0.1	10.5 ± 0.1	3.4 ± 0.4	3.6 ± 0.2	5.7 ± 0.1
Y	117.1 ± 0.7	146.1 ± 1.7	143.7 ± 1.0	145.1 ± 0.9	122.6 ± 0.8	124.5 ± 0.7	128.9 ± 0.9	118.3 ± 0.3	138.8 ± 0.2	142.5 ± 0.3	143.9 ± 1.0	142.9 ± 0.4	144.8 ± 0.3
Zr	1141 ± 3.9	1187 ± 2.1	1156 ± 4.3	1146 ± 2.1	1119 ± 3.3	1056 ± 2.3	1114 ± 4.1	1158 ± 3.9	1140 ± 4.1	1148 ± 2.3	1161 ± 1.7	1132 ± 3.0	1135 ± 1.9
Nb	93.3 ± 0.7	95.8 ± 0.7	93.7 ± 0.9	91.4 ± 0.4	89.0 ± 0.5	82.7 ± 0.9	88.1 ± 1.6	90.8 ± 2.7	91.9 ± 1.0	92.4 ± 0.5	93.9 ± 0.8	91.4 ± 1.0	93.2 ± 0.8
Ba	88.0 ± 2.3	38.5 ± 1.7	26.3 ± 2.5	26.9 ± 3.0	27.4 ± 1.7	19.6 ± 1.2	19.7 ± 2.3	28.6 ± 5.2	29.9 ± 1.6	67.0 ± 0.9	31.1 ± 4.6	29.1 ± 2.8	37.0 ± 2.6
La	76.5 ± 1.3	98.1 ± 1.2	90.8 ± 0.5	93.5 ± 1.7	76.3 ± 1.7	77.7 ± 0.6	82.2 ± 0.9	75.9 ± 2.9	85.0 ± 1.3	88.5 ± 1.0	90.7 ± 0.6	89.6 ± 0.9	89.4 ± 1.0
Ce	190.8 ± 1.9	221.9 ± 2.6	205.7 ± 2.0	212.4 ± 3.1	177.4 ± 2.3	183.1 ± 1.1	196.5 ± 3.2	205.1 ± 3.1	194.1 ± 3.1	204.6 ± 1.3	206.0 ± 2.0	204.7 ± 2.0	201.4 ± 2.9
Pb	24.5 ± 0.6	24.8 ± 0.6	24.7 ± 0.7	26.7 ± 0.4	26.4 ± 0.7	24.2 ± 1.2	25.3 ± 0.7	26.6 ± 0.2	24.3 ± 1.2	24.2 ± 0.9	25.0 ± 0.9	25.4 ± 0.7	26.9 ± 0.7
Th	18.0 ± 0.3	17.9 ± 0.6	17.3 ± 0.5	18.0 ± 0.7	16.0 ± 0.4	17.2 ± 0.7	17.2 ± 1.0	18.2 ± 0.4	17.6 ± 0.5	17.1 ± 0.5	18.7 ± 0.6	17.3 ± 0.4	17.5 ± 0.7
U	3.9 ± 0.6	3.4 ± 0.3	5.1 ± 0.5	5.0 ± 0.2	4.7 ± 0.1	4.8 ± 0.3	5.2 ± 0.3	3.3 ± 0.2	5.0 ± 0.2	5.7 ± 0.5	4.5 ± 0.8	5.1 ± 0.5	4.9 ± 0.2

Interpretations for variations in the major element profiles of the Pre-8 ka flow are constrained by the lack of a result for the basal obsidian layer, owing to difficulty in bead preparation for XRF analyses. A sharp decline from the top to the base of the Pre-8 ka flow of 1.5% in SiO_2 (Table 6.1a) may suggest some small compositional heterogeneity is inherent in the lava. This tentative interpretation will need to be tested in the future with a more thorough sampling programme including other pre-caldera shield lavas.

For the 8 ka flow (Fig 6.6) the upper and lower OBS layer chemistry is equivalent and any depletion in the RHY layer is most pronounced near the top of the unit. For SiO_2 a depletion of 0.6 wt% occurs between the upper OBS and the top of the RHY unit. The flow, best represented by the OBS unit, has a bulk SiO_2 value of 73.5%, lower than the 8 ka lapilli and the phreatomagmatic layer (of 74 and 75 wt % respectively). In contrast, an enrichment of 4.4% occurs for Al_2O_3. K_2O shows no variation throughout the flow, whereas Na_2O is depleted in the RHY layer by 15.5% suggesting a significant post emplacement mobilisation of sodium.

6.4.2. Trace element variations.

For each sample analysed duplicate beads were made, so that interfabric and intrafabric variation could better be constrained with a mean, standard deviation and 95% confidence interval. For all three flows, no intraflow variation occurs in Sc, V, Cr, Ni, or Cu.

For the Panui flow (Fig. 6.7), the most significant enrichments within the central RHY layer occur for Ba, with Zn and Zr having lower enrichment factors respectively. Limited variation occurs in the upper OBS, RHY and lower OBS layers for Rb. However, in contrast to the bulk of the flow profile, the FVP and basal breccia layers are depleted by 7 and 11 ppm respectively. Significant depletion factors are characteristic of the La and Y profiles. In contrast, a depletion of 28 ppm at the OBS/RHY transition and an enrichment of 18 ppm occurs for Ce, relative to the upper and lower OBS layers.

Trace element profiles for the Pre-8 ka and 8 ka flows, illustrated in Fig. 6.8a and 6.8b show the following:

a. no significant variation occurs within the flows for Ga, Pb, Th, U, As, Ni, Cu, Sc, V, and Cr;
b. depletions within the RHY layer occur for Y, Rb, La, and Ce, and enrichments in Ba and Sr;
c. unlike the 8 ka flow, the Pre-8 ka flow shows down-profile enrichment in Y, Nb, Zr, Zn, La, Ce.

Sr is enriched at the base of the RHY layer for the Pre-8 ka flow, and between 12 to 29 ppm toward the top of the RHY layer of the 8 ka flow, declining sharply over approximately 1m to the upper OBS layer (2-3 ppm Sr). The minimum enrichment of 12 ppm was greater than that found by Weaver (oral.comm. 1989) from his unpublished data.

Ba is enriched by 65 ppm within the upper RHY of the 8 ka flow with the profile mimicking that of Sr. La and Ce show a basal enrichment, an upper depletion within the RHY layer and a pronounced increase from the phreatomagmatic unit (sample 18) to the basal OBS (16). Trends are less marked for the Pre-8 ka flow. The 8 ka flow shows no interfabric variation for Zn. Zr and Nb are enriched within the lower RHY layer for the 8ka flow, whereas the large error bar for the upper RHY level precludes any interpretation of intra- and interfabric variation. Y shows a major depletion of 25 ppm at the top

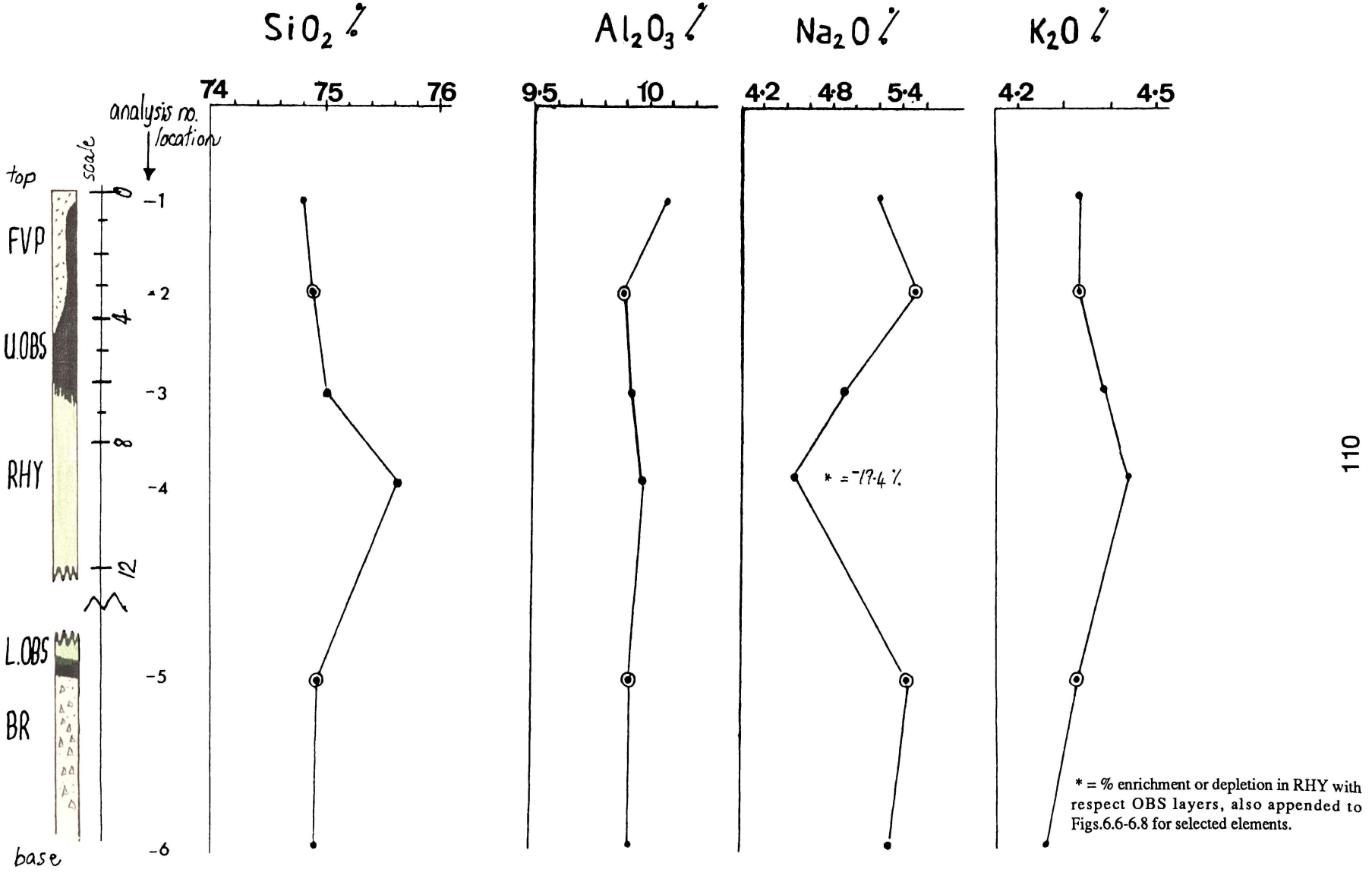

Fig. 6.5. Major element oxide variations (wt%) for the Panui flow. Oxides are plotted on a volatile-free basis.

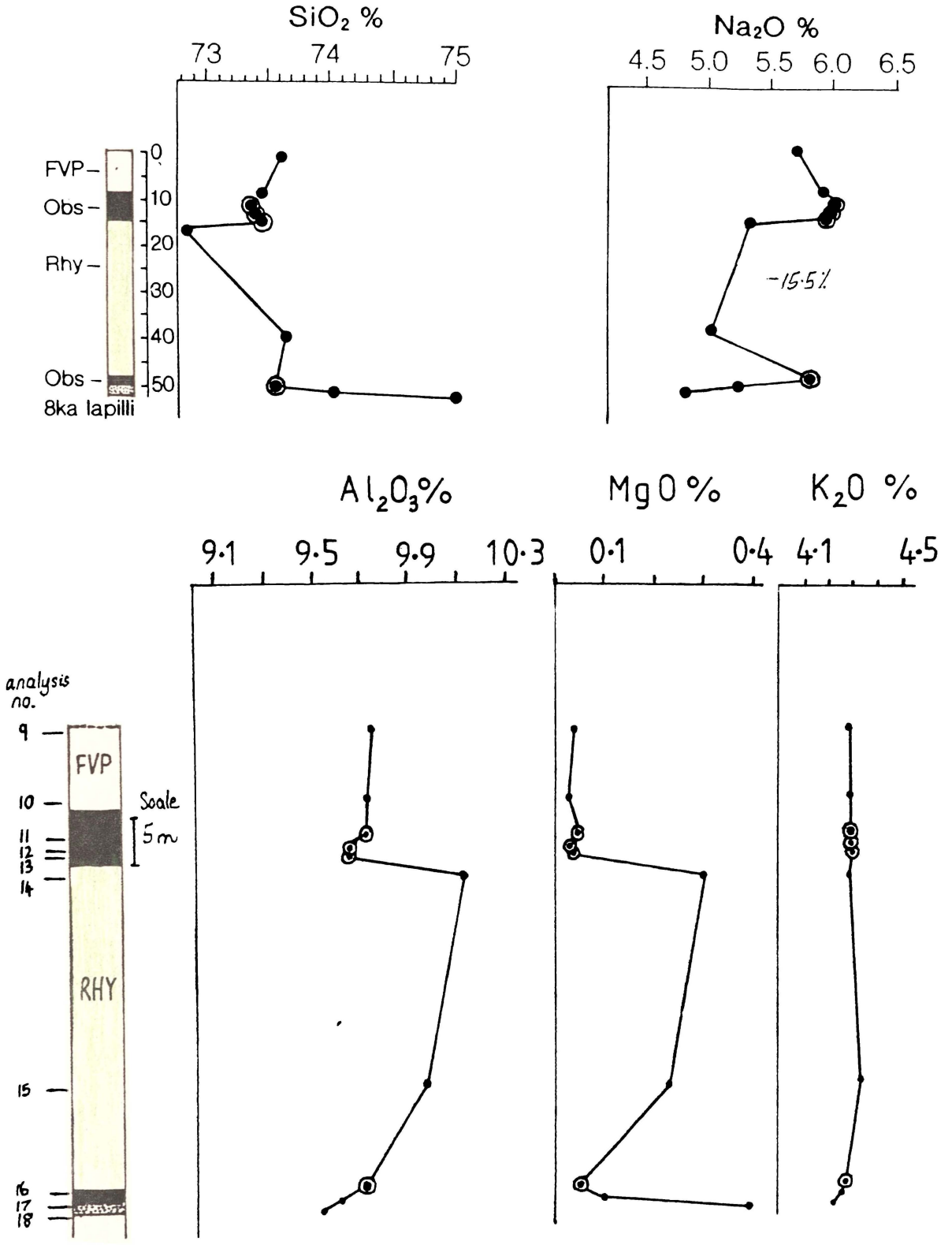

Fig. 6.6. Major element oxide variations (wt%), 8 ka flow. Oxides have been plotted on a volatile-free basis.

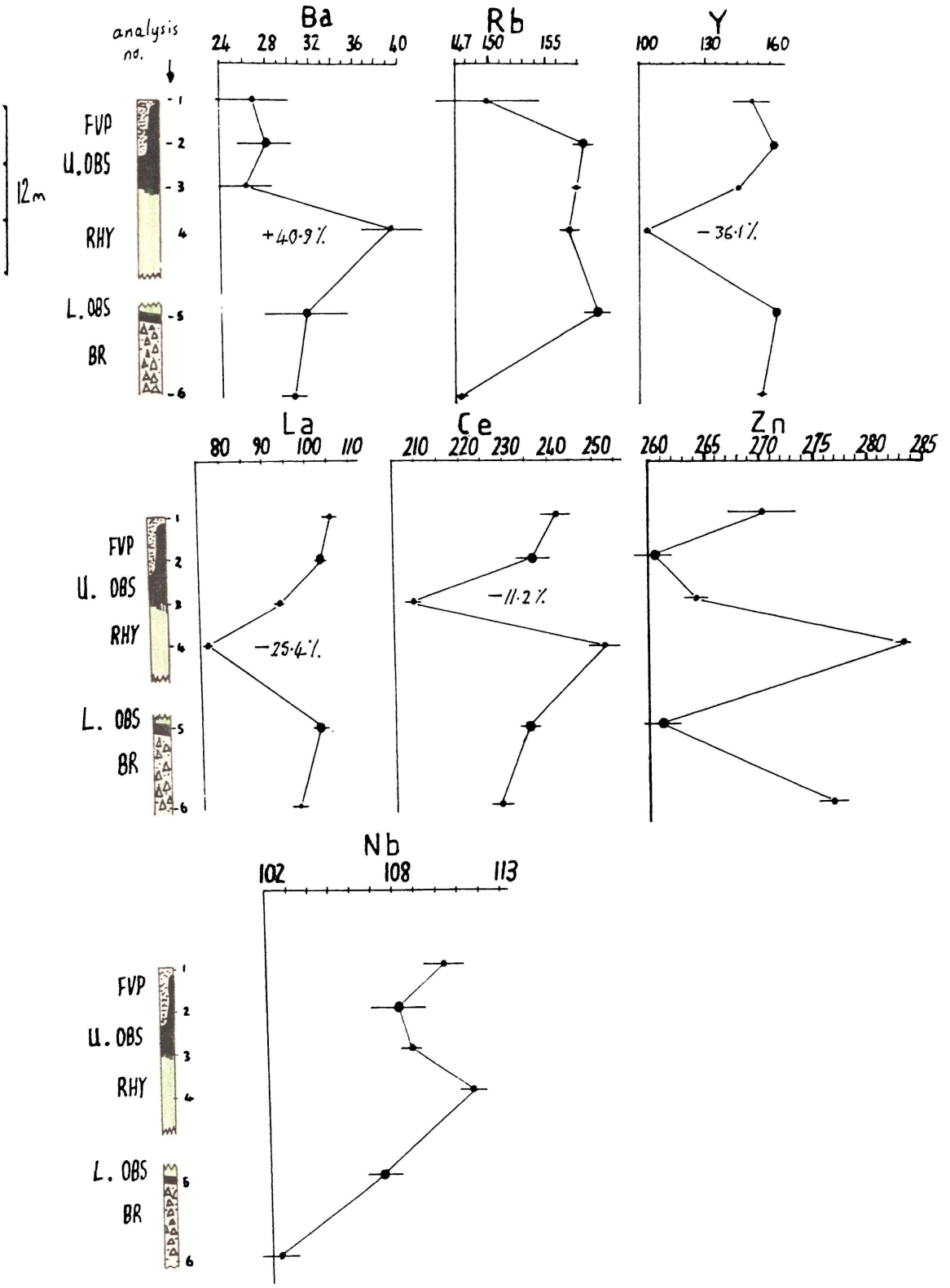

Fig. 6.7. Trace element variations, Panui flow. Values are in ppm. Error bars represent two standard errors.

of the RHY zone and an increase by 30 ppm between the basal phreatomagmatic layer and basal OBS. Depletion in Y is less pronounced in the Pre-8 ka flow profile. Rb variations are less significant being depleted by 5 ppm at the top of the RHY layer of the 8 ka flow, but less pronounced for the Pre-8 ka flow.

6.4.3. Trace element mobility - interpretations.

XRF data demonstrate that the Mayor Island flows were emplaced as chemically homogeneous units (Weaver et al. 1985). Fresh anhydrous obsidians can be used to determine the eruptive chemistry of the magma. The major and trace element chemistry is comparable for the upper and lower OBS layers. However, flow interiors are either depleted or enriched corresponding to the devitrified RHY layer.

According to Weaver et al. (1985) flow interiors lost up to 60% of their original abundances of rare earth elements (REE). During this loss the REE were not significantly fractionated and the magnitudes of the negative Eu anomalies characterising peralkaline rhyolites were preserved. Magmatic oxygen isotope ratios of glassy and devitrified samples preclude low temperature aqueous leaching (Weaver et al. 1985). Thus it seems likely that Na, La, Cl, and Y losses accompanied high temperature devitrification.

Physical evidence (chapter 5) indicates that isobaric crystallisation was initiated at high temperatures, prior to flow cessation. Therefore mobile trace elements migrated as a 'front' initially by diffusion and later by crack migration associated with increasing crystallisation with time in the flow centre. If enrichments occur in the lower part of the RHY zone and depletion in the upper part of the RHY, a downward migration is inferred (e.g. La and Ce, 8 ka flow). Alternatively, if depletions occur in the upper RHY only (e.g. Y) volatiles must migrate either downwards or upwards out of the system during crystallisation, progressing from the centre of the flow.

Plots of Na_2O against Y, La, Ce and Ba for the Panui and 8 ka flows are illustrated in Fig 6.9. Inter-unit compositional enrichment in Na, Y, La and Ce occurs from the phreatomagmatic unit to the Ruru welded tuff. Superimposed secondary post-emplacement trends dominate the 8 ka flow. Ba is enriched in the RHY layer, independent of sodium depletion. For the Panui flow direct correlations occur between Na_2O/Y and Na_2O/La.

The 8 ka flow obsidian is aphyric with sparse microlites, in contrast with the finely crystalline groundmass of the RHY layer. The Panui flow (with 5% sanidine, and a microlite-rich glass) shows a similar magnitude of OBS/RHY variation. Thus sanidine does not influence the relative concentrations of the fabric layers.

The basal breccia of Panui flow (sample 6) is strongly enriched in Sr together with sample 14. Both samples are from coastal sections, and are probably contaminated by seawater Sr. With OBS layer Sr concentrations of 2 - 3 ppm on average, Weaver et al. (1985) ascribes within-flow variation in Sr to surficial seawater contamination.

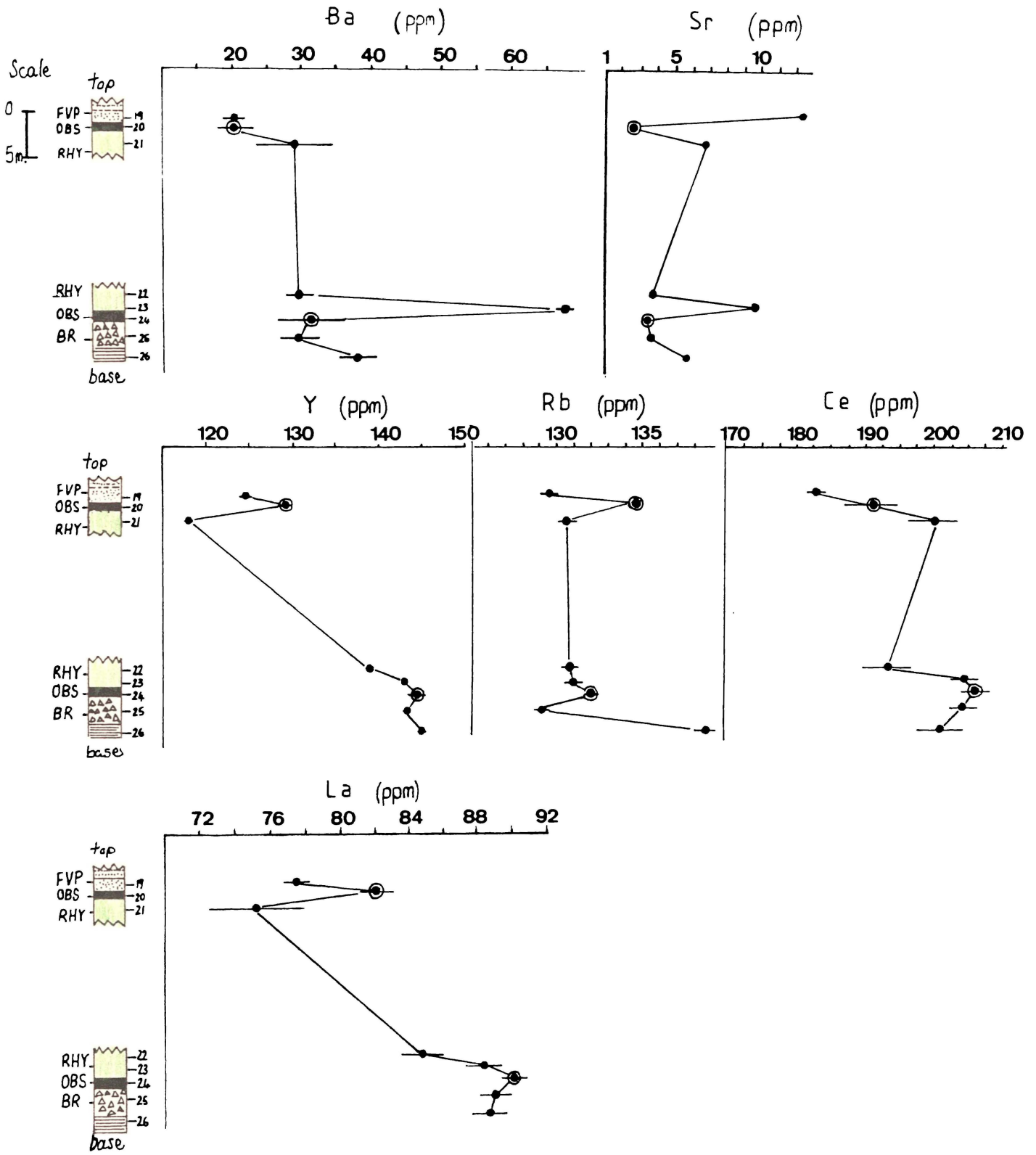

Fig. 6.8a. Trace element variations, Pre-8 ka flow.

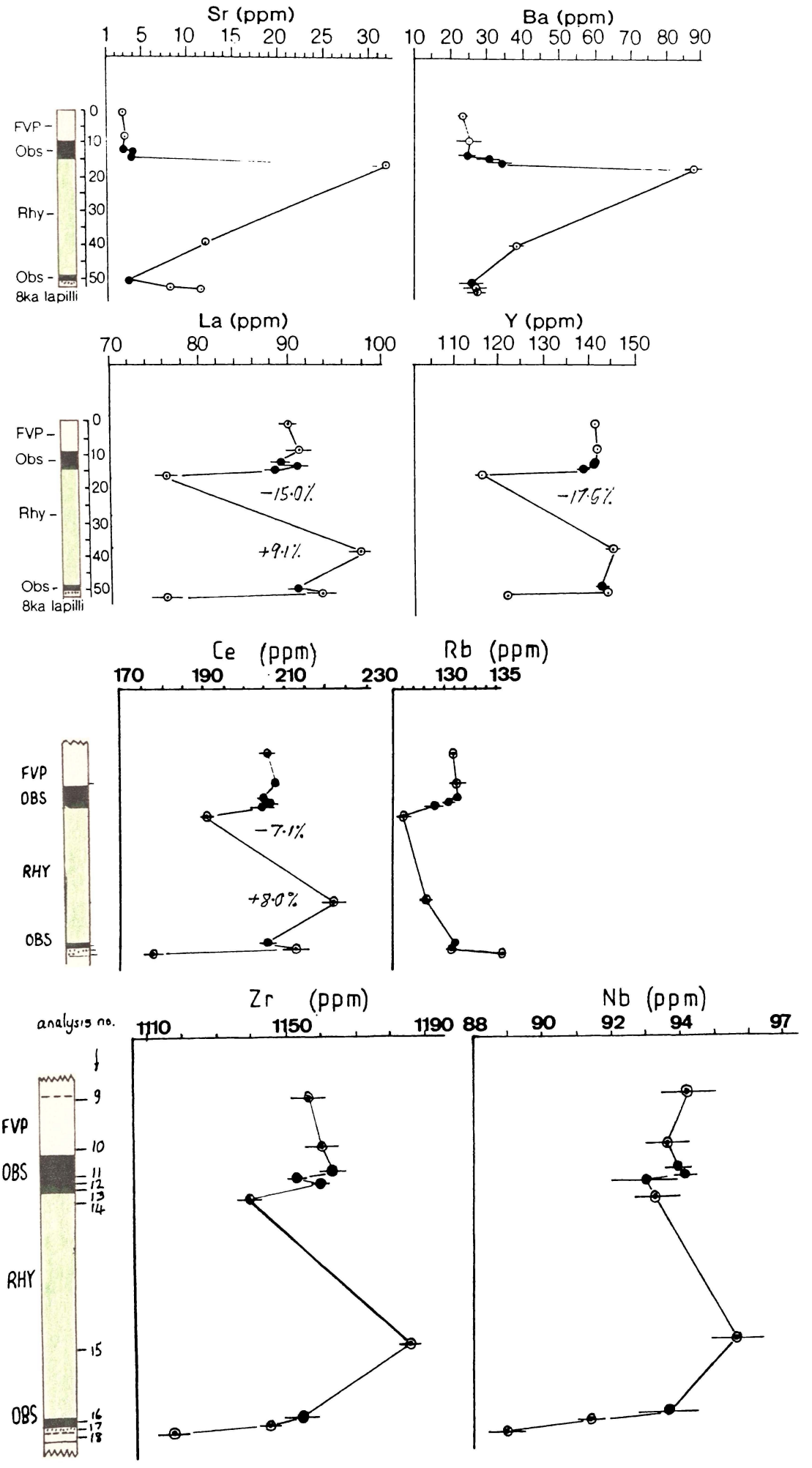

Fig. 6.8b. Trace element variations, 8 ka flow.

Table 6.2 shows significant depletion of Cl in RHY with respect to OBS in the Panui, Pre-8 ka and 8 ka flows. F contents of Mayor Island flows are typically 1000 ppm. The concentrations of F and Cl are approximately 1.8 - 2.1 times greater than that for the calc-alkaline Ben Lomond rhyolite, and water in the Mayor Island glass is estimated as being at least 2 - 10 times lower than the OBS and explosion breccia units from Ben Lomond respectively. Thus halogens are 3.6 - 21 times more concentrated in the lava.

The approximately 20% depletion factor for Na_2O (with respect to the OBS layer) within the RHY layer of the pantelleritic flows points to the mobility of sodium-halogen solutions within the lava flow profiles during crystallisation of the central RHY layer. Hence in contrast to Ben Lomond, owing to significantly more concentrated volatile phases, more pronounced intraflow trends occur for the most soluble of trace elements for the Mayor Island flows.

6.5. The Viscosity of the Mayor Island Pantellerites.

Viscosity for the Mayor Island flows was calculated using the method of Shaw (1972) and for the porphyritic Panui flow, the effective viscosity via Murase et al. (1984). As the chemical data of the OBS layers are interpreted as being best representative of the original lava, the Fe^{2+}/Fe^{3+} ratios of 2 - 2.5 from Ewart et al. (1968) may be used to calculate FeO% and Fe_2O_3% for the three flows studied. These values are included in the calculation of the viscosity of the liquid using the method of Shaw (1972). In addition, mean crystal width (Dm) was calculated as the sum of A(x).Dm(x), where A is the proportion of phenocryst (x) of size Dm. The estimated $\log_{10}\eta_{eff}$ (effective viscosity) of the Panui, Pre-8 ka, and 8 ka flows respectively is 7.70, 7.80, and 7.25 respectively using equation 4.13. Estimated temperature and viscosity profiles throughout the 8 ka flows is shown in Fig. 6.10.

The thermal profile of the flow is constrained by the presence of a fused basal 8 ka airfall lapilli below the 8 ka flow, charcoal logs in the coarse-grained lapilli, microlites of greatest length in the upper and lower OBS excluding post-emplacement modification during isobaric crystallisation in the RHY. A temperature difference of about 900°C is inferred in approximately the top 10 m of the flow. A uniform central temperature of 950°C continues into the fused basal tuff, and a temperature difference of 650 to 700°C occurs over 0.1 m to a volatile-rich lapilli with a temperature of 300°C based on the presence of charcoal logs (Maury, 1973, in Fisher and Schminke, 1984).

The high Fe/(Si+Al), high alkali contents, and high $Na_2O + K_2O/Al_2O_3$ ratio tends to decrease polymerisation of viscous silicate melts (Schminke, 1974). For a peralkaline rhyolite at 950°C, the viscosity is 3 - 4 orders of magnitude lower than for a calc-alkaline magma at 750°C of comparable water content (0% water). Estimates of $\log_{10}$ viscosity for the 8 ka flow, Mayor Island and Ben Lomond are 7.4 and 11 respectively. However, if emplacement temperatures were comparable, the contribution of the more depolymerised peralkaline chemistry to the estimated viscosity would be a lowering of the viscosity by only one order of magnitude. Thus the greatest contribution to the viscosity difference is the elevated temperature (T [peralkaline lava] = T[calc-alkaline lava] + [150 - 200°C]) contributing at least 66% (2 orders of magnitude) to the viscosity decrease between both lava types. Water contents are two times lower than in the equivalent OBS layer of a calc-alkaline rhyolite. Cl has a lesser effect

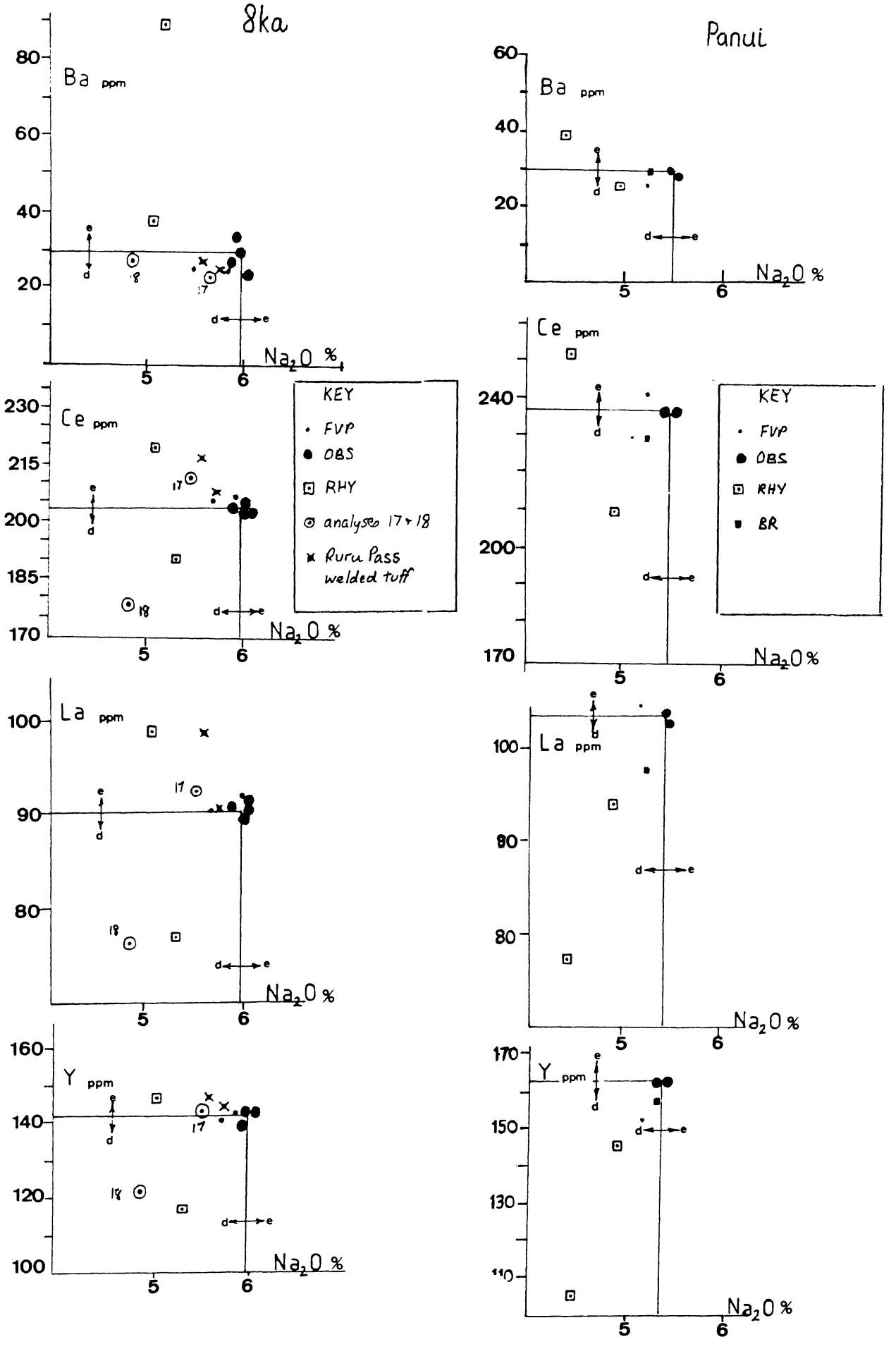

Fig. 6.9. Enrichment (e) and depletion (d) diagrams for the 8 ka and Panui flows.

Table 6.2. Cl concentrations for the representative fabrics of Mayor Island flows. Analyses were performed by S. Weaver, Geology Dept., University of Canterbury.

	sample	unit	[Cl] ppm
8ka flow	M9	FVP	1640
	M11	U OBS	1630
	M15	RHY	130
	M16	L OBS	1440
	M17	8ka lapilli	1720
Pre-8ka flow	M20	U OBS	1660
	M21	RHY	640
Panui	M2	U OBS	1900
	M4	RHY	850

than F in decreasing the polymerisation of silicate melts (Kovalenko et al. 1989). Using Fig.7 from Dingwell et al. (1985), data for F and X_{SiO2} (where X = mole fraction) was substitued for Mayor Island and Ben Lomond rhyolites. At a temperature of 1000°C, the value of $\Delta\eta$ compared to fluorine-free melts is 1.3 - 2.7 times greater for Mayor Island. Although the influence of F on the viscosity of Ben Lomond magma is 1.5 times more than for Mayor Island magmas, Mayor Island contains 2 - 4 times more F than Ben Lomond lavas. However, the most dramatic effects of fluorine addition occur in high-silica fluorine-rich anhydrous rhyolites (Dingwell et al. 1985; Congdon and Nash, 1988).

For Mayor Island lavas, temperature, chemistry (major elements), H_2O and F contribute in decreasing order of importance to the low viscosity of pantelleritic melts.

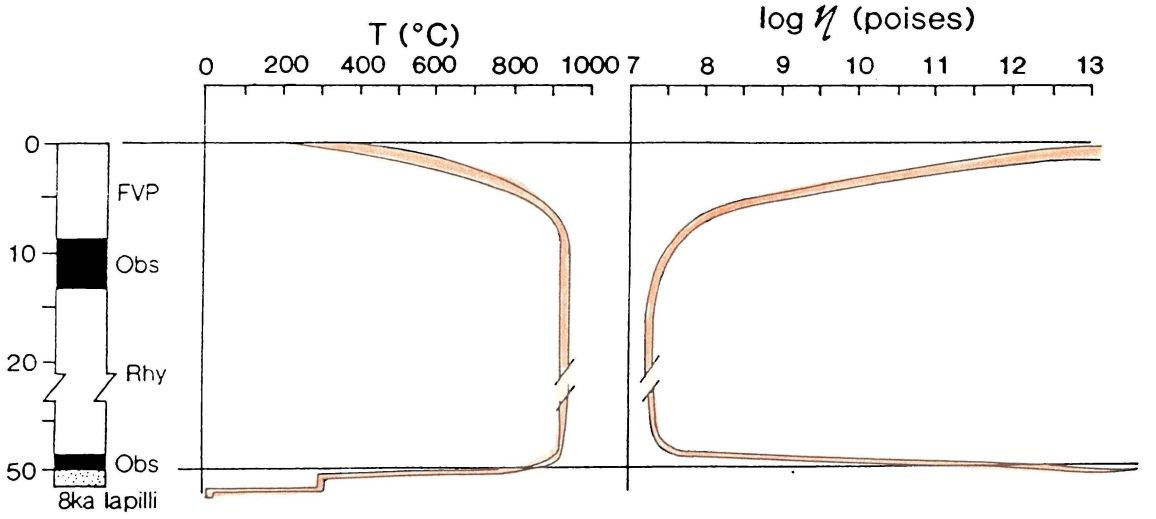

Fig. 6.10. Inferred temperature and viscosity profiles for the 8 ka flow.

6.6. Summary

Major and trace element variations are more extreme for peralkaline lavas in contrast to calc-alkaline rhyolites. Thus the effects of high temperature and low temperature volatile migration may be better isolated.

For Mayor Island flows, La, Ce, Y, Na_2O and Cl variations are similar down flow profiles. For all these elements, little variation occurs between obsidian and finely vesicular pumice fabrics. Thus the mobility of these elements may be ascribed primarily to high-temperature migration of volatiles in response to crystallisation of the flow interior. Little significant variation occurs in Rb with a small depletion of approximately 5 ppm in pumiceous fabrics, possibly from rainwater metasomatism. Large enrichments in Sr for the Panui and 8 ka flows, occur for those vesicular samples nearest sea level. Thus seawater metasomatism is responsible for Sr mobility. Although the profile for Ba matches the Sr profile for the 8 ka flow, Ba trends usually do not mimic Sr and hence sea water metasomatism as an agent of mobility, may be discounted.

The more subtle trends for the calc-alkaline lavas of Ben Lomond can now be better interpreted. The depletion of Cl and slight loss of Na_2O within the central rhyolite layer, is exclusively of a high temperature secondary origin. Y, Ce and La show no significant variation. Sea water metasomatism is not a contributing factor for Lomond lavas. Thus, the depletions of Sr and Rb, and enrichments of Ba, Zn and Zr that occur for both primary and secondary vesicular fabrics, may be either a low-temperature and/or a high-temperature phenomena. Variations between the finely vesicular pumice and obsidian fabrics of Mayor Island, are not significant for Sr or Ba. Thus for Ben Lomond, Ba and Sr variation is most likely from low temperature aqueous metasomatic effects. Large-scale variations in magmatic Ba (e.g. for Inyo domes) do not occur for Ben Lomond. Interpretations for low temperature as opposed to high temperature mobility is more ambiguous for Zn, Rb and Zr in increasing order.

The high temperature, high alkali content, and thus low viscosity enables a spatter fed mode of emplacement. In addition, modification of microlite length via diffusion, aided by concentrated halogen-rich fluids was able to occur during and after flow emplacement.

CHAPTER 7.

APPLICATIONS OF THE CALC-ALKALINE FLOW EMPLACEMENT MODEL - PAUANUI AND OKATAINA VOLCANIC CENTRE FLOWS.

7.1. Introduction.

In contrast to the young, uneroded carapaces of the Inyo domes, calc-alkaline rhyolite domes in New Zealand are poorly preserved. From detailed physical volcanological studies of the Ben Lomond dome, a well constrained emplacement model was assembled. Such a model may be applied and tested on two poorly outcropping rhyolites: Pauanui, an eroded dome complex of Miocene age; and flows of the Okataina Volcanic Centre of 19 - 5.5 ka age.

The Pauanui lavas have a vegetated and dissected poorly preserved carapace, but coastal sections provide partial cross-sections through flow lobes. No fresh obsidian occurs at Pauanui and all flow units show varying degrees of devitrification.

The Okataina Volcanic Centre lavas comprising the Haumingi flow (19,000 yrs B.P.), Waiti flow (7500 yrs B.P.) and Haroharo dome (5500 yrs B.P.) (Nairn, 1981) are characterised by excellent areal exposures. Flow dimensions with the exception of thickness (h) are easily determined, as the flows have steep well defined flow fronts and carapace ridges that are concave toward the inferred vent and convex toward the flow toe (Nairn, 1981). Although fresh obsidians occur, outcrops are sparse and complete composite profiles through the entire thickness of the flows are unobtainable.

7.2. Pauanui.

7.2.1. Previous work.

Previous studies of the volcanic rocks at Pauanui have been few. Pauanui was mapped as a Minden Rhyolite by Schofield (1967), but misidentified as a hornblende dacite in Skinner (1979). Stevenson (1986) documented the geotechnical properties of the suite of pitchstone fabrics at Pauanui and attempted a preliminary interpretation of the rheology and emplacement of the rhyolite lavas. Selby et al. (1988) described the modelling of rock slopes and the relation of genesis of volcanic rocks with their physical properties and resulting landforms, including Pauanui as a case study example. Most recently, Stevenson and Hodder (in press), described the fabric controls on the strength of the Pauanui pitchstones.

7.2.2. Setting.

The Pauanui dome complex, Coromandel Volcanic Zone, is built up of a succession of flow units and lobes of Minden Rhyolite (approx 7 - 8 m.y. B.P.) from at least two vents. Coastal sections comprise cliffs and wave cut platforms through at least four flow lobes. Flow banding declinations are usually steep on the inland eroded upper surface of the dome and are usually orientated toward the inferred vent under the highest part of the dome (387 m) (Fig. 7.1). At the coastal sections (e.g. area P1), flow

banding orientations are shallowly dipping (20°) and have a curvilinear strike. This line of evidence together with air photograph interpretation, the curvilinear strike of the major joint set, and the presence of an unrelated epiclastic breccia at area P2, indicate the existence of an eroded flow lobe. Four flow lobes have been identified, radiating from the summit of Pauanui: P1 lobe (0.9 km length); P3 lobe (1.1 km length); Western Coulee (2 km length) and Storm Beach Coulee (1.5 km length). The P3 lobe comprises 4 flow units (Fig. 7.2), in which profiling was undertaken for density, porosity, clast aspect ratio and chemistry.

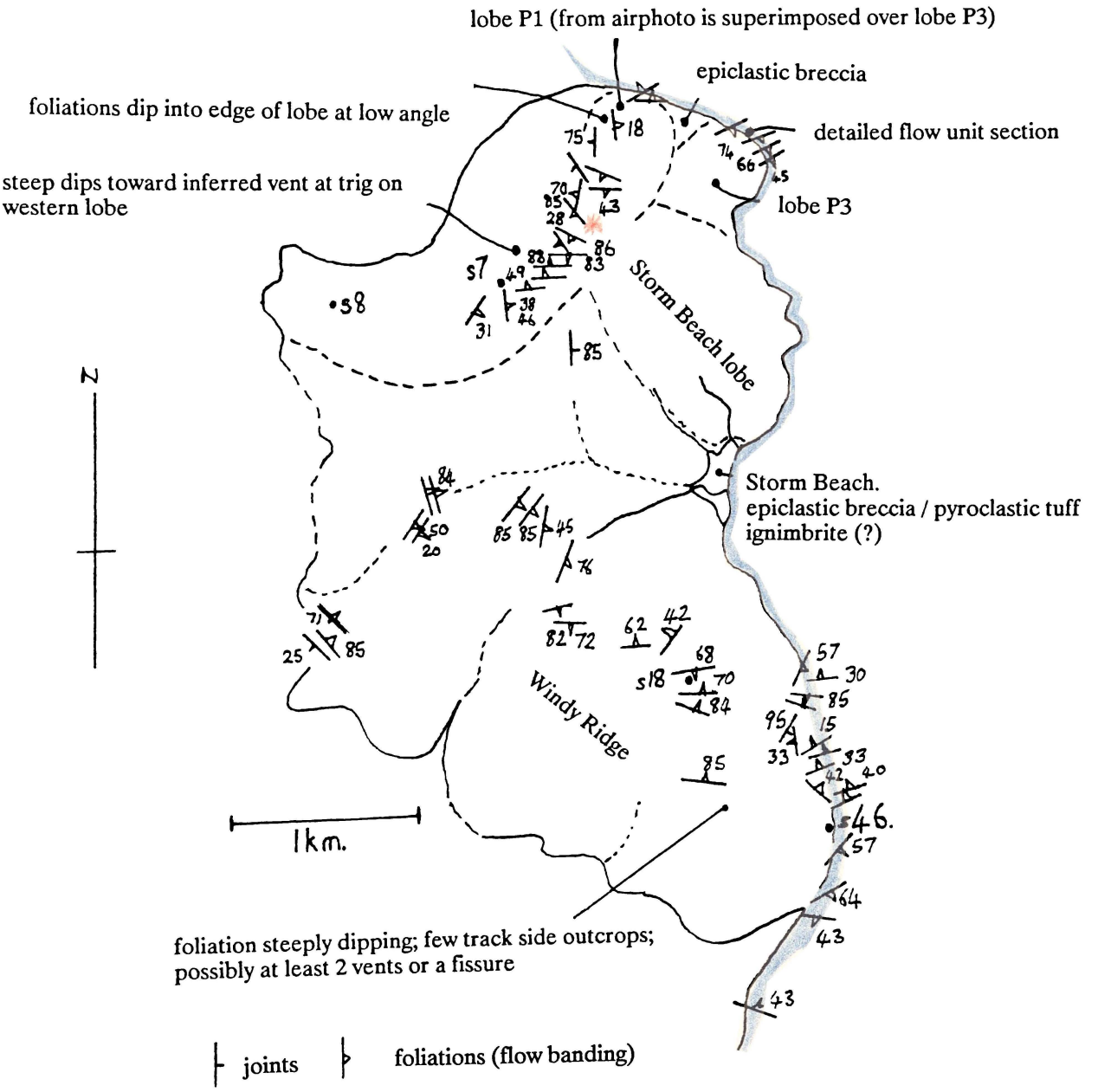

Fig. 7.1. Flow banding and joint orientations, Pauanui and Ohui-Windy Ridge.

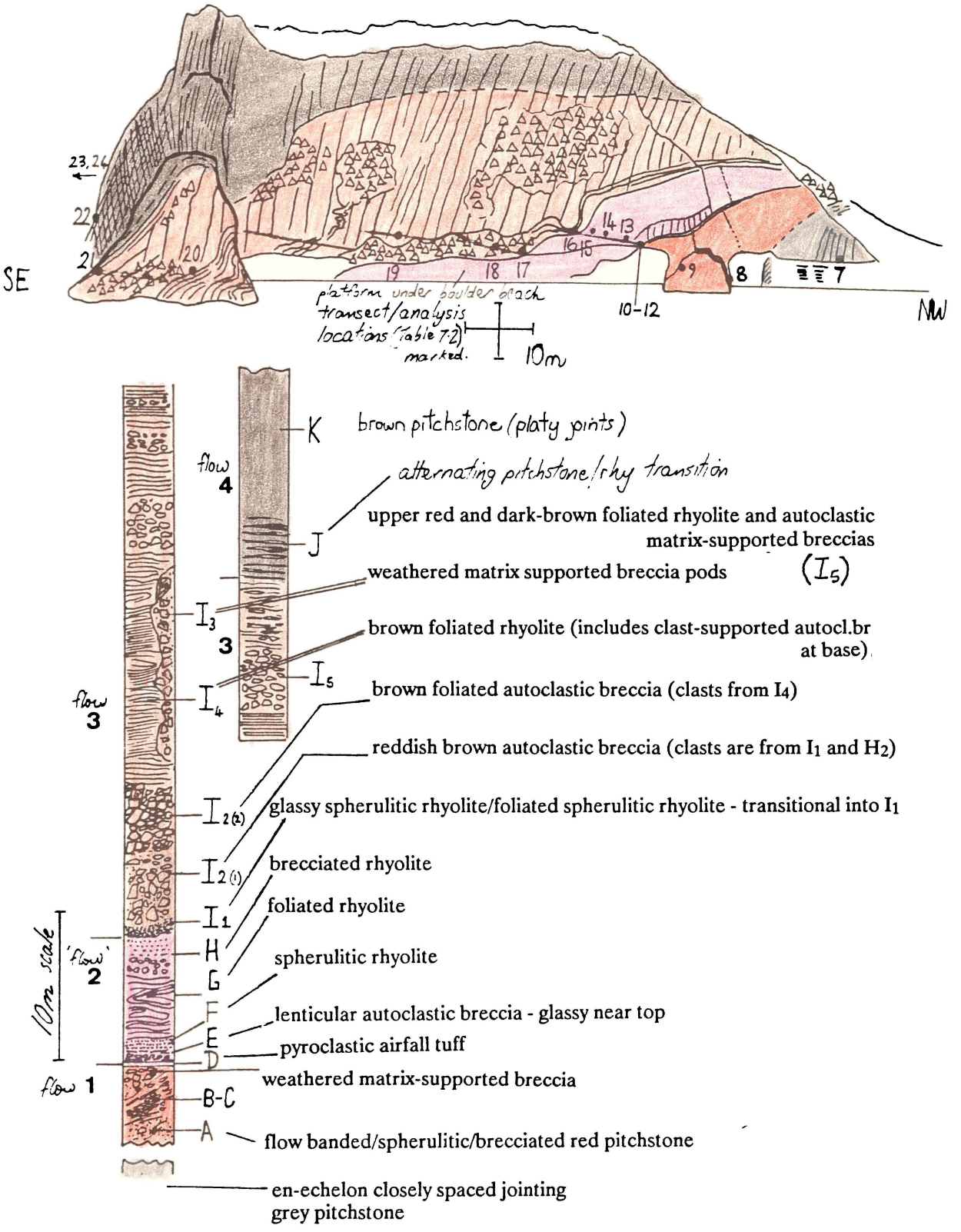

Fig. 7.2. Composite column of the P3 area flows.

7.2.3. Physical profiling - flow lobe P3

Coastal sections as cliffs and wave cut platforms provide a partially oblique cross-section through lobe P3 which is comprised of 4 flows, based on the following criteria:

a. the presence of a pyroclastic unit of airfall origin between flow 1 and 2;
b. the existence of upper and basal autoclastic breccias for flows 1 - 3;
c. variations in joint spacing with breaks between flows;
d. fabric variations.

In contrast to the Ben Lomond flow, no fresh unaltered obsidian and pumiceous fabrics are present.

Flow 1 underlies a pyroclastic unit (Unit D). Above and below this marker bed are two autoclastic breccias occurring as the upper member of flow 1 and the lower unit of flow 2 respectively. The latter unit has clasts of high aspect ratio and is delineated by regular columnar joint blocks with annealed surfaces.

Flow 3 comprises approximately 35 m of brown flow-lineated rhyolite with continuous columnar joints of moderate joint spacing throughout the flow unit. The base of flow 3 consists of a relict glassy selvedge broken into a matrix supported autoclastic breccia. The fabric of the clasts comprising the breccia is also identical to the upper breccia of flow 2. However the dry density of the latter is low and almost all joints are not continuous with the overlying flow 3. Hence on this basis, both are separate flows although flow 2 is very thin for a rhyolite lava being approximately 10 m thick. As no clearly identified pyroclastic marker is present between flows 2 and 3, flow 3 is likely to have been emplaced shortly after flow 2. Flow 2 may have been remobilised by flow 3 during its emplacement in that the clasts of the upper breccia (unit H) are incorporated as part of the basal autoclastic breccia of the overlying flow, and that the contact between both units is gradational. In addition the basal breccia of flow 3 forms a southeastward thickening wedge grading from the glassy selvedge to the matrix- and clast-supported autobreccias (unit I_2) of flow 3.

The clast-supported breccia is made up of brown flow banded rhyolite exclusively from flow 3. Matrix-supported breccia pods with clasts of low aspect ratio occur throughout flow 3 and interrupt the foliated interior consisting of tight asymmetric and isoclinal flow folds. Interlayered breccias with flow-aligned clasts, and flow banded zones typify the upper 15 m of flow 3. Flow band partings are usually steeply dipping, and are characterised by surface striations.

Flow 4 lies above a 5 - 7 m gradational contact with flow 3 comprising interlayered foliated rhyolite and pitchstone. The outer portion of flow 4 is characterised by closely-spaced platy jointing enveloping the flow interior comprising joint columns with diamond-shaped or rhomb cross-sections (Stevenson, 1986).

The density and porosity profile (Fig. 7.3 a,b) separates flows 1 - 4 into discrete units with uniform central flow banded zones and lower density autoclastic breccias. Close sampling throughout the basal units of flow 2 (D - F), verifies the existence of sharp density changes at contacts best described as a step function. The pronounced low density zone between flows 1 and 2 correspond to the pyroclastic layer. Secondary pseudomorph cavities and perlitic fractures contribute to unit F (flow 2) having a lower bulk density than the original inferred density of approximately 2.3, similar to the upper part of unit E.

No pumiceous fabrics occur throughout the sequence and only a few primary voids occur in flow 3 where primary flow banding deforms around vug outlines. The porosity of the densest units in flows 1 - 3 is secondary and microscopic. The lowest porosity of approximately 0.2% in the densest pitchstone in flow 4 is due to microcracks of up to 5 mm length radiating around sparse phenocrysts (Stevenson and Hodder, in press.)

Fig. 7.3c and d show the clast aspect ratio (Rc) and strain analysis plots respectively of the autoclastic breccias in the P3 lobe section.

The theoretical basis for interpretation of Fig. 7.3 is as follows. Flow banding is formed by plastic processes where separation occurs during flow of microlites and crystallites into discrete bands, which may have minute differences in water content, usually enhanced by post-flow devitrification. During late flow stages, plastic deformation into isoclinal and asymmetric flow folds is usually followed by brittle processes of boundinage, necking cracks and lozenge formation. Brittle fracture occurs in basal and upper flow zones, where rheological, thermal, and velocity gradients are the greatest. High aspect ratios (Rc = 5 - 10) may result from two processes:

a. low overburden/shear stress ratios characteristic of the thickness of upper breccias (e.g. upper flow 1 and upper flow 3).
b. high basal shear stresses together with increasing temperature toward the flow centre which may cause flattening of clasts and tapering of the clast edges (breccia of unit E, flow 2).

Strain analysis diagrams clearly show no preferred clast orientation of the basal $l_{2.1}$ breccia supporting the scenario of a thickening basal wedge, the incorporation of clasts from unit H and l_1, avalanching down the margin of flow 2 while being overriden by flow 3. The ratio hb/h where h = flow thickness and hb is the thickness of the basal breccia, is smaller for basal breccias of flow 3 compared to the basal breccia of flow 2. This indicates sub-glass transition temperatures in a "dead-zone" unaffected by clast flow orientation. At the base of flow 2, rheomorphic modification from flow-induced friction under high basal shear stresses or high thermal gradients is typified by the upward increasing Rc and Rs value between the lower and upper parts of unit E respectively.

7.2.4. Pauanui petrography

The phenocryst assemblage of Pauanui rhyolite comprises plagioclase + hypersthene ± augite + opaques, comprising between 5 - 10% of the rock mass.

Flow banded fabrics predominate with hydrated glassy and more devitrified layers comprising flow aligned laths of plagioclase (50 μm long) as in flow 3, or differing densities of crystallites as in the pitchstones of flow 4. Necking structures (tensile-pinching of flow bands) occurs in the flow foliated centre of flow 2. Flow-induced rotation of the long axes of plagioclase phenocrysts is common. Symmetric folds have a wavelength to thickness ratio of less than 10 within central flow folded parts of flows 2 and 3 and is typical of fluids with a power-law rheology (cf. Fink, 1984). Usually flow folds are disharmonic and tight asymmetric or isoclinal, suggesting a mobile thermally insulated flow interior of low viscosity with respect to the autobrecciated margins.

The fabrics of units F and I_1 are composed of reddish-brown and greyish-brown hydrated glass respectively, characterised by spherulites of 5 - 9 mm diameter. Unit F shows three types of crystallite/spherulite associations. Crystallite strings deviating around spherulite margins indicate that spherulites formed prior to flow cessation. This particular association is rare. Crystallites radiating from spherulite nucleii suggest that both the crystallites and spherulites form contemporaneously. When crystallites appear as flow-aligned across spherulitic masses, the spherulites formed after the crystallites that delineate primary flow banding, after flow cessation. Many nucleii were present, but crystallite growth was arrested owing to slow diffusion of ions in a cooling margin of a viscous flow. Spherulite formation could occur over longer time intervals via slow metastable transition from glass to finely acicular needles of K feldspar and quartz.

Unit E with its increasing density, clast aspect ratio and glass content upwards from the base and tapered clast morphology (within the uppermost 0.5 m), indicates a high thermal gradient, increasing temperature and an increasing likelihood of rheomorphic modification after brecciation. Thus units D-G represent a section where variations in the original flow rheology and temperature can be qualitatively assessed.

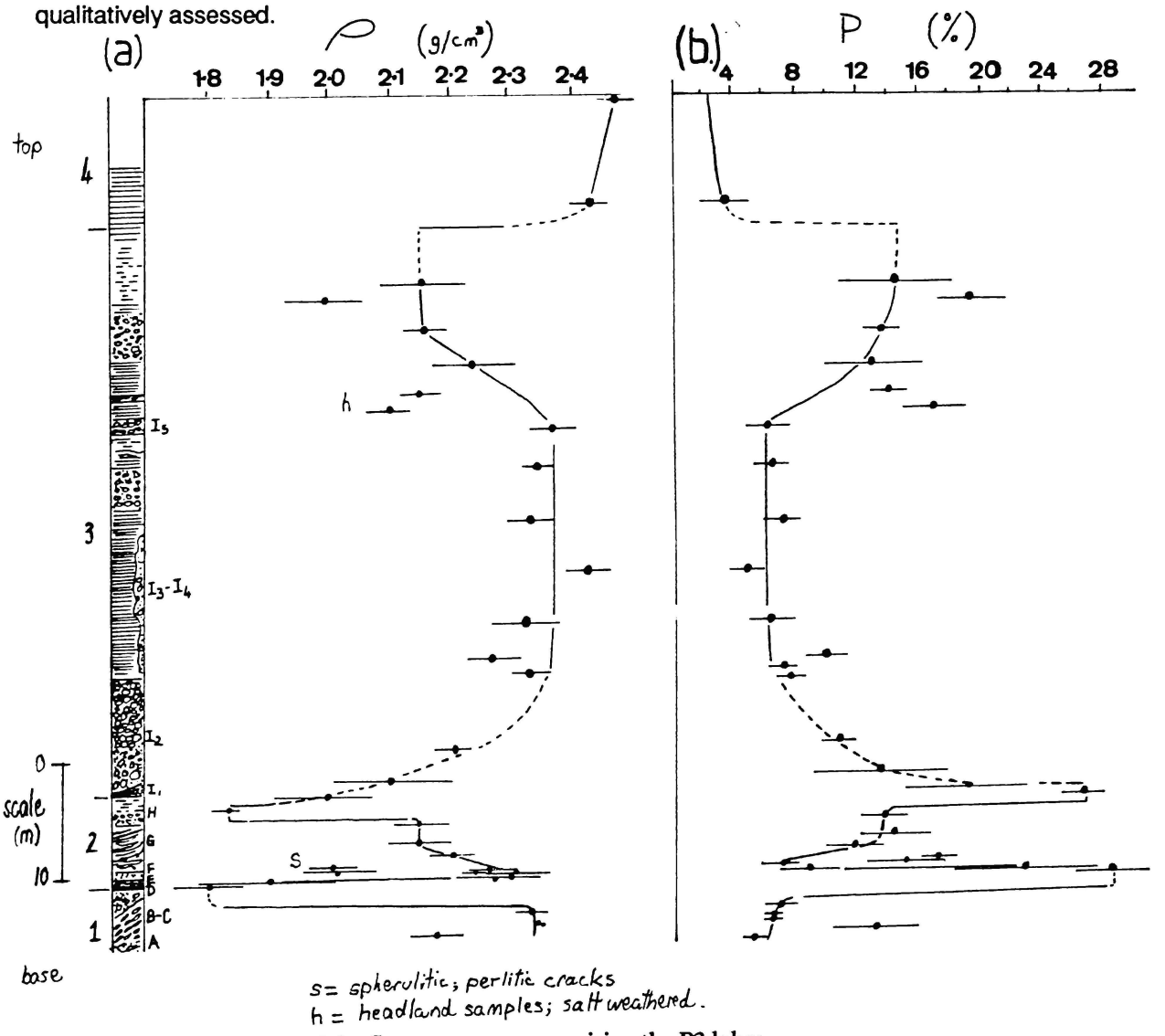

Fig. 7.3. Physical profiles of the flow sequence comprising the P3 lobe:
(a) density; (b) porosity;

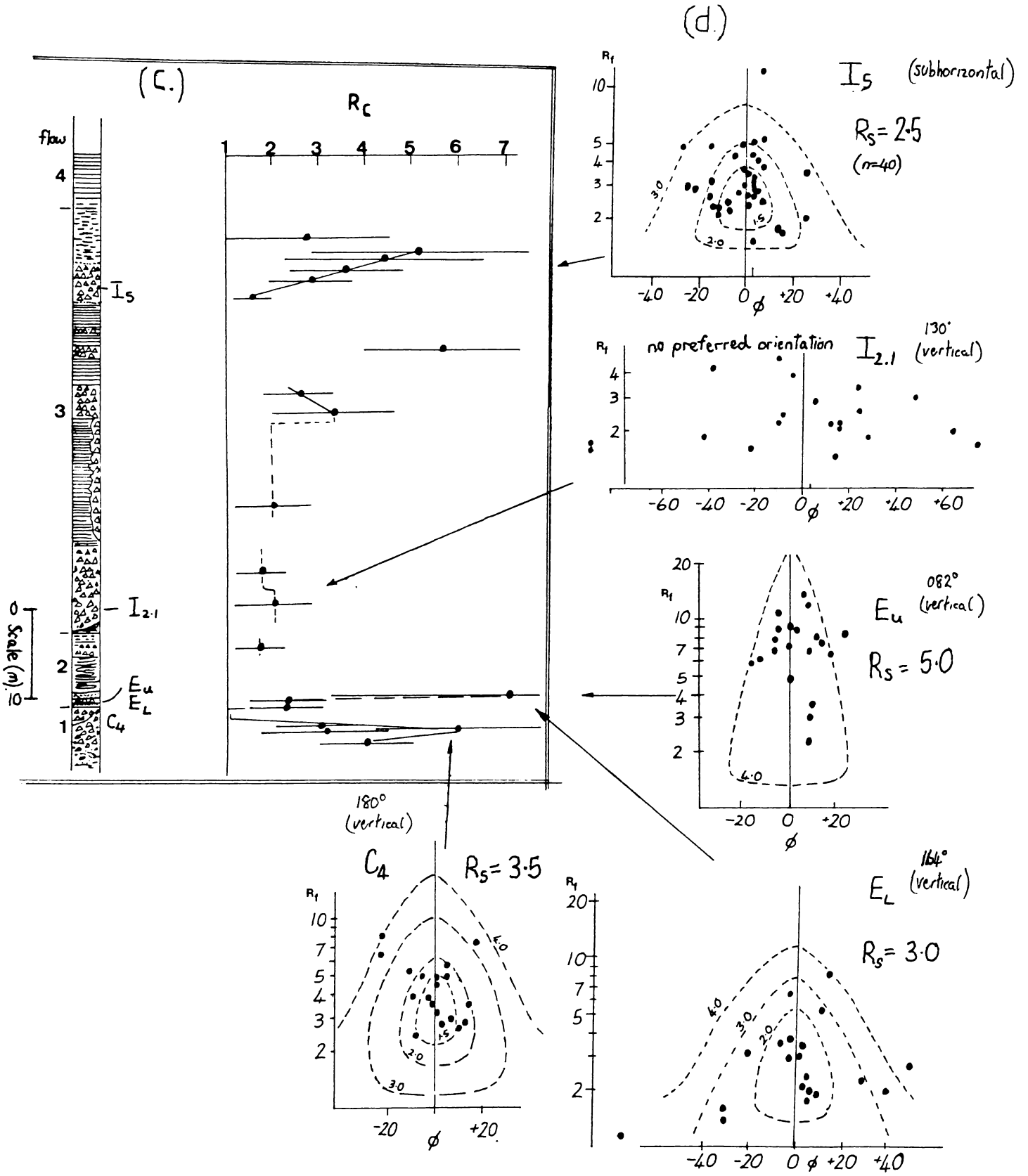

Fig. 7.3. Physical profiles of the flow sequence comprising the P3 lobe: (c) clast aspect ratio; (d) Rf/ϕ plots for autoclastic breccias. Plots illustrate flattening ratio and orientation of the long axes of autoclasts. Refer to Fig. 5.2c for the basis of strain analysis and the cautionary note on its applicability to lava flows. Strain interpretation is prevented by the lack of outcrop in three dimensions, and forces other than compaction (e.g. lava flowage) causing apparent alignment of clasts particularly for upper breccias such as C4 or I5. The orientation of each outcrop is appended to the plots.

Pitchstone fabrics within flow 4 are more uniform than the fabric units of flows 1 - 3, largely consisting of a dull resinous, partly devitrified groundmass, with flow lineations comprising differing sizes, types and orientations of crystallites (Stevenson, 1986). The dense dark green pitchstone contains black lozenge-shaped clasts that are finely lineated, non devitrified and globulite-rich.

7.2.5. An emplacement history for Pauanui.

Phenocrysts formed in the magma chamber and were embayed via partial resorption on ascent. Plagioclase phenocrysts show oscillatory zoning supporting an interrupted magmatic ascent. Smaller plagioclase laths formed after the phenocrysts as they are flow-aligned into flow bands which deviate around phenocrysts. Further diffusion and crystal growth was limited, there being no significant variation in lath length (in flow 3) indicating crystallisation prior to emplacement. Crystallites formed over the greatest interval of time, as is evident from:

a. globulite-rich zones around embayed plagioclase crystals indicating globulite formation during ascent;
b. flow around early-formed spherulites just prior to flow cessation.

The lack of microlites is either due to low undercooling on magmatic ascent or masking by isobaric crystallisation.

Early formed spherulites are usually weakly birefringent, ovoid in shape and occur in clusters as compound spherulites.

Convincing evidence of primary vesiculation in the form of pumiceous textures or gas blisters is lacking. However, vesiculation (primary voids) must have occurred during ascent and flow and contributed to the high viscosity of the brittle carapace.

Matrix textures of breccias are finely comminuted with secondary crystallisation of quartz rimming some clasts. Secondary textures have thus obliterated primary textures. Breccia formation occurred during flow and at cessation. Those autoclasts with the highest aspect ratio are invariably flow-aligned and are inferred to have had a longer brecciation history, occurring within the upper portions of flows 1 and 3. Clasts of low aspect ratio comprise irregular shaped pods that cut across the flow banded fabric of the interior of flow 3, and show no preferred flow alignment. Thus, these intraflow breccias formed at, or after, flow cessation.

Devitrification textures were initiated at high temperatures above the softening point of glass (T_g), evident from ovoid spherulites. Most groundmass devitrification textures however, were formed below the glass transition temperature.

Flow 2 appears to be too thin to be a lava flow. Basal clasts have a high aspect ratio (with values increasing upwards from the base), and the interior has fluidal fold features. An alternative explanation for the origin of flow 2, is that it may be a rheomorphic tuff. Evidence for a particulate emplacement origin is obliterated by devitrification and hydration textures approaching the "false pyroclastic" textures described by Allen (1989).

7.2.6. H_2O^+ and temperature estimates

Both LOI, from heating a tetraborate flux bead to 1000°C, and from heating powdered samples between 105 - 1000°C in a furnace, give high values of 0.5 - 1.5%.

These values indicate post-emplacement hydration of the original glass. Supportive evidence includes variations in the colour of the glass from mauve and brown to dark greyish-green, and curvilinear perlitic fractures in some units.

LOI was determined on powdered samples heated from 500°C to 1000°C, on representatives of all four flows, comprising area P3 and flow lobe P1 (Table 7.1). The value for the dark green pitchstone (0.15%) compares favourably with the value for total water (0.173%) determined by Karl-Fischer titration (Westrich writt. comm., 1989). The maximum water loss on step-wise pyrolysis occurred at 400°C over temperature range of 100 - 700°C, in contrast to the sharp mass loss peak at 600°C for fresh non-hydrated obsidian.

Table 7.1. Loss on ignition (LOI) and estimated H_2O^+ as LOI(500-1000°C) for Pauanui rhyolites.

sample	rock type	LOI (%)	LOI (500 - 1000 C) (%)
P1a	dacite	1.85	0.293
P1b	rhyolite	1.02	0.157
P3 A1 (1)	red pitchstone	0.80	0.186
P3 A1 (2)	"	"	0.197
P3 F2	spherulitic rhyolite	2.02	0.214
P3 I1	spherulitic rhyolite	1.28	0.219
P3 I4	flow banded rhyolite	n.d.	0.238
P4	dark green pitchstone	n.d.	0.149

Values of 0.15% to 0.22% are greater than those typical of obsidians (0.1%), and are representative of the eruptive water content of the lava together with a significant component from post-flow hydration.

The co-existence of hypersthene and augite (anhydrous minerals) with plagioclase indicate their crystallisation in a magma with an average temperature of 860°C and an average water content of 2.5% at 200 kbar pressures (Naney, 1983, Fig. 7.4).

7.2.7. Pauanui chemistry and inferred viscosity

Major element oxides and trace elements were analysed for twenty-four Pauanui samples, of which seventeen were from the composite flow section of lobe P3. Of the remaining seven analyses representing other Pauanui rhyolites, two were from lobe P1. The aim was to seek evidence of interdome variation (e.g. Pauanui vs Ohui - Windy Ridge), interflow and intraflow differences. Major and trace elements are tabulated in Table 7.2.

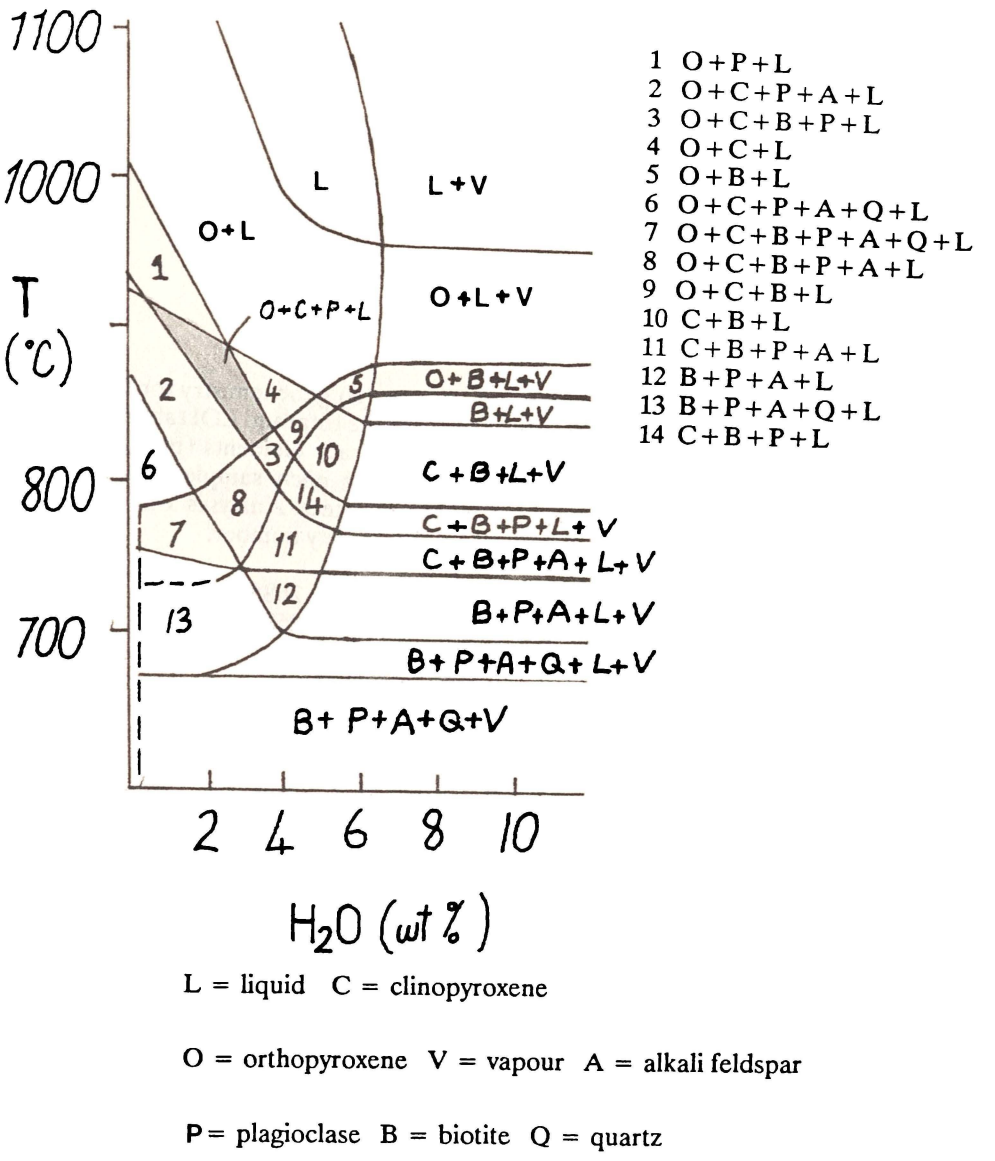

Fig. 7.4. T / H_2O phase diagram for a synthetic granite at 200 MPa pressure (after Naney, 1983). The shaded area represents the T / H_2O conditions under which the Pauanui phenocryst assemblage is stable.

Chemical variation is minimal throughout the Pauanui - Ohui region, with the exception of flow lobe P1. The basal part of lobe P1 is dacitic (69% SiO_2) comprising dark dense bands (density of 2.57 g/cm^3) with 13.7% phenocrysts of 0.7 mm average diameter, interlayered with pale pink rhyolitic bands (73% SiO_2, ϕ = 7%, Dm = 0.5 mm). Thus during the emplacement of the P1 lobe, co-mingling of two magmas occurred.

For the composite flow sequence (Fig 7.5) true intraflow variation appears random with little comparison of trends between like elements. Unlike Ben Lomond or Mayor Island, there is no fresh non-hydrated or non-devitrified glass as a benchmark for comparison within the flow as representative of the original liquid. Zig-zag trends may only indicate migration of trace elements during devitrification and low temperature hydration superimposed on the subtle chemical differences between flows.

Table 7.2. Major (a) and trace element (b) geochemistry for Pauanui rhyolites. Major elements (wt%) are tabulated on a volatile-free basis with the total and LOI tabulated as original analytical values (*). Total FeO + Fe_2O_3 is expressed as Fe_2O_3t. Trace elements (ppm) are tabulated as the mean ± 2 standard errors. Duplicate pellets were made for each sample giving four measurements of trace element concentration per sample. n.d. = not detected. Analyses 1-24 are listed below with sample description, fabric unit, sample site and Waikato University number.

1 rhyolite, Western Coulee, (s7)Pauanui (WT. 26859).
2 rhyolite, Western Coulee,(s8), Pauanui (WT.26860)
3 rhyolite, Trig Road (s15), Pauanui (WT. 26861).
4 rhyolite, Windy Ridge (s18) (WT. 26862)
5 rhyolite, Ohui (s46) (WT. 26863).
6 dacite, lobe P1, Pauanui (WT. 26864).
7 rhyolite, lobe P1, Pauanui (WT. 26865).
8 rhyolite (grey pitchstone), flow 1 (P3tT) Pauanui (WT. 26866).
9 red pitchstone, flow 1(P3), Pauanui (WT. 26867).
10 autobrecciated rhyolite, upper flow 1(P3), Pauanui (WT. 26868).
11 autobrecciated rhyolite lower unit E, basal flow 2 (P3) Pauanui, (WT. 26869).
12 autobrecciated rhyolite, upper unit E, basal flow 2 (P3) Pauanui (WT. 26870).
13 spherulitic rhyolite, unit F, flow 2 (P3) Pauanui (WT.26871).
14 flow banded rhyolite, unit G, flow 2 (P3) Pauanui (WT. 26872).
15 autobrecciated rhyolite, unit H, flow 2 (P3) Pauanui (WT. 26873).
16 dark grey glassy spherulitic rhyolite, unit I_1 (basal flow 3, P3) Pauanui (WT. 26874).
17 matrix-supported autobrecciated rhyolite (unit $I_{2.1}$) flow 3 (P3) Pauanui (WT. 26875).
18 clast-supported autobrecciated rhyolite (unit $I_{2.2}$) flow 3(P3) Pauanui (WT. 26876).
19 flow banded rhyolite (unit I_4) flow 3 (P3) Pauanui (WT. 26877).
20 autobrecciated rhyolite (unit I_5) flow 3(P3) Pauanui (WT. 26878).
21 rhyolite/brown pitchstone (flow 3/4 boundary, P3) Pauanui (WT. 26879).
22 brown pitchstone, flow 4, (P3) Pauanui (WT. 26880).
23 grey pitchstone, flow 4, (P3) Pauanui (WT. 26881).
24 dark green pitchstone, flow 4, (P3) Pauanui (WT. 26882).

	1	2	3	4	5	6	7	8	9	10	11	12
SiO_2	74.08	74.22	74.59	74.26	73.93	69.07	73.64	73.40	73.50	73.52	73.59	73.63
TiO_2	0.35	0.35	0.35	0.35	0.34	0.50	0.34	0.35	0.36	0.36	0.37	0.37
Al_2O_3	13.87	15.18	14.18	14.28	13.93	15.24	13.82	14.11	14.34	14.30	14.69	14.57
Fe_2O_3t	2.59	2.56	2.36	2.46	2.19	4.60	2.82	2.48	2.62	2.55	2.54	2.47
MnO	0.03	0.03	0.03	0.04	0.05	0.04	0.03	0.03	0.07	0.03	0.06	0.04
MgO	0.28	0.23	0.21	0.22	0.39	0.96	0.34	0.31	0.33	0.35	0.27	0.26
CaO	1.64	1.17	1.44	1.48	1.87	3.19	1.84	2.01	1.70	1.79	1.54	1.71
Na_2O	4.11	3.26	3.84	3.80	4.24	3.91	4.12	4.35	4.15	4.22	3.88	4.11
K_2O	3.02	2.97	2.97	3.08	2.94	2.43	2.98	2.87	2.89	2.84	3.05	2.81
P_2O_5	0.02	0.02	0.02	0.03	0.06	0.08	0.05	0.07	0.04	0.03	0.02	0.03
Total*	99.76	99.20	99.44	99.27	99.60	99.64	99.62	99.80	99.81	99.94	99.20	99.49
LOI*	1.44	2.50	1.26	1.30	0.60	1.85	1.02	0.59	0.80	0.94	1.46	1.10

	13	15	16	17	18	20	21	22	23	24
SiO_2	73.75	73.68	73.75	73.70	73.87	73.40	73.54	73.46	73.36	73.17
TiO_2	0.37	0.38	0.37	0.37	0.36	0.38	0.36	0.35	0.35	0.35
Al_2O_3	14.49	14.85	14.47	14.72	14.45	15.15	14.19	14.19	14.16	14.10
Fe_2O_3t	2.48	2.63	2.40	2.61	2.43	2.70	2.51	2.50	2.33	2.51
MnO	0.02	0.05	0.02	0.03	0.02	0.08	0.04	0.04	0.05	0.06
MgO	0.20	0.26	0.32	0.38	0.32	0.39	0.25	0.31	0.22	0.33
CaO	1.66	1.40	1.67	1.52	1.71	1.40	1.88	1.94	1.98	1.99
Na_2O	4.06	3.76	4.07	3.79	4.03	3.60	4.26	4.29	4.56	4.52
K_2O	2.94	2.99	2.89	2.85	2.78	2.89	2.91	2.84	2.89	2.88
P_2O_5	0.03	0.02	0.03	0.02	0.02	0.02	0.05	0.07	0.08	0.09
Total*	100.17	99.77	99.98	99.84	99.28	99.76	100.04	99.94	99.97	99.91
LOI*	2.02	2.00	1.28	1.56	1.22	2.20	0.79	0.69	0.45	0.20

	1	2	3	4	5	6	7	8	9	10	11	12
Sc	8.2 ± 0.5	6.9 ± 0.7	7.9 ± 0.3	8.0 ± 0.9	7.5 ± 0.4	15.0 ± 0.5	8.7 ± 0.9	7.9 ± 0.6	7.8 ± 0.7	8.3 ± 0.6	8.3 ± 0.8	8.4 ± 0.2
V	14.4 ± 1.6	12.0 ± 1.0	12.9 ± 0.7	12.8 ± 0.9	13.8 ± 0.7	67.6 ± 1.3	19.9 ± 0.7	13.7 ± 0.6	14.5 ± 0.7	14.3 ± 0.2	15.8 ± 0.6	14.5 ± 1.1
Cr	3.2 ± 0.1	1.9 ± 0.8	1.8 ± 1.0	1.3 ± 0.7	1.9 ± 0.2	36.4 ± 0.4	4.5 ± 0.6	1.8 ± 0.2	1.2	2.4 ± 0.4	1.3 ± 0.4	2.0 ± 0.2
Ni	1.2 ± 0.[illegible]	4.4 ± 0.3	2.8 ± 0.1	2.7 ± 0.2	2.3 ± 0.6	7.1 ± 0.1	2.5 ± 0.4	0.5 ± 1.1	3.5 ± 0.8	0.9 ± 0.4	7.2 ± 0.3	0.8 ± 0.2
Cu	7.7 ± 1.1	9.0 ± 1.7	6.6 ± 0.5	9.4 ± 3.6	6.8 ± 0.6	17.8 ± 0.5	9.3 ± 1.6	7.5 ± 1.4	7.9 ± 3.7	7.6 ± 2.7	7.3 ± 0.5	5.9 ± 0.7
Zn	48.1 ± 0.4	6[illegible].9 ± 1.0	55.4 ± 0.7	55.0 ± 2.4	56.4 ± 0.4	68.8 ± 0.5	56.7 ± 0.7	55.6 ± 1.0	59.9 ± 1.4	60.2 ± 1.6	56.1 ± 0.6	56.5 ± 0.4
Ga	14.9 ± 1.1	15.[illegible] ± 0.8	15.0 ± 0.4	15.4 ± 0.7	14.7 ± 0.9	15.5 ± 0.7	15.7 ± 0.9	15.6 ± 0.7	15.7 ± 0.4	16.2 ± 0.1	16.2 ± 0.4	15.6 ± 0.4
As	2.6 ± 0.4	3.1 ± 0.6	2.4 ± 0.1	2.5 ± 0.2	2.6 ± 0.4	2.9 ± 0.5	3.6 ± 0.3	2.3 ± 0.2	3.2 ± 0.3	3.9 ± 0.3	4.3 ± 0.6	3.8 ± 0.2
Rb	99.9 ± 1.2	104.8 ± 0.9	103.2 ± 0.3	109.7 ± 0.3	90.4 ± 0.5	87.2 ± 0.8	100.4 ± 0.6	99.2 ± 0.4	102.5 ± 0.2	99.2 ± 0.4	103.2 ± 0.7	99.5 ± 0.4
Sr	120.3 ± 0.7	100.9 ± 0.8	111.2 ± 0.4	125.5 ± 0.3	131.2 ± 0.2	172.4 ± 0.8	129.3 ± 1.0	143.8 ± 0.8	126.8 ± 0.7	133.1 ± 0.6	125.1 ± 0.4	128.1 ± 0.3
Y	30.9 ± 0.3	24.7 ± 0.4	78.6 ± 0.7	32.1 ± 0.7	31.9 ± 0.2	35.2 ± 0.6	27.4 ± 0.2	35.3 ± 0.6	28.1 ± 0.8	28.5 ± 0.3	24.4 ± 0.6	22.2 ± 0.4
Zr	188.9 ± 0.7	197.4 ± 1.7	192.0 ± 1.0	191.3 ± 0.9	189.6 ± 0.5	154.5 ± 0.3	182.9 ± 0.3	185.9 ± 4.6	189.5 ± 2.3	185.2 ± 2.4	186.4 ± 0.5	187.7 ± 1.6
Nb	6.3 ± 0.6	6.8 ± 1.0	7.0 ± 0.9	6.4 ± 0.6	6.3 ± 0.4	5.7 ± 1.4	6.8 ± 0.1	6.5 ± 0.5	7.2 ± 0.1	6.9 ± 0.2	6.1 ± 0.4	5.6 ± 0.6
Ba	624.4 ± 1.6	618.0 ± 3.0	643.0 ± 4.4	711.6 ± 3.9	645.5 ± 3.7	546.2 ± 2.3	637.8 ± 2.7	604.6 ± 2.5	621.9 ± 16.6	596.1 ± 8.6	625.2 ± 2.5	596.0 ± 4.1
La	17.6 ± 0.5	24.5 ± 0.9	67.9 ± 1.3	59.9 ± 0.9	18.9 ± 0.4	20.9 ± 1.1	16.4 ± 0.6	20.3 ± 0.4	14.6 ± 0.9	21.7 ± 0.5	17.2 ± 0.6	13.3 ± 0.9
Ce	35.7 ± 0.9	31.8 ± 1.0	47.7 ± 0.5	46.7 ± 1.8	40.0 ± 2.0	37.2 ± 2.0	34.2 ± 2.1	35.3 ± 1.6	37.1 ± 0.9	32.8 ± 2.0	39.0 ± 0.7	32.9 ± 2.1
Pb	14.0 ± 0.5	13.9 ± 0.6	16.5 ± 0.9	13.3 ± 0.7	15.2 ± 0.5	12.8 ± 0.9	12.5 ± 0.3	13.9 ± 0.3	14.3 ± 0.7	13.1 ± 0.9	11.1 ± 0.7	12.3 ± 0.4
Th	11.7 ± 0.3	12.5 ± 0.5	12.3 ± 1.2	11.9 ± 0.3	12.1 ± 0.4	10.2 ± 0.7	11.6 ± 0.5	11.3 ± 0.6	11.5 ± 0.4	10.9 ± 0.6	11.4 ± 0.5	10.9 ± 0.6
U	2.9 ± 0.5	2.7 ± 0.2	2.5 ± 0.3	2.9 ± 0.3	3.0 ± 0.5	1.9 ± 0.2	2.6 ± 0.3	2.8 ± 0.2	2.8 ± 0.3	2.7 ± 0.4	2.6 ± 0.4	2.7 ± 0.7

	13	14	15	16	17	18	19	20	21	22	23	24
Sc	8.0 ± 0.6	8.3 ± 0.9	8.3 ± 0.5	8.4 ± 0.7	8.0 ± 1.0	7.9 ± 1.4	8.8 ± 0.7	8.3 ± 0.4	8.2 ± 0.6	8.1 ± 0.7	8.2 ± 0.8	8.2 ± 0.3
V	15.5 ± 0.2	14.4 ± 0.5	15.3 ± 0.7	14.6 ± 0.3	14.6 ± 1.0	14.7 ± 0.6	14.7 ± 0.4	15.9 ± 0.3	15.1 ± 0.7	13.9 ± 0.6	14.3 ± 0.7	13.9 ± 0.2
Cr	2.6 ± 0.1	1.4 ± 0.1	1.5 ± 0.8	2.5 ± 0.4	1.8 ± 0.3	1.2 ± 0.1	1.6 ± 0.2	1.1 ± 0.4	2.0 ± 0.2	1.1 ± 0.2	1.6 ± 0.5	1.0 ± 0.3
Ni	0.5 ± 0.4	0.5 ± 0.4	0.8 ± 0.5	2.4 ± 0.1	0.2 ± 0.4	0.2 ± 0.3	5.5 ± 0.2	3.6 ± 0.3	0.2 ± 0.3	0.2 ± 0.1	0.5 ± 0.3	1.1 ± 0.3
Cu	7.6 ± 0.9	7.1 ± 1.8	7.3 ± 1.9	6.7 ± 1.7	5.7 ± 0.6	4.9 ± 0.2	5.1 ± 0.2	5.5 ± 0.5	5.1 ± 0.5	5.6 ± 0.9	7.1 ± 2.4	5.1 ± 0.5
Zn	59.9 ± 0.4	56.2 ± 0.9	64.0 ± 0.6	59.7 ± 0.8	62.2 ± 0.7	61.2 ± 0.1	54.9 ± 0.3	56.3 ± 0.5	49.2 ± 0.4	52.6 ± 0.3	50.7 ± 2.3	56.6 ± 0.6
Ga	16.0 ± 0.4	15.8 ± 0.3	16.5 ± 0.9	15.9 ± 0.3	15.8 ± 0.3	15.9 ± 0.4	15.6 ± 0.6	16.3 ± 0.2	15.8 ± 0.4	15.4 ± 0.3	16.2 ± 0.7	15.5 ± 0.1
As	3.7 ± 0.2	2.7 ± 0.4	1.7 ± 0.7	3.2 ± 0.4	3.4 ± 0.4	3.3 ± 0.4	3.4 ± 0.1	4.0 ± 0.2	3.7 ± 0.3	4.4 ± 0.4	2.3 ± 0.5	3.0 ± 0.5
Rb	101.4 ± 1.1	102.5 ± 0.6	104.1 ± 0.4	100.4 ± 0.9	100.3 ± 0.5	98.5 ± 0.4	100.6 ± 0.1	99.0 ± 0.2	100.7 ± 0.6	98.0 ± 0.3	99.5 ± 0.4	99.6 ± 0.4
Sr	129.3 ± 1.65	129.3 ± 0.5	120.0 ± 0.8	120.0 ± 0.8	120.2 ± 0.7	131.0 ± 0.6	127.8 ± 1.03	118.4 ± 0.6	139.6 ± 0.7	140.9 ± 0.5	140.2 ± 0.5	141.9 ± 0.9
Y	23.1 ± 0.4	19.1 ± 0.9	24.6 ± 0.3	31.0 ± 0.2	20.5 ± 0.7	25.7 ± 0.7	25.2 ± 0.6	21.8 ± 0.5	29.4 ± 0.2	29.6 ± 0.3	25.2 ± 0.6	30.3 ± 1.0
Zr	188.1 ± 0.6	184.2 ± 1.3	183.8 ± 1.1	186.8 ± 1.4	186.6 ± 0.2	185.3 ± 0.4	188.9 ± 1.8	190.3 ± 0.6	185.4 ± 1.7	182.4 ± 0.5	185.2 ± 0.6	182.9 ± 0.6
Nb	6.9 ± 0.8	6.6 ± 0.6	6.3 ± 0.4	6.5 ± 0.6	6.3 ± 0.6	6.3 ± 0.9	6.7 ± 0.5	6.5 ± 1.1	6.9 ± 0.7	6.4 ± 0.3	6.5 ± 0.2	5.9 ± 0.4
Ba	602.3 ± 4.4	615.1 ± 1.9	622.7 ± 0.6	602.4 ± 1.6	598.1 ± 2.1	601.8 ± 0.4	633.6 ± 3.0	642.7 ± 2.4	618.0 ± 10	630.9 ± 1.4	620.2 ± 2.5	622.4 ± 4.4
La	16.5 ± 0.4	14.8 ± 0.2	15.9 ± 0.7	17.2 ± 0.5	16.2 ± 0.7	22.3 ± 0.7	16.4 ± 1.2	14.3 ± 0.9	25.2 ± 0.3	18.6 ± 0.4	15.9 ± 0.2	18.1 ± 0.7
Ce	30.8 ± 1.1	36.1 ± 0.6	33.8 ± 1.1	33.4 ± 1.8	26.9 ± 0.4	27.0 ± 0.8	31.8 ± 1.4	31.6 ± 0.5	40.7 ± 2.0	38.6 ± 0.9	38.1 ± 0.8	40.2 ± 0.7
Pb	14.0 ± 0.9	13.3 ± 0.3	14.2 ± 0.5	14.5 ± 1.2	15.6 ± 0.5	14.0 ± 1.0	12.1 ± 0.6	14.1 ± 0.7	14.7 ± 0.8	14.1 ± 0.8	14.6 ± 0.8	13.7 ± 0.8
Th	12.0 ± 0.5	10.8 ± 4.4	11.1 ± 0.5	11.7 ± 0.6	11.0 ± 0.2	11.3 ± 0.4	11.7 ± 0.7	11.4 ± 0.9	11.6 ± 0.5	11.2 ± 0.6	11.0 ± 0.5	11.2 ± 0.7
U	2.4 ± 0.6	2.1 ± 0.5	2.5 ± 0.3	2.4 ± 0.4	2.7 ± 0.5	2.9 ± 0.5	2.6 ± 0.4	3.0 ± 0.1	2.7 ± 0.3	2.6 ± 0.2	2.4 ± 0.5	2.7 ± 0.6

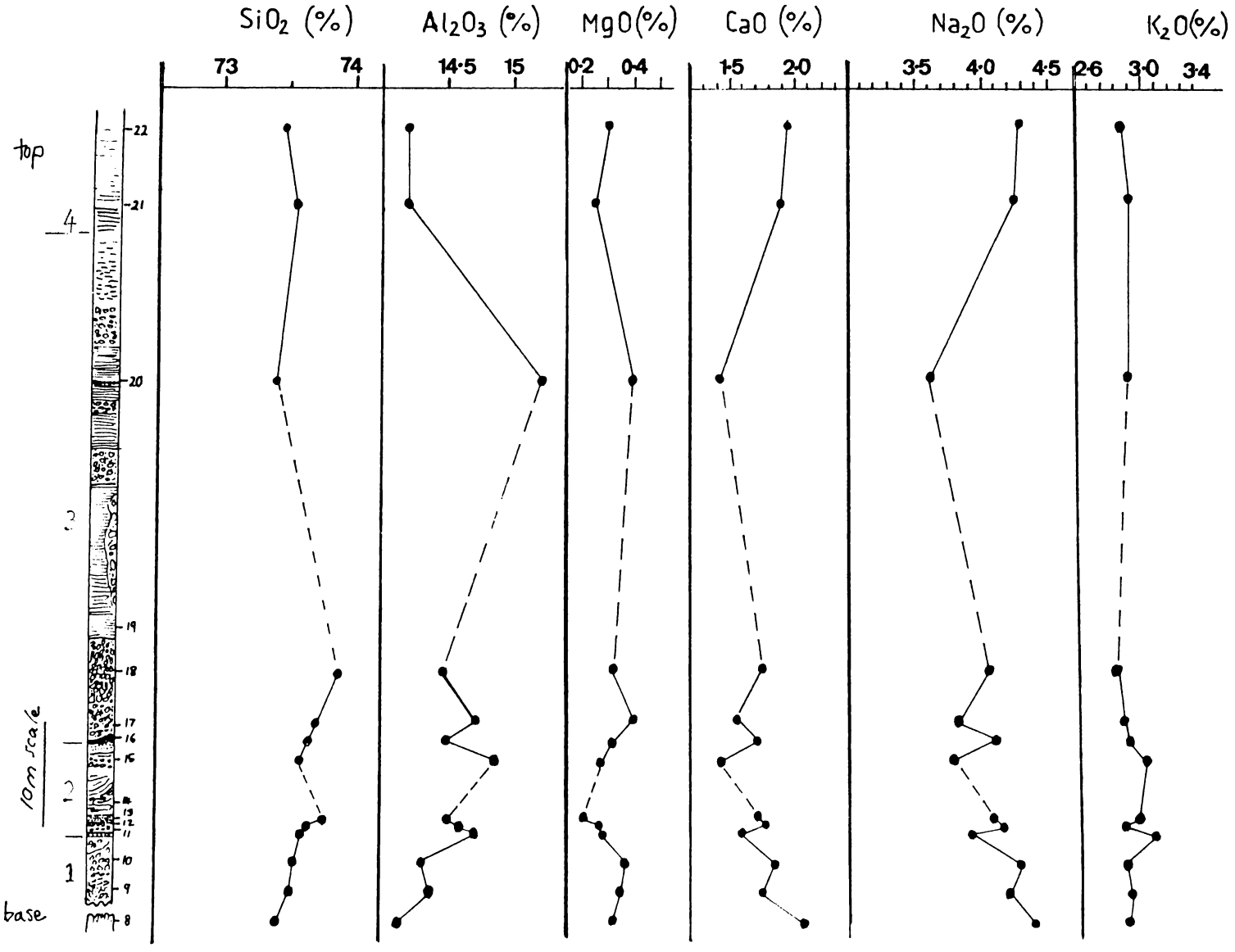

Fig. 7.5. Major and trace element variations for the Pauanui flow sequence, P3. Major elements are plotted on a volatile free basis (wt%). Trace element values are in ppm. Error bars represent two standard errors.

trace elements on following two pages.

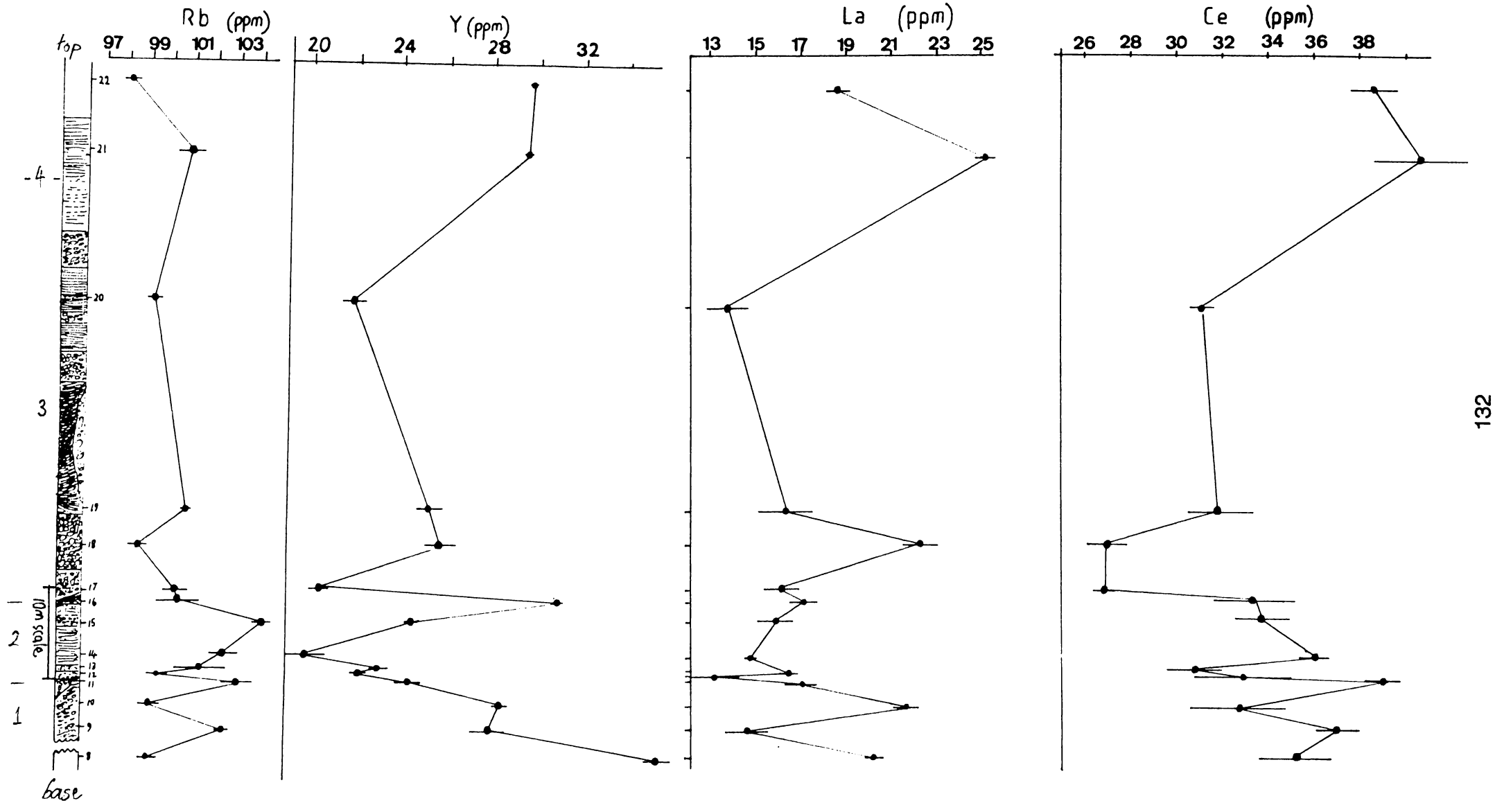

Fig. 7.5 continued; Trace elements; Pauanui

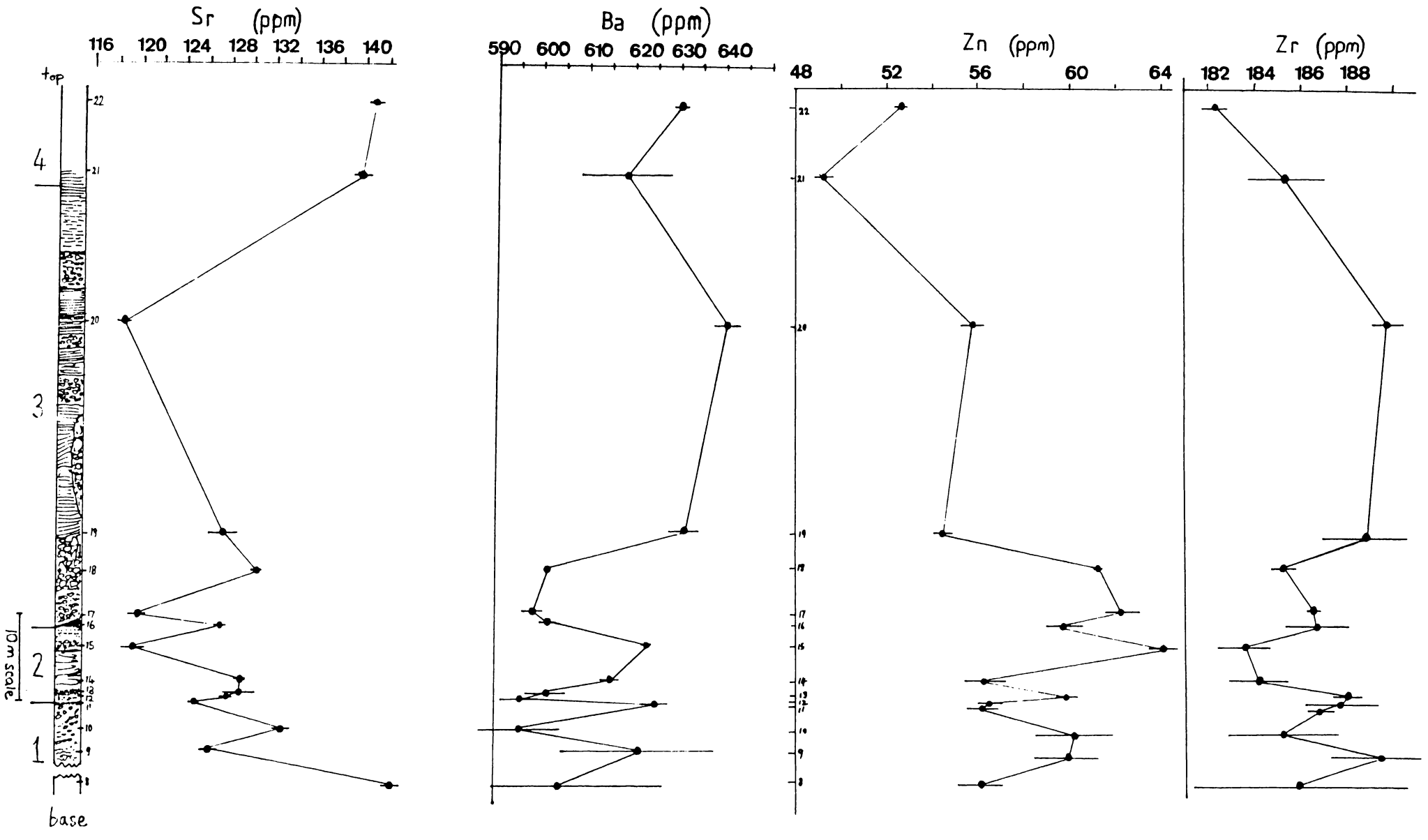

Fig. 7.5. continued; trace elements; Pauanui

The viscosity of the Pauanui lavas calculated by the method of Shaw (1972), Shaw (1965), and Murase et al. (1984) for effective viscosity including suspended crystals, is summarised in Table 7.3. There seems to be no relation between lobe length and viscosity of the liquid plus suspended crystals, indicating that the effusion rate or volume of the emplacing lava was the major contributing factor to the variations in flow length.

Table 7.3. Viscosity results, Pauanui. For each sample, the first value for effective viscosity (ηe) represents the method of Shaw (1965) (equation 4.11) and the second, Murase et al. (1984) (equation 4.13).

	T = 820 C		T = 860 C		T = 900 C		T = 940 C		T = 960 C	
log 10 η	ηo	ηe	ηo	ηe	ηo	ηe	ηo	ηe	ηo	ηe
P1a	8.80	9.02	8.31	8.53	7.86	8.07	7.43	7.65	7.23	7.44
		8.96		8.48		8.02		7.59		7.39
P1b	9.93	10.04	9.39	9.50	8.89	9.00	8.42	8.54	8.20	8.31
		9.98		9.45		8.95		8.48		8.26
P3A1 flow 1	9.94	10.06	9.41	9.52	8.90	9.02	8.44	8.55	8.21	8.33
		9.99		9.46		8.96		8.49		8.27
Eu flow 2	10.03	10.11	9.49	9.57	8.98	9.06	8.50	8.59	8.29	8.37
		10.06		9.52		9.01		8.54		8.32
I flow 3	9.93	10.02	9.32	9.48	8.89	8.98	8.42	8.51	8.20	8.29
		9.96		9.42		8.92		8.46		8.23
P3 flow 4	9.85	9.96	9.32	9.42	8.82	8.93	8.36	8.46	8.14	8.24
		9.90		9.37		8.87		8.41		8.19

The co-mingling of rhyolite and dacite magmas near the base of the P1 lobe is manifest in the interlayered dark crystal-rich and light crystal-poor zones. The difference in viscosity between the layers is approximately one order of magnitude. No lozenge or pinchout structures typical of the co-mingling of immiscible magmas and generation of hybrid textures as at South Deadman Creek Dome, Long Valley Caldera, northern California, were observed at Pauanui.

7.3. The Rheology of the Okataina Volcanic Centre Flows.

7.3.1. Introduction

Although the flows and domes of the Okataina Volcanic Centre are the youngest of the four major rhyolite eruptive centres of the Taupo Volcanic Zone (Nairn, 1981), and have excellent areal exposures, flow outcrops are sparse. However in light of the model from the older, dissected and comparatively better exposed Ben Lomond flow, insights into the flow behaviour can be determined. In addition, contrasts can be made between the different methods of estimating viscosity.

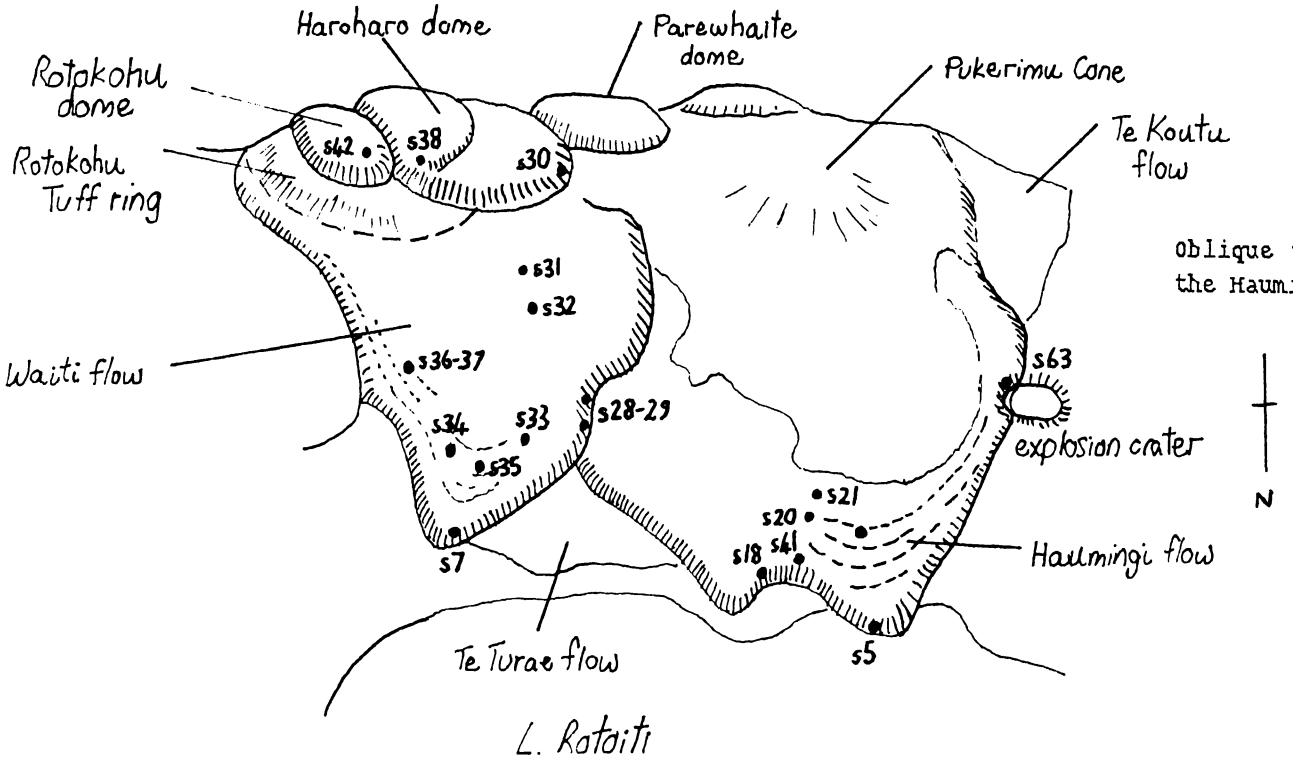

Oblique view sketch of the location of sites on the Haumingi and Waiti flows.

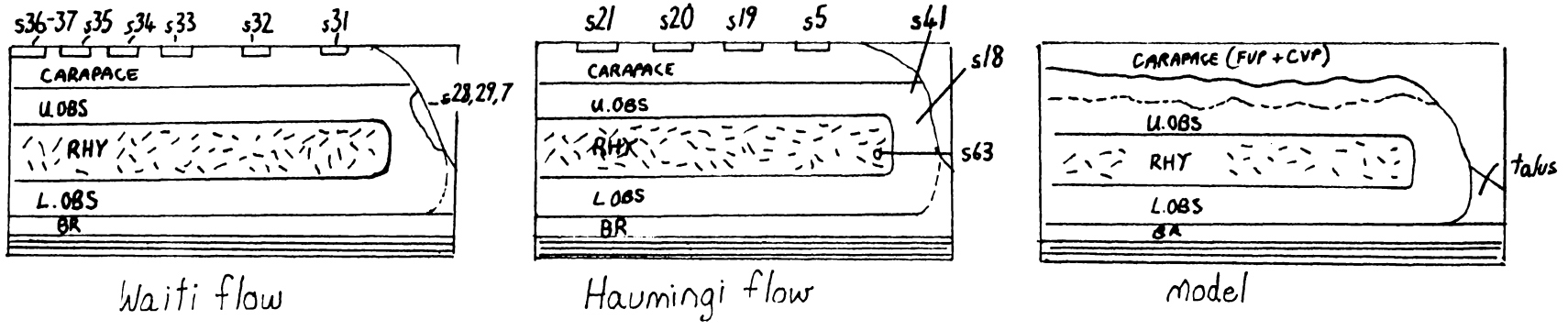

Fig. 7.6. Outcrop interpretation, Haumingi and Waiti flows.

Table 7.4. Exposure of flow stratigraphic units, Okataina Volcanic Centre.

flow / dome	FVP	CVP	U OBS	RHY	L OBS	BR
Haumingi f.	*	*	*	*	-	-
Waiti f.	*	*	*	-	-	-
Te Koutu f.	-	-	-	*	-	-
Parewhaite d.	*	-	-	*	-	-
Haroharo d.	*	-	-	-	-	-
Rotokohu d.	*	-	-	-	-	-
Okataina f.	*	-	*	-	-	-
Kaipara f.	-	-	-	*h	-	-
Hanini d.	*	-	*v	-	-	-
Hanini f.	*	-	-	*	-	-
Makatiti f / d.	*	*e	-	-	-	-
Tapahoro d.	-	-	-	*	-	-

e = explosion pits
v = vesiculated
h = hydrothermally altered

* = outcrop
- = no outcrop; not observed or obscured.

CVP = low density foam with void shapes unlike the CVP of Fink and Manley (1987)

Table 7.5. Physical properties Okataina Volcanic Centre flows: Haumingi, Waiti, Haroharo and Rotokohu rhyolites.

flow	site	fabric	n	density (ρ) g/cm^3	porosity	void size (mm)	Rv
Haumingi flow	s5	CVP	4	0.65 ± 0.01	70.81 ± 0.44	-	-
	s5	OBS clasts	4	2.33 ± 0.004	-	-	-
	s19	vesic. OBS clasts	4	1.07 ± 0.12	53.21 ± 5.00	5	1.85 ± 0.35
	s19	OBS clasts	4	2.33 ± 0.01	-	-	-
	s20	CVP	5	0.84 ± 0.05	61.85 ± 2.33	1.33 ± 0.42 0.07 ± 0.03	1.85 ± 0.57 14.60 ± 6.71
	s20	CVP	5	0.62 ± 0.10	71.90 ± 4.20	-	-
	s18	OBS	6	2.20 ± 0.06	3.88 ± 2.50	~ 10 (average)	3.03 ± 0.75
	s21	FVP	-	-	-	0.07 ± 0.05	13.14 ± 6.8
Waiti flow	s29	OBS	3	2.28 ± 0.02	0.84 ± 0.85	-	
	s31	FVP	1	2.05	10.75	-	
	s32	FVP	4	1.94 ± 0.41	16.96 ± 6.52	-	
	s36	FVP	10	2.00 ± 0.08	12.81 ± 3.58	0.13 ± 0.06	
	s36	(CVP)	4	0.66 ± 0.03	71.19 ± 1.36	-	
	s37	FVP	4	1.26 ± 0.03	44.88 ± 1.51	-	
Haroharo dome	s30	FVP	5	1.25 ± 0.03	45.94 ± 1.03	-	
	s38	FVP	5	1.87 ± 0.12	19.32 ± 5.63	0.03 ± 0.02	
Rotokohu dome	s42	FVP	5	1.98 ± 0.05	14.83 ± 1.99	0.02 ± 0.01	

7.3.2. Flow stratigraphy and petrofabrics; description and interpretations.

The general flow stratigraphy of the Okataina Volcanic Centre flows is summarised in Table 7.4. Of the Okataina Volcanic Centre Flows, the Haumingi and Waiti flows were studied in most detail. Available exposures are interpreted in Fig 7.6 in terms of a flow stratigraphy model developed for Ben Lomond. Physical properties are described in Table 7.5.

The finely vesicular pumice is brecciated with steeply dipping flow banding (e.g. 026/68°W at s21). Road cut sections bisect ridges interpreted as pressure ribs in the carapace, and are draped with airfall

tephra. As the flow surface cooled, the top of the flow locally contracted and extended and was thrown into a series of folds, corresponding with surface ridges convex in a down-flow direction.

Parts of the carapace contain dense obsidian blocks, and foamy obsidian indicating late phase inflation of voids from volatile migration from within the crystallising flow centre. The H_2O^+ value for the foam is more than 0.3%, comprising interconnecting voids of approximately 5 mm size, akin to the coarsely vesicular pumice of Fink and Manley (1987). However, void shapes are less variable than the coarsely vesicular pumice of Obsidian Dome. The volatile-rich zone model above is supported by the following textural evidence:

a. domains or zones of inflation occur (eg. s.20);
b. clasts have void septa perpendicular to flow banding or cooling surfaces.

The latter indicates effervescence on release of overburden confining pressures such as during tension crack propagation. On the Makatiti flow three explosion pits (30 m deep) occur with associated deposits comprising monolithologic ash, lapilli, and block breccia, with pumiceous and glassy blocks attaining 1 m diameter (Nairn 1981). According to Nairn, (1981) all Makatiti pits occur in valleys between flow ridges, suggesting that pit-forming explosions originated by the concentration of infiltrating surface water onto underlying hot lava. In contrast, the outcrop at s20 on the Haumingi flow, comprising coarsely vesicular glassy foam, bisects a flow ridge and is inferred to be associated with the migration and collection of volatiles late in the flow history.

On the flow margin, the FVP avalanched down the flow front exposing the underlying OBS layer. Blocks of FVP, OBS and RHY occur in the talus apron below large rib-like outcrops of obsidian which wrap around the central devitrified core of rhyolite. Such a core is exposed at Lake Rotoatua (s63) where an explosion crater excavated a notch in the flow margin. The central rhyolite is finely spherulitic and massive with widely spaced shrinkage joints. The obsidian ribs of s18 have steeply inclined flow banding (138/72°SW) with pockets of primary vesiculation (Rv = 3, with void long axes of approximately 75 mm in length), that distort the primary flow banding, and is typified by thin septa perpendicular to flow banding and cooling surfaces (Fig. 7.7a). Similar textures have been seen at the Panum dome, northern California (Fig. 7.7b) where vesiculation of volatile-rich flow layers occurred on sudden removal of overburden, during the overturning and opening of tension cracks within the upper flow stratigraphy. Avalanches of carapace debris on the flow margin during late-flow phase could account for the formation of the vesiculation textures at s18. Surfaces within the OBS layer of both the Haumingi and Waiti flows have striations and cracks that dissect a thin pale greyish orange skin. Crack propagation and the removal of overburden stresses would cause the release of gases, resulting in the oxidation and sudden cooling of the surficial skin. Tensile fracture of the cool block surfaces by more fluid thermally insulated lava results in the widening of the central portions of the crack segments.

7.3.3. Water content and temperature

The petrography of the Okataina Volcanic Centre lavas has been well documented (Ewart and Healy. 1965; Ewart, 1967; Ewart et al. 1971; Ewart et al. 1975) comprising an assemblage of plagioclase, quartz, cummingtonite, hypersthene and magnetite.

a

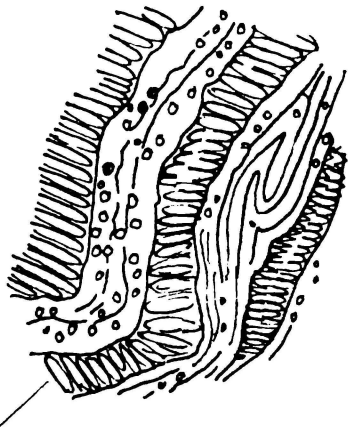

s18 Haumingi flow

Vesiculated units characterised by glassy septa between vesicles normal to original cooling surface.

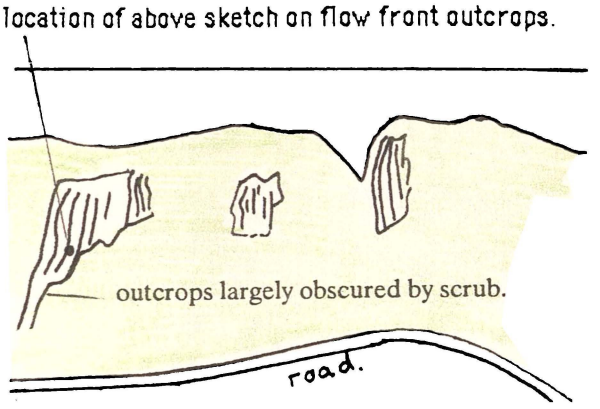

Panum dome, Mono Craters northern California; vesiculated zones and boudinage. Void long axes are perpendicular to flow layers as at s18.

Fig. 7.7. Vesiculation textures: Haumingi flow (a); versus Panum dome, Mono Craters, northern California (b).

Mineral pair geothermometry of lavas using Fe-Ti oxides, gives closure equilibrium temperatures of 730 - 780°C (Ewart et al. 1971; 1975). The original volatile content of the lava during emplacement is best approximated as LOI between 500 - 1000°C. Heating over this interval releases water bound within silanol groups comprising the glass polymers (Eichelberger and Westrich, 1981). Estimated H_2O^+ from LOI(500 - 1000°C) is approximately 0.2% and is typical of obsidians. Experiments in a synthetic system (Naney, 1983) similar to the OVC magmas show the dependence of liquidus temperature and amphibole stability on water content at 2 and 8 kbars. Amphibole minerals become stable at water contents of 3 - 4 wt%. Hence there must have been a significant degassing (ΔH_2O = 4%) between the chamber and the surface. In contrast for Pauanui the ΔH_2O between the chamber and surface is inferred to be approximately 2.5 wt%.

7.3.4. Estimation of rheological parameters

Table 7.6a lists the inferred viscosity of the liquid (η_o) and effective viscosity (η_e) of the Haumingi flow, Waiti flow and Haroharo dome. The overlapping lobes building the Haroharo dome have a marginally larger ϕ and Dm value than the preceding Waiti flow, but the same order of magnitude of viscosity. This indicates that the dome-flow dichotomy is not due to a greater crystallinity contributing to a more viscous lava, as both ϕ and η_e are roughly similar.

Table 7.6b lists other parameters measured from airphotos and topographic maps. Although outcrops are sparse, the clearly defined flow morphology allows other methods of estimating rheological parameters to be attempted. Such methods (such as those in Hulme, 1974) cannot be employed for Pauanui or Mayor Island where identification of levees, ridges and channels is difficult owing to lack of areal exposure.

Table 7.6a. Inferred viscosity of the liquid (ηo) and suspension (ηe) for the Okataina Volcanic Centre flows - Haumingi, Waiti and Haroharo.

flow	H_2O^+ (%)	T (C)	ϕ (%)	Dm (mm)	log η o	log η e (1)	log η e (2)
Haumingi	0.18	770	6.9	0.306	11.09	11.20	11.1
Waiti	0.12	740	9.7	0.426	11.55	11.70	11.62
Haroharo	(0.16 - 0.20)	(730 - 740)	10.1	0.499	11.71	11.86	11.79

$\eta e(1)$ is calculated from equation 4.11 and $\eta e(2)$ from equation 4.13.

Table 7.6b. Flow morphological parameters for the Haumingi, Waiti and Haroharo flows.

flow	length L (m)	thickness h (m)	aspect ratio L/h	basal slope	average width w	yield strength Y (x 10^3 Pa)
Haumingi	6780	120 - 150	48.4	5.6	3166	245.5
Waiti	5000	150	33.6	5.5	2922	318.9
Haroharo	2670	130	20.6	4.5	2266	109.2

Yield strength is calculated using equation 4.1. However, the equation for effusion rate (F) (equation 4.4), gives 14 m^3/s for Waiti flow. When substituted into equation 4.6 for viscosity, a value of approximately 2 x 10^{12} poise is obtained. This may be considered an upper limit for viscosity as F is calculated from the dimensionless Graetz number (Gz) related to the cooling of a warm fluid moving through a cold pipe (Hulme and Fielder, 1977; Zimbelman, 1985). Such a method is thus more applicable to tube-fed basalt flows.

Alternative means of estimating F are as follows. Firstly, the velocity of a moving lava may be estimated by using the Jeffery's equation for laminar flow of an extensive sheet on a uniform slope:

$$v = \rho g \sin\theta h^2 / 3\eta \qquad (7.1)$$

where ρ = density, g = gravitational acceleration,

θ = basal flow slope, h = flow thickness and

η = viscosity.

Velocity v (m/s) may be solved for Waiti by substituting $\eta = 5.25 \times 10^{11}$ poise, calculated independently via equation 4.7 (Shaw, 1972), and equation 4.13(Murase et al. 1984). The Jeffrey's equation assumes a Newtonian rheology. The use of this equation as an estimate of viscosity yields only crude values as it takes no account of the fact that most of the velocity gradient in lavas may be in a relatively thin basal layer and that viscosity can vary between the base, interior and crust of the flow (McBirney and Murase, 1984). The flow velocity for Waiti is 0.0003 m/s. Flow time may be estimated assuming a constant velocity by:

$$t = L / v \qquad (7.2)$$

where L is flow length. For the Waiti flow, t is about 0.5 years. Effusion rate may be calculated using:

$$F = v h w \qquad (7.3)$$

where h.w represents the cross sectional area of the flow.

Alternatively F may be estimated via

$$F = 2/3 \zeta_s w v U \qquad (7.4)$$

where critical flow depth is

$$\zeta_s = Y / g \rho \theta \qquad (7.5)$$

ζ_s implies that there will be a region along each side of the flow where the depth is less than ζ_s and where there will be no longitudinal flow. Also the dimensionless parameter U is solved from expression (7.6):

$$U = w / 2 wb \qquad (7.6)$$

where w = flow width and wb = levee width.

The Waiti flow has well defined flow ridges some parallel to the margins of the flow (Fig. 7.8a). However, from cross sections (Fig. 7.8b) levee width is difficult to accurately determine. For the Waiti flow values of F are high, comparable to basalt flows (Zimbleman, 1985) at 1.3×10^2 m^3/s from equation (7.3) and

1.9×10^2 m^3/s depending on cross sectional area and the choice of w, wb and hence U. Further discussions on this method of estimating F occurs in chapter 8.4.4.

When F is substituted into the viscosity equation 4.6

namely $\eta = w^{2.75} Y^{1.25} \sin^{1.5}\theta / 24 F g^{0.25} \rho^{0.25}$

with $\theta = 5.5^o$, and $\rho = 2300$ kg/m^3, η becomes 1.3×10^{10} Pa s or 1.3×10^{11} poise. This value provides a lower limit for the central viscosity of the flow.

Air photographs of the Waiti flow show well defined arcu ate flow ridges. Regularly spaced ridges on rhyolite flows may be analysed through the use of a surface folding model (Fink, 1980a) first applied to ropy structures on pahoehoe basalt flows (Fink and Fletcher, 1978). The average ridge spacing is 119 m from 25 measurements off airphotos. The initial distance between ridges can be approximated by their arc lengths (Fink and Fletcher, 1978) which are always greater than their final spacing. For rhyolite flows the arc length is at most 23% greater. Therefore ridge spacing (Ld) becomes 145 m. The following constraints apply on three dimensionless parameters related to the properties of the lava.

The ratio between gravitational stress due to the weight of the lava and the compressional stress due to flow (S), needs to be less than 0.02. For folds to form $Ld / (1 / \gamma) > 28$ and

$$R = \eta_{exterior} / \eta_{interior} \geq \exp 28 H / Ld \qquad (7.7)$$

H is the average height of the ridges, inferred to be coincident with the thickness of the cooler brittle crust of the flow. Solving equation 7.7 gives $R \geq 39.2$.

To estimate the minimum surface viscosity at the time of folding, the limitation on the stress ratio $s < 0.02$, $H = 1.9 \times 10^3$ cm, $R = 39.2$, $\rho = 2.0$ g/cm^3, $g = 10^3$ cm/s and $\varepsilon_{xx} = 1.4 \times 10^{-4}$ s^{-1} derived from the definition of s, namely:

$$s = \rho g (1 / \gamma) / 4 \eta o \varepsilon_{xx} \qquad (7.8)$$

where γ = exponential decay parameter for viscosity increase, ηo being the outside viscosity, and ε_{xx} the compressive strain rate.

ηo may be solved from equation (7.9) namely

$$\eta o > \rho g H / (4 \ln R \varepsilon_{xx} 0.02) \qquad \text{(Fink 1980a).(7.9)}$$

For the Waiti flow the exterior viscosity is calculated as 1.02×10^{12} poise.

With $R = 39.2 = \eta o / \eta i$

the interior viscosity (ηi) becomes 2.6×10^{10} poise. While such a method is useful for viscosity estimates of both terrestrial and planetary lavas via remote sensing, the applicability to rhyolite flows

Fig. 7.8a Aerial photograph of the Waiti flow, Okataina Volcanic Centre, showing arcuate flow ridges that largely parallel the flow margins. Transverse ridges aligned NE - SW occur in the central part of the flow lobe nearest Haroharo dome (lower edge of photo) and are partly obscured by deposits from the Rotokohu tuff cone. The flow margin of the Waiti flow is outlined in pink. Finely radial features are cultural artefacts (rows of pine trees). Breaks between ridge segments are either tension fractures infilled by shower-bedded tephra or erosional features cutting the upper surface of the flow.

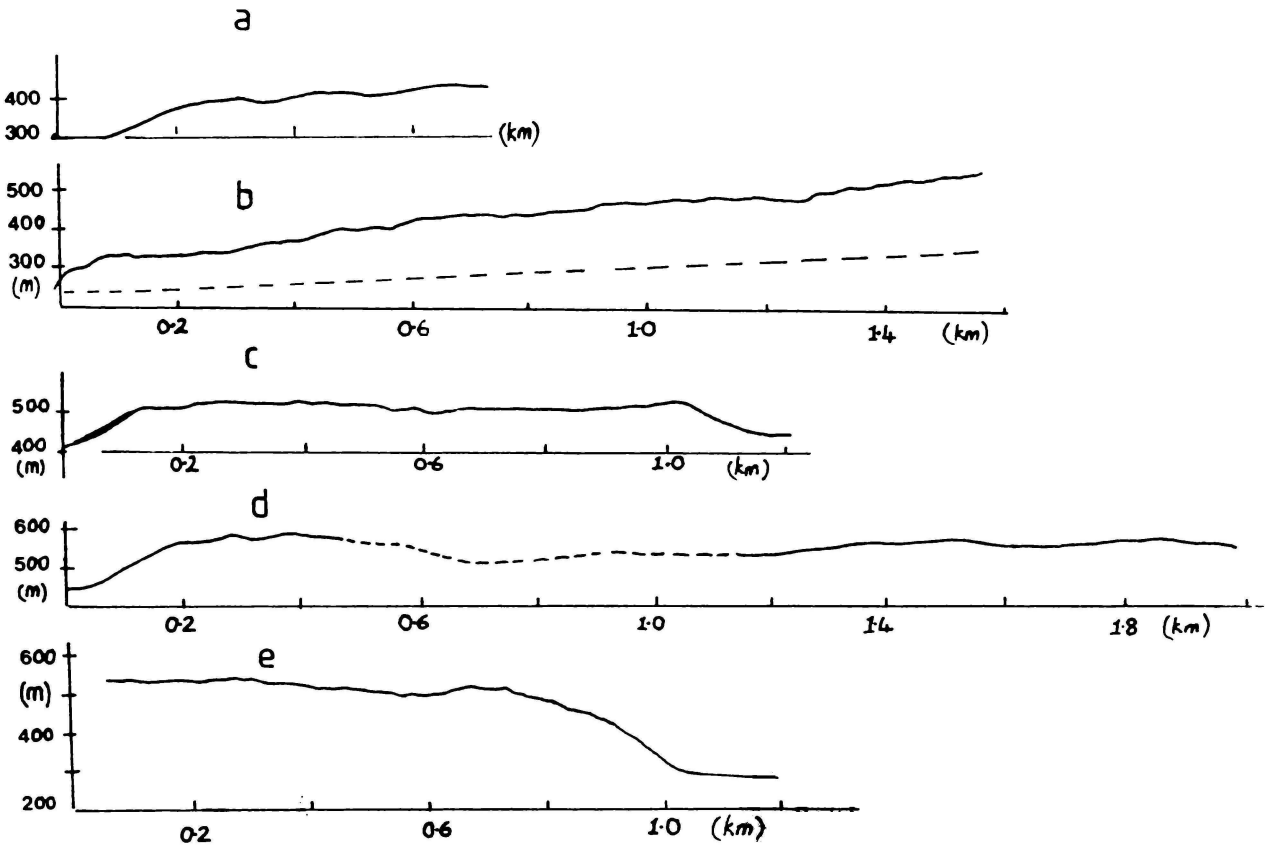

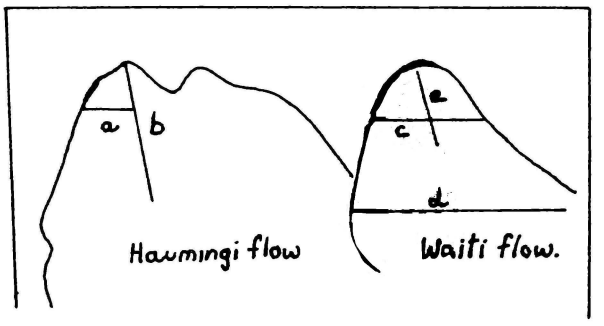

Fig. 7.8b. Topographic cross-sections (natural scale) for the Haumingi and Waiti flows. Inset shows location of the sections.

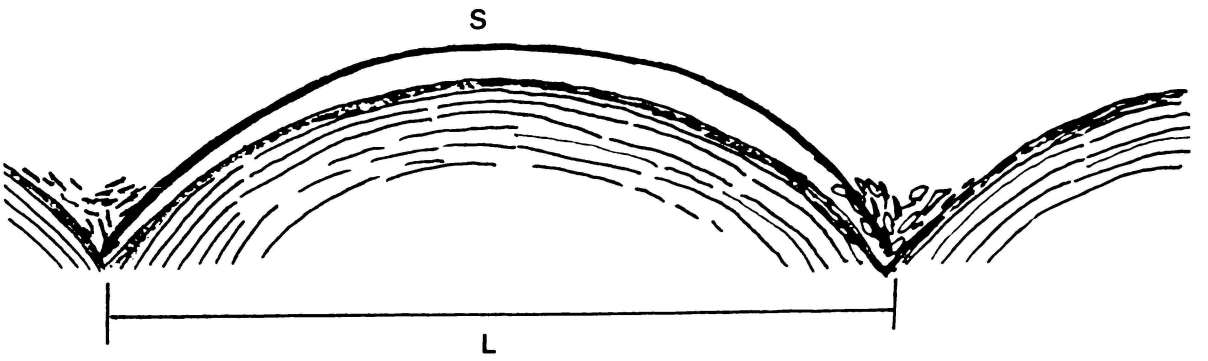

Fig. 7.9a. Cross-section of two ridges on an obsidian flow showing the relation between arc length (s) and wavelength (l). The initial distance between ridges can be approximated by their arc lengths which are ~23% greater than their final spacing.

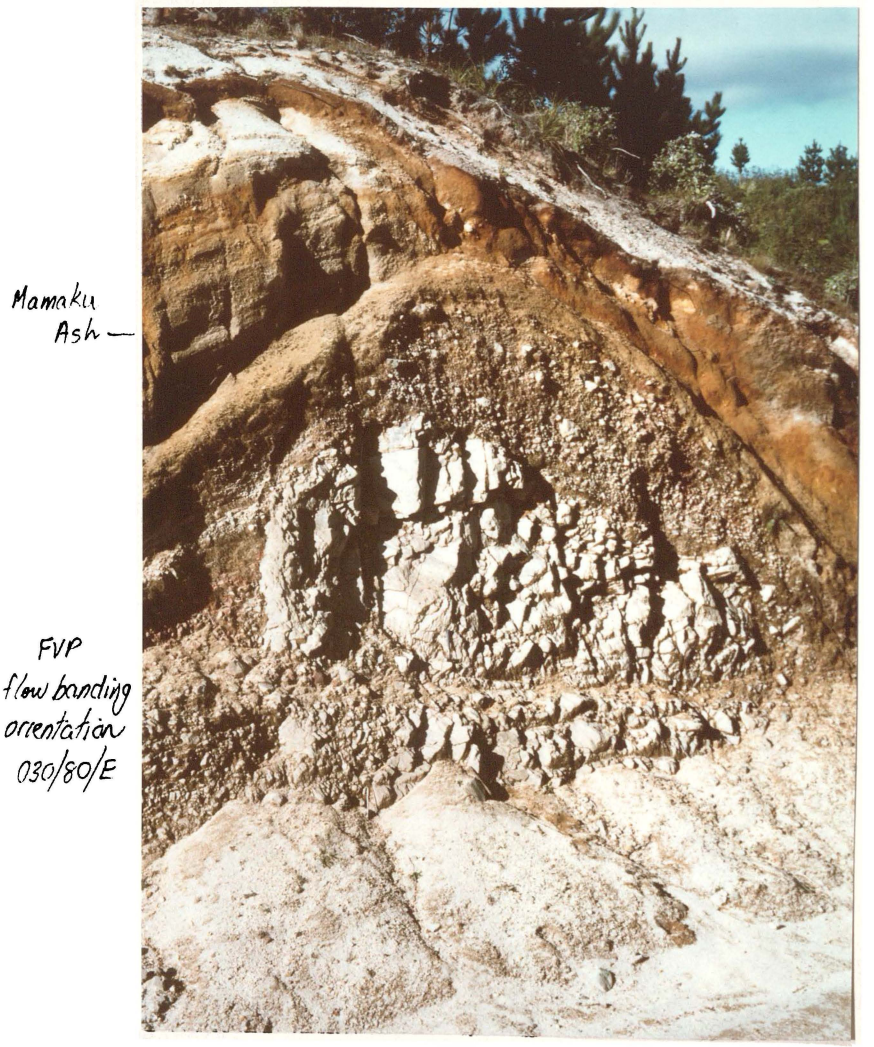

Fig. 7.9b. Cross-section of a ridge at s36, Waiti flow.

may be limited when surface ridge cross-sections are observed more closely. Fig. 7.9a summarises the basis of determination of Ld. Fig. 7.9b shows a cross-section of a flow ridge on the Waiti flow (site 35). The flow ridge here represents a rampart structure derived from later flow brittle disruption of the carapace. However, examination of adjacent roadcuts through ridges of similar foliation orientation can enable crude estimation of Ld, assuming former continuity of the fold.

In summary, the best estimates of viscosity are based on chemical and physical data from profiling throughout a lava flow unit. Thus a viscosity profile may be constructed as in Figs 4.10 and 6.10 for Ben Lomond and Mayor Island flows respectively. From the limited outcrop an estimate of 5×10^{11} poise is obtained assuming that the interior temperature (from mineral pair geothermometry using the data of Ewart et al. 1975) is constant, and that the internal lava contains no primary porosity.

The estimation of flow viscosity using flow morphological parameters is hampered by: accurate estimation of basal slope (θ) and flow thickness (h); the width of the active channel over which flow velocity would vary; the choice of F; and the use of an expression (equation 4.6) that takes no account of the behaviour of different thermal and velocity layers within the flow or the restraining effect of the cool brittle carapace. Estimates of viscosity from surface fold analysis are hampered by accurate field identification of Ld and estimates of H. Ideally surface coring or the measurement of tension crack depths in fresh non-vegetated flows not draped with airfall tephra, can constrain H. The basis for the flow fold analysis of Fink is a Newtonian rheology. However, all estimates from both morphology and folding analyses fall within one order of magnitude of the viscosity range for a calc-alkaline flow as in Fig 4.10; 10^{13} poise for the brittle carapace of the flow surface; to 10^{11}poise for the interior viscosity of a thermally insulated liquid including suspended crystals.

7.4. Summary

The flow stratigraphic framework and emplacement model generated for the Ben Lomond flow was tested on Pauanui, and the Waiti and Haumingi flows of the Okataina Volcanic Centre. Older flows such as Pauanui have no preserved fresh glass or pumice. Instead, flows are distinguished by weathered pyroclastic marker beds, autobreccia units jointing and textural variation.

Close examination of textural features, can generate an order of events during emplacement that differs in detail from Ben Lomond owing to more mafic compositions at higher inferred emplacement temperatures.

Although glass is preserved on the young Okataina Volcanic Centre flows, outcrop exposure is poor. However, unlike Pauanui and Ben Lomond, flow morphology is preserved. Thus differing methods of calculating viscosity may be compared. The lava flows are twice the length of the flow lobes forming the Ben Lomond dome, and viscosity estimates based on flow chemistry and petrography are marginally higher. Controls on the emplacement viscosity as well as differences/similarities in fabric features and thus emplacement mechanisms will be addressed in chapter 8.

CHAPTER 8.

COMPARISONS WITH OTHER FLOWS

8.1. Introduction

The Ben Lomond and Mayor Island flows may now be placed within the wider picture of effusive rhyolitic volcanism. Initially a comparison will be made of textural variations within and between the contrasting flow types, followed by a section describing parameters that can act as useful approximations to viscosity and temperature. Comparisons and contrasts will also be made between the New Zealand lavas and overseas examples.

8.2. Variations in Textural Zonation

Fig 8.1 summarises the stratigraphy of six rhyolite flows: Ben Lomond flow; Obsidian dome (Inyo Chain, Long Valley Caldera, northern California); Banco Bonito flow (Valles caldera, New Mexico), and the three Mayor Island peralkaline rhyolite flows.

The layer thickness ratios of textural units within the Ben Lomond flow more closely approach those of the Banco Bonito flow rather than the young Obsidian dome extrusion. The explosion breccia of Ben Lomond occurs as a pod and appears to be discontinuous. In contrast, the coarsely vesicular pumice of Obsidian Dome occurs at a drillhole depth of 17 m (Fink, oral comm., 1989) and outcrops on the flow carapace and at flow fronts suggesting a lateral continuity of the unit (Baum et al. 1989). For Ben Lomond, the relative viscosity between the explosion breccia pod and the upper obsidian layer was lower, and the thickness of the overlying lava too great to cause gravity instability or lateral spreading of the vesicular explosion breccia. Thus differing emplacement modes of textural zones caused by secondary vesiculation characterises Ben Lomond and Obsidian Dome - namely the explosive release of volatiles by tension cracks forming breccia cones after flow cessation, and diapirism via Taylor instability during flow movement. According to Manley and Fink (1987), the coarsely vesicular pumice layer of the Banco Bonito flow is thinner and its vesicles are smaller and fewer than is the case for other flows studied. Variations in textural zonation occur between flows and domes. The summit area of Obsidian dome (RDO 2B site) lacks a significant upper OBS layer in contrast to the distal RDO 2A site. Similarly, pumice and vesiculated obsidian outcrops on Hanini dome, and a lack of an upper OBS unit occurs for Parewhaite and Haroharo domes. Higher heat flows and thinner carapaces (equivalent to the FVP layer) proximal to the vent area (Manley and Fink, 1987), or a lack of foam collapse during dome extrusion (Eichelberger and Westrich, 1989), could account for the absence of a significant obsidian layer.

In published volcanological literature, no peralkaline flows have been texturally profiled. Thus calc-alkaline flows provide the basis for comparison of the Mayor Island textural unit stratigraphy.

The upper obsidian layer of the Ben Lomond flow is approximately five to six times the thickness of the comparable flow layer of the Mayor Island peralkaline lavas. Although carapace and flow

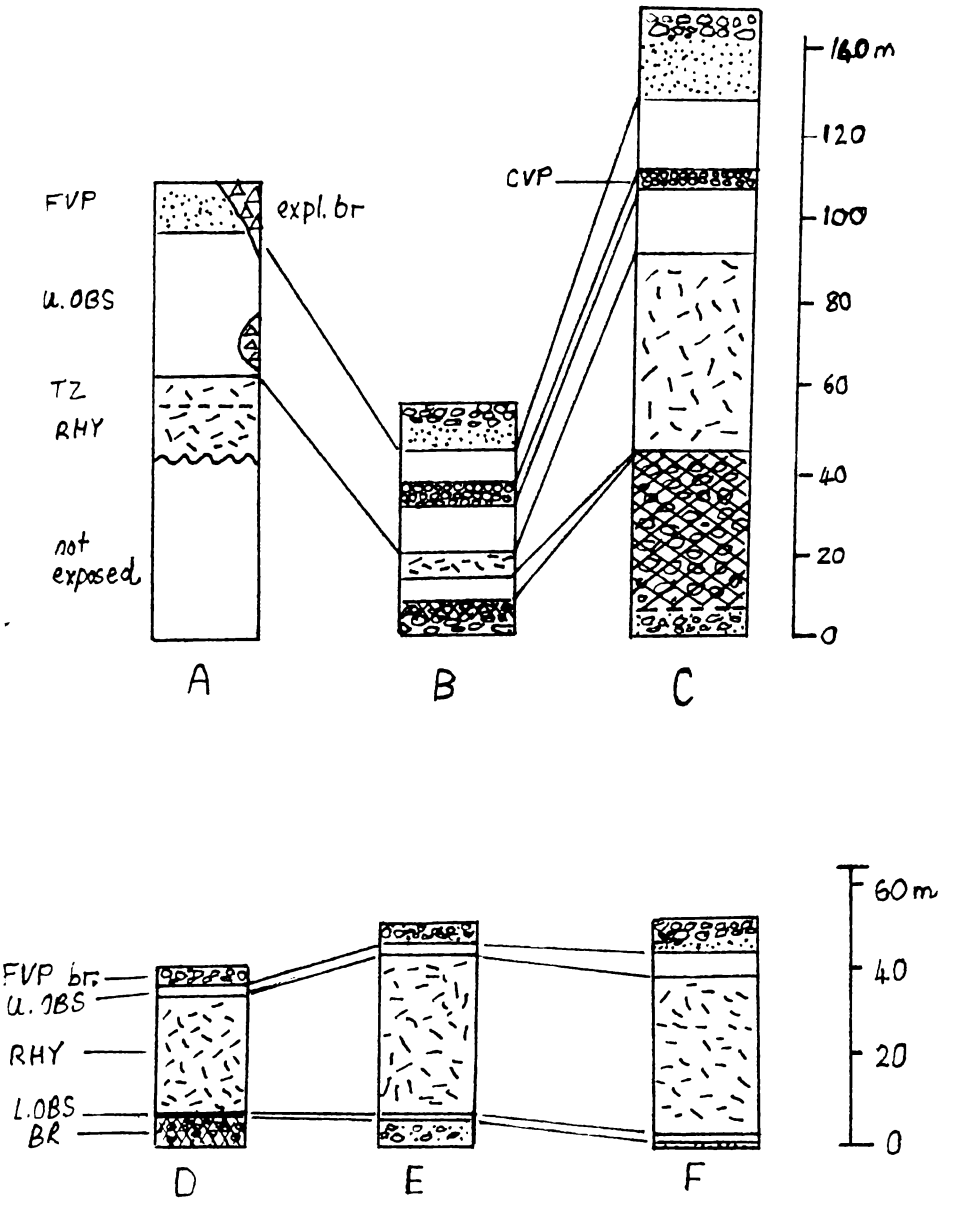

Fig. 8.1. Cross-sections through six rhyolite flows:
A. Ben Lomond; B. Obsidian Dome; C. Banco Bonito; D. Panui flow; E. Pre-8 ka flow; F. 8 ka flow. The FVP (finely vesicular pumice) is usually brecciated, but for B. and C. is divided into breccia above and coherent rock below. The upper obsidian layer (U.OBS) is usually cut by coarsely vesicular pumice (CVP) for colums B and C, equivalent to the explosion breccia of Ben Lomond. Other abbreviations are TZ (transition zone), RHY (crystalline rhyolite), and L.OBS (lower obsidian). The basal breccia is divided into welded (hatched) and non welded (stippled) zones. Diagonal lines between columns show correlations between textural zones among various flows. Columns B and C are from Manley and Fink (1987).

Fig 8.2. General trends of physical volcanological parameters and their comparison to theoretical curves for temperature and viscosity for a profile through a rhyolite lava flow. Profiles of inferred primary porosity (P), void aspect ratio (Rv), and water content approximate the theoretical viscosity curve (η). Density (ρ) and microlite length (l) for Mayor Island pantellerites approximate the temperature curve (T). The dashed line for the H_2O profile represents an enriched peak corresponding to explosion breccias or CVP layers for calc-alkaline lava flows, and is not characteristic of peralkaline lavas. Likewise, the dashed line for l represents the uniform microlite length of calc-alkaline lavas such as Ben Lomond.

As η and T have never been directly measured, related physical parameters can only be correlated and compared to the shape of theoretical profiles. BL and M refer to correlations compiled from Ben Lomond and Mayor Island data respectively. The correlations are discussed on p.147 and interpretations are limited by few common data points and natural variability of carapace FVP values particularly from Rv and P.

cross-sectional exposure is limited for the Ben Lomond flow, the upper part of the Ben Lomond lava was less readily able to deform into surface folds owing to a smaller value for relative viscosity between exterior to interior parts of the flows.

The upper obsidian layers of Mayor Island flows are stressed into folds with synclines and compressed anticline spines suggesting zones of high thermal and viscosity gradients. The rhyolite/obsidian layer thickness ratio for Mayor Island flows is greater than that of Obsidian dome because the upper obsidian layer insulated the central part of the flow where microlites were able to lengthen under conditions of high temperature and low viscosity for a time period of up to 10.5 years duration. This value is estimated using equation 4.17. Thus devitrification was suppressed in the upper and lower obsidian units. For Ben Lomond, microlite growth was uniform throughout the grey lineated obsidian layer. The black obsidian at roadcut section quenched rapidly and is therefore microlite-poor.

8.3. Approximations to Viscosity and Temperature.

Fig 8.2 illustrates the general trends of physical profiles of textural parameters together with theoretical temperature and viscosity curves.

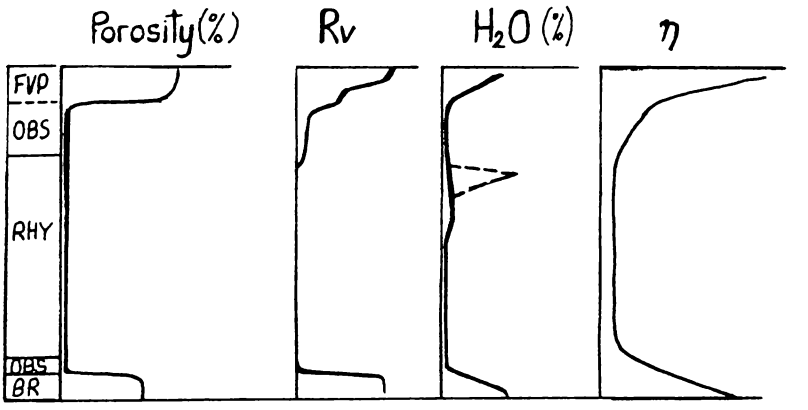

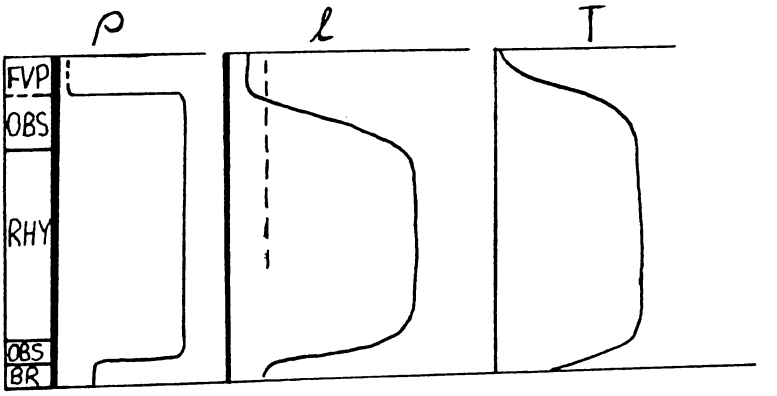

	y	x		r		n
BL	P	H_2O	P = -2.44 + 88.86 (H_2O)	0.96	*	10
	P	Rv	P = 1.85 + 1.93 Rv	0.82		6
	Rv	H_2O	Rv = 0.33 + 36.07 (H_2O)	0.92	*	6
M	ρ	l	ρ = 1.95 + 0.008 l	0.20		18
	P	Rv	P = 7.68 + 1.16 Rv	0.53		12

r = correlation coefficient n = number of data points
* = significant to 1% level.

For a rhyolite lava flow, viscosity and temperature have never been directly measured. Hence viscosity and temperature profiles are formulated by: comparison with basalt lava flow data (thermal profiles, refer to Helz and Thornber, 1987; viscosity measurements, Shaw et al. 1968); theoretical models (Carslaw and Jaeger, 1959; Manley, 1989); or empirical models (Sherman, 1968; Shaw, 1972; Murase et al. 1984; Spera et al. 1988). Hence, parameters approximating viscosity and temperature need to be found to satisfy objective 8. For example, primary porosity, void aspect ratio, and water content profiles best approximate the shape of the theoretical viscosity profile. However, low correlation coefficients, particularly for porosity/Rv for the 8 ka flow result from few common data points and wide natural variations in Rv and vesicularity from carapace FVP samples. A close sampling programme in intact FVP rather than brecciated FVP would limit variation, but accurate water determination by Karl Fischer titration is still hampered by the large adsorbed water peak in pumiceous samples (Westrich oral comm., 1989).

Void shape variations in basalt flows are more limited owing to low viscosity and a lesser viscosity gradient. Voids of high aspect ratio correspond only to the chilled outer skin of the flow of only a few centimeters thickness.

High viscosity and low overburden pressures contribute to elongation and deflation of voids in finely vesicular pumices. High overburden pressures and lower viscosities contribute to lower void aspect ratio (Rv) values in the upper obsidian layer. Thus Rv is a function of overburden pressure, temperature and volatile content and viscosity.

As no iron oxide minerals occur in Mayor Island lavas, paleomagnetism via the method of Audunnson and Levi (1988) cannot be used to generate a temperature profile. Microlite length for more fluid lavas such as Mayor Island can be used to approximate the form of the thermal profile, constrained by textural variations such as: a cold phreatomagmatic layer (100°C); an airfall lapilli layer containing charcoal (basal part of 8 ka tuff ~ 300°C); a fused lapilli (500 - 850°C); and a collection of gas blisters at the base of lava at an estimated temperature of 850°C. The shortest microlites within the FVP were unable to grow by diffusion owing to the high viscosity of the rapidly cooled outer skin of the flow. Therefore the growth of microlites in the FVP layer occurred in the conduit during ascent of the magma. Microlites in the central parts of the flow were able to elongate under high temperature and low viscosity conditions after flow emplacement. Variations in microlite length within the upper OBS layer of the 8 ka flow, profiled at Parekoura Point are interpreted as resulting from overturning of the upper flow stratigraphy during middle to late stages of emplacement. This factor and variations in vesicularity of the FVP layer, lower the r value for the density/microlite length correlation.

Such a method is limited in its applicability to the Ben Lomond flow owing to the presence of microlites of uniform length.

Clast aspect ratio may similarly be used for relative temperature estimates or relative velocity of flow particularly for rheomorphic tuffs (cf. Peterson, 1979) as can the curvature of flow ridges for the velocity of flow carapaces relative to marginal levees. This can only be applied to young silicic flows with unvegetated and totally preserved carapaces.

8.4. Comparisons With Other Flows.

8.4.1. Introduction

Table 8.1 lists the physical data for the New Zealand flows studied, and other North American examples. The rhyolites can be divided into the following groups:

a. a plug of low flow length/thickness or aspect ratio within a tuff ring;
b. small flows and domes (aspect ratios of between 5 and 50);
c. voluminous flows of high aspect ratio;
d. pantellerite flows.

The calc-alkaline Ben Lomond and Okataina Volcanic Centre lavas best fit into the second group - namely lavas of moderate aspect ratio that form short flow lobes or coulees. The physical volcanology of some North American flows will be outlined, as well as the peralkaline flows of Pantelleria to compare with the flows studied on Mayor Island.

Finally, the assertions of Walker (1973) are tested for rhyolite lava flows, with data from Table 8.1.

8.4.2. Physical volcanology of some North American rhyolites.

While the chemistry and the petrography of the Panum dome and Southern Coulee of the Mono Craters is comparable, the form of these extrusions are different. The emplacement history of deposits associated with Panum Crater are documented in Sieh and Bursik (1986) and Bailey et al. (1989). Panum dome is largely pumiceous with a lack of a significant obsidian layer and has a carapace split by tension cracks (Fig 8.3a). Panum dome appears to have been emplaced as a series of semi-solid bulbs of lava from an inflated foam that had collapsed within the upper conduit, contrary to the flow-collapse hypothesis of Eichelberger et al.(1986). Microfaulting (Fig 8.3b) , boudinage, and vesiculation from the release of confining overburden pressures (refer Fig. 7.7b), contributed to the fracture of the carapace and confinement to within the tuff ring. During an earlier extrusive phase, the collapse of part of the flow front and tuff ring triggered a block and ash avalanche, resulting in the rapid inflation of clasts of lava, breadcrusting of clast skins, and impact marks where the pink pumiceous angular clasts of the tuff ring were impressed (Fig 8.3c). The Southern Coulee has a greater diversity of textures, consisting of three different pumices of contrasting vesicularity, and obsidian within the lower two-thirds of the flow. Flow pumices show strain-slip cleavage (Loney, 1968) and are indicative of plastic flow after extrusion.

The Inyo domes form mushroom-shaped structures up to two kilometers diameter. The finely porphyritic (FP) lavas represent the co-mingling of high-Ba hornblende bearing rhyodacitic magma and low-Ba rhyolitic magma that does not contain hornblende. These lavas have three textures that outcrop on the carapace and the flow front: finely vesicular pumice; obsidian; and coarsely vesicular pumice. Obsidian dome consists solely of FP lava wheras South Deadman dome comprises a low margin of FP lava and a raised vent area of coarsely porphyritic (CP) lava (Fig 8.4a). Both lava types co-erupted with the final extrusion of CP lava piling up over the vent. CP lavas in the hybrid mixing zone occur as blobs (Fig 8.4b), which with increasing distance from the vent become spread out into bands where the large phenocrysts of the CP zone float into the glass of the FP lava (Fig 8.4c)

Table 8.1 Key to symbols.

η_o	viscosity of original liquid, Shaw (1972), (eq. 4.7)
$\eta_{e(1)}$	effective viscosity, eq. 4.11 (Shaw, 1965)
$\eta_{e(2)}$	effective viscosity, eq. 4.13 (Murase et al. 1984)
$\eta_{e(3)}$	effective viscosity, eq. 4.14 (McBirney & Murase, 1984)
T	temperature
ϕ	crystal proportion
Dm	crystal size
Y	yield strength (eq. 4.1)
F1	effusion rate (eq. 4.4)
F2	effusion rate (eq. 7.3)
η_1, η_2	η_1 incorporating F1, η_2 incorporating F2 using equation 4.6 (morphological method)
η_{ext}, η_{int}	exterior and interior viscosities using surface fold analysis (eq. 7.9; Fink, 1980).

Values for CP lavas, S Deadman Dome are in brackets.

Table 8.1. Physical data for New Zealand and overseas rhyolite flows. Some of the data for Okataina Volcanic Centre flows is from: Ewart (1968); Ewart et al. (1971), (1975); Nairn, (1981). Morphological data was derived from topographic maps for these flows. Data from overseas rhyolites is from: Loney (1968), Newman et al. (1988). (Mono flows); Vogel et al. (1985, 1987), Sampson (1987) (Inyo domes); Goff et al. (1989) (Banco Bonito); Fink (1978, 1983)(Little Glass Mountain); Duffield (1989)(Taylor Creek); Henry et al. (1988, 1989)(Trans-Pecos); Bonnichsen (1982)(Bruneau-Jarbidge); and Villari (1973) Mahood (1984), Mahood and Hildreth (1986) for Pantelleria. Abbreviations n.a. = not applicable, n.d. = no data, and a gap indicates not calculated.

	Ben Lomond	Mayor Island				Pauanui			
	southwestern flow	8ka	Pre-8ka	Panui	2d	P1	P3 flow 3	Haumingi	Waiti
log ηo	11.1	7.25	7.80	7.66	7.05	8.3 - 9.3	9.4	11.09	11.55
log ηe (1)	n.a	n.a	7.81	7.77	7.25	8.55 - 9.5	9.48	11.2	11.70
log ηe (2)	n.a	n.a	7.80	7.70	7.09	8.49 - 9.45	9.42	11.12	11.62
log ηe (3)	n.a	n.a	8.23	8.94	11.81	11.51 - 11.34	10.88	12.05	13.23
Av log ηe (2,3)	n.a	n.a	8.02	8.32	9.45	10 - 10.4	10.15	11.59	12.43
T (C)	780 - 800	~ 950	~ 950	~ 950	~ 950	860	860	770	740
ϕ (%)	aphyric	aphyric	0.5	7.0	12.5	13.4 - 7.3	5.8 - 6.7	6.9	9.7
Dm (mm)	n.a	n.a	0.5	0.4	1.0	0.61 - 0.65	0.45 - 0.53	0.31	0.43
H_2O+ (%)	0.1 - 0.5	0.05	0.05	0.05	(0.05)	0.16 - 0.29	0.21 - 0.15	0.18	0.12
length L (m)	3500	600 - > 1100	100 - > 1400	r=230,d=460	1428	(1000)	(1200)	6780	5000
thickness h (m)	~ 105	~50 (35)	~ 50	40	36	> 150	65 +	120 - 150	150
L / h	33	> 22	(28)	5.8 (11.6)	39.7	6.7	18.5	48.4	33.6
width w (m)	1250	2050	500	n.a	910	(330)	(200)	3166	2922
basal slope Θ	4.5	9	up to 25	n d	5.5	n.d	n.d	5.6	5.5
Volume (km^3)	0.46	0.07 min	n d	0.007	0.046	((0.06)	(0.01)	3.2	2.2
SiO_2 (%)	76.9 - 77.1	73.47	74.88	74.91	73.4	69.07 - 73.64	73.87	75.75	74.99
Al_2O_3 (%)	12.49	9.73	10.23	9.89	8.8	15.24 - 13.82	14.45	13.10	12.82
$Na_2O + K_2O$ (%)	7.48	10.2	9.73	9.84	10.8	6.34 - 7.1	6.81	7.46	7.31
Y (x 1000 Pa)	189.5				79.5			245.5	318.9
F1 (F2)	3.9 - 8.1 (39.4)	6.77 (74500)		0.22 (440)	4.1 - 6.9 (9500)			23.9 (427.4)	14 (131.4)
η1 (η2)	10.5 - 11.06 (10.35)				10.4 - 10.7 (7.3)			11.99 (10.7)	12.24 (11.29)
velocity (cm / s)	0.05				(29.8)			0.1	0.03
η ext (η int)									12 (10.4)

	Okataina	Volcanic	Centre				Tarawera	Volcanic	Centre
	Haroharo	Okataina	Haninif	Haninid	Tapahoro	Parewhaite	Ruawahia	Hawea	L Pokohu
log ηo	11.71	11.74	11.70	11.57	11.73	11.86	11.48	11.39	11.96 - 11.63
log ηe (1)	11.86	11.94	11.96	11.85	11.97	12.05	11.88	11.49	12.06 - 11.73
log ηe (2)	11.79	11.88	11.91	11.79	11.94	11.96	11.89	11.43	12.00 - 11.67
log ηe (3)	13.24	14.32	14.89	14.77	15.15	13.49	15.15	12.93	13.32
Av log ηe (2,3)	12.48	13.1	13.4	13.28	13.55	12.73	13.52	12.18	12.58
T (C)	740	750	750	750	730 - 740	730	750	750	750
ϕ (%)	10.1	12.6	15.9	16.5	14.7	11.6	22.7	5 - 8	6.3
Dm (mm)	0.50	0.55	0.58	0.56	0.65	0.43	0.5	0.5	0.5
H_2O+ (%)	0.2	0.15	0.2	0.2	0.2	0.2	0.2	0.1	0.1
length L (m)	2673	5500	4330	r = 768	5128	2161	1822	4000 - 6000	7590
thickness h (m)	130	210	150	150	150	181	478 (300)	120	120
L / h	20.6	26.2	28.8	5.12	34.2	11.95	3.8	33 - 50	63.3
width w (m)	2266	1985	1450	n.a	1780	1225	1355	5000 (max)	4680 (av)
basal slope Θ	4.5	6.4	7.5	n.d	5.98	5.6	(2)	n.d	n.d
Volume (km^3)	0.9	2.2	0.9	0.27	1.37	0.4	1.1	1.8	4.2
SiO_2 (%)	75.91	75.84	76.66	76.41	76.92	76.19	76.03	75.53	76.57
Al_2O_3 (%)	12.46	12.22	12.57	12.56	12.59	12.70	12.66	12.98	12.53
$Na_2O + K_2O$ (%)	7.29	7.37	7.45	7.29	7.39	7.56	7.03	7.49	7.33
Y (x 1000 Pa)		533.9	367.5		360.1	390.5			
F1 (F2)		7.8 (166.7)	6.3 (43.5)		9.13 (50.73)	2.2 (44.3)	0.87 (222.8)		
η1 (η2)		12.46 (11.14)	12.08 (11.24)		11.99 (11.15)	12.15 (9.9)			
velocity (cm / s)		0.04	0.02		0.02	0.02			

	Inyo		Mono		Medicine Lake	Valles	Mogollon-Datil
	Obsidian dome	S Deadman dome	S. Coulee	Panum	LGM	Banco Bonito	Taylor Ck.
log ηo	9.65 - 8.66	9.05 - 8.45 (11.13)	10.73 - 9.87	11.01 - 10.13	9.50	10.45	12.7 - 9.61
log ηe (1)	9.70 - 8.70	9.10 - 8.49 (11.69)	n.a	n.a	n.a	10.64	n.d
log ηe (2)	9.67 - 8.67	9.07 - 8.46 (12.85)	n.a	n.a	n.a	10.65	n.d
log ηe (3)	10.90 - 9.91	10.06 - 9.46 (25.43)	n.a	n.a	n.a	14.56	n.d
Av ηe (2 , 3)	10.29 - 9.29	9.57 - 8.96 (19.14)	n.a	n.a	n.a	12.61	n.d
T (C)	850 - 930	850 - 900 (780 est)	790 - 850	790 - 850	860	(775)	700 (min)- 900
ϕ (%)	1-2 (2-9)	3 (25 - 40)	aphyric	aphyric	aphyric	12	n.d
Dm	(0.5)	0.5 (1.5)	"	"	"	0.5 - 2 (0.9)	n.d
H_2O	0.1	0.1 (0.3)	0.3	0.1	0.1	0.24	0.2 est
L (r,d)	1000, 2000	620,1240 (420,840)	3600	d = 390 total	r = 2000	7900	n.d
h	55	70 (150, av = 113)	90 (75)	45	20 dome,50 flow	150	> 125 eroded
L / h	18	8.9 (4.1)	40	4.3	40	52.6	n.d
w	n.a	n.a	1200	n.a	n.a	1900 av	n.d
Θ	n.d	n.d	(11)	n.d	n.d	(5.0)	n.d
Volume	0.15	0.08 (0.06)	0.3	0.002	0.6	3.4	(0.2 - 10.5)
SiO_2 (%)	72.95	71.21 (glass = 75.77)	75.3 - 76.2	76.73	73.58	73.68	77.82
Al_2O_3 (%)	14.20	15.17 (glass = 13.33)	13.1 - 12.6	12.86	14.03	13.59	12.2
$Na_2O + K_2O$	9.63	9.43 (8.75)	8.8 - 9.2	8.51	8.38	8.00	8.29
F1 (F2)	2.73 (220)	(0.23,(0.0006))	8.64 (119.7)		3 (30)	15.01 (960.5)	

	Trans Pecos		Bruneau - Jarbidge		Pantelleria		
	Star Mt.	Bracks	Trguero	Dorsey	C. Randazzo	C. Sciuvechi	M.Gelkhamar
log ηo	7.67 - 6.84	7.74 - 6.91	7.78	8.07	6.22	6.29	6.45
log ηe (1)	7.83 - 7.00	7.90 - 7.07	n.d	n.d	6.47	n.d	n.d
log ηe (2)	7.76 - 6.93	7.83 - 6.99	n.d	n.d	6.38	n.d	n.d
log ηe (3)	9.68 - 8.81	9.75 - 8.92	n.d	n.d	8.86	n.d	n.d
Av ηe (2 , 3)	8.72 - 7.87	8.79 - 7.96	n.d	n.d	7.62	n.d	n.d
T (C)	860 - 940	860 - 940	950	950	950 - 1025	950 - 1025	950 - 1025
ϕ (%)	10	10	n.d	n.d	15 - 20	n.d	n.d
Dm	# (0.5 est)	# (0.5 est)	n.d	n.d	(0.5)	n.d	n.d
H_2O	0.2	0.6	(0.2)	(0.2)	(0.05)	(0.05)	(0.05)
L (r.d)	70,000	55,000	n.d	n.d	2000	1600	2060 (680)
h	80 - 240	50 - 120	150	150	25 - 50	n.d	n.d
L / h	600	700	n.d	n.d	74.7	n.d	n.d
w	21400	10700	n.d	n.d	300	260	640 (86)
Θ	n.d	n.d	n.d	n.d	n.d	n.d	n.d
Volume	240	50	n.d	75	n.d	n.d	n.d
SiO_2 (%)	65.8 - 71.87	66.64 - 69.17	71.02	71.7 - 72.1	67.90	70.31	68.08
Al_2O_3 (%)	15.7 - 12.58	13.00 - 12.52	13.26	13.4 - 12.8	10.01	8.22	10.62
$Na_2O + K_2O$	9.6 - 9.7	9.31 - 9.74	8.16	7.70 - 8.22	11.48	10.36	10.94
F1 (F2)	1404 (3.56E6)	1038.5 (2.4E5)		500 (8.5E6)			

(Sampson, 1987). CP lavas are more viscous than FP lavas owing to higher crystal contents, larger crystals, greater vesicularity, and higher SiO_2 content of the glass. The viscosity difference between CP and FP lavas is at least four orders of magnitude. This factor contributes to the different aspect ratios and resultant shape of both lavas comprising the dome as the extrusion volumes of both lava types are comparable. In addition, from U^{238} - Th^{230} data, crystals of hornblende and allanite formed about 20,000 years ago in CP lavas. As these phenocrysts are larger than those of the FP lavas, and that both lavas erupted approximately 550 years ago, a longer residence time is implied for the CP magma in an upper level magma chamber.

Taylor Creek lavas have a SiO_2 content similar to that of Ben Lomond. These deposits show evidence of welded-particulate and lava flow origin within individual eruptive units. The co-existing textures have been generally interpreted as the result of a pyroclastic flow so hot that part of it was remobilised as a lava flow after the main eruptive mass came to rest. Alternatively, the lava flow locally collapsed to feed a welded pyroclastic phase. Duffield (1989a,b) speculates that lavas having similar mixed textures are the products of fountains of silicate lava whose fall-back was hot enough to rehomogenise into a flow, but was in part cool enough to preserve a welded particulate nature. High volumetric rates of eruption, high eruptive temperatures or an enrichment of volatiles would need to be pre-requisites for a fountain-fed emplacement mode.

For the Bruneau-Jarbidge and Trans-Pecos flows of high temperature and high aspect ratio, fragmental eruption and rheomorphism, or extrusion as a lava are modes of emplacement that could equally account for their extensive exposure. Evidence for both scenarios is summarised in Bonnichsen and Kauffman (1987) and Henry et al. (1989). By comparison, the Chao dacite flow has 60% crystals contributing to very high internal viscosities of 10^{14} - 10^{23} Pa s (Self et al. 1989). However, an effusion volume of 26 cubic km (Guest and Sanchez, 1969) and a basal slope of 3 - 6° caused long coulees of high aspect ratio (L/h = 30) to form rather than domes. For the Bruneau-Jarbidge lavas, high temperatures of about 950°C and a rhyodacitic composition (SiO_2 = 67 - 72%) contribute to the low

(a)

Fig. 8.3. Panum dome, Mono Craters, northern California, showing the tuff ring moat, flow front talus and an upper surface split by tension cracks (a).

(b)

Fig.8.3 (c)

Semi solid emplacement processes are evident from microfaulted offsets in glassy bands within the finely vesicular pumice layer (b).

Voids of low aspect ratio and breadcrusted surfaces characterise the bombs from the block and ash avalanche deposit (c).

(a)

Fig. 8.4. South Deadman Dome, Inyo Chain, northern California: form and petrofabrics.

(a) South Deadman Dome, photographed from Deer Mountain. The lower FP lavas show three textures and arcuate ridges. The elevated CP lavas of the summit region are split by seven radial fractures cutting the concentric strike pattern of the flow banding.

(c)

(b)

Fig. 8.4

(b) Blobs of CP lava are enclosed by fluidal FP lavas. Flow banding is steeply dipping on the upper surface of the FP lavas, South Deadman Dome.

(c) CP lava strands with enclosing FP lava (or hybrid lava) characterised by large CP crystals.

viscosity of the interior liquid. Results from thermal modelling (Manley, 1989) imply that given great volume and thickness, large masses of rhyolite lava will be able to travel many kilometers from their vents before they cool and solidify.

8.4.3. Strongly peralkaline flows: Pantelleria and Mayor Island.

Previous work on pantelleritic centres has largely been concerned with petrology or isotope chemistry of samples not tied to a detailed eruptive stratigraphy. Only a small number of centres have been adequately mapped. Many studies were undertaken before the present understanding of caldera formation and welded tuffs, and units were described from a calc-alkaline perspective (Mahood, 1984). No detailed profiling of physical volcanological properties of pantelleritic flows has been undertaken prior to this study. However, comparisons between strongly peralkaline Mayor Island and Pantelleria can be made.

The rheology of the Pantelleria lavas resembles silicic andesites despite SiO_2 contents up to 70% (Mahood, 1984). The high agpaitic index (molecular Na + K / Al ratio) of 1.65 - 2 exceeds that of Mayor Island (1.3 - 1.7) and a lower SiO_2 content (66 - 70%) promotes lower values for the viscosity of the liquid.

Pantellerian shields typically have a subdued topography. The distinction between true flows and remobilised fountain-fed flows is arbitrary although the former can be traced coherently back to source (Mahood & Hildreth, 1986). The extent of agglutination or welding is very sensitive to fountain height and accumulation rate. For a layer 10 cm thick to agglutinate, the time for welding is estimated as 7.7 - 77 seconds (Mahood, 1984).

Monte Gelkhamar, described as an endogenous dome by Villari (1974) and Cornette et al. (1983), refers to a lava dome growing by internal expansion (Williams & McBirney, 1979). No true endogenous domes occur on Pantelleria. M. Gelkhamar and C. Randazzo have been described by Mahood and Hildreth (1986) as lava cones, and form from magmas with effective viscosities intermediate between shield lavas and lava-breached domes (Fig. 8.5). The Khaggia flows are thicker than shield flows, (25 - 50 m) and are 0.3 - 1 km wide. Early flows in C. Randazzo contained 15 - 20% feldspar of less than 2 mm length. The final flows form stubby lobes with 25% phenocrysts up to 1 - 10 mm length. (Mahood and Hildreth, 1986).

A similar landform sequence occurs on Mayor Island. The pre-caldera shield flows and the 8 ka flow are aphyric or phenocryst-poor and are spatter fed. Small extra-caldera domes formed (e.g. Panui) that ponded within a tuff ring and had a greater effective viscosity from 7% phenocrysts. The intracaldera lavas (e.g. flow 2d) contain up to 15% phenocrysts thus forming subdued lobate flows surmounted by Tarewakoura dome. Brothers (1957) claimed observing lava tubes on these flows. However, the morphology of the flow lobes is not like that of a tube-fed basaltic flow and the estimated effective viscosity is too high. Likewise no evidence of tube-feeding occurs at Parekoura Point.

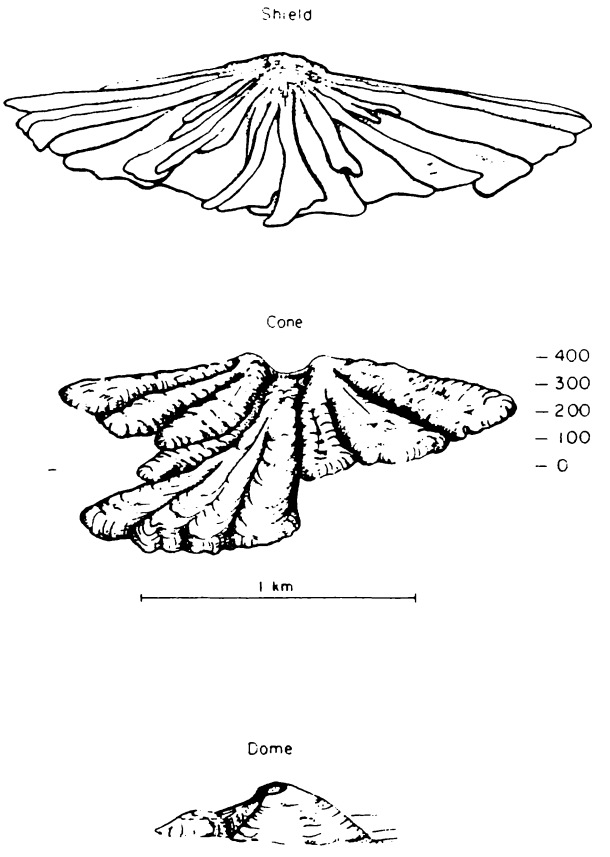

Fig. 8.5. The morphology of flows comprising shield cones and domes, Pantelleria (from Mahood and Hildreth, 1986).

8.4.4. Controls on the morphology of rhyolite flows.

Walker's (1973) original assertion that eruption rate was the most important influence governing the lengths of lava flows countered the long held belief that flow length was governed by viscosity. Walker's data base comprised 40 flows from 19 volcanoes ranging from basaltic to rhyolitic in composition. Malin (1980) examined the relationship between actual effusion rate (volume divided by length of time the flow was active) and flow length. His results, for Hawaiian basalts, did not confirm those of Walker (1973) in that Hawaiian basalts are tube fed rather than channelised (e.g. Etna). Lava tubes are effective in extending flow length for many kilometres for flows of low effusion rates (4 m^3/s), thus thermally insulating the lava. A paucity of field measurements for active flows forced Malin to calculate eruption rates by determining the volume of the entire system, and attributing eruption rates to individual flows in proportion to their volume. Also the log length / log volume correlation is high as length is incorporated in calculations for volume, thus prejudicing the outcome. However, the cross-sectional area of the flow and flow length are mutually dependent. Roth and Sanders (1983), cited in Pieri and Baloga (1986), found that silicic lava flows were shorter than basaltic flows although some had comparable eruption rates counter to the findings of Walker (1973). Pieri and Baloga (1986) found that eruption rate is highly correlated with planimetric area by using simple models incorporating heat loss by radiation to estimate flow rate.

Fig 8.6a shows that many of the rhyolites from Table 8.1 plot outside Walker's (1973) field, particularly the voluminous Trans-Pecos and Bruneau-Jarbidge flows. Results from the mildly peralkaline La Primavera (agpaitic indices from 1.02 - 1.14) are included, from Clough et al. (1982). Most have aspect ratios (V/H as defined by Walker, 1973) from 1:7 to 1:25 and are thicker than strongly peralkaline flows from Pantelleria and Mayor Island.

A good correlation occurs between length and cross-sectional area supporting the results of Malin (1980) from basalt flows (Fig. 8.6b)

However plots of effective viscosity versus volume or a morphological parameter such as h/A, H/V, or length, separates the rhyolites into four groups (Fig. 8.6c):

a. high-silica calc-alkaline;
b. low-silica calc-alkaline;
c. low viscosity, high temperature, voluminous mildly alkaline flows;
d. low viscosity, low volume peralkaline pantellerities.

The range of eruptive morphology for the Okataina Volcania Centre lavas - namely dome, coulee and flow of comparable eruptive temperature, chemistry and thus viscosity, suggest that effusion volume and effusion rate influence the shape of the resultant landform. No rhyolite lava flows have been observed to erupt. Therefore, effusion rates have been estimated by two methods: F(1) from equation (4.4) and F(2) involving an estimate of velocity from equations (7.1) and (7.3) where the velocity is multiplied by the average cross-sectional area of the flow. Walker (1973) included two historical silicic flows in his data set; the Hibok-Hibok dacite (1948) and Trident rhyodacite with measured effusion rates of approximately 1.2 and 7.5 m^3/s respectively. Mt St Helens dacite and Santiaguito dacite have measured effusion rates of a similar magnitude (Swanson et.al. 1987).

Thus the values of F(1) are closer to those from active silicic lavas. In contrast the values of F(2) are very high, particularly for the voluminous Trans-Pecos flows and peralkaline lavas. Values for F(2) are large for wide flows as cross-sectional area is involved in the calculation from equation 7.3. For the Trans-Pecos flows effusion rates of $\sim 10^5 - 10^6$ m^3/s exceed those measured for basalts in Lipman and Banks (1987) of 10^3 m^3/s, and are similar in magnitude to highly explosive ignimbrites ($10^4 - 10^7$ m^3/s) (Cas and Wright, 1987). While a particulate mode of emplacement could be inferred from these results for the Trans-Pecos flows, the estimates of F(2) are exaggerated, and thus the effusion rate from method (1) is considered more realistic. When F(1) is plotted with viscosity, two trends emerge (Fig. 8.6d):

a. calc-alkaline trend, terminating at the high temperature Trans-Pecos and Bruneau-Jarbidge flows;
b. peralkaline pantellerites.

In addition, a weak relationship is implied between crystal proportion and effusion rate with those lavas of highest phenocryst proportion having the lowest effusion rate.

The high temperature pantellerities have the highest $Na_2O + K_2O / Al_2O_3$, are the thinnest of flows (Fig. 8.6e), hence have the lowest yield strength. Fig. 8.6f includes temperature in the chemical

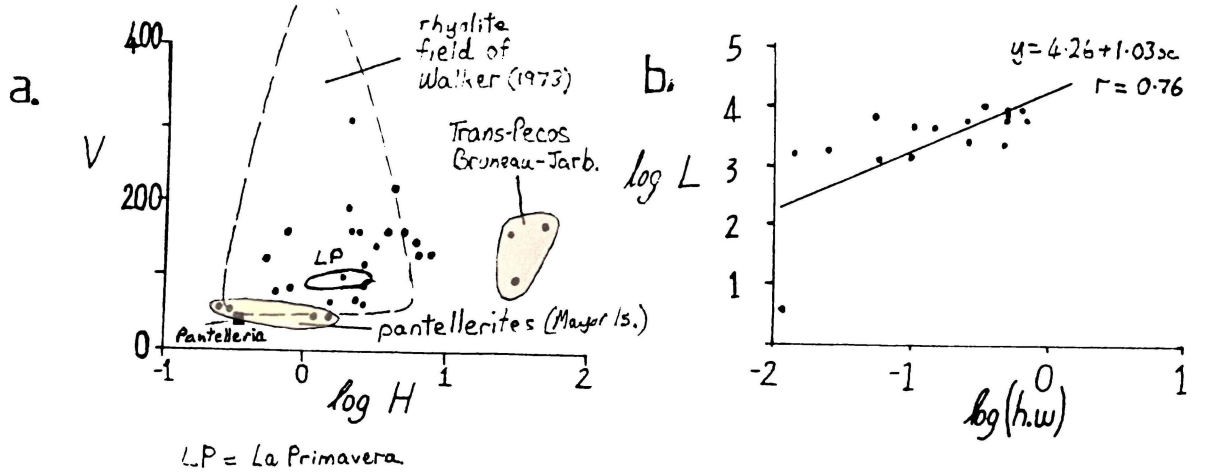

Fig. 8.6a. Thickness (V) plotted against diameter (H) for rhyolite lavas tabulated in Table 8.1. Walker's (1973) field for rhyolite lavas is based on 176 data points. Flows from La Primavera are included.

Fig. 8.6b. Length versus cross-sectional area.

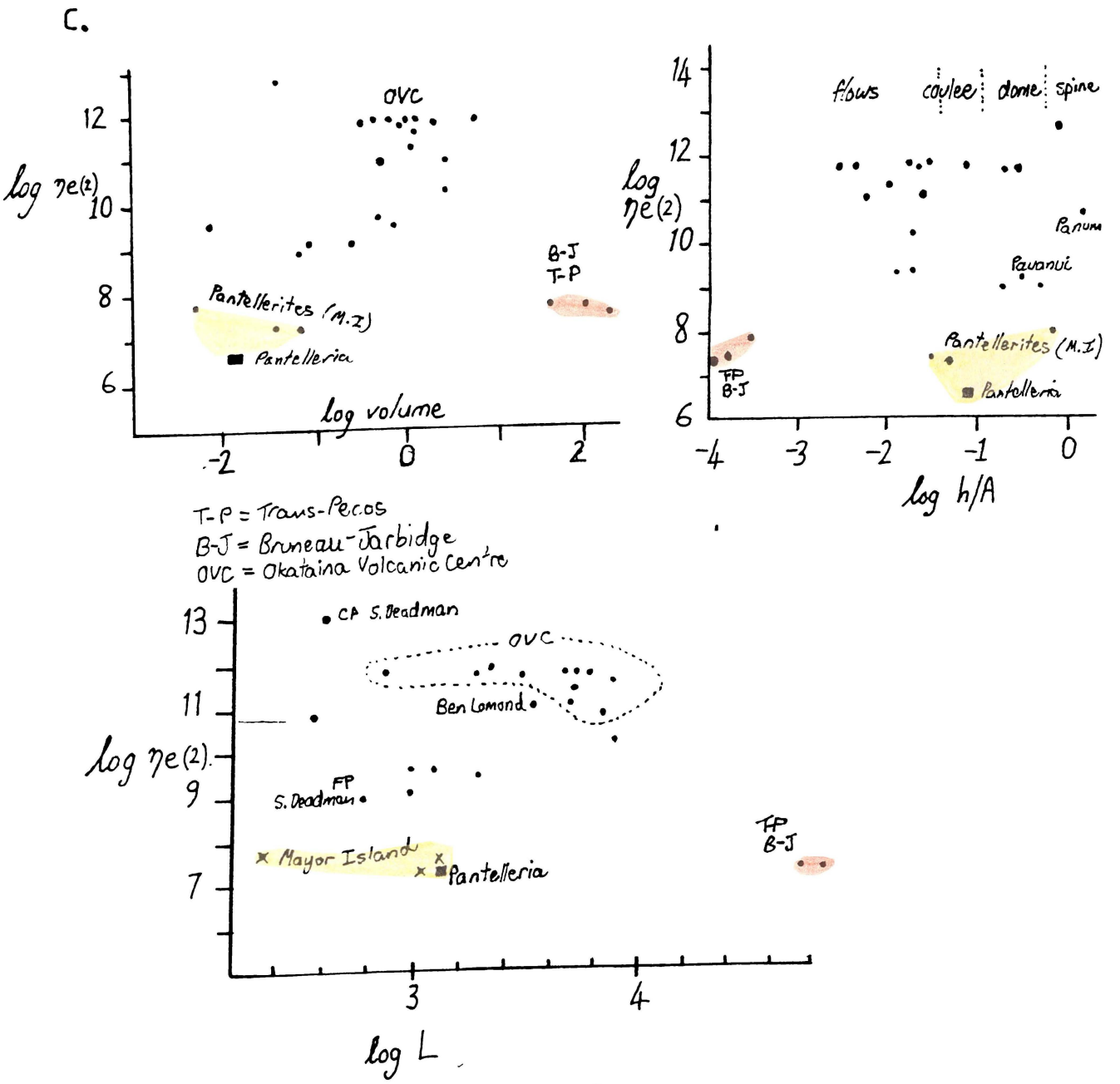

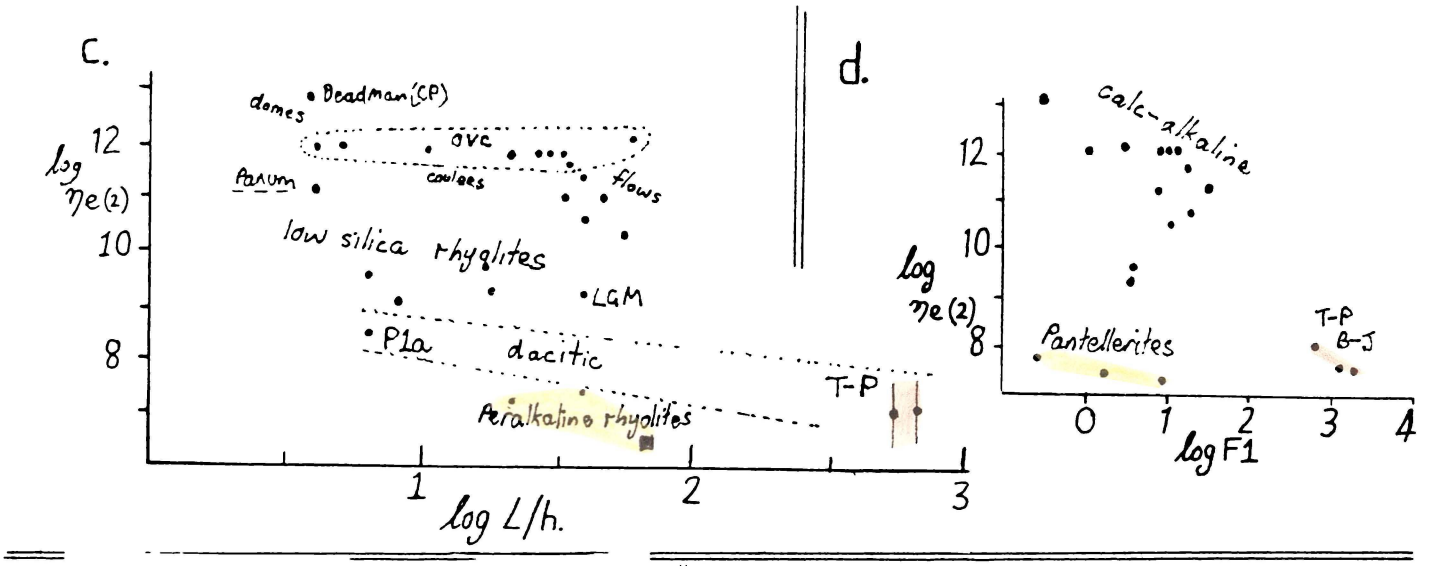

Fig. 8.6c. Effective viscosity ($\eta e(2)$, Table 8.1) versus a morphological parameter: volume; h/A; length; L/h. A = flow area.

Fig. 8.6d. Effective viscosity versus effusion rate (F1).

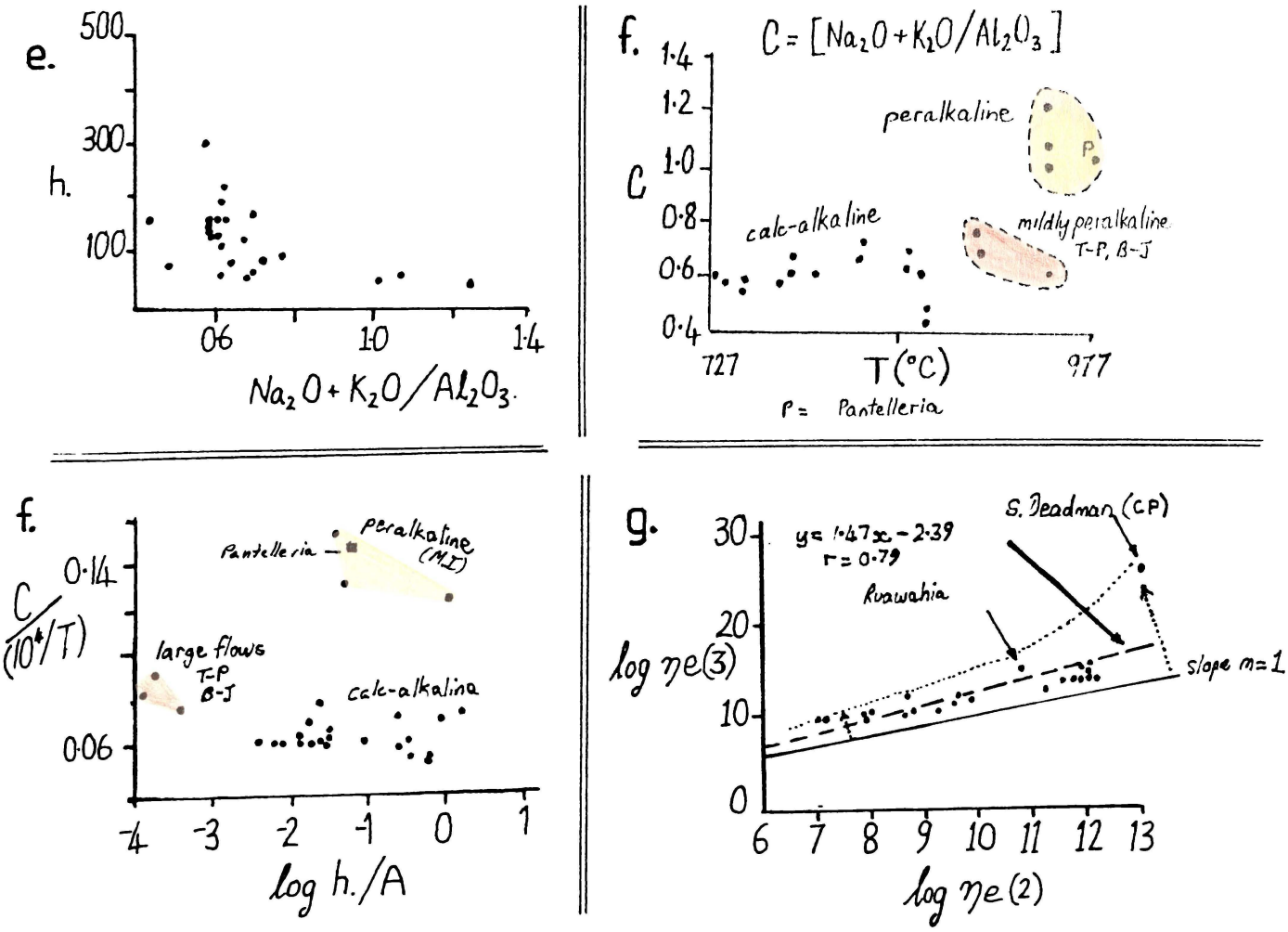

Fig. 8.6e. Flow thickness (h) versus a parameter for chemical composition ($Na_2O + K_2O / Al_2O_3$)

Fig. 8.6f. Chemistry (as $Na_2O + K_2O / Al_2O_3$) versus temperature (T) and a parameter including chemistry and temperature plotted against log h/A where A = flow area.

Fig. 8.6g. Comparison between two estimates of effective viscosity.

parameter, and when plotted with a morphological parameter, separates the strongly peralkaline flows from the other rhyolites. An important result is that the Trans-Pecos flows of smallest log h/A and large eruption volume would have a viscosity approaching other low-temperature low-silica rhyolites, if temperatures were equivalent at 860°C.

Fig 8.6g compares two estimates of effective viscosity: $\eta e(2)$ from Murase et al. (1984) and $\eta e(3)$ using the computer programme in McBirney and Murase (1984). The latter method inflates effective viscosity for crystal proportions and sizes of more than 10% and 1 mm respectively. Values for the coarsely porphyritic lava of S. Deadman Dome (excluding the effect of voids) gives an inflated value of 10^{25} poise. This contrasts with approximately 10^{13} from $\eta e(2)$. The high value for method (3) is largely from the natural logarithmic construction involved in calculating the relative viscosity. Large crystal sizes inflate values of η_R and hence resultant ηe. With this method many flows are calculated as erupting at viscosities above the brittle transition viscosity of glass (10^{13} poise at 670°C). Thus, if this were so, the flows would show no fluidal deformation structures. Murase et al. (1984) used an equation from Huppert et al. (1982) to solve viscosity of the crystal-rich Mt St Helens dacite dome.

Their equation (5.4) is written as:

$$h = (14 / 9\pi)[\, c(\alpha)\,]^{-2} (3\, v\, S / g)^{0.25} t^{(\alpha - 1)/4} [1 - (r / r_N)]^{1/3} \quad (8.1)$$

where h = height, v = viscosity, t = time, r = radius and total radius r_N, S is rate of supply. If S is assumed to be constant, α is 1.00 and c (α) is about 0.72. For Mt St Helens, when h = 120 m during late 1981, $v = 5.1 \times 10^{16}$ poise. Murase et al. (1984) concluded that such a value was unreasonably high, and may be due to the assumption of a con stant rate of growth and Newtonian properties of the magma. For crystal-rich rhyolite magmas, values exceeding 10^{14} poise, particularly for Ruawahia and S. Deadman Dome calculated via method $\eta e(3)$, may also be considered unreasonably high. Murase et al. (1984) concluded that none of the theoretical models so far derived is strictly adaptable to the problem of viscous crystal-rich lavas.

8.4.5. Summary

Cross-sectional area is related to flow length. Eruptive volume is intuitively important, however, the correlation coefficient is biased, owing to common terms (length) in both parameters. Plots of effective viscosity versus morphology (e.g. volume) show no viscosity difference between dome, coulee and flow. Effusion rate (F) and volume, cannot be independently determined, owing to morphological terms common to both parameters. However, a viscosity/effusion rate relationship is implied for calc-alkaline flows. This relationship is influenced by temperature and chemistry.

8.5. Addressing Major Questions.

In light of data obtained from both Ben Lomond and Mayor Island flows, and after comparison with other rhyolites, the three major questions stated in Chapter 1 may be addressed.

Firstly, what control do the volatiles in the system have on ultimate emplacement properties?

An understanding of an approach to attempt an answer is via objectives 3,4,5,6 and 9 - namely textural profiling, critical interpretation of degassing models, analysis of chemical profiles, and implications from constraints on eruption modes from textural features and inferred viscosity. The presence of 4% volatiles in the magma chamber lowers the viscosity of the liquid. But degassing and high undercooling on ascent causes void inflation and thus increases the effective viscosity of the melt. The ability for void inter-connection within the upper conduit and the permeability of the conduit pyroclastic funnel will, in part, control whether the magma erupts explosively, emplaces as a lava, or fails to reach the surface. Hydrostatic head within the conduit and magmatic volume are also important controlling factors. When emplacing, rhyolitic obsidian lava flows have similar water contents of between 0.1 and 0.2%. However, the presence of zones of vesicularity will depend on flow thickness and the relative viscosity of the vesiculated and non-vesiculated layers will contribute to the ease of Taylor instabilities within the upper part of the flow profile.

Secondly, what is the relative importance or contribution of the chemical composition, temperature, and volatile contents of rhyolite lavas?

To arrive at an answer, an approach using results from objectives similar to those for the first question may be pursued. Relative importance of each of the above three parameters cannot be assessed unless viscosity and temperature could be measured independently. Lag times for the fusion of powdered samples in furnace experiments with high silica rhyolites (e.g. Ben Lomond), prevent the direct measurement of viscosity. For aphyric lavas that are chemically uniform, the effect of temperature on flow rheology is greatest. Slight variations of water content within the polymerised fluid do not significantly alter the viscosity of the original liquid. However, when the vapour pressures of bubbles containing volatiles exceed the pressures exerted from the overlying lava, the effective viscosity of the lava is increased. This increase is concomitant with decreasing lava temperature within the carapace resulting in increasing yield strength and the lateral restraint of advancing lava.

Thirdly, what controls the differences in the flow behaviour of lava creating domes and flows?

The effusion rate, eruptive volume and basal slope are the most important variables in contributing to the contrasting dome, coulee, and flow landforms for lavas of similar chemistry, temperature and inferred viscosity from lavas of the Okataina Volcanic Centre. The Panum Crater - Southern Coulee comparison is another example. In contrast, significantly greater crystallinity and vesicularity contribute to the greater viscosity of the coarsely porphyritic lava with respect to the finely porphyritic lava. The FP lava has a flattened shape and is thinner than the more domical fractured flow carapace of the CP extrusion. The more viscous CP lava was impeded from lateral spreading owing to a rough basal topography while overiding and co-mingling with the FP lavas that were still partly fluid.

CHAPTER 9.

CONCLUSIONS

9.1. Introduction.

Rhyolite lava flows have never been observed to erupt. Little is known about the rheological properties of rhyolite lavas. Thus flow behaviour can only be inferred from detailed studies of pre-historic examples. No physical volcanological studies have been done on lavas in New Zealand, especially rhyolite lava flows. In contrast silicic ignimbrites and pyroclastic deposits have been well documented. Also, no detailed physical profiling of peralkaline flows have appeared in the published literature. Thus, this study is a new contribution to physical volcanology, looking at a variety of physical parameters for rhyolite lavas of contrasting composition - calc-alkaline versus peralkaline. In contrast to North American examples, New Zealand rhyolitic flows and domes are poorly exposed. Therefore the rhyolites chosen were young, had sufficient carapace outcrop, fresh glass, and cross-sectional exposure. Thus, this study will contribute to the data accumulated by some North American volcanologists from better exposed rhyolite lavas. Information derived from detailed physical volcanological studies is pre-requisite in deducing emplacement history and inferred viscosity for two different rhyolites from New Zealand. This information is important as rhyolite lavas, common in the Taupo Volcanic Zone and Coromandel Volcanic Zone, will erupt in the future, and are potential volcanic hazards in populated calderas such as Rotorua or Taupo.

Results will be summarised including the contrasting of the emplacement modes for Mayor Island and Ben Lomond lavas respectively. Finally, the possibilities for future work are briefly listed and the significance of studies of silicic lava flows is stated.

9.2. Ben Lomond - an overview

A flow stratigraphy for the Ben Lomond flow was assembled from three main sections (roadcut, airstrip and scarp) that collectively cut the upper 60 m of the flow stratigraphy, comprising: finely vesicular pumice (carapace); obsidian (the upper two units cut by an explosion breccia); a transitional spherulitic layer; and a central crystalline rhyolite. Flow banding from the deeper parts of both flow lobes dip toward the inferred circular vent, whereas near-surface carapace outcrops have a more variable dip direction. The flow carapace is poorly preserved. The roadcut section represents a lateral section across a flow ridge cut by an inverted cone-shaped exposure of explosion breccia. The scarp section penetrates two thirds of the inferred thickness of the Ben Lomond flow. A pod of pumiceous explosion breccia occurs above the rhyolite core and transition layer at a depth of about 30 m.

Methods from the physical volcanological studies of pyroclastic rocks, were adapted and applied to produce profiles of the textural characteristics of the Ben Lomond flow. A suppression of vesicularity occurs below about 10 m. The long axes of primary vesicles of high aspect ratio are parallel to the direction of flow. Voids of lower aspect ratio in the carapace have long axes perpendicular to the flow direction, from local foaming during flow on sudden removal of confining pressures. Void aspect ratio

and volatile content are anomalously high in the explosion breccia pod. Also, secondary spherulite proportion and diameter are greatest beneath the breccia pod suggesting late-flow migration of volatiles from a crystallising rhyolite core. Flattened lithophysae in the rhyolite layer indicate plastic deformation during flow above the brittle glass transition temperature. Rod-like microlites are of similar length throughout the flow as they formed during magmatic ascent within the conduit prior to flow emplacement.

Subsurface evidence (via microlite shape) points to a rising water saturated liquidus, increasing undercooling and the degassing of an originally hydrous magma that collapsed from an inflated foam in the upper part of the conduit prior to emplacement. Effervescence in the carapace occurred during flow: groundmass crystallisation in the central rhyolite layer during late-flow and cessation stages triggered explosion breccia formation. Spherulites formed at and below the glass transition temperature (approximately 670°C).

The uniformity of major and trace element chemistry in the obsidian layer supports the hypothesis that this unit best represents the chemistry of the original lava. The dense obsidian layer is least affected by isobaric crystallisation or groundwater metasomatism. Subtle variations occur between the obsidian, explosion breccia, and rhyolite layer chemistry. Late-flow migration of soluble trace elements formed a halo zone above the crystallising rhyolite core, consistent with variations in Na_2O, Cl, H_2O, and the development of secondary fabrics. Trace elements migrated by diffusion and in vapour phase between temperatures of 700 - 500°C over an estimated period of at least 16 years. The solubility of salts in hot water is a poor approximation to the mobility of large ions. Thus, at supercritical temperatures, transport as complex ions in dilute vapour-phase solutions containing Na, F, and Cl is favoured. Enrichments occur in the explosion breccia pod and the unconsolidated pumiceous matrix of the uppermost carapace for Al_2O_3, Ba, Zn, and Zr. These enrichments are not reflected in the explosion breccia of the roadcut section within the flow carapace. Enrichments for the porous, unconsolidated pumiceous fabrics occur owing to large surface area/volume ratios and short diffusion path lengths for the adsorption and migration of ions via low temperature groundwater metasomatism. Thus, it is difficult to distinguish between the effects of secondary high temperature deuteric migration of volatiles, and low temperature metasomatism.

In order to generate a semi-quantitative viscosity profile, the method of Shaw (1972) which empirically relates chemical composition to the viscosity of the original liquid was used. No general model for the rheology of dispersive systems in terms of size, shape, rigidity, and number/density distributions of inclusions (as crystals or gas bubbles) currently exists (Wilson et al. 1987). The Ben Lomond obsidian is aphyric and hence crystals did not contribute to the effective viscosity of the lava. The presence of bubbles as suspended spheres increases the effective viscosity and is estimated via Sibree (1933), Shaw (1965), or Murase et al. (1984). In conjunction with a thermal model adapted from Manley (1989), the viscosity increases by 2 - 3 orders of magnitude within the upper 10 - 15 m of the flow stratigraphy coinciding with the large thermal gradient. The estimated $\log_{10}$ viscosities (poise) of the magma in the chamber and inflating foam in the upper conduit are 7 and 11-12 respectively and is 11 for the central part of the flow during emplacement.

The emplacement model developed for the Ben Lomond flow was applied to the devitrified Pauanui flow lobes of Miocene age and the flow stratigraphy and rheology of the Okataina Volcanic Centre flows was deduced. For the Waiti flow, three methods for estimating flow viscosity were compared. While the methods gave broadly comparable results between 10^{10} - 10^{12} poise, the morphological and surface fold analyses were less reliable owing to difficulty of accurately estimating parameters such as flow thickness and carapace thickness.

9.3. Mayor Island Flows.

In contrast to calc-alkaline lavas, the pantelleritic flows of Mayor Island have a different flow morphology. Lava ponded within a tuff ring (Panui), formed distally tapering flow sheets (Pre-8 ka and 8 ka flows), or thin flow lobes (intracaldera lavas). The flow stratigraphy comprises: finely vesicular pumice; upper obsidian; central rhyolite; lower obsidian; and a basal breccia sequence above a pre-flow tuff. Flows are typically thin ($\sim$50 m), with a steep basal slope. None of the Mayor Island flows have explosion breccia fabrics, or any significant spherulitisation or lithophysae. For the 8 ka flow, spill-back of the lava occurred down the caldera wall toward the inferred vent fissure, and a fused basal lapilli support a spatter-fed emplacement mode. Parekoura Point is a distal carapace section with compressional obsidian flow ridges that curve around the point, and dip inland indicating primary flow directions. Brecciated rhyolite correspond to synclines and possible superimposed tension cracks. Anticlines are compressed into spines suggesting significant shortening of the carapace during cooling over a large thermal and viscosity gradient. Finely vesicular pumice occurs as an angular breccia in troughs between the ridges.

In contrast to Ben Lomond, void aspect ratio is lower in the flow pumice. More bubbles occur in the upper obsidian indicating a less viscous magma by analogy to the distribution and morphology of vesicles in the alkali basalt flows of Hawaii (cf. Aubele et al. 1988; Walker, 1989). Water contents are also very low, averaging 0.05%. Gravity instability occur between the upper rhyolite and the upper obsidian layers as elongated zones of brecciated and vesiculated rhyolite parallel to flow ridges. Thus devitrification (or isobaric crystallisation) of the rhyolite layer commenced at high temperature while the flow was still moving. For the 8 ka flow, the basal breccias have tapered clasts of high aspect ratio (Rc = 5), are re welded and have no matrix, suggesting a high flow temperature and large basal thermal gradient. The fusion of the upper 0.2 m of the basal tuff and the presence of charcoal in the 8 ka fall lapilli support basal flow temperatures of at least 300°C. Microlite length increases upward within the basal obsidian layer in the caldera wall section and is lowest in the finely vesicular pumice layer. The downward increase in microlite length within the upper obsidian layer suggests two possibilities: that the microlite length is affected by the post-emplacement thermal history of the flow; and that the viscosity of the flow was low enough to permit microlite growth via diffusion. Length variations within the upper obsidian layer profile compiled from Parekoura Point may reflect the overturning of the upper flow stratigraphy. The main difference between the calc-alkaline emplacement history of Ben Lomond and the Mayor Island model is microlite growth during flow, high temperature isobaric crystallisation during flow, and a spatter-fed emplacement mode.

Major element chemistry is significantly different from Ben Lomond - Na + K / Al > 1 and Na and K as silicate bond breakers assist in lowering the polymerisation of the melt. A minimum estimate for the water content of the 8 ka lapilli is 0.4 % prior to the emplacement of the 8 ka flow, whereas the water content of the flow obsidian is 0.05 %. Quenched basaltic xenoliths in both the 8 ka and Pre-8 ka flows support a low water content for the Mayor Island magma. Central flow temperature is estimated as approximately 950°C. Supportive evidence is from partial remelting of microlites when samples are heated to 1000 and 1050°C. This temperature approximates to the "no oxide" field of Nicholls and Carmichael (1969). When heated in a furnace powdered samples and obsidian blocks fuse and inflate respectively, followed by viscous deformation. Thus, for Mayor Island lavas, microlite length variations, vesiculation and vesicle collapse at surface pressures can occur within the time frame of emplacement.

Chemical variation in major and trace elements is pronounced between the obsidian and rhyolite layers. Depletions and enrichments correspond to a halo zone or front in the upper part of the rhyolite layer. Variations are more significant than for Ben Lomond as Cl and F is more concentrated in a lava containing 2 - 10 times less water. Sr concentration is most susceptible to seawater metasomatism.

Estimates of viscosity are 3 - 4 orders of magnitude lower than Ben Lomond because the melt is less polymerised and the emplacement temperature is ~ 150°C higher. F and Cl contents of 1000 and 1600 ppm respectively are less significant in promoting lower flow viscosities. Flow rheology was not sufficiently fluid to cause variations in size and concentrations of phenocrysts for the Panui flow via crystal settling (cf. Rowland and Walker, 1988).

9.4. Contrasting modes of emplacement: Mayor Island versus Ben Lomond

A schematic model for successive stages of rhyolite flow/dome emplacement is illustrated in Fig. 9.1 for both Ben Lomond calc-alkaline and Mayor Island peralkaline rhyolites.

Apart from the main lines of evidence for the spatter feeding of the Mayor Island flows - namely fusion of the upper part of the basal tuff, spill-back down the caldera wall and distal thinning down steep topographic slopes, convincing examples of spatter or agglutinate have not been observed. Of the flows studied, no distal basal exposures were available for study, where spatter may occur. Spatter may have rehomogenised within the basal obsidian layer at the proximal caldera wall sections. The tapered clasts in the fused layer of the fall lapilli may be the remains of spatter or represent the fusion and rheomorphism of the fall lapilli caused by the high temperature 8 ka flow that erupted shortly afterwards.

There is no evidence of the 8 ka flow emplacing en-masse from the central caldera vent, as no vent-funnel pyroclastics outcrop on the caldera wall. The spilling of lava down the caldera wall could not have occurred after the down-dropping of the caldera floor as no evidence of brittle or plastic dislocation of the 8 ka flow occurs. Therefore, the lava must have erupted from a fire fountain from a northeast trending caldera fissure. Most of the spatter fell on the caldera rim and remobilised as a

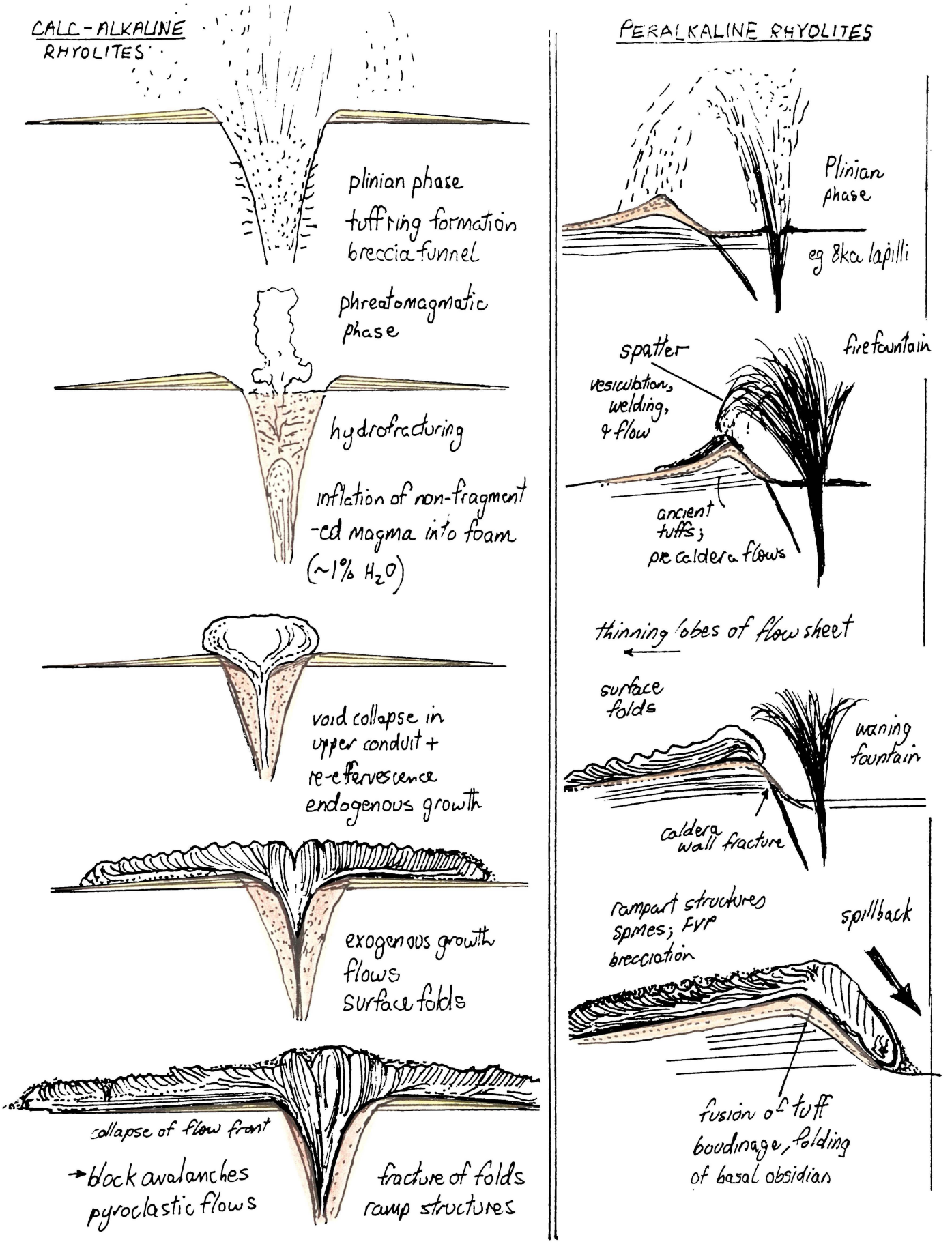

Fig. 9.1. Schematic diagram showing the emplacement histories and development of textures for calc-alkaline and peralkaline rhyolites.

distally tapering sheet over an arc of 90° from Halls Pass to Pighunters Pass. All evidence of the original fragmental nature of the eruption has been obliterated by rehomogenisation and the flow became overthickened on the caldera rim and spilled back down the caldera wall during mid-flow stage.

The contrasting morphology of the intracaldera lavas - namely a pile of overlapping lobate flows, results from a highly vesicular carapace up to 80 % porosity and 10 - 15 % phenocrysts of 1 mm average diameter. The average effective viscosity of the carapace of flow 2d is similar to that calculated based on flow shape from the method of Hulme (1974), Zimbelman (1985) and others. Thus the viscosity boundary between a spatter-fed pantelleritic sheet and a lobate flow is approximately $10^{8.5}$ - 10^{9} poise.

Three flow emplacement models have been postulated for calc-alkaline rhyolite lavas. Firstly, Fink (1983) proposed that the earliest emplaced lava contained the highest volatile content and was over-ridden by less volatile-rich obsidian lava. This model was based on carapace and flow-front exposure. Secondly, Eichelberger et al. (1986) proposed the emplacement of rhyolite lavas as a collapsed foam although did not discriminate between different vesiculated lava textures. Thirdly, Manley and Fink (1987) proposed that volatiles are released via microcracks from the interior of advancing flows and become trapped below a rigid carapace. From studies of Inyo drill holes, model 1 seems less plausible as the coarsely vesicular pumice does not extend to the base of the flow. From observations of diapir spacings of coarsely vesicular pumice both models 2 and 3 are supported (Baum et al. 1989).

Observations from variations in vesicularity, water content (H_2O^+), and trace element variations support a modified version of model 2 plus model 3 as best representing the emplacement of Ben Lomond flow. However, the scarp exposures show that the explosion breccia occurs as a pod, not as a continuous sheet such as the coarsely vesicular pumice of Inyo domes. In addition, the explosion breccia was emplaced after flow cessation. The presence of primary voids in the obsidian margin surrounding the explosion breccia pod constrains the formation of the pod after the flow stopped moving but while the interior was still plastic. No primary voids exist in the explosion breccia/obsidian contact within the roadcut section, suggesting emplacement after the flow stopped moving and after cooling of the carapace through the brittle glass transition temperature. The formation of the explosion breccia was driven by pressure release via tension cracks. In contrast, at the Inyo domes, Taylor instability of the coarsely vesicular pumice and overturning of the upper flow stratigraphy occurred both during and after flow as evident from elongate and circular outcrops respectively. Thus the flow viscosity of Inyo domes is lower than the Ben Lomond flow.

The emplacement of Ben Lomond occurred as a degassed deflated foam prior to extrusion from the vent. Voids were flattened and elongated within the upper part of the conduit. According to Henry et al. (1989, p.269) "a wet rhyolite, initially at 750°C is thoroughly degassed upon eruption and is emplaced some 300°C below the rhyolite solidus. Magma may emerge in a semi-solid condition in addition to being highly viscous owing to low temperature emplacement conditions." Firstly, the water-saturated liquidus at 1 MPa has not been measured. Crystallisation experiments under pressures less than 8 bar and realistic water contents of approximately 0.2 % have not been performed owing to a time-lag

in crystallisation. The solidus is unknown and the glass transition temperature is also poorly known. Magma may emerge below the solidus (50°C below solidus estimated for Inyo domes, Swanson et al. 1989) and behave as a Bingham plastic prior to brittle failure below the glass transition temperature. Platy obsidian clasts in the carapace of the Ben Lomond flow show plastic deformation prior to brittle failure, and bubble walls have been deformed by inflation during sudden overburden release or local foaming due to volatile migration from within flow.

9.5. Possibilities for Future Study and the Significance of Studying Rhyolite Lava Flows.

Some possibilities for future work include:

a. detailed longitudinal and cross-sectional profiling of the physical and chemical characteristics of pre-caldera lavas of the northeast or northwestern shield segments of Mayor Island;
b. isotopic tagging (via oxygen or hydrogen isotopes) of the water contents of carapace pumices and explosion breccias to separate the relative effects of secondary deuteric volatile migration and groundwater metasomatism for vesicular samples;
c. more sophisticated laboratory experiments to model crystallisation, viscosity, solidus and glass transition temperatures for the Ben Lomond obsidian;
d. constructing a viscometer for testing on rhyolite lavas;
e. detailed measurements of void shapes, void population studies including using backscatter electron microscopy to better quantify lava flow textures.

New eruptions of rhyolite lavas are only a matter of time (e.g. Long Valley Caldera, North America). Hence it is important for the nature of rhyolite emplacement to be investigated, particularly for young domes in active silicic calderas.

This study could not be based on visual observation of active rhyolites. It could only be based on outcrops of pre-historic rhyolite lava and interpretations using a degassing model from the North American literature for calc-alkaline lavas. This study has generated an emplacement history from detailed physical profiling of poorly exposed rhyolite lavas and has inferred the rheological behaviour of lavas that have never been observed to erupt. In addition, the documentation of a post-emplacement sequence of events is strengthened by chemical profiling, which, together with textural variations, record secondary migration of volatiles. Parameters were found that may approximate the form of the viscosity and temperature profiles which cannot be determined independently, at least for the Mayor Island and Ben Lomond lavas. Such studies involving the quantifying of flow textures provide a greater understanding of flow behaviour, and ultimately, volcanic hazards in active rhyolitic volcanic centres. While less dangerous than ignimbrite eruptions, volcanic hazards for slow moving viscous rhyolite lavas become greater as flow length increases such as explosion pit formation, and the generation of pyroclastic flows from flow front collapse.

REFERENCES.

Allen, R.L., 1989. False pyroclastic textures in silicic lavas. Continental Magmatism Abstracts. IAVCEI General Assembly, June 25 - July 1, 1989. Bull. 131 New Mexico Bureau of Mines and Mineral Resources. p. 3.

Anderson, D.J., Lindsley, D.H., 1988. Internally consistent solution models for Fe - Mg - Mn oxides: Fe - Ti oxides. American Mineralogist. 73, 714-723.

Aubele, J.C., Crumpler, L.S., Elston, W.E., 1988. Vesicle zonation and vertical structure of basalt flows. Journal of Volcanology and Geothermal Research. 35, 349-374.

Audunsson, H., Levi, S., 1988. Basement heating by a cooling lava: paleomagnetic constraints. Journal of Geophysical Research. 93 B4, 3480-3496.

Bailey, D.K., Cooper, J.P., Knight, J.L., 1974. Anhydrous melting and crystallisation of peralkaline obsidians. Bulletin Volcanologique. 38(3), 653-665.

Bailey, R.A., Miller, C.D., Sieh, K., 1989. Excursion 13B: Long Valley caldera and Mono-Inyo Craters volcanic chain, eastern California. New Mexico Bureau of Mines and Mineral Resources Memoir 47. 227-254.

Baum, B.A., Krantz, W.B., Fink, J.H., Dickinson, R.E., 1989. Taylor instability in rhyolite lava flows. Journal of Geophysical Research. 94 B5, 5815-5828.

Best, M., 1982. Igneous and Metamorphic Petrology. W.H. Freeman & Co.

Bonnichsen, B., 1982. Rhyolite lava flows in the Bruneau Jarbidge eruptive centre, southwestern Idaho., in Bonnichsen, B., and Brechenridge, R.M. (eds.) Cenozoic geology of Idaho: Idaho Bureau of Mines and Geology Bulletin 26, 283-320.

Bonnichsen, B., Citron, G.P., 1982. The Cougar Point Tuff, southwestern Idaho and vicinity., in Bonnichsen, B., and Brechenridge, R.M., (eds.) Cenozoic geology of Idaho: Idaho Bureau of Mines and Geology Bulletin 26, 255-281.

Bonnichsen, B., Kauffman, D.F., 1987. Physical features of rhyolite lava flows in Snake River Plain volcanic province southwestern Idaho. Geological Society of America Special Paper. 212, 119-145.

Bottinga, Y., Weill, D.F., 1972. The Viscosity of magma silicate liquids: a model for calculation. American Journal of Science. 272, 438-475

Brothers, R.N., 1957. The volcanic dome at Mayor Island New Zealand. Trans. of the Royal Society of New Zealand. 84 (3), 549 - 560.

Buck, M.D., 1978. Pyroclastic deposits on Mayor Island, Bay of Plenty, New Zealand. M.Sc thesis, University of Waikato.

Buck, M.D., Briggs, R.M., Nelson, C.S., 1981. Pyroclastic deposits and volcanic history of Mayor Island. New Zealand Journal of Geology and Geophysics 24, 449-467.

Buddington, A.F., Lindsley, D.H., 1964. Iron-titanium oxide minerals and their synthetic equivalents. Journal of Petrology. 5, 310 - 357.

Carmichael, I.S.E., 1967. The iron-titanium oxides of salic volcanic rocks and their associated ferromagnesian silicates. Contributions to Mineralogy and Petrology. 14, 36-64.

Carmichael, I.S.E., Turner F.J., Verhougen T, 1974. Igneous Petrology. McCraw-Hill, New York.

Carmichael, R.D., 1982. CRC Handbook of the physical properties of rocks. CRC Press Inc. Boca Raton, Florida.

Carslaw, H.S., Jaeger, J.C., 1959. Conduction of Heat in Solids, 2nd ed. Oxford University Press, New York. 496p.

Cas, R.A.F., Wright, J.V., 1987. Volcanic successions - modern and ancient. Allen & Unwin Publishers, Sydney 487p.

Chester, D.K., Duncan, A.M., Guest, J.E., Kilburn, C.R.J., 1985. Mount Etna: the anatomy of a volcano. Stanford University Press, Stanford California. 404p.

Christiansen, R.L., Lipman, P.W., 1966. Emplacement and thermal history of a rhyolite lava flow near Fortymile Canyon, Southern Nevada. Geological Society of America Bulletin 79, 671 - 684.

Cornette, Y., Crisci, G.M., Gillot, P.Y., Orsi, G., 1983. Recent volcanic history of Pantelleria: A new interpretation. Journal of Volcanology and Geothermal Research. 17, 371-373.

Clemens, J.D., 1984. Water contents of silicic to intermediate magmas. Lithos. 17, 273-287.

Clough, B.J., Wright, J.V., Walker, G.P.L., 1982. Morphology and dimensions of the young comendite lavas of La Primavera Volcano, Mexico. Geological Magazine. 119 (50), 477-485.

Cole, J.W., 1966. Tarawera Volcanic Complex. PhD Thesis. Victoria University of Wellington.

Cole, J.W., 1970. Structure and eruptive history of the Tarawera Volcanic Complex. New Zealand Journal of Geology and Geophysics. 13, 879-902.

Cole, J.W., 1972. Distribution of high alumina basalts in the Taupo Volcanic Zone Publication. Victoria University of Wellington, Geology Department. 1, 1-15.

Cole, J.W., 1973. High-alumina basalts of the Taupo Volcanic Zone, New Zealand. Lithos. 6, 53-64.

[1] Dragoni, M., Bonafede, M., Boschi, E., 1986. Downslope flow models of a Bingham liquid Implications for lava flows. Journal of Volcanology & Geothermal Research. 30, 305-325.

[2] Druitt, T.H., Anderson, A.T., Jr. and Nagle, F., 1982. Water in rhyolitic magma, Bishop, California Eos. (American Geophysical Union Transactions) 63 p.451.

New Zealand
Cole, J.W., 1978. Tectonic setting of Mayor Island, New Zealand. Journal of Geology and Geophysics. 21, 645-647.

Cole, J.W., 1979. Chemical analyses of lavas and ignimbrites of the Taupo Volcanic Zone. Geology Dept. Publ. 13. Victoria University of Wellington.

Congdon, R.D., Nash, W.P., 1988. High fluorine rhyolite: an eruptive pegmatite magma at Hoeneycomb Hills, Utah. Geology. 16(11), 1018-1021.

Dingwell, D.B., Scarfe, C.M., Cronin, D.J. 1985. The effect of fluorine on viscosities in the system Na_2O-Al_2O_3-SiO_2: implications for phonolites, trachytes and rhyolites. American Mineralogist. 70, 80-87.

Dragoni, M., 1989. A dynamical model of lava flows cooling by radiation. Bulletin of Volcanology. 51(2), 88-95.

1,2 •

Duffield, W.A., 1989. Days 6 and 7: Field guide to the Taylor Creek Rhyolite, Black Range, New Mexico in Ratte, J.C., Cather, S.M., Chapin, C.E., Duffield, W.A., Elston, W.E., McIntosh, W.C., 1989. Excursion 6A: Eocene-Miocene Mogollon-Datil volcanic field, New Mexico. New Mexico Bureau of Mines and Mineral Resources Memoir 46. pp107-110.

Duffield, W.A., 1989. Fountain-fed silicic lava flows. Continental Magmatism Abstracts. IAVCEI General Assembly, Santa Fe June 25 - July 1 1989. Bull. 131 New Mexico Bureau of Mines and Mineral Resources. p. 76.

Dunbar, N.W., Kyle, P.R., 1989. Volatile contents of obsidian from the Taupo Volcanic Zone, New Zealand, and implications for eruption processes. Continental Magmatism Abstracts IAVCEI General Assembly June 25 - July 1 1989. Bull. 131 New Mexico Bureau of Mines and Mineral Resources. p. 77.

Dunbar, N.W., Kyle, P.R., 1986. H_2O and Cl contents and temperature of Taupo Volcanic Zone rhyolitic magmas. International Volcanological Congress 1986 Abstracts p.148.

Dunnet, D., 1969. A technique of finite strain analysis using elliptical particles. Tectonophysics. 7(2), 117-136.

Eichelberger, J.C., 1989. Are extrusive rhyolites produced from permeable foam eruptions? A reply. Bulletin of Volcanology. 51, 72-75.

Eichelberger, J.C., Westrich, H.R., 1981. Magmatic volatiles in explosive rhyolitic eruptions. Geophysical Research Letters. 8, 757-760.

Eichelberger, J.C., Carrigan, C.R., Westrich, H.R., Price, R.H., 1986. Non-explosive silicic volcanism. Nature. 323, 598-602.

Eichelberger, J.C., and Hildreth, W., 1986. Research drilling at Katmai, Alaska. Eos (American Geophysical Union Transactions), (Oct 14., 1986) VGP news.

Eichelberger, J.C., Vogel, T.A., Younker, L.W., Miller, C.D., Heiken, G.H., Wolhetz., K.H., 1988. Structure and stratigraphy beneath a young phreatic vent: South Inyo Crater, Long Valley Caldera, California. Journal of Geophysical Research. 93 B11, 13208-13220.

Elliot, D., 1970. Determination of finite strain and initial shape from deformed elliptical objects. Geological Society of America Bulletin. 81, 2221-2236.

Ewart, A., 1968. The petrography of the central North Island rhyolitic lavas. Part 2 - Regional petrography including notes on associated ash-flow pumice deposits. New Zealand Journal of Geology and Geophysics. 11, 478-545.

Ewart, A., Healy, J., 1965. Rotorua - volcanic geology. Information Series NZ DSIR Res.No. 50, 10-26.

Ewart, A., Taylor, S.R., Capp, A.C., 1968. Trace and minor element geochemistry of the rhyolitic volcanic rocks, Central North Island, New Zealand: total rock and residual liquid data. Contributions to Mineralogy and Petrology. 18, 76-104.

Ewart, A., Taylor, S.R., Capp, A.C., 1968. Geochemistry of the Pantellerites of Mayor Island, New Zealand. Contributions to Mineralogy and Petrology. 17, 116-140.

Ewart, A., Green, D.C., Carmichael, I.S.E., Brown, F.H., 1971. Voluminous low temperature rhyolitic magmas in N.Z. Contributions to Mineralogy and Petrology. 33, 128-144.

Ewart, A., Hildreth, W., Carmichael, I.S.E., 1975. Quaternary acid magma in New Zealand. Contributions to Mineralogy and Petrology. 51, 1-27.

Ferrara, G., Treuil, M., 1974. Petrological implications of trace element and Sr isotope distributions in basalt - pantellerite series. Bulletin Vocanologique. 38(3), 548-574.

Fink, J.H., 1978. Surface structures on obsidian flows. PhD Thesis. Stanford.

Fink, J.H. 1980a. Gravity instability in the Holocene Big and Little Glass Mountain rhyolitic obsidian flows, northern California. Tectonophysics 66. 147-166.

Fink, J.H. 1980b. Surface folding and viscosity of rhyolite flows. Geology. 8, 250-254.

Fink, J.H. 1983. Structure and emplacement of a rhyolitic obsidian flow. Little Glass Mountain, Medicine Lake Highland, N.California. Geological Society of America Bulletin. 94. 362-380.

Fink, J.H. 1984. Structural geologic constraints on the rheology of rhyolitic obsidian. Journal of Non Crystalline Solids. 67, 135-146.

[1] Fink, J., Manley, C., Krinsley, D., 1985. Volatile migration, crystallisation and vesiculation during emplacement of Inyo Obsidian Dome. Eos. (American Geophysical Union Transactions) 66, 18 p 387

[2] Fink, J., Manley, C. 1986. Explosive volcanic activity generated from within advancing rhyolite lava flows. International Volcanological Congress 1-9 Feb 1986, New Zealand. Abstracts p 241

Fink, J.H. and Fletcher, R.C., 1978. Ropy pahoehoe:Surface folding of a viscous fluid. Journal of Volcanology and Geothermal Research. 4, 151-170.

Fink, J.H., Park, S.O., Greeley, R., 1983. Cooling and deformation of sulphur flows. Icarus. 56, 38-50.

1,2 •

Fink, J.H., Zimbelman, J.R., 1986. Rheology of the 1983 Royal Gardens basalt flows Kilauea Volcano Hawaii. Bulletin of Volcanology. 48, 87-96.

Fink, J.H., Manley, C.R., 1987. The origin of pumiceous and glassy textures in rhyolite flows and domes. Geological Society of America Special Paper 212, 77-88.

Fisher, R.V., Schminke, H-U., 1984. Pyroclastic Rocks. Springer-Verlag. Heidelberg.

Froggatt P.C., 1981a. Karapiti Tephra Formations, a 10,000 years B.P. rhyolitic tephra from Taupo. New Zealand Journal of Geology and Geophysics. 24,95-98.

Froggatt P.C., 1981b Motutere Tephra Formation and redefinition of Hinemaiaia Tephra Formation, Taupo Volcanic Centre, New Zealand. New Zealand Journal of Geology and Geophysics. 24, 99-105.

Froggatt P.C., 1982a. A study of some aspects of the volcanic history of the Lake Taupo area, North Island, New Zealand. PhD Thesis, Victoria University of Wellington.

Froggatt P.C., 1982b. Review of methods of estimating rhyolitic tephra volumes: application to the Taupo Volcanic Zone, New Zealand. Journal of Volcanology and Geothermal Research. 14, 301-318.

Friedman, I. 1989. Are extrusive rhyolites produced from permeable foam eruptions. Bulletin of Volcanology. 51, 69-71.

Friedman, I., Long, W., Smith, R.L., 1963. Viscosity and water content of rhyolite glass. Journal of Geophysical Research. 68, 6523-6535.

Gable, G.W., Shankland, T.J., 1984. Radiation heat transfer in molten and glassy obsidian. Journal of Geophysical Research. 89 B8, 7107-7110.

Goff, F., Gardner, J.N., Baldridge, W.S., Hulen, J.B., Nielson, D.L., Vaniman, D., Heiken, G., Dungan, M.A., Broxton, D., 1989. Excursion 17B: Volcanic and hydrothermal evolution of Pleistocene Valles caldera and Jemez volcanic field. New Mexico Bureau of Mines and Mineral Resources Memoir 46, 381-403.

Grange, L.I., 1937. The geology of the Rotorua-Taupo subdivision. New Zealand Geological Survey Bulletin no. 37.

Grindley, G.W., 1960. Sheet 8, Taupo. Geological Map of New Zealand 1:250,000. NZ DSIR Wellington.

Grindley, G.W., 1961. Sheet N94, Taupo. Geological Map of New Zealand 1:63,350. NZ DSIR Wellington.

Grindley, G.W., 1965. The geology structure and exploitation of the Wairakei geothermal field, Taupo, New Zealand. New Zealand Geological Survey Bulletin no.75.

Grindley, G.W., 1982. The deeper structure of the Wairakei geothermal field. Proc. Pacific Geothermal Conference 1982. Part 1, 69-74. Geothermal Institute University of Auckland.

Guest, J.E., Sanchez, J., 1969. A large dacitic lava flow in Northern Chile. Bulletin Volcanologique. 33(3), 778-790.

Healy, J., Schofield, J.C., Thompson, B.N., Rotorua. Geological map of N.Z. Sheet 5 1:250,000. DSIR NZ.

Healy, J., 1984. Wairakei geothermal field in review. New Zealand Geological survey unpublished Geothermal Circular JH-10.

Heiken, G., Wohletz, K., Eichelberger, J., 1985. Intrusive pyroclasts, Inyo Domes CA. Eos (American Geophysical Union Transactions). 66(18) p.387

Helz, R.T., Thornber, C.R., 1987. Geothermometry of Kilauea Iki lava lake, Hawaii. Bulletin of Volcanology. 49, 651-668.

Henry. C.D., Price, J.G., Rubin, J.N., Parker, D.F., Wolff, J.A., Self, S., Franklin, R., Barker, D.S., 1988. Widespread, lavalike silicic volcanic rocks of Trans-Pecos Texas. Geology. 16, 509-512.

Henry, C.D., Price, J.G., Parker, D.F., Wolff, J.A., 1989. Excursion 9A: Mid-Tertiary silicic alkalic magmatism of Trans-Pecos Texas: Rheomorphic tuffs and extensive silicic lavas. New Mexico Bureau of Mines and Mineral Resources Memoir 46, 231-274.

Hervig, R.L., Dunbar, N., Westrich, H.R., Kyle, P.R., 1989. Pre-eruptive water content of rhyolitic magmas as determined by ion microprobe analyses of melt inclusions in phenocrysts. Journal of Volcanology and Geothermal Research. 36, 293-302.

Hogg, A.G., McGraw, J.D., 1983. Late quarternary tephra of Coromandel Peninsula, North Island, New Zealand: a mixed peralkaline and calcalkaline tephra sequence. New Zealand Journal of Geology and Geophysics. 26, 163-188.

Houghton, B.F., Wilson C.J.N., Weaver, S.D., 1985a. Strombolian deposits at Mayor Island: "basaltic" eruption styles displayed by a peralkaline rhyolitic volcano. New Zealand Geological Survey record 8, 42-51.

Houghton, B.F., Wilson, C.J.N., Weaver, S.D., 1985b. The Ruru Pass Tephra: a peralkaline welded airfall tuff from Mayor Island. New Zealand Geological Survey record 8, 30-36.

• Houghton, B.F., Wilson, C.J.N., Lloyd, E.F., Gamble, J.A., Kolelaar, B P , 1987 A catalogue of basaltic deposits within the central Taupo Volcanic Zone. New Zealand Geological Survey Record 18 95 - 101.

Houghton, B.F., Wilson, C.J.N., 1986. A1 Explosive rhyolite volcanism: the case studies of Mayor Island and Taupo Volcanoes. in Houghton, B.F., Weaver, S.D., 33-100 New Zealand Geological Survey record 12.

Houghton, B.F., Wilson, C.J.N., Weaver, S.D., 1987. The Opo Bay Tuff Cone, Mayor Island: interaction between rising gas-poor pantellentic magma and external water. New Zealand Geological Survey record 18, 79-85.

Hulme, G., 1974. The interpretation of lava flow morphology. Geophysical Journal of the Royal Astronomical Society. 39, 361-384.

Hulme, G., & Fielder, G., 1977. Effusion rates and rheology of lunar lavas. Philosophical Transactions of the Royal Society, London. A 285, 227-234.

Huppert, H.E., Shepherd, J.B., Sigurdsson, H., Sparks, R.S.J., 1982. On lava dome growth, with application to the 1979 lava extrusion of the Soufriere of St. Vincent. Journal of Volcanology and Geothermal Research. 14, 199-222.

Hutchinson, C.S., 1974. Laboratory handbook of petrographic techniques. John Wiley & Sons. New York. 527p.

Johnson, A.M. 1970. Physical Processes in Geology: San Francisco Freeman, Cooper & Co., 577p.

Kasameyer, P.W., Younker, L.W., Eichelberger, J.C., Lysne, P.C., Vogel, T.A., 1985. Thermal evolution of the Inyo magma. Eos (American Goeophysical Union Transactions). 66(18) p.385.

Kohn, B.P. 1973. Some studies of New Zealand Quaternary pyroclastic rocks. PhD Thesis, Victoria University of Wellington.

Kovalenko, V., Hervig, R.L., Sheridan, M.F., 1988. Ion-miocroprobe analyses of trace elements in anorthoclase, hedenbergite, aenigmatite, quartz, apatite and glass in pantellerite. Evidence for high water contents in pantellerite melt. American mineralogist. 73, 1038-1045.

Kovalenko, V.I., Hervig, R.L., Schauer, S., 1989. Volatile contents of pantellerite. Continental Magmatism Abstracts, IAVCEI General Assembly June 25 - July 1 1989, Bull. 131 New Mexico Bureau of Mines and Mineral Resources. p156.

Lawless, J.V., 1975. The geology of the Cashmores Road perlite occurrence, Atiamuri. MSc Thesis, University of Waikato.

Lechler, P.J., Desilets, M.O., 1987. A review of the use of loss of ignition as a measurement of total volatiles in whole-rock analysis. Chemistry Geology. 63, (3/4) 341-344.

Lipman, P.W., Banks, N.G., 1987. Aa flow dynamics, Mauna Loa 1984. United States Geological Survey Professional Paper 1350., 1527-1567.

Lofgren, G. 1974. An experimental study of plagioclase crystal morphology: Isothermal crystallisation. American Journal of Science. 274 (3), 243-273.

Loney, R.A. 1968. Flow structure and composition of the Southern Coulee Mono Craters, California - A pumiceous rhyolite flow. Geological Society of America Memoir 16, 415-440.

McBirney, A.R., Murase, T., 1984. Rheological properties of magmas Annual Review of Earth and Planetary Sciences. 12, 337-357.

MacDonald, R., & Bailey, D.K. 1973. Data of Geochemistry Sixth Ed. Ch.N. Chemistry of Igneous Rocks. Part 1. The Chemistry of the peralkaline oversaturated obsidians. United States Geological Survey Professional Paper 440-N-1

Mahood, G.A., 1984. Calderas associated with strongly peralkaline volcanic rocks. journal of Geophysical Research. 89, 8540-8552.

Mahood, G.A., Hildreth, W., 1986. Geology of the peralkaline volcano at Pantelleria, Strait of Sicily. Bulletin of Volcanology. 48, 143-172.

Malin, M.C., 1980. Lengths of Hawaiian lava flows. Geology. 8., 306-308.

Manley, C.R. 1989. Cooling, devitrification and flow of large hot rhyolite lava flows: numerical modelling results. Continental Magmatism Abstracts IAVCEI General Assembly June 25 - July 1, 1989. Bull. 131 New Mexico Bureau of Mines and Mineral Resources p.174.

Manley, C.R., Fink, J.H., 1987. Internal textures of rhyolite flows as revealed by research drilling. Geology. 15, 549-552.

Mathez, E.A., 1973. Refinement of the Kudo - Weill plagioclase geothermometer and its application to basaltic rocks. Contributions to Mineralogy and Petrology. 41, 61-72.

Moore, H.J., Arthur, D.W.G., Schaber, G.G., 1978. Yield strengths of flows on the Earth, Mars and Moon. Proceedings of the 9th Lunar and Planetary Science Conference (1978) 3351-3378.

Moore, H.J., 1987. Preliminary estimates of the rheological properties of the 1984 Mauna Loa lava United States. Geological Survey Professional Paper 1350, 1569-1588.

Muncill, G.E., Lasaga, A.C., 1988. Crystal-growth kinetics of plagioclase in igneous systems: Isothermal H_2O-saturated experiments and extension of a growth model to complex silicate melts. American Mineralogist. 73, 982-992.

Murase, T., McBirney, A.R., 1973. Properties of some common igneous rocks and their melts at high temperatures. Geological Society of America Bulletin 84, 3583-3592.

Murase, T., McBirney, A.R., Melson, W.G., 1984. Viscosity of the Dome of Mount St Helens. Journal of Volcanology and Geothermal Research. 24, 193-204.

* Nairn, I.A., 1986. Okataina Volcanic Centre. (Intra- Congress Tours B2 and B3) International Volcanological Congress 1986 handbook p. 99-111.

Nairn, I.A., 1981. Some studies of the geology, volcanic history and geothermal resources of the Okataina Volcanic Centre, Taupo Volcanic Zone, New Zealand. PhD Thesis, Victoria University of Wellington.

•

Naney, M.T., 1983. Phase equilibria of rock-forming ferromagnesian silicates in granitic systems. American Journal of Science. 283 (10), 993-1033.

Navrotsky, A., 1981. Thermodynamics of mixing in silicate glasses and melts. in Newton, R.D., Navrotsky, A., Wood, B.J.,(eds.) Advances in Physical Geochemistry Vol.1. The Thermodynamics of Minerals and Melts Springer Verlag. New York. 189-206.

Nelson, S.A., 1981. The possible role of thermal feedback in the eruption of siliceous magmas. Journal of Volcanology and Geothermal Research. 11, 127-137.

Newman, S., Epstein, S., Stoper, E., 1988. Water, carbon dioxide, and hydrogen isotopes in glasses from the ca. 1340 AD eruption of Mono Craters California: constraints on degassing phenomena and initial volatile content. Journal of Volcanology and Geothermal Research. 35, 75-96.

Nicholls, J., Carmichael, I.S.E., 1969. Peralkaline acid liquids: a petrological study. Contributions to Mineralogy and Petrology. 20, 268-294.

Northey, D.J., 1983. Seismic studies of structure beneath Lake Taupo PhD. Thesis. Victoria University of Wellington.

O'Neil, J.R., Taylor, B.E., 1985. Degassing of Obsidian Dome magma: hydrogen and oxygen isotope studies in the Inyo Dome chain, Long Valley area, California. Eos (American Geophysical Union Transactions). 66(18) p.387.

Orowan, E., 1949. Discussion. In Meeting of British Glaciological Society, the British Rheologists Club, and the Institute of Metals. Journal of Glaciology 1: 231-240.

Peterson, D.W., 1979. Significance of the flattening of pumice fragments in ash-flow tuffs. Geological Society of America Special Paper. 180, 195-204.

Pickett, D.A., Stolper, E.M., 1984. Thermometry of rhyolitic obsidians based on water speciation Eos (American Geophysical Union Transactions). 65 (45), p1128.

Pieri, D.C., Baloga, S.M., 1986. Eruption rate, area and length relationships for some Hawaiian lava flows. Journal of Volcanology and Geothermal Research. 30, 29-45.

Pinkerton, H., and Sparks, R.S.J., 1978. Field measurements of the rheology of lava. Nature. 276, 383-385.

Piwinskii, A.J., Wyllie, P.J., 1968. Experimental studies of igneous rock series. A zoned pluton in the Wallowa Batholith, Oregon. Journal of Geology. 76, 205-234.

• Shaw, H.R., Wright, T.L., Peck, D.L., Okamura, R., 1968. The viscosity of basaltic magma: an analysis of field measurements in Makaopuhi lava lake, Hawaii. American Journal of Science 266, p. 225-264.

Robson, D.S., Whitlock, J.H., 1964. Estimation of a truncation point. Biometrika. 51, 33-40.

Roscoe, R., 1952. The viscosity of suspensions of rigid spheres. British Journal of Applied Physics. 3, 267-269.

Rose., W.I., 1987. Volcanic activity at Santiaguito volcano 1976-1984. Geological Society of America Special Paper 212, 17-28.

Rowland, S.K., Walker, G.P.L. 1988. Mafic-crystal distributions, viscosities, and lava structures of some Hawaiian lava flows. Journal of Volcanology and Geothermal Research. 35, 55-66.

Rutherford, N.F., 1978. A comment on the source of Mayor Island pantelleritic magma. New Zealand Journal of Geology and Geophysics. 21, 449-453.

Sampson, D.E., 1987. Textural heterogeneities and vent area structures in the 600 year old lavas of the Inyo Volcanic Chain, E. California. Geological Society of America Special Paper 212, 89-101.

Sampson, D.E., Cameron, K.L., 1987. The geochemistry of the Inyo Volcanic chain: Multiple magma systems in the Long Valley region E. California. Journal of Geophysical Research 92 B10, 10,403-10,421.

Schofield, J.C., 1967. Sheet 3 Auckland (1st ed.) Geological Map of New Zealand 1:250,000. DSIR Wellington.

Schminke, H-U., 1974. Volcanological aspects of peralkaline silicic welded ash-flow tuffs. Bulletin Volcanologique. 38(3), 594-636.

Selby, M.J., Augustinus, P., Moon, V.G., Stevenson, R.J., 1988. Slopes on strong rock masses: modelling and influences of strong distributions and geomechanical properties. in Anderson, M.G., Modelling Geomorphological Systems. John Wiley & Sons. London.

Self, S., 1983. Large-scale phreatomagmatic silicic volcanism: a case history from New Zealand. Journal of Volcanology and Geothermal Research. 17, 433-469.

Self, S., Silva, S.L., Francis, P.W., 1989. Large-scale dacite effusive volcanism, Chao Volcano, North Chile. Continental Magmatism Abstracts, IAVCEI General Assembly. June 25 - July 1, 1989. Bull. 131. New Mexico Bureau of Mines and Mineral Resources, p238.

Shaw, H.R., 1965. Comments on Viscosity crystal settling and convection in granitic magmas. American Journal of Science. 263, 120-152.

Shaw, H.R., 1969. Rheology of basalt in the melting range. Journal of Petrology. 10, 510-535.

Shaw, H.R., 1972. Viscosities of magmatic silicate liquids: an empirical method of prediction. American Journal of Science. 272, 870-893.

Sherman, P., 1968. Emulsion Science. New York. Academic Press. 351pp.

Sibree, J.O., 1933. The viscosity of froth. Faraday Society Transactions 35, 325-337.

Sieh, K., Bursik, M., 1986. Most recent eruption of the Mono Craters eastern central California. Journal of Geophysical Research. 91 B12, 12539-12571.

Skinner, D.N.B., 1979. Anzaas Auckland 1979. Geology Tour 1; Volcanic and geothermal geology, Coromandel and Central North Island, New Zealand. New Zealand Geological Survey Report G37. DSIR Wellington.

Sparks, R.S.J., 1978. The dynamics of bubble formation and growth in magmas: A review and analysis. Journal of Volcanology and Geothermal Research 3, 1-37.

Spera, F.J., Borgia, A., Strimple, J., 1988. Rheology of melts and magmatic suspensions 1. Design and calibration of concentric cylinder viscometer with application to rhyolitic magma. Journal of Geophysical Research. 93 B9, 10,273-10,294.

Smith, J.V., 1974. Feldspar Minerals. Springer Verlag. Berlin.

Stevenson, R.J., 1986. The Geotechnical Properties of Minden Rhyolite at Pauanui and Onemana, Eastern Coromandel. MSc Thesis University of Waikato.

Stevenson, R.J., Hodder, A.P.W., (in press) Technical Note: Fabric controls on the strength properties of some rhyolites. Engineering Geology.

Stipp, J.J., 1968. The geochemistry and petrogenesis of the Cenozoic volcanics of the North Island, New Zealand. PhD thesis Australia National University, Canberra.

Suemnicht, G.A., Varga, R.J., 1988. Basement structure and implications for hydrothermal circulation patterns in the western moat of Long Valley Caldera, California. Journal of Geophysical Research. 93 B11, 13,191-13,207.

Swanson, D.A., Dzurisin, D., Holcomb, R.T., Iwatsubo, E.Y., Chadwick, Jnr.W., Casadevall, T.J., Ewert, J.W., Heliker, C.C., 1987. Growth of the lava dome at Mount St. Helens, Washington (USA) 1981-1983. Geological Society of America Special Paper 212, 1-16.

Swanson, S.E., 1977. Relation of nucleation and crystal-growth rate to the development of granitic textures. American Mineralogist. 62, 966-978.

Swanson, S.E., Naney, M.T., Westrich, H.R., 1985a. Crystallisation of rhyolite of Inyo Obsidian Dome: Eos (American Geophysical Union Transactions) 66(18), p.384.

Swanson, S.E., Naney, M.T., Westrich, H.R., 1985b. Origin of microlites in rhyolite: an example from Inyo Domes, California. Eos (American Geophysical Union Transactions) 66 (46), p1112.

Swanson, S.E., Naney, M.T., Westrich, H.R., Eichelberger, J.C., 1989. Crystallisation history of Obsidian Dome, Inyo Domes, California. Bulletin of Volcanology. 51, 161-176.

Taylor, B.E., Dunbar, N., Kyle, P.R., 1986. Stable isotope studies of the volatile history and degassing of rhyolitic magmas in the Taupo Volcanic Zone, New Zealand. International Volcanological Congress New Zealand. Abstracts p217.

Taylor, B.E., Eichelberger, J.C., Westrich, H.R., 1983. Hydrogen isotopic evidence of rhyolite magma degassing during shallow intrusion and eruption. Nature. 306, 541-545.

Topping, W.W., Kohn, B.P., 1973. Rhyolitic tephra marker beds in the Tongariro area, North Island, New Zealand. New Zealand Journal of Geology and Geophysics. 16, 375-395.

Villari, L., 1974. The Island of Pantelleria. Bulletin Volcanologique. 38, 680-724.

Vogel, T.A., Schuraytz, B.C., Younker, L.W., 1985. Preliminary geothermometry of the conduit to Obsidian Dome based on coexisting ilmenite, magnetite and augite-orthopyroxene. Eos (American Geophysical Union Transactions). 66, 1112.

Vogel, T.A., Younker, L.W., Schuraytz, B.C., 1987. Constraints on magma ascent, emplacement and eruption: geochemical and numeralogical data from drillcore samples at Obsidian dome, Inyo Chain, California. Geology. 15, 405-408.

Vucetich, C.G., Pullar, W.A., 1973. Holocene tephra formations erupted in the Taupo area and interbedded tephras from other volcanic sources. New Zealand Journal of Geology and Geophysics. 16, 745-780.

Vucetich, C.G., and Howorth, R. 1976a. Proposed definition of the Kawakawa tephra, the ca. 20,000 years B.P. horizon in the New Zealand Region. New Zealand Journal of Geology and Geophysics. 19, 43-50.

Vucetich, C.G., Howarth, R., 1976b. Late Pleistocene tephrostratigraphy in the Taupo District, New Zealand. New Zealand Journal of Geology and Geophysics. 19(1), 51-69.

Walker, G.P.L., 1973. Lengths of lava flows. Philosophical Transactions of the Royal Society, London. 274, 107-118.

Walker, G.P.L., 1981. The Waimihia and Hatepe Plinian deposits from the rhyolitic Taupo Volcanic Centre. New Zealand Journal of Geology and Geophysics. 24 305-324.

Walker, G.P.L., 1989. Spongy pahoehoe in Hawaii: a study of vesicle-distribution patterns in basalt and their significance. Bulletin of Volcanology. 51, 199-209.

Warshaw, C.M., Smith, R.L., 1988. Pyroxenes and fayalites in the Bandelier Tuff New Mexico: Temperatures and comparisons with other rhyolites. American Mineralogist. 73, 1025-1037.

Weaver, S.D., Gibson, I., Spiro, B., Houghton, B., Wilson, C., 1985. Rare-earth element mobility in peralkaline rhyolite obsidians, Mayor Island. Geological Society of New Zealand Miscellaneous Publication 32A p.88.

Westrich, H.R., 1987. Determination of water in volcanic glasses by Karl-Fischer titration. Chemical Geology. 63, 335-340.

Westrich, H.R., Eichelberger, V.C., 1985. Water content and lithology of Obsidian Dome flow Eos (American Geophysical Union Transactions) 65 (45) p1127.

Westrich, H.R., Stockman, H.W., Taylor, B.E., 1985. Volatile content of Obsidian Dome and the Inyo Dike. Eos (American Geophysical Union Transactions). 66(18) p387.

Westrich, H.R., Stockman, H.W., Eichelberger, J.C., 1988. Degassing of rhyolitic magma during ascent and emplacement. Journal of Geophysical Research. 93 B6, 6503-6511.

Westrich, H.R., Eichelberger, J.C., 1989. Obsidian lava: a permeable foam eruption model. Continental Magmatism Abstracts, IAVCEI General Assembly June 25 - July 1, 1989. Bull. 131 New Mexico Bureau of Mines and Mineral Resources p.291.

Whitham, A.G., Sparks, R.S.J., 1986. Stable isotope studies of the volatile history and degassing of ryholitic magmas in the Taupo Volcanic Zone, New Zealand. International Volcanological Congress New Zealand. Abstracts p217.

Whitney, J.A., 1975. The effects of pressure temperature and X H_2O on phase assemblage in four synthetic rock compositions Journal of Geology. 83(1), 1-32.

Whitney, J.A., 1988. The origin of granite: The role and source of water in the evolution of granitic magmas. Geological Society of America Bulletin. 100, 1886-1897.

Williams, H. McBirney, A.R., 1979. Volcanology. Freeman Cooper & Co. San Francisco.

Wilson, C.J.N., 1986. Tour C5. King Country Ignimbrites., in Houghton, B.F., Weaver, S.D., 1986. Taupo Volcanic Zone Tour Guide, New Zealand Geological Survey Record 11, 115-144.

Wilson, C.J.N., Rogan, A.M., Smith, I.E.M., Northey, D.J., Nairn, I.A., Houghton, B.F., 1984. Caldera Volcanoes of the Taupo Volcanic Zone, New Zealand. Journal of Geophysical Research. 89 B10, 8463-8484.

Wilson, C.J.N., Houghton, B.F., Lloyd, E.F., 1986. Volcanic History & Evolution of the Maroa-Taupo Area, Central North Island. Royal Society of New Zealand. Bull.23, 194-223.

Wilson, L., Head III, J.W., 1983. A comparison of volcanic eruption processes on Earth, Moon, Mars, Io and Venus. Nature. 302 (5910), 663-669.

Wilson, L., Pinkerton, H., Macdonald, R., 1987. Physical processes in volcanic eruptions. Annual Reviews of Earth and Planetary Sciences. 15, 73-95.

Wright, T.L., Kinoshita, W.T., Peck, D.L., 1968. March 1965 eruption of Kilauea Volcano and the formation of Makaopuhi Lava Lake. Journal of Geophysical Research. 73, 3181-3205.

Zimbelman, J.R., 1985. Estimates of rheological properties for flows on the Martian volcano Ascraeus Mons. Proceedings of the 16th Lunar and Planetary Science Conference, Part 1. Journal of Geophysical Research. 90 Supplement, 157-162.

APPENDIX I

SOUTHERN STARS

VOLUME 32 NO 8 1988 SEPTEMBER

OBSERVATIONS AND INFERENCES ON PLANETARY VOLCANISM FROM A TERRESTRIAL PERSPECTIVE*

Richard J Stevenson

Department of Earth Sciences,
University of Waikato, Hamilton.

ABSTRACT

From a terrestrial perspective, the nature of volcanic deposits on other planets is reviewed. The viscosity of extra-terrestrial lavas, calculated from flow morphology, gives an insight into lava composition. Ultimately, the range of lava types and their volcanic landforms provide insights into planetary evolution.

Introduction

Volcanic activity is a fundamental mechanism of heat loss from planetary interiors. The nature and stratigraphy of ancient volcanic deposits provides insights into:

1. The relation of volcanism to tectonism (internally derived deformation);

2. eruptive style; and

3. chemistry and volatile content.

The distribution and types of volcanic lavas and airfall deposits from currently active or extinct centres, gives an indication of the thermal and evolutionary state of a rocky planet. Volcanic deposits on planetary surfaces are either fragmental explosion-derived pyroclastic deposits (eg. volcanic ash), or effusive lava flows.

Lava flows on Earth have a range of compositions from low-silica fluid basalt flows of high length/height or aspect ratio, to high-silica viscous rhyolite flows of low aspect ratio. The properties of volcanic rock types, their origins and tectonic settings are listed in Table 1.

* Based on a paper presented at the 1987 Top Half Symposium, Rotorua.

Active basalt flows are usually fed by lava tubes (Greeley, 1987) where the hot molten lava is insulated by a chilled crust of vesicular blocky lava. An experimental analogy is a fluid clay slurry flowing down an incline. Rhyolite lava eruptions form short lobate flows with steep flow edges and may be modelled using a stiff water-poor clay slurry, or by squeezing thick honey out of a small opening. A relationship therefore exists between lava composition, morphology (eg. aspect ratio) and viscosity. By calculating the viscosity based on the morphology of arrested flows, the composition of the lavas on other planets can be deduced. Ancient flow deposits are observed on the surfaces of many planets. Although samples are not available for detailed study, volcanism on the **terrestrial** planets, including Io and the ice moons reviewed, provide insights into planetary evolution.

Viscosity of Lavas

The viscosity of lavas on Earth may be either measured on active flows in the field, or performed on samples under high temperatures in the laboratory. A more convenient method is calculating the viscosity based on the morphology of arrested flows (Hulme 1974) where terms for density (ρ), flow thickness (h), width (w) and basal slope (ϑ) may give yield strength (Y) by the following formula:

$$Y = \rho g h \sin \vartheta \qquad (1)$$

Yield strength is the resistance to deformation of the restraining lava skin or carapace.

Effusion rate (F) may be estimated incorporating a term for thermal diffusivity (κ) and flow length (L) by the following equation:

$$F = 300\ \kappa w/Lh \qquad (2)$$

Using equations (1) and (2), viscosity (η) is, for channelised flows, as is often the case for terrestrial basalts

$$\eta = w^3 Y \sin^2 \vartheta/24\ F \qquad (3)$$

and for non-channelised flows as for terrestrial rhyolite flows

$$\eta = w^{2.75} Y^{1.25} \sin^{1.5} \vartheta/24\ Fg^{.25} \rho^{.25} \qquad (4)$$

The above equations can be used to calculate the viscosity of lavas on other planets. Flow dimensions, using photo-interpretation methods (Moore et al. 1978), which include shadow length estimate to establish flow thicknesses, are subject to the image resolution of unmanned probe photographs.

Volcanism on Other Planets

Lunar Volcanic Deposits

Large low-relief flood basalt flows up to 1200 km length with flow-edge scarps 10-35 m height (Schaber, 1973) are associated with and fill giant impact basins (Fig. 1), suggesting very fluid lavas of low viscosity. High mass eruption rates are suggested by the extreme length of some lava flows and sinuous rilles, requiring fissure systems with widths of up to 10 m (Kaula et al. 1986).

This appears to be consistent with a lunar tectonic regime dominated by extensional fractures associated with the major impact basins. The eruption of lunar basalt lavas appears to be impact generated. Lunar basalt lavas show textures consistent with fairly rapid near-surface crystallisation of silicate melts (Lofgren et al, 1975). Large calderas are not expected on the moon. Calderas are formed by collapse or magma withdrawal into shallow chambers but lunar basalts probably do not accumulate in such chambers (Head, 1976). Unlike terrestrial basalts, lunar basalts contain no detectable water (BSVP. 1981). This implies that the viscosity must be different from Earth's volcanics of comparable basaltic materials or that the original lava temperature must be correspondingly higher. This is one of the reasons why there is no modern active lunar volcanism.

Mars

Mars shows a range of volcanic landforms, from flow plains (associated with Tharsis and Elysium) comprising flows hundreds of kilometres length and 10-80 m thick, to huge basaltic shields like Olympus Mons. The shield flanks contain coalesced pits and embayments inferred as the source of large quantities of lava forming fan-shaped flow arrays on lower slopes. The middle and upper slopes have a fine radial fabric caused by long thin flows and lava channels (Carr, 1984).

Inferences can be made about the composition of the flows from their shape, spectral reflectance data and composition of weathered debris at the Viking landing sites. Most data suggest that the flows are basic (low silica) and iron-rich. Moore et al. (1978) showed that the yield strength of a flow is dependent on local slopes and suggested that Martian flows are more akin to terrestrial basalt than more silica-rich andesites and rhyolites. The presence of lava channels and levees (lateral flow-edge ridges) and their extreme length suggest that they have rheologic properties similar to basalt.

Flow morphology has provided estimates of viscosity from 6.4 x 10^6 to 2.1 x 10^9 poise (poise: cgs unit of viscosity) for flows on Ascraeus Mons (Zimbelman, 1985). These are interpreted as more highly evolved basalts. Theilig and Greeley (1986) noted festoon and pressure ridges on some flows. Using a method for

calculation of viscosity from ridge spacing (Fink and Fletcher, 1978) they derived a value of 10^9 poise for the interior of these flows, inferring a high viscosity basalt owing to a high crystal content or cooler emplacement temperature. Cattermole (1987) deduced high effusion rates calculated from Alba Patera shield lavas of 5 - 1610 x 10^3 m^3/s for earlier flows.

Other volcanic features present include small cones $\leq$ 1 km size, cinder cones (Frey and Jarosewich, 1982), a young airfall deposit at Hecatus Tholus (Mouginis-Mark et al., 1982) and possible welded ash flow deposits (ignimbrites) (Scott, 1982). On Earth, ignimbrites are derived from vents that have collapsed to form calderas. Silicic lava domes usually form within or around the edge of the calderas (Cas & Wright, 1987). Such structures occur at continental subduction centres. According to Francis and Wood (1982), the identification of Martian ignimbrites by Scott and Tanaka (1982) is speculative and unfounded. Coulon and Thorpe (1981) suggest that the presence of granitic continental crust at least 25 km thick is essential for the production of large volume ignimbrites. The apparent lack of such large-scale silicic volcanism (>100 - 1000 km^3) on Mars is circumstantial evidence that Mars is deficient in volatiles and lacks a granitic crust.

Venus

Venera lander imagery shows surficial plates with polygonal vertical fractures, interpreted by Garvin et al (1984) as being analagous to terrestrial ropy basalt flows. Lava flows have been identified by Head and Wilson (1986) from low resolution Arecibo radar images. They predicted that shield volcanoes should be wide (several hundred km across) but low ($\leq$2 km high), as a larger temperature gradient exists and consequent shallow magma chambers. High atmospheric pressure (90 times Earth's) may retard bubble coalescence of magmas, making explosive volcanism unlikely.

Io

Active volcanism on Io was discovered during the Voyager fly-bys of 1979. Umbrella-shaped plumes up to 300 km high with ballistic velocities of 500-1000 m/s (Strom et al., 1981) were derived from low-relief caldera-like structures (Fig. 2). Smith et al., (1979a, b) and Sagan (1979) interpreted the lava flows associated with the calderas (eg. Ra Patera) as being entirely sulphur. However, Young (1984) argued, from precise colour interpretation, that no sulphur flows occur on Io and that the dark hot-spot caldera lava lakes are basalt. Although sulphur has been positively identified on Io, Carr (1986) believes that sulphuro-silicate volcanism is more likely, with a dominant silicate component, thus being able to support steep caldera scarps 2 km high (Clow & Carr, 1980).

McEwen and Soderblom (1985) have found hot-spot temperatures more consistent with liquid sulphur (perhaps ponding over a

silicate magma) with albedos and colours best matching sulphuro-silicate mixtures. The low albedo hot-spot areas appear to be lava lakes. Carr (1986) states that the implicit assumption made by McEwen & Soderblom is that the lava lakes are active and that the 400-600 K temperatures are too low for basaltic lavas. However, even if the lava had a chilled surface basaltic skin, temperatures may still be too low to support Carr's basalt-lake model.

This controversy may be resolved when Galileo orbits Jupiter's moons some time after 1992.

Ice Moons

A number of icy satellites show evidence of resurfacing. The most reasonable explanation is that the process was derived from within the body (Squyres and Croft, 1986). Ammonium hydrate melts of low viscosity (~10^2 poise), ascend via cracks to flood the surface (Stevenson, 1982).

Generally flow margins are difficult to observe because of the low resolution of the Voyager imagery (Allison & Clifford, 1987).

Resurfacing brine, slush or warm ice allows a wide range of estimated viscosities from 10^{-2} poise (water) to 10^{15} poise (ice, near melting) (Squyres & Croft, 1986). Smith et al (1986) identified possible flow features on Miranda (Fig. 3). Using equations 1, 2 and 4, (where ρ is assumed to be 0.93 g/cm^3, κ = 2 x 10^{-7} m^2/s, g = 0.039 m/s^2), viscosity is calculated as approximately 10^{12} poise, comparable to terrestrial glaciers (Selby, 1985). This value is similar to that inferred by Stevenson and Lunine (1986) who predicted short thick flows. They deduced that pressure solution creep (T $\leq$100 K) occurs in which very fine grained water ice or clathrate (~X.6H_2O; X = CO, N_2, CH_4) is mobilised by small amounts of intergranular cryogenic fluid (CH_4, CO or N_2). The presence of ices contaminated with low melting point condensates like NH_3 and CH_4 may have prolonged interior thermal activity and tectonic evolution for the small icy moons (Stevenson, 1987).

Summary

The viscosity of lava flows on the Moon and Mars can be calculated from an expression based on the morphology of the arrested flow (equations 3, 4). From the viscosities, the nature of the lava can be elucidated. Lunar flows are impact generated, filling impact basins. Martian flows are derived from magma chambers and are typically more evolved with characteristically higher inferred viscosities. Image resolution is poor for Venusian flows, as well as the icy flows responsible for flood resurfacing of the outer Solar System moons.

Table 2 shows a summary of volcanic landforms and deduced lava types, based on morphological calculations of lava viscosity for Moon and Mars and inferred for Venus, for Io and for the ice moons. Table 2 shows a much greater variety of terrestrial volcanic lava types as compared with the narrow compositional range of luna lavas. Lava compositions can provide a probe into the interior of a planet, and from the landforms and their stratigraphic relationships, the thermal and evolutionary history of planets can be deduced.

Crater ages and radiometric ages (from Apollo samples) suggest that the Moon has the oldest surface of the terrestrial planets. Lunar basalts are old (3.8 - 2.5 billion years before present) and form a small proportion of the lunar surface (Fig. 4a). Lavas are impact generated and water is absent.

Mars, being larger (lower surface-area/volume ratio), retained more heat and was able to - in addition to mare-style impact generated volcanism - show three phases of hot-spot volcanism: Hellas, Elysium and Tharsis (Tanaka, 1986) (Fig. 4b). Mars shows magma-chamber derived volcanism with large shield volcanoes composed of finger-like basaltic flows of higher viscosity, and less primitive magma compositions are inferred.

Venus shows a range of unusual tectonic features including ridge and groove terrain with horizontal and lateral deformation (Barsukov et al., 1986; Basilevsky et al., 1986). Volcanic features so far identified have been of poor resolution, but the products of volcanism are interpreted to be widespread (Head, 1986).

In contrast to the Moon and Mars (Figs. 4a, 4b), ~70% of the Earth's surface is ocean floor basaltic crust (0 - 180 million years age), ~30% being older continental crust (Fig. 4c). Also compared to the other planets, Earth has the greatest range of volcanic landforms and lava types. Active continental-arc volcanism (eg. Taupo Volcanic Zone) is expressed by a range of evolved lava types (eg. andesite, dacite, rhyolite) derived ultimately from partial melting of a subducted plate (Gill, 1981) or the inclusion of recycled continental crust (eg. Kay 1980, Hoffman and White, 1982). As these lavas are unique to Earth, this indicates that the Earth has the greatest tectonic and crustal evolution, and consequently greatest internal differentiation of the terrestrial planets.

Acknowledgement

It is a pleasure to thank Dr Peter Hodder (Department of Earth Sciences, University of Waikato) for helpful discussion and suggestions for this paper.

References

Allison, M.L., Clifford, S.M., 1987. Ice-covered water volcanism on Ganymede. *J. Geophys. Res.* 92, B8, 7865-7876.

Bursukov, V.L. et al., 1986. The Geology and Geopmorphology of the Venus surface as revealed by the radar images obtained by Veneras 15 and 16. *J. Geophys. Res.* 91, B4, 378-398.

Basaltic Volcanism Study Project, 1981. Basaltic Volcanism on the Terrestrial Planets. Pergamon Press, New York.

Basilevsky, A.T. et al., 1986. Styles of tectonic deformations on Venus: Analysis of Venera 15 and 16 Data. *J. Geophys. Res.* 91, B4, 399-411.

Carr, M.H. (ed), 1984. The Geology of the Terrestrial Planets. NASA SP469.

Carr, M.H., 1986. Silicate Volcanism on Io. *J. Geophys. Res.* 91, B3, 3521-3532.

Cas, R.A.F., and Wright, J.V., 1987. Volcanic Successions. Modern and Ancient. Allen & Unwin, 487p.

Cattermole, P., 1987. Sequence, Rheological properties and effusion rates of volcanic flows at Alba Patera, Mars. *J. Geophys. Res.* 92, B4, 553-560.

Clow, G.D., and Carr, M.H.,1980. Stability of Sulphur slopes on Io. *Icarus* 44, 268-279.

Coulin, C., Thorpe, R.S., 1981. Role of continental crust in petrogenesis of orogenic volcanic associations. *Tectonophysics* 77, 79-93.

Fink, J.H., and Fletcher, R.C., 1978. Ropy pahoehoe surface folding of a viscous fluid. *J. Volcanol. Geotherm. Res.* 4, 151-170.

Francis, P.W. and Wood, C.A., 1982. Absence of Silicic Volcanism on Mars: Implications for Crustal Composition and Volatile Abundance. *J. Geophys. Res.* 87, B12, 9881-9889.

Frey, H., Jarosewich, M., 1982. Sub-kilometer Martian volcanoes: Properties and possible Terrestrial analogs. *J. Geophys. Res.* 87, B12, 9867-9879.

Garvin, J.B., Head, J.W., Zuber, M.T., Helfenstein, P., 1984. Venus: The Nature of the surface from Venera Panoramas. *J. Geophys. Res.* 89, B5, 3381-3399.

Gill, J.B., 1981. Orogenic Andesites and Plate Tectonics. Springer-Verlag, Amsterdam.

Greeley, R., 1987. The role of lava tubes in Hawaiian Volcanoes, in *Volcanism in Hawaii USGS Prof. Paper 1350*, 1589-1602.

Head, J.W., 1976. Lunar volcanism in space and time. *Rev. Geophys. Space Phys.* 14, 265-300.

Head, J.W., Wilson, L., 1986. Volcanic processes and land forms on Venus. Theory predictions and Observations. *J. Geophys. Res.* 9407-9446.

Hoffman, A.W., White, W.M., 1982. Mantle plumes from ancient oceanic crust. *Earth Planet Sci. Lett.*, 57, 421-436.

Hulme, G., 1974. The Interpretation of Lava flow morphology. *Geophys. J.R. Astr. Soc.* 39, 361-383.

Kaula, W.M., Drake, M.J., Head, J.W., 1986. The Moon. In Burns, J.A., Matthews, M.S., (eds) Satellites p. 581-628. University of Arizona Press, Tuscon.

Kay, R.W., 1980. Volcanic arc magmas : implications of a melting-mixing model for element recycling in the crust-upper mantle system. *Journal of Geology*, 88, 497-522.

Lofgren, G.E., Donaldson, C.H., Usselman, T.M., 1975. Geology, petrology and crystallisation of Apollo 15 quartz-normative basalts. *Proc. Lunar Sci. Conf. 6th.* pp.79-99.

McEwen, A.S., Matheson, D.L., Johnson, T.V., Soderblom, L.A., 1985. Volcanic hot spots on Io: Correlation with low-albedo calderas. *J. Geophys. Res.* 90, B14, 1345-1379.

Moore, H.J., Arthus, D.W.G., Schaber, G.G., 1978. Yield strengths of flows on the Earth, Mars, and Moon. *Proc. Lunar Planet. Conf. 9th*, 3351-3378.

Mouginis-Mark, P.J., Wilson, L., Head, J.W., 1982. Explosive volcanism on Hecatus Tholus, Mars: Investigation of eruption conditions. *J. Geophys. Res.* 87, B12, 9890-9904.

Sagan, C., 1979. Sulphur Flows on Io. *Nature* 280, 750-753.

Schaber, G.G., 1973. Lava flows in Mare Imbrium: Geologic evidence from Apollo orbital photography. *Proc. Lunar Sci. Conf.* 4, 73-92.

Scott, D.H., 1982. Volcanoes and volcanic provinces: Martian Western Hemisphere. *J. Geophys. Res.* 87, B12, 9839-9851.

Scott, D.H., Tanaka, K.L., 1982. Ignimbrites of Amazonis Planitia region of Mars. *J. Geophys. Res.* 87, 1179-1190.

Selby, M.J. 1985. Earth's changing surface. Clarendon Press, Oxford.

Smith, B.A. et al., 1979(a). The Jupiter system through the eyes of Voyager 1. *Science* 204, 951-972, 1979.

Smith, B.A. et al., 1979(b). The Galilean Satellites and Jupiter, Voyager 2 Imaging Results. *Science* 206, 927-950.

Smith, B.A. et al., 1986. Voyager 2 in the Uranian system: Imaging science results. *Science* 233, 43-64.

Squyres, S.W., Croft, S.K., 1986. The tectonics of icy satellites in Burns, J.A., Matthews, M.S., (eds). Satellites p.293-341. University of Arizone Press, Tuscon.

Stevenson, D.J., 1982. Vulcanism and Igneous processes in small, icy satellites. *Nature* 298, 142-144.

Stevenson, D.J. and Lunine, J.I., 1986. Mobilisation of cryogenic ice in outer Solar System satellites. *Nature* 323, 46-48.

Stevenson, R.J., 1987. An evolutionary framework for the Jovian and Saturnian satellites. *Earth, Moon and Planets* 39, 225-236.

Strom, R.J., Schneider, N.M., Terrile, R.J., Cook II, A.F., Hanson, C., 1981. Volcanic eruptions on Io. *J. Geophys. Res.* 86, 8593-8620.

Tanaka, K.L., 1986. The stratigraphy of Mars. Proc. 17th Lunar and Planet. Sci. Conf. Part 1. *J. Geophys. Res.* 91, B13, 139-158.

Theilig, E., and Greeley, R., 1986. Lava flows on Mars: Analysis of small surface features and comparisons with terrestrial analogs. Proc. 17th Lunar and Planet. Sci. Conf. Part 1. *J. Geophys. Res.* 91, B13, 193-206.

Young, A.T., 1984. No sulfur flows on Io. *Icarus* 58, 197-226.

Zimbelman, J.R., 1985. Estimates of Rheologic properties of flows on the Martian Volcano Ascraeus Mons. Proc. 16th Lunar and Planet. Sci. Conf. Part 1. *J. Geophys. Res.* 90 Supplement D157-162.

TABLE 1

	Basalt	Andesite	Dacite	Rhyolite
Origin	Partial melt	partial melt of subducted plate + crustal contamination.		
Tectonic setting	Subduction zone hot-spot mid-ocean ridge	Subduction zone - continental volcanic arc.		
SiO %	45-52	57-63	63-68	70
Temperature t (°C)	1000-1200	950-1200	800-1100	700-900
Density g/cm³	2.6-2.7	2.4-2.5	2.3	2.2-2.3
Yield strength Y (Pa)	10^3	10^4	10^4 -10^5	10^5 -10^6
Viscosity η (poise)	10^2 -10^4	10^7 -10^8	10^9	10^{10} -10^{12}
Aspect ratio (L/h)	100-3000 high	300-100	50-5	<50 flows <10 domes low
Flow rate m³/s	100-5000 high			0.3-20 low
Silicate structure	single SiO_4^-			long chain -Si-O- polymers
Silicate composition	olivine, plagioclase - discrete crystals phenocrysts + ground mass.			phenocrysts and metastable glass

TABLE 1: Distinguishing features of terrestrial volcanic rock types.

TABLE 2: (next page) Summary of volcanic land forms and inferred lava types present on the terrestrial planets, Io and the ice moons.

TABLE 2

VOLCANIC LAND FORM

	Flood flows in impacts	Sinuous flows	Shields	Cones	Tuff rings	Stratovolcanoes	Calderas	Domes
Moon	✓	✓	x	x	x	x	x	x
Mercury	✓	✓	x	x	x	x	x	x
Mars	✓	✓	✓	✓	?	x	?	x
Venus	✓	✓	✓	?	?	X	coronae	X
Earth	✓	✓	✓	✓	✓	✓	✓	✓
Io	covered	✓	✓	x	✓	x	paterae	x

Ice moons: flood resurfacing, flows associated with faults and rifts.

LAVA - TYPE.

	Basalts	Alkali basalts	Andesites	Rhyolites	Sulphuro-silicate	Ice + $NH_3.H_2O$
Moon	✓	-	-	-	-	-
Mercury	✓	-	-	-	-	-
Mars	✓	✓	?	-	-	-
Venus	✓	✓	?	-	-	-
Earth	✓	✓	✓	✓	-	-
Io	✓	?	-	-	✓	-
Ice moons	-	-	-	-	-	✓

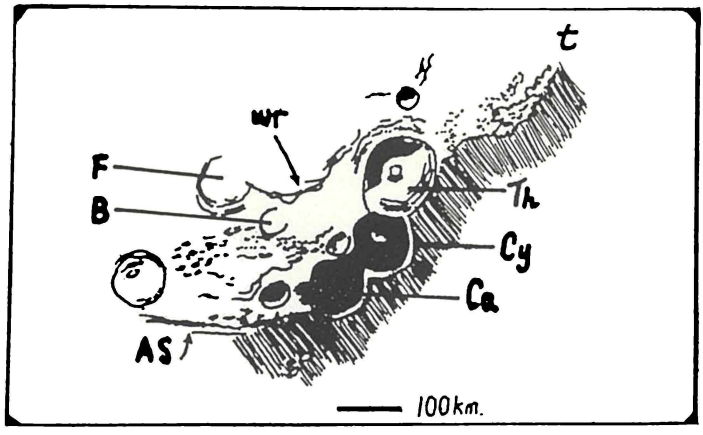

Fig. 1: Sketch of a small part of Mare Nectaris (from an observation made on 9/9/86), showing superposition of geological units. The older craters [Catherina (Ca), Cyrillus (Cy), Fracastorius (F), Beaumont (B)] impacted onto Nectarian basin inner deposits (primary ejecta and ring materials) - 3.92 b.y. age. The inner edge of Cyrillus and Catherina partly defines the middle ring scarp of the Nectaris impact. The Altai scarp (AS) is the outer ring. Old basalts at the centre of Nectaris were covered with 3.8 - 3.3 b.y. basalt flows related to the huge Imbrium impact - 3.8 b.yrs. ago, post-dating Nectaris. These basalts flooded old craters such as Fracastorius and Beaumont. Compressional wrinkle ridges (wr) formed on the mare basalt plains at this time. About 2 b.y. ago, Theophilus (Th) impacted, obliterating a former Nectarian crater and destroying the edge of the older Cyrillus.

Next page:
Fig. 2: Ionian volcanic landscape; a painting by R. Stevenson, 1984.

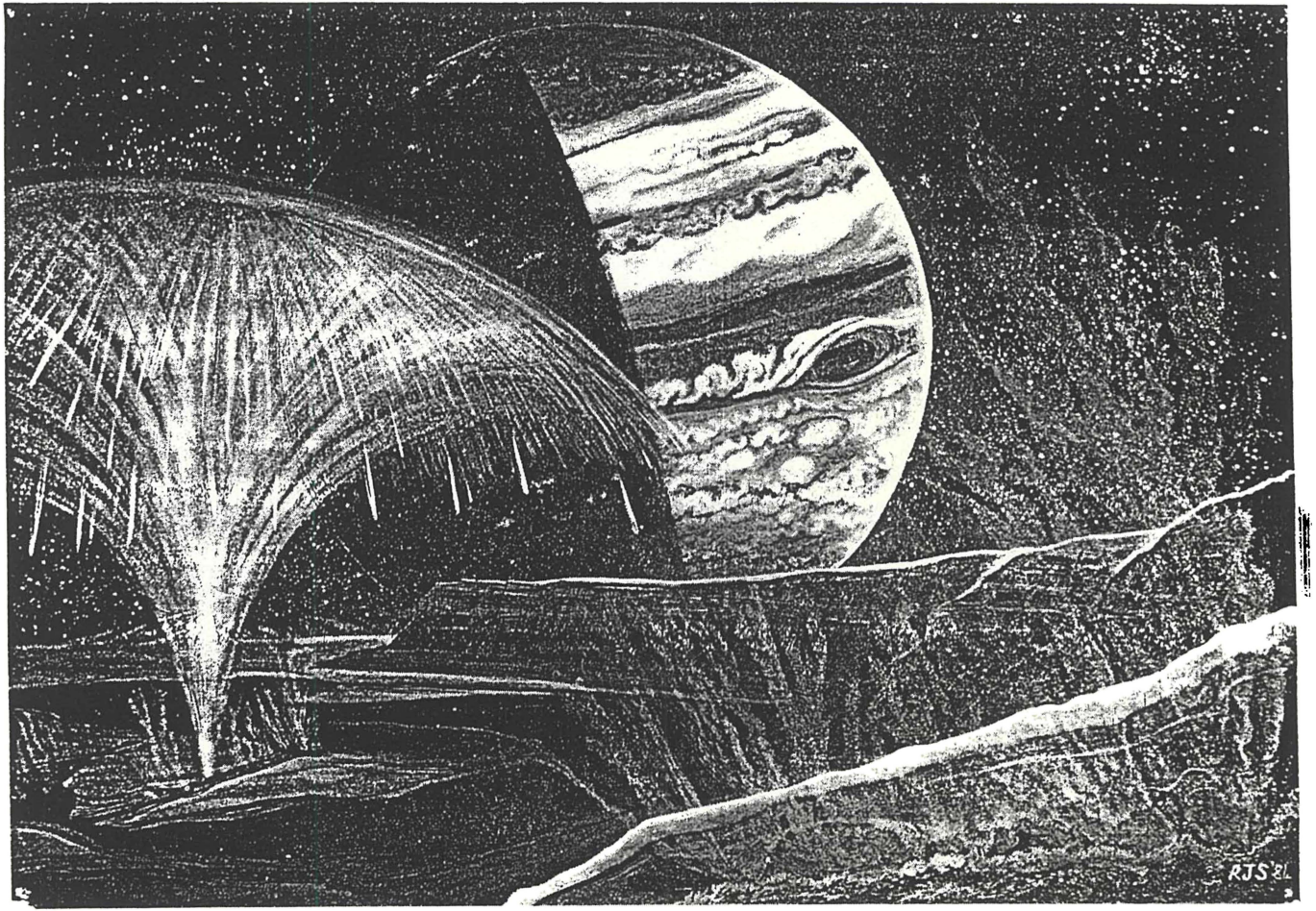
RJS '81

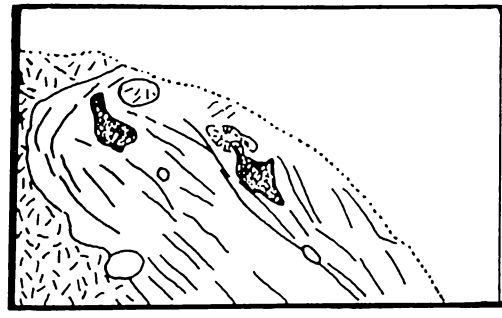

Fig. 3: Possible flow features (stippled) in the grooved terrain of Miranda (based on Smith et al., 1986).

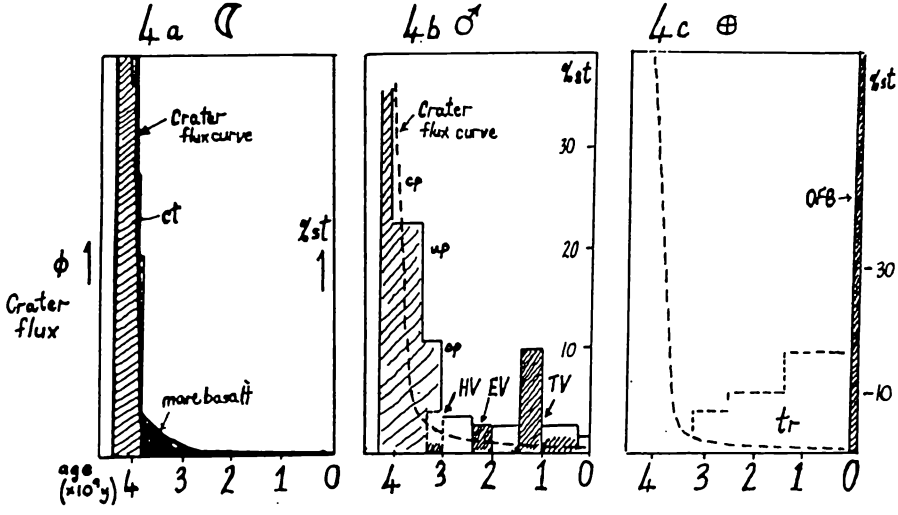

Fig. 4: Crater flux (Φ) and proportion of surface terrain (st) vs. age of geological units for the Moon (4a), Mars (4b) and Earth (4c).

Footnote: 4a ct = cratered terrain (Imbrium and preImbrium)
4b cp = cratered plains HV = Hellas Volcanism
up = upland plains EV = Elysium Volcanism
op = outwash plains TV = Tharsis Volcanism
4c tr = continental terrestrial rocks
OFB = ocean floor basalt

APPENDIX II

DRY DENSITY AND POROSITY DETERMINATIONS

BEN LOMOND

site	lithology	no.	$\bar{\rho}$	1s	$\bar{P}_1$	1s	$\bar{P}_2$	1s
s7	carapace plates	25	2.02	0.14	3.97	3.11	11.72	5.99
s7	carapace pumice	8	1.39	0.14	40.07	5.28	40.57	5.32
s7	Low density	(4)	1.27	0.02	44.40	3.68	45.30	2.35
	high density pumice	(4)	1.52	0.03	35.74	1.22	35.83	0.84
"	vesicular clasts	4	1.97	0.06	9.97	1.83	16.27	2.40
"	grey obs cl (expl.br)	3	2.21	0.06	5.55	2.44	6.09	2.59
"	brown perlite	7	2.26	0.03	4.72	2.70	4.18	1.30
"	spherulitic obsidian	14	2.16	0.07	7.46	3.21	7.59	2.85
"	explosion breccia	9	1.82	0.05	21.26	2.15	22.57	2.09
s11	grey lin. obs	10	2.35	0.002	0.08	0.03	0.15	0.10
s11b	spherulitic obs	8	2.20	0.035	5.68	1.64	6.62	1.47
s10b	spherulitic obs	9	1.88	0.01	18.83	5.38	19.99	4.19
s16	RHY	11	2.21	0.05	10.66	2.02	6.01	2.08
s6	RHY	11	2.28	0.03	7.60	0.93	3.05	1.09
s1	black obs	6	2.35	0.003	0.09	0.02	0.49	0.44
"	flecked obs	8	2.33	0.005	0.14	0.06	1.12	0.22
"	black obs	5	2.34	0.015	0.83	0.76	0.84	0.67
"	spherulitic obs	5	2.31	0.04	7.95	1.41	5.96	1.59
"	spherulitic obs	6	2.10	0.04	12.05	2.11	10.82	1.58
" (Tz)	brown glass	7	2.29	0.04	3.07	2.64	2.68	1.87
s1-s (Tz)	brown glass	8	2.33	0.02	0.16	0.09	1.18	0.64

$\bar{P}_1 = (M_{sat} - M_{dry}/\rho_w) / V_t \times 100\%$ $\quad \bar{P}_2 = (- Mdry/\rho g) + V_t / V_t \times 100\%$

$\bar{P}_1$ = apparant or effective porosity. Values are usually lower than $\bar{P}_2$ (true porosity) as interior voids are not saturated.

NB. all other porosity values are P_1.

MAYOR ISLAND.

unit	site	height(m)	$\bar{P}$	1s	$\bar{P}$	1s	no.
		TOKOMATA POINT			PANUI FLOW		
FVP	Zy	1.2	1.61	0.21	28.33	11.45	10
FVP	s1	0.2	1.77	0.05	24.08	3.00	5
OBS	s2	0.8	2.20	0.04	2.455	0.89	5
OBS	s3	1.8	2.31	0.03	2.463	0.89	5
OBS	s4	3.4	2.38	0.03	0.85	0.61	6
OBS	s5	4.0	2.41	0.02	0.642	0.42	6
OBS	s6	5.4	2.41	0.006	0.27	0.15	6
U.OBS	s7	5.75	2.42	0.004	0.266	0.05	6
U.OBS	s8	7.10	2.40	0.003	0.262	0.16	4
U.OBS	s9	7.90	2.40	0.086	2.99	1.67	7
U,OBS	s11	8.20	2.40	0.007	2.24	0.90	7
RHY	s10	8.80	2.35	0.025	9.51	0.51	5
RHY	R1	10.0	2.31	0.053	10.70	1.75	7
RHY	R2	11.15	2.33	0.036	9.62	0.75	10
RHY	R3	12.60	2.33	0.014	10.34	1.14	6

T13		TOKOMATA PT					
FVP	s1	1.80	1.57	0.05	33.95	3.03	6
FVP	s2	2.75	1.50	0.25	34.87	12.74	8
OBS	s3	4.30	2.39	0.29	1.44	1.19	5
RHY	s4	5.35	2.39	0.028	7.93	1.04	6
RHY	R4	10.4	2.36	0.018	10.69	0.82	6
RHY	s5	7.20	2.35	0.01	9.34	0.32	7
RHY	s5b	8.65	2.34	0.06	10.04	0.90	5
RHY	s6	10.4	2.376	0.0099	9.58	0.58	4
RHY	s6g	10.4	1.695	0.013	36.39	0.47	5

TE MORE-O-MOITERANGI

OBS	s1	0	2.362	0.014	1.22	0.65	6
RHY	s2	4	1.973	0.012	24.03	4.55	11
RHY	s3	6.0	2.169	0.076	14.03	2.12	4
RHY	s4	4.4	1.992	0.024	23.03	1.23	9
RHY	s5	2.8	1.823	0.06	30.58	2.34	6
RHY	s6	1.2	2.015	0.14	25.44	11.78	7

OBS	s7	7.40(o)	2.054	0.09	12.46	1.76	5
OBS	s8a	0.1	2.215	0.035	9.649	1.59	6
OBS	s8b	0.5	2.406	0.003	0.434	0.103	5
OBS	s9	0.6	2.363	0.007	1.037	0.31	6
BR	s10	7.0	2.034	0.06	16.02	3.16	12
BR pumice	s11	7.0	1.613	0.031	24.49	1.98	5
BR(OBS)	s12	10.8	2.408	0.004	0.244	0.09	9
BR	s13	10.7	2.086	0.09	12.55	3.23	6
BR	s14	1.25	1.65	0.063	31.97	3.86	8

CENTRAL TARARUMI — UPPER PRE-8ka flow

	site	fabric unit	height(m)	$\bar{\rho}$	1s	$\bar{P}$	1s	no.
top	s1	FVP	0.20	1.08	0.04	42.40	1.95	3
	s2	FVP	0.55	1.52	0.07	27.16	3.95	3
	s3	FVP	0.75	1.51	0.02	25.64	2.19	3
	s4	FVP	0.95	1.42	0.14	32.10	7.17	4
	s5, s5b	U.OBS	1.25	2.39	0.004	0.20	0.22	6
	s6	RHY	1.80	2.15	0.024	12.48	1.27	4
	s7	RHY	2.20	2.14	0.037	16.64	2.35	5
	s8	RHY	2.85	2.09	0.052	17.13	2.21	6
	s9	RHY	4.50	1.82	0.069	31.06	3.02	4
base	s10	RHY	5.00	1.91	0.088	27.71	3.61	5

PIGHUNTERS PASS BASAL PRE-8ka flow

	unit	site	height (m)	$\bar{\rho}$	1s	$\bar{P}$	1s	number
base	tuff	s1	-0.1	1.59	0.006	35.01	.24	n=3
	BR pumice	s2	0.25	1.52	0.02	26.64	2.95	n=3
	"	s3	0.9	1.31	0.18	32.93	3.86	n=3
	"	s4	1.25	1.71	0.02	21.93	0.84	n=3
	"	s5	1.75	1.24	0.14	38.96	4.28	n=3
	"	s6	1.90	1.06	0.24	46.33	9.72	n=3
	"	s7	2.10	1.38	0.09	33.49	5.87	n=3
	L.OBS	s8	2.20	2.23	0.04	0.42	0.43	n=4
	L.OBS	s9	2.40	2.29	0.10	2.76	2.29	n=4
	L.OBS	s10	2.50	1.70	0.15	15.50	2.71	n=3
	BR.	s6*	1.90	1.80	0.06	18.08	2.46	n=3
	RHY/L.OBS	s11	2.60	2.13	0.20	15.66	9.74	n=3
	RHY	s12	2.70	2.13	0.06	14.12	3.71	n=5
	RHY	s13	3.00	2.10	0.02	17.61	0.89	n=5
	RHY	s14	3.20	2.09	0.012	18.42	0.33	n=2
top	RHY	s15	4.20	2.19	0.09	14.02	3.52	n=4
base	BR clast (basaltic)	s17(1)	0.05	2.03	0.03	19.86	2.36	n=3
	" " "	s17(2)	0.05	1.44	0.05	27.80	2.04	n=4
	" " (obsid.)	s18	0. 0	2.38	0.05	0.438	0.53	n=3
	" " "	s19	1.00	2.29	0.02	5.964	0.70	n=4
	" " (rhyol.)	s20	1.30	2.14	0.03	10.03	1.73	n=3
top	" " "	s21	2.00	2.16	0.01	5.54	0.61	n=3
	" " "	s22	1.60	2.20	0.04	10.01	1.98	n=3

HALLS PASS (8ka flow)

unit	sample site	height (m)	$\bar{\rho}$	1s.	$\bar{P}$	1s	number
top ↑	s1	0.6	1.460	0.18	29.10	4.89	4
	s2	1.8	1.38	0.05	32.92	2.97	4
F.V.P.	s3	2.2	2.03	0.004	10.55	0.81	2
	s4	2.6	1.65	0.09	25.29	4.42	3
	s5	3.9	1.75	0.07	14.42	1.795	3
	s6	4.2	2.27	0.01	3.52	1.59	3
↓	s7	5.2	1.81	0.05	12.49	2.31	7
↑	s8	5.6	2.26	0.015	4.299	0.69	3
U.OBS ↓	s9a	6.6	1.86	0.035	29.40	1.24	5
	s9b	6.6	1.95	0.08	23.06	4.08	4
↑	s10	7.1	2.14	0.022	18.21	0.53	3
	s11	8.0	2.10	0.03	20.34	1.25	3
	s12	13.6	1.90	0.098	28.07	0.21	2
	s13	19.2	2.22	0.044	16.17	1.72	7
*	s14	23.8	2.26	0.030	6.49	1.28	5
*	s15	25.7	2.35	0.04	1.93	1.54	3
	s16	23.5	2.20	-	15.08	-	1
RHY	s17	26.4	2.38	0.03	12.55	2.00	6
base ↓	s18	35.2	2.25	0.02	14.40	0.93	6
top ↓	s19	0.24	2.18	0.117	12.32	7.38	2
	s20	0.42	2.14	0.05	11.09	2.22	5
↑	s21	0.60	2.29	0.08	3.60	2.30	7
	s22	0.70	2.39	0.02	0.864	0.65	4
L.OBS.	s23	0.80	2.42	0.003	0.294	0.21	5
↓	s24	1.12	2.39	0.02	1.44	0.85	6
8ka lapilli — fused	s25	1.24	2.22	0.02	10.20	1.25	4
8ka lapilli	s26	1.64	1.46	0.07	29.64	2.39	6
alluvial layer	s27	1.96	1.47	0.05	39.05	2.24	8
8ka lapilli	s28	1.28	1.60	0.05	26.89	3.86	2
base							

s19-28 = basal Halls Pass (2π section Fig.(5.14b)

* basal obs selvedge (Halls Pass) area A, (Fig. 5.14a)

PAREKOURA POINT (Upper 8km flow)

	unit		sample site	h(m)	$\bar{\rho}$	1s	$\bar{P}$	1s.	no.
top	UNIT A TUHUA		s1	-	3.679	0.120	67.74	3.04	6
		FVP	s2	0.6	1.007	0.05	17.23	2.05	4
		FVP	s3	1.4	1.247	0.10	39.54	4.73	5
		FVP	s7	3.1	1.246	0.06	n=3, 5.417 ± 1.24 n=2 44.67 ± 0.41		5
		FVP	s8	7.8	0.95	0.11	51.19	8.84	6
		FVP/OBS	s9	9	1.841	0.23	18.55	6.76	
	Pink	OBS	N1		2.268	0.065	0.77	0.66	9
	flecked	OBS	N2		2.308	0.018	0.65 ± 1.10 (n=4 3.15 ± 0.06)		5
	flecked	OBS	N3		2.245	0.085	2.061	1.42	4
	yellow	OBS	N4		2.163	0.04	0.75	0.16	5
	black	OBS	N5		2.152	0.03	1.52	1.67	2
		RHY	N6'		2.072	0.06	23.02	2.31	5
	black	OBS	N7		2.143	0.03	8.71	0.13	2
	black	OBS	N8		2.329	0.01	2.47	0.44	3
		RHY	R1	14.6	1.835	0.027	26.89	0.74	3
			R2	15.2	2.033	.084	11.46	4.34	5
		RHY	R3	16.4	2.133	0.07	15.06	6.75	8
base		RHY	R4	17	1.842	0.23	25.72	10.02	6
top	vertical OBS ridge profile		L1	10.4	2.364 1.841	0.003 0.131	1.595 18.61	0.02 3.11	2 3
			L2	11	2.287	0.04	5.49	1.72	5
			L2b	11.	2.357	0.012	2.25	0.56	3
			L4	11.7	2.376	0.006	0.149	0.036	5
			L5	12.4	2.426	0.004	0.17	0.10(n=4)	5
			01	12.4	2.345	0.01	0.25	0.11	5
base			s5b	12.6	2.081	0.05	6.73	3.51	5

Fig 5.17c. (Lateral section OBS UNIT)

PAUAHAU

		no.	h(m)	$\bar{\rho}$ ± 1s	$\bar{P}$ ± 1s
(top)	P4	12	(+6m)	2.46 ± .02	1.41 ± .68
flow 3	s1	10	3.1	2.43 ± .03	3.55 ±1.63
	s2	9	9.8	2.15 ± .07	14.61 ±3.16
	s3	10	11.4	2.00 ± .06	19.63 ±2.13
	s4 (br)	7	13.8	2.16 ± .03	13.77 ±1.03
	s5	7	16.8	2.24 ± .07	13.16 ±3.12
	s6 (br)	9	19.3	2.15 ± .03	14.27 ±1.20
	s7	12	20.6	2.10 ± .04	17.17 ±2.10
	s8 (br)	5	22.1	2.31 ± .03	6.19 ±1.25
	s9	9	25.4	2.34 ± .02	6.76 ± .83
	s10	10	30	2.37 ± .03	7.33 ± .98
	s11	10	34.1	2.42 ± .03	4.93 ± .88
	(P3.1)	12	38.7	2.32 ± .05	6.52 ± 1.22
	s14	5	41.7	2.27 ± .04	10.05 ± 1.19
	s15	5	42.8	2.33 ± .03	7.31 ± 0.95
	$I_{2.2}$ (br)	11	43.2	2.34 ± .01	7.76 ±0.87
	$I_{2.1}$ (br)	11	49.3	2.21 ± .025	10.87 ±0.81
	I_1	7	51.8	2.16 ± .097	13.57 ±4.05
flow 2	s18 H(banded)	7	53.15	2.01 ± .09	19.35 ±3.99
	s19 H brecciated	7	54.25	1.84 ± .024	26.87 ± .93
	s20 H/g	6	55.50	2.15 ± .04	13.89 ±1.69
	s21 g	7	57.1	2.15 ± .05	14.38 ± 2.37
	s22 g	6	58.55	2.20 ± .04	11.92 ± 1.73
	s23 F3	7	59.54	2.06 ± .03	17.24 ± 1.28
	F2	6	59.59	2.07 ± .06	15.12 ± 2.50
	F1a	7	59.73	2.27 ± .03	8.88 ± 0.95
	F1a	3	59.85	2.24 ± .01	9.48 ± 0.51
	F/E	2	59.88	2.31 ± .04	7.27 ± 1.58
	Eu	4	59.93	2.30 ± .01	7.94 ± 0.36
	Em br	4	60.13	2.27 ± .07	8.84 ± 2.31
	E1	6	60.43	1.90 ± .11	23.12 ± 4.26
	D s24	6	60.71	1.81 ± .06	28.45 ± 2.54
upper flow 1	c4 s25	7	64.41	2.35 ± .006	6.66 ± .22
	c4/2 s26	10	64.91	2.18 ± .039	13.03 ± 1.72
	c4b s27	4	64.45	2.35 ± .008	6.52 ± .25
	B s28	7	62.91	2.34 ± .022	7.19 ± .93
	P3.2 (A1 s44)	14	65.4	2.33 ± .02	5.37 ± .53

base